

Investigation into the use of Carbon Nanofilaments in Bone Repair Applications

Daniel Mark Walter BSc (Hons)



Thesis submitted to the University of Nottingham for the degree
of Doctor of Philosophy, June 2007

Abstract

The potential of carbon nanofilaments for use in surface modification of implants and as fillers in biocompatible polymer composites was investigated with particular respect to nanofilament size and structure. Carbon nanofilaments were synthesised using chemical vapour deposition or obtained commercially, which provided a range of carbon nanofilament average diameters (13 nm, 134 nm, 142 nm, 155 nm) and structures (platelet, platelet and herringbone, multi-walled nanotubes and vapour-grown nanofibres).

The topography and texture of pressed nanofilament substrates was dependent on the nature of the nanofilaments, producing lower micron-scale roughness (R_a) values in the GNF samples (0.5-2.0 μm) compared to the MWNT9 and PR19PS substrates (3-4 μm), but no significant differences in nanoscale roughness ($R_a \sim 150$ nm). Human osteoblast response to these substrates was measured. Cells attached and spread to substrates with average nanofilament diameters of 134-155 nm (GNF1, GNF3 and PR19PS) rather than 13 nm (MWNT9) after 90 minutes, but proliferated and differentiated greater on the rougher nanotube samples over 14 days (MWNT9 and PR19PS).

Investigation of polymer/carbon nanofilament composites revealed the following. Low concentrations of nanofilament addition into poly(ethyl methacrylate)/tetra furfuryl methacrylate reduced the surface roughness of the polymer (R_a : 1.7 μm) by up to 88 % (5 wt% GNF composite), and reduced the storage modulus by 26-68 % of the unfilled polymer (1591 MPa at 37 °C). The electrical resistivity of the composites was significantly reduced

due to addition of nanofilaments; all samples reaching percolation just above 10 wt% but with different resistivities ($\sim 30 \Omega \cdot \text{m}$ at 15 wt% PR19PS, $\sim 10 \Omega \cdot \text{m}$ at 15 wt% GNF and $\sim 0.15 \Omega \cdot \text{m}$ at 15 wt% MWNT9).

Human osteoblast attachment on the PEMA/THFMA composites followed trends in roughness, attaching in higher quantities but with less spreading to rougher surfaces (i.e. higher nanofilament concentrations) on all samples except on the 5 wt% MWNT9 composite, which showed high spreading and attachment. This sample also showed the greatest degree of proliferation and differentiation over 14 days of culture. Faradic stimulation of human osteoblasts was investigated by pulsing 10 μA of electrical current through 5 wt% MWNT9 composite samples for 6 hours daily over 14 days. There was a slight increase in osteoblast proliferation when stimulating the 5 wt% MWNT9 composite sample with pulsed current compared to unstimulated 5 wt% MWNT9 composite controls.

The investigation indicated that the size and nature of carbon nanofilaments affected the surface and bulk properties of pressed nanofilament substrates and nanofilament -PEMA/THFMA composites. Human osteoblasts responded to the size of nanofilaments, especially their diameter, but also with respect to their effect on surface roughness. This was thought to be related to their dimensional similarity to extracellular matrix components in bone tissue. Carbon nanofilaments could therefore potentially be used to texture surfaces and improve bulk properties in biomaterials, particularly in total joint components, bone cements, or tissue engineered scaffolds that could also be electrically stimulated to promote osseointegration. This work also instigates further investigation into the toxicity and reinforcing capabilities of carbon nanofilaments.

Acknowledgements

There are so many people who have helped and supported me throughout this project. I would like to take this opportunity to thank both my supervisors, Gavin Walker and Colin Scotchford, for all their help, assistance and guidance. I would also like to thank all of the technical staff, especially Keith Dinsdale, who helped with most of the techniques used, as well as making me laugh. My thanks also go to Terry Parker, John Middleton, Steve Booth and Jonathan Radcliffe, who all assisted in the design, set-up and testing of the electrical stimulation work.

The support of both the Biomaterials and Carbon/Hydrogen research groups have been an amazing help and made the whole experience great fun. Wolfson W204 office, may she rest in peace and all who had coffee in her. Long live W301! I have appreciated all the support from those at Trinity; you've been a great encouragement and a breath of fresh air.

Special thanks go to my family, without whom none of this could have happened and especially to Vic, you are truly amazing.

Contents

Abstract	i
Acknowledgements	iii
Contents	iv
List of Abbreviations	vi
1. Introduction	1
2. Literature Review	5
2.1. The Problem with Bone Repair	5
2.1.1. Structure and function of bone	5
2.1.2. Bone injury	13
2.1.3. Bone repair materials and their limitations	15
2.2. Carbon Nanofilaments	17
2.2.1. Nanofilament structure and synthesis	18
2.2.2. Nanofilament properties	26
2.3. The Potential of Carbon Nanofilaments in Bone Repair	30
2.3.1. Surface modification of biomaterials	31
2.3.2. Improvement of bulk properties of implants	39
2.3.3. Electrical stimulation of osteogenesis	49
2.3.4. Biomedical concerns of carbon nanofilaments	56
2.4. Summary	59
3. Carbon Nanofilament Preparation and Characterisation	61
3.1. Introduction	61
3.2. Materials and Methods	63
3.2.1. Catalyst Preparation	63
3.2.2. Chemical vapour deposition	64
3.2.3. Pyrograf® III sample	66
3.2.4. Summary of samples	66
3.2.5. Purification techniques	67
3.2.6. Characterisation techniques	67
3.3. Results	69
3.3.1. CVD yields	69
3.3.2. Nanofilament characterisation	70
3.4. Discussion	81
4. Investigation of Osteoblast Response to Pressed Nanofilament Substrates	86
4.1. Introduction	86
4.2. Materials and Methods	88
4.2.1. Nanofilament Pressing	88
4.2.2. Nanofilament disc characterisation	89
4.2.3. Osteoblast attachment studies	90
4.2.4. Proliferation and differentiation of human osteoblasts	92
4.2.5. Statistical analysis	94
4.3. Results	94
4.3.1. Surface composition, morphology and topography	94
4.3.2. Osteoblast attachment results	99
4.3.3. Osteoblast proliferation results	103
4.4. Discussion	106

5. Investigation Osteoblast responses to Carbon Nanofilament-Methacrylate Composites.....	116
5.1. Introduction	116
5.2. Methods	118
5.2.1. PEMA/THFMA preparation	118
5.2.2. Nanofilament incorporation	118
5.2.3. Composite characterisation	119
5.2.4. Osteoblast Attachment studies	120
5.2.5. Proliferation and differentiation of HOBs	121
5.2.6. Statistical analysis	121
5.3. Results	122
5.3.1. Carbon incorporation into carbon-composites.....	122
5.3.2. Dynamic mechanical analysis of composites.....	123
5.3.3. Temperature Transitions in the composites.....	127
5.3.4. Morphology and topography of the composites.....	128
5.3.5. Osteoblast attachment results.....	138
5.3.6. Osteoblast proliferation and differentiation results	141
5.4. Discussion	146
6. Electrical Stimulation of Human Osteoblasts Using Carbon Nanofilament Composites	158
6.1. Introduction	158
6.2. Methods	161
6.2.1. Composite preparation	161
6.2.2. Four-point probe resistivity measurements	162
6.2.3. Rig assembly for stimulation of osteoblasts.....	163
6.2.4. Electrical stimulation of osteoblasts	166
6.2.5. Statistical analysis	166
6.3. Results	167
6.3.1. Resistivity of carbon nanofilament-composites	167
6.3.2. Human osteoblast response to electrically stimulated composites	168
6.4. Discussion	170
7. General Discussion	177
8. Conclusions.....	183
9. Suggested Future Work	186
10. References.....	188
11. Appendix: <i>An in vitro study of the potential of Carbon Nanotubes and Nanofibres to Induce Inflammatory Mediators and Frustrated Phagocytosis.....</i>	200

List of Abbreviations

4-HNE	4-hydroxynonenal
AB	Alamar blue
AFM	Atomic force microscopy
ALP	Alkaline phosphatase
ANOVA	Analysis of variance
BET	Brunauer, Emmett and Teller surface area
BPO	Benzoyl peroxide
CLSM	Confocal laser scanning microscopy
CNT	Carbon nanotube
-COOH	Carboxyl groups
CVD	Chemical vapour deposition
d.c.	Direct current
DABCO	1,4-diazabicyclo[2.2.2]octane
DLS	Dynamic light scattering
DMA	Dynamic Mechanical Analysis
DMEM	Dulbecco's modified Eagle's medium
DmpT	N,N dimethyl-p-toluidine
DNA	Deoxyribonucleic acid
DSC	Differential scanning calorimetry
E	Young's modulus
E'	Storage modulus
E''	Loss modulus
EAD	Electric arc discharge
ECM	Extracellular matrix
EDTA	Ethylene diamine tetraacetic acid
EDX	Energy dispersive X-ray
ESEM	Environmental Scanning Electron Microscopy

FBS	Foetal bovine serum
GNF	Graphitic nanofibre
GRFL	Grafoil
GSE	Gaseous secondary electron
HBMSC	Human bone marrow stromal cells
HBSS	Hank's balanced salt solution
HDPE	High-density polyethylene
HF	Hydrofluoric acid
HMDS	Hexamethyldisilazone
HOBs	Human osteoblasts
HRTEM	High-resolution transmission electron microscopy
IMS	Industrial methylated spirits
L-Glut	L-Glutamine
LA	Laser ablation
LDH	Lactate dehydrogenase
MA	Methacrylic acid
μ -CT	Micro-computerised tomography
MMA	Methyl methacrylate
MWNT	Multi-walled nanotube
NEAA	Non-essential amino acids
PABS	Poly(m-amino benzene sulphonic acid)
(s)PBS	(sterile) Phosphate buffered saline
PC	Polycarbonate
PCB	PC-board
PCS	Photon correlation spectroscopy
PCU	Poly(carbonate urethane)
PEEK	Poly(ether ether ketone)
PEG	Poly(ethylene glycol)
PEMA	Poly(ethyl methacrylate)

PEMF	Pulsed electromagnetic field
Pen/strep	Penicillin/Streptomycin
PGA	Poly(glycolic acid)
PHEMA	Poly(hydroxyethyl methacrylate)
PLA	Poly(lactic acid)
PM	Particulate matter
PMMA	Poly(methyl methacrylate)
PTFE	Poly(tetrafluoro ethylene)
RGD	Arginine-Glycine-Aspartic acid
SAD	Selected area diffraction
SEM	Scanning Electron Microscopy
sem	Standard error of the mean
SLS	Static light scattering
SWNT	Single-walled nanotube
TCPS	Tissue culture polystyrene
TEM	Transmission electron microscopy
T _g	Glass transition temperature
THFMA	Tetra hydro furfuryl methacrylate
THR	Total hip replacement
TJR	Total joint replacement
TKR	Total knee replacement
T _m	Melting temperature
TNE	Tris(hydroxymethyl) methylamine, sodium chloride, ethylene-diamine tetraacetic acid
UHMWPE	Ultra-high molecular weight polyethylene
UV	Ultra-violet
VGNF	Vapour-grown nanofibre
XRD	X-ray diffraction

1. Introduction

The potential of carbon nanofilaments, namely carbon nanotubes (CNTs) and graphitic nanofibres (GNFs), has been recognised more in the last two or three decades because of developments in microscopy techniques.¹ Their nanoscale dimensions and mechanical and electrical properties in particular, offer potential in biomedical applications, especially bone and neural repair applications.²⁻⁴ Recently, the rate of publications into nanofilament application in biomedical devices has increased, investigating the effect of morphology of pressed nanofilament surfaces,^{5,6} functionalisation of nanotubes,⁷⁻⁹ and the effects of their incorporation into composites^{4,6,10,11} upon cell interactions.

Bone, a hard tissue, can be replaced or repaired using metals, ceramics, polymers or composites. The complexity and importance of bone in everyday life has prompted clinicians to attempt to repair bone tissue for centuries, initially in dental applications,¹² but still continues to present challenges for long-term repair. Repair of defective bone tissue caused by fracture, disease, or misalignment can be repaired using bone plates, screws, nails, rods, wedges or alternatively replaced using total joint replacements in the case of defective joints. Common examples of orthopaedic biomaterials are titanium and its alloys, stainless steel, cobalt chromium alloys, titania, hydroxyapatite, high density and ultra high molecular weight polyethylene and poly(methyl methacrylate).^{12,13} These biomaterials are currently used to support or replace bone, but materials could preferably be optimised to regenerate bone to its natural state, especially in tissue engineering scaffolds, which encourage osseointegration and support of healing tissue.

Carbon nanofilaments could be used to promote bone repair or replacement in a number of applications, such as in surface modification of total joint replacement components, reinforcement and surface modification of bone cements, tissue engineering scaffolds, and accelerated healing via electrical stimulation. In all these applications osseointegration around the implant is desirable with a minimal inflammatory response.

The number of surgeries and revisions of total joint replacements during the 2005-06 financial year are displayed in table 1.1, along with the number of bone grafts fitted. Many replacements used bone cements to secure the implant (approximately 75% in hip replacement and 90% in knee replacements).¹⁴

Table 1.1: Number of total hip (THR), knee (TKR) replacements, with and without cement, and bone grafts performed in England during the 2005-06 financial year¹⁴

	Number of finished surgeries	Number of revisions
THR with cement	32,993	2,820
THR without cement	11,322	878
TKR with cement	44,679	2,028
TKR without cement	4,930	141
Bone graft	748	-

The main drawbacks in total joint replacements are loosening of the joint because of inadequate bonding between the biomaterial and bone tissue, mismatch of mechanical properties between bone and biomaterial, or due to inflammatory responses caused by the production of wear particles.¹² The number of bone grafts utilised for repair of bone is much less than the number of total joint replacements fitted in one year. This is because the repair of bone is primarily solved by replacement of materials capable of load-

bearing. Porous synthetic scaffolds offer an alternative as 3-dimensional structures that provide volume fill, mechanical integrity and a surface that can provide chemical and architectural guidance for regenerating tissues.¹⁵ Polymer scaffolds offer biocompatibility, design flexibility, ductility and are light weight, which are beneficial in 3-dimensional scaffolds, although they have low stiffness that can cause problems in supporting bone during healing.¹⁶

Carbon nanofilaments could be used for surface modification and reinforcement of polymer composites. Surface texture modification achieved using nanofilaments may be anticipated to show similarities to bone extracellular matrix features.^{5,17,18} Nanofilaments could also optimise bulk properties of biocompatible polymers used as load-bearing implants to match that of bone, similar in application to the reinforcing properties of micron-scale carbon fibres used in clinical applications.¹⁹ As carbon nanofilaments are also electrically conductive to various degrees depending on their graphene orientation,²⁰ they could also be used to electrically stimulate accelerated²¹⁻²³ or enhanced^{4,24,25} healing of bone in these applications.

The purpose of this project, therefore, is to assess the potential role of carbon nanofilaments in bone repair applications, with particular respect to surface and bulk requirements of the material for mechanical and biological stability. The three main aims of this project are to:

- i. Investigate the effect of nanofilament diameter and structure on surface properties of compacted carbon nanofilament substrates and the osteoblast responses to such substrates,
- ii. Investigate the effect of nanofilament size, structure and composition on the mechanical and thermal properties of a selected co-polymer- carbon nanofilament composite. The

surface effects of incorporated carbon nanofilaments on the polymer system with respect to osteoblast responses will also be investigated,

- iii. Investigate the effect of nanofilament size, structure and composition on the electrical properties of a selected polymer/carbon nanofilament composite. The effects of applying a pulsed current through the carbon nanofilament-filled polymer on osteoblast proliferation and differentiation are also studied.

The thesis comprises of a review of the current literature (chapter 2) surrounding bone, its repair and limitations with clinical devices, the nature and classification of carbon nanofilaments, and detailing potential advantages of carbon nanofilaments in the three areas mentioned above. The third chapter investigates the parameters and conditions necessary to control the growth of carbon nanofilaments using chemical vapour deposition (CVD), with particular respect to structure and diameter. The fourth chapter investigates the effects of carbon nanofilament shape and size on the morphology and topography of pressed nanofilament substrates. The osteoblast response to these different substrates is then assessed. In chapter 5, the various nanofilament samples are then used as fillers in poly(ethyl methacrylate)/tetra hydro furfuryl methacrylate (PEMA/THFMA) polymer and the resultant composite analysed for the effects on both bulk and surface characteristics due to nanofilament incorporation. The final experimental chapter, chapter 6, discusses the potential improvement of electrical properties of nanofilament-filled composites and how this can potentially be used to enhance osteoblast growth through electrical stimulation. The final discussion in chapter 7 aims to address the possible role that carbon nanofilaments may have in bone repair and this is followed by conclusions (chapter 8) and suggested future work (chapter 9).

2. Literature Review

2.1. The Problem with Bone Repair

2.1.1. Structure and function of bone

Bone is a highly specialised form of connective tissue.²⁶ Connective tissues primarily are used to support, connect, as well as protect, soft tissue and organs in the body, and in the case of bone, to bear weight. The composition of bone separates it from other connective tissue, producing a hard, dense, regular structure. There are two types of bone structure, which are cortical and cancellous bone. Cortical bone, also termed compacta, is hard and dense and located in the shafts of long bones (i.e. femur, tibia and humerus). Cancellous bone, also known as spongiosa, consists of a network of fine interlacing partitions (trabeculae), enclosing cavities that contain red or fatty marrow and is located in the vertebrae, at the ends of long bones and often found in flat bones.²⁶⁻²⁹ Cortical and cancellous bone are both found in long bone (figure 2.1).

Cortical bone comprises of approximately 80-85% of bone in the human body. It is very dense and is significant in contributing to the mechanical and protective properties of bone. The outer surfaces of cortical bone are either connected to articular cartilage or to the periosteum. Cancellous bone comprises the rest of human bone. It has a higher metabolic activity than cortical (compact) bone. This is because bone remodelling predominantly takes place on the surfaces of bone and as cancellous bone has a porous structure, it has more surface area enabling a greater metabolic activity.

Bone consists of living cells embedded within or lining the surfaces of a mineralised organic matrix. The tissue is in a dynamic form, where molecular, cellular and metabolic changes occur in order to adapt to its loading conditions. Figure 2.2 illustrates the structure of bone. The fibrous protein, type I collagen, takes up around 95% of the organic constituent of bone tissue.³⁰ Its structure is arranged in a triple helical structure, tropocollagen. The chemical composition of the amino acids in tropocollagen is one third glycine, and a quarter proline and hydroxyproline.^{12,30} Hydroxyapatite, the mineral component in bone, is a calcium phosphate salt, $\text{Ca}_{10}(\text{PO}_4)_6(\text{OH})_2$. Magnesium, strontium, bicarbonate and fluoride are also found in small amounts replacing the calcium or phosphate component of the bone salt.^{12,30}

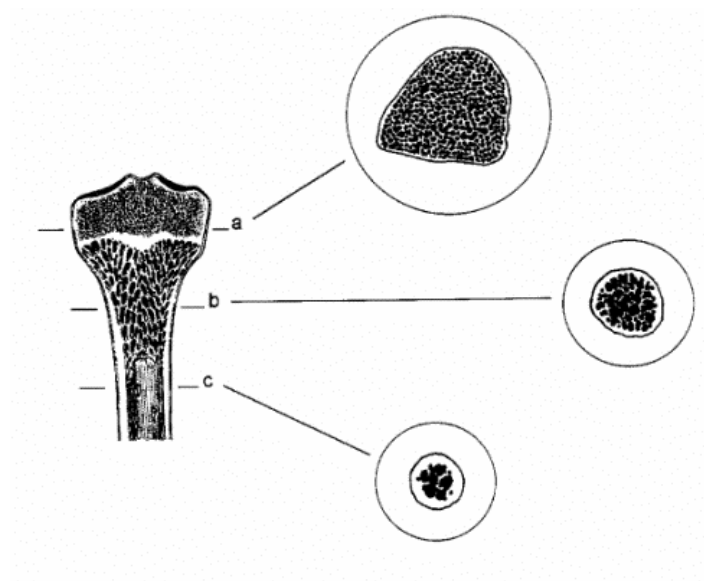


Figure 2.1: Microanatomic organisation of a long bone highlighting cortical and cancellous bone. a) Epiphysis, b) Metaphysis, and c) Diaphysis³¹

The cellular and structural organisation of bone is critical for its form and function. Figure 2.2 illustrates the organisation of the structure of bone. There are 3 or 4 levels of organisation within cortical bone. At the molecular level, the first level of organisation in bone, are the structures of tropocollagen and crystalline hydroxyapatite. It is thought that hydroxyapatite

forms within and in between collagen fibrils to make up the second level of organisation. These first two levels of organisation have nano-scale dimensions and features. Specifically, hydroxyapatite crystals are typically 2 nm x 20 nm x 40 nm in size, the tropocollagen molecule is 1 nm in diameter, and these two components form a composite structure of collagen fibrils (up to 500 nm in diameter). Fibrils are arranged into a fibrous structure of collagen fibres and fibre-bundles in a lamellar structure (3-7 μm). This lamellar structure is the third level of bone organisation and has micron-scale features. These lamellar structures can be organised concentrically to form Haversian systems, which are important in the growth and nourishment of bone.¹² It is important to consider the significance of both the macro-features of bone tissue as well as the nano-structure. Figure 2.2 illustrates the interaction of these structural features within each other including osteocyte cells in accomplishing the dynamic structure and function of bone as a tissue.

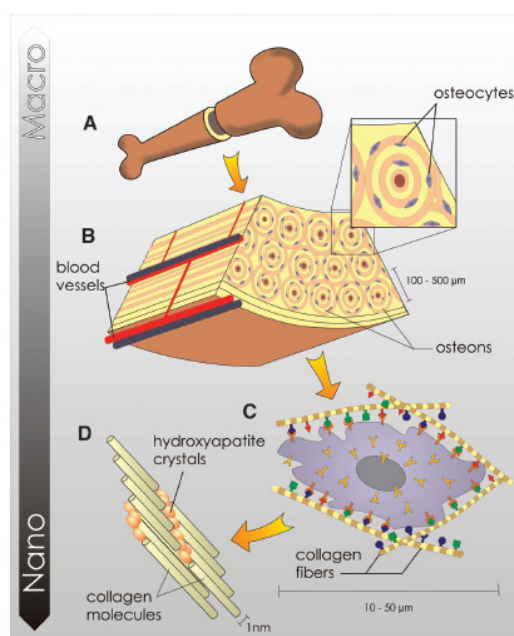


Figure 2.2: Diagram illustrating the connection between macro and nano-scale biology of bone tissue¹⁷

Osteoblasts are responsible for the formation of mineralised bone. As illustrated in figure 2.3, some osteoblasts become encapsulated by mineral and mature into osteocytes. Osteoclasts simultaneously resorb mineralised bone and break the inorganic components down into calcium and phosphate ions, which are released into the blood to be excreted or remineralised as bone elsewhere. Osteoclasts are critical in the control of calcium levels in the blood. If levels are low, parathyroid hormone is released from the parathyroid and osteoclasts resorb mineralised bone to release calcium. Calcitonin is released from the thyroid to reduce calcium levels in the blood by mineralising bone via osteoblasts.^{32,33} The organic components of the bone matrix, predominantly type I collagen, are then resorbed by proteolytic enzymes after the dissolution of the inorganic matrix by acid secretion.^{34,35} For healthy remodelling of bone through osteogenesis (by osteoblasts) and osteoclasts (by osteoclasts) there needs to be adequate cell metabolism, adequate nutrition and adequate stimulus.³³ Overall, this produces dynamic, continuous remodelling throughout adult life.^{27,32}

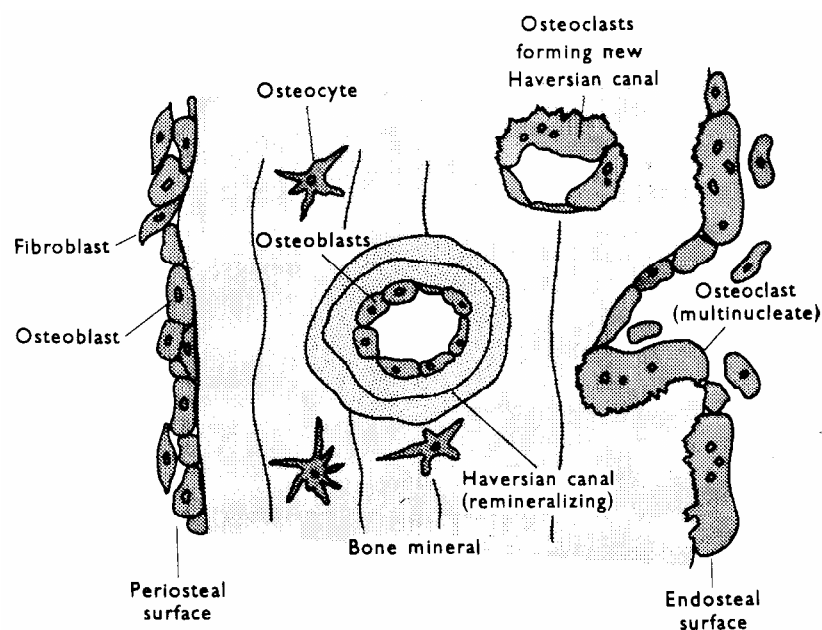


Figure 2.3: Diagram of the main cellular constituents of bone, i.e. osteoblasts, osteoclasts and osteocytes³²

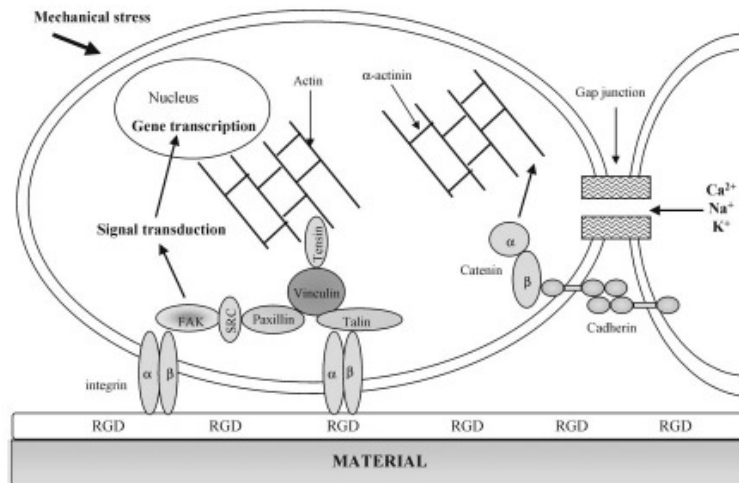


Figure 2.4: Diagram of proteins involved in cell adhesion to biomaterials³⁶

The adhesion of osteoblasts to a surface, matrix or between cells involves extracellular matrix (ECM) proteins, cell membrane proteins and cytoskeletal proteins. These biological molecules interact together to induce signal transduction, which promotes the action of transcription factors and consequently regulates gene expression. In bone, osteoblasts are responsible for synthesising the extracellular matrix, including collagen, osteocalcin, osteonectin, bone sialoprotein, proteoglycans, osteopontin, vitronectin and fibronectin.³⁶ The adhesion of osteoblasts to the matrix is dependent on most of these proteins. Fibronectin, osteopontin, bone sialoprotein, type I collagen and vitronectin all contain the tripeptide, Arginine-Glycine-Aspartic acid (RGD), which promotes cell adhesion.³⁷ The RGD sequence enhances binding of cells using specific surface receptors called integrins (figure 2.4). Integrins are thought to be the dominant mechanism by which cells communicate with noncellular surroundings^{29,36,38} and are composed of one α and one β transmembrane glycoprotein chain. There are several integrin α and β subunits and combinations, which are capable of binding more than one peptide sequence (figure 2.5).^{29,36}

	Subunits	Ligands
$\beta 1$	$\alpha 1$	Collagens, Laminins
	$\alpha 2$	Collagens, Laminins
	$\alpha 3$	Laminins, Fibronectin, Thrombospondin
	$\alpha 4$	Fibronectin, VCAM
	$\alpha 5$	Fibronectin
	$\alpha 6$	Laminins
	$\alpha 7$	Laminins
	$\alpha 8$	Fibronectin, Tenascin
	$\alpha 9$	Tenascin
	$\alpha 10$	Collagens
	$\alpha 11$	Collagens
$\beta 2$	αv	Fibronectin, Vitronectin
	αL	ICAMs
	αM	Fibrinogen, ICAMs, iC3b
	αX	Fibrinogen, iC3b
$\beta 3$	αD	VCAM, ICAMs
	αIIb	Collagens, Fibronectin, Vitronectin, Fibrinogen, Thrombospondin
$\beta 4$	αv	Fibronectin, Vitronectin, Fibrinogen, Thrombospondin
	$\alpha 6$	Laminins
$\beta 5$	αv	Vitronectin
$\beta 6$	αv	Fibronectin, Tenascin
$\beta 7$	$\alpha 4$	Fibronectin, VCAM, MAdCAM
	αE	E-cadherin
$\beta 8$	αv	Collagens, Laminins, Fibronectin

Figure 2.5: Integrin subunit combinations and their binding ECM protein ligands^{29,36}

The overall interaction between a cell and its non-cellular surroundings via integrins are called focal contacts or adhesion plaques. Within the cell, the transmembrane integrin receptor interacts with cytoskeletal proteins, such as talin, paxillin, vinculin and tensin, which further interact with actin filaments (figure 2.4).³⁶ Actin filaments are partly responsible for changes in cell shape and degree of attachment on a surface. Actin filaments, when arranged in cross-linked filament bundles can form filopodia, which are cytoplasmic finger-like protrusions. If assembled into a meshwork, actin filaments can also support sheet-like protrusions called lamellipodia. These cytoplasmic extensions also form focal contacts that further interact with the surrounding

environment.³⁹ Cell to cell interactions in osteoblasts are mediated by transmembrane glycoproteins called cadherins, which interact with intracellular proteins that also directly affect the cytoskeleton.³⁶ Osteoblast interactions with its noncellular surrounding (via integrins) and other cells (via cadherins) are essential for signal transduction and gene expression of the cell. Changes in cell shape because of its mediation with the ECM will affect the nuclear matrix and modify gene expression, which in turn will affect proliferation and differentiation of the cell.

The differentiation of osteoblasts into osteocytes involves a multi-step series of events modulated by an integrated cascade of gene expression.⁴⁰ Osteoblast differentiation, *in vitro*, is defined by three distinct stages that initially support proliferation and the sequential expression of genes associated with the biosynthesis, organisation and mineralisation of extracellular matrix. The three stages of osteoblast differentiation are proliferation, matrix maturation and mineralisation. The proliferative state of osteoblasts involves cell growth and type I collagen deposition. Collagen is synthesised initially and throughout the differentiation process as it is the major constituent of bone ECM. The maturation phase is characterised by a peak in alkaline phosphatase, which prepares the ECM for mineralisation. Peak levels of osteopontin, osteocalcin and then calcium are deposited by osteoblasts in the mineralisation phase. The expression of collagen, alkaline phosphatase, osteopontin, osteocalcin and calcium by osteoblasts are typical markers used in characterising their differentiation.⁴⁰

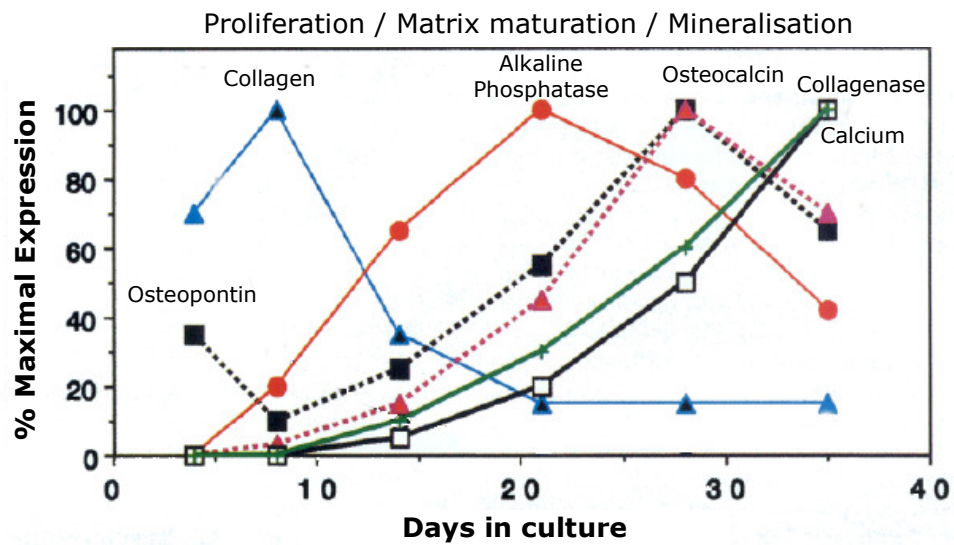


Figure 2.6: Stages of osteoblast differentiation; proliferation, matrix maturation and mineralisation. Levels of collagen[▲], osteopontin[■], alkaline phosphatase[●], osteocalcin[▲], calcium[□] and collagenase[◆] are indicated at each of the stages. adapted from 40

Although the mechanism is still poorly understood, electromagnetic fields are thought to also be involved in regulating the gene expression in osteoblasts and osteoprogenitor cells.⁴¹ The effects of electromagnetic stimulation are thought to alter the charges associated with the cell membrane and affect signal transduction through the cell membrane and stimulate gene expression (figure 2.7). Electromagnetic stimulation has been suggested to affect signal transduction in osteoblasts either by altering transmembrane voltage-gated ion channels, especially calcium channels.^{41,42} Figure 2.7 summarises the signal transduction pathways that could be affected by electromagnetic stimulation specifically from one study that employed capacitive, inductive and combined electromagnetic stimulation techniques.⁴² The mechanisms of electric stimulation of osteoblast growth are discussed in further detail later in section 2.3.3.1.

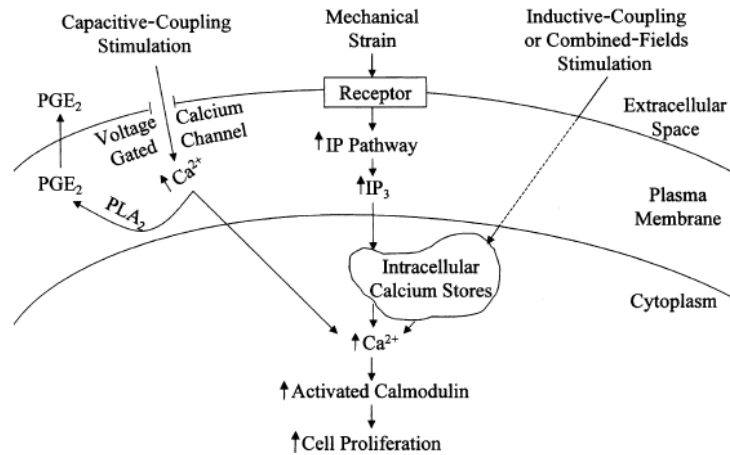


Figure 2.7: Schematic of the signal transduction pathways affected by electromagnetic and mechanical stimulation. PGE₂:prostaglandin E₂; PLA₂:phospholipase A₂; IP:inositol phosphate; IP₃:inositol triphosphate⁴²

The effects of electromagnetic stimulation on gene expression of osteoblasts through signal transduction is thought to stimulate synthesis of growth factors that induce osteogenesis, specifically bone morphogenic proteins⁴¹ and TGF- β .^{25,41}

2.1.2. Bone injury

One of the main functions of bone is to bear mechanical loads associated with body weight and movement. Therefore, any degenerative or damaging condition related to bone will affect the patient seriously in motion, agility and cause pain. Such conditions can be trauma (e.g. accidents), birth defects (e.g. cleft palate etc.), degenerative disease (osteoarthritis and osteoporosis), primary bone cancer (e.g. osteosarcoma, Ewing's sarcoma, spindle cell sarcoma, chordoma) or secondary bone cancer.^{27,43}

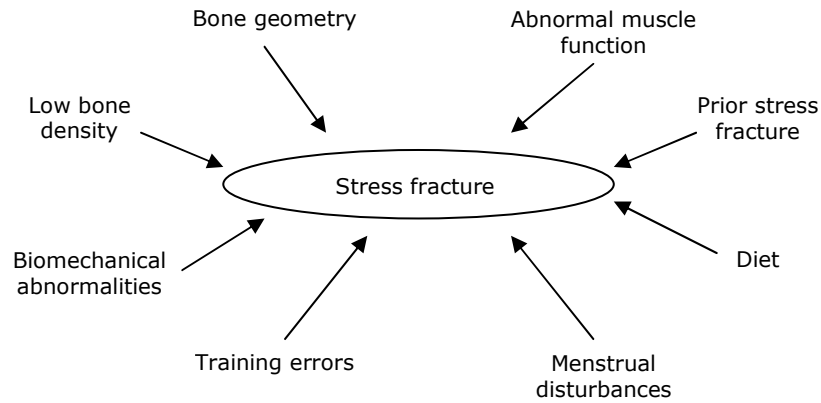


Figure 2.8: Factors that can influence the risk of a stress fracture in bone²¹

The aforementioned disorders are generally caused by abnormalities in the biomechanical or biological behaviour of bone. Many of the conditions are caused by, or lead to a change in bone tissue structure, which could ultimately lead to fracture or joint damage. For example, osteoporosis is caused by an imbalance in bone mineralisation and resorption, causing a reduction in bone mass and density and increases the chances of fracture. Figure 2.8 illustrates the factors that can induce stress fractures and can also contribute to other types of bone injury.

In cases where bone is not expected to regenerate spontaneously, clinicians attempt to induce formation of new bone. Ideally, the aim is to restore the bone to its original state prior to fracture or degenerative disease. For large defects or replacing degenerated tissue, a substitute material can be used to either replace the tissue (non-biodegradable implant) or encourage new tissue formation (biodegradable or porous implant). This may be achieved by total joint replacement or stabilising the bone with a fixation device.⁴⁴

2.1.3. Bone repair materials and their limitations

The suitability of a material in the body will depend on whether the material adversely affects or is affected by its biological environment.¹² Therefore, an understanding of the environment that the implant will be entering is necessary when designing or considering a biomaterial for a given function.^{12,27} In the case of orthopaedic devices, a good understanding of a potential biomaterial and its interaction with bone tissue is a major factor in its suitability.

As the main function of long bone is to bear load, it is not surprising that metals were first used to replace joints, since their stiffness, rigidity and strength are capable of bearing the loads that are exerted on bone. Metals such as stainless steel (316L) and cobalt-chromium alloys were used because of their relatively good corrosion resistance and reasonable fatigue life within the body. Most hip replacement prostheses are based around the Charnley total hip arthroplasty. The Charnley hip prosthesis consisted of a stainless steel femoral component held in place by poly(methyl methacrylate) (PMMA) cement and an acetabular prosthesis made originally of poly(tetrafluoroethylene) (PTFE), but ultimately replaced by ultrahigh-molecular-weight polyethylene (UHMWPE), which was also cemented in place. Other metals have also been used since then, such as cast and wrought cobalt-chromium alloys, commercially pure titanium and titanium-aluminium-vanadium alloys.¹²

One reason for the interest into other materials for orthopaedic devices is because of the mismatch of modulus between the prosthetic material and bone. This mismatch will alter load distributions transferred through the bone causing differences in stress. Quantitatively, the modulus of elasticity of bone has been reported to be between 10-20 GPa^{45,46} and the metals referred to

above exhibit a modulus of between 100-250 GPa.⁴⁶ According to Wolff's law, the internal structure of bone adapts to withstand the mechanical loads imposed on it, thus determining its form and function.²⁷ Any changes in the stresses applied will change the structure of bone. Metals can fail to replace bone as they are too stiff and carry the load during healing. This impedes full healing of the tissue as the implant "stress-shields" the bone and can lead to further fracture or even osteoporosis of the bone.^{12,47} Stress shielding is also a common failure mechanism in fracture fixation plates, which are used to support fractured bone during healing. The viscoelastic properties of bone allow the tissue to give, so flexural properties of the fixation device in particular, need to match that of the supporting bone; otherwise the load is dissipated along the implant and shielded from bone.

Corrosion and fatigue life are also common limitations in metallic orthopaedic devices.^{12,48} Chromium and titanium are termed passivating metals as they produce an oxide film, which reduces corrosion in their alloys. Chromium and titanium do not eliminate corrosion in the body but significantly reduce it. Corrosion will release metal ions into the surrounding tissue (even in passivated alloys), which may cause a toxic response. The other problem associated with corroding metallic implants is the structural integrity as it corrodes.⁴⁸ Metals and their alloys used for orthopaedic devices are also susceptible to fatigue failure, especially in total joint replacements, which result from repetitive cyclic stresses. These stresses may be less than the ultimate tensile stress of the material, but are likely to cause and propagate small cracks over a period of time,¹² i.e. fatigue failure.⁴⁹

Another limitation that can often shorten the life of a total joint replacement prosthesis is aseptic loosening. This occurs when the prosthesis loosens and detaches from the bone tissue or cement surrounding the

implant. This can be due to repeated cyclic stresses on the joint or osteolysis (bone tissue resorption) caused by an inflammatory response to wear particles produced from the articulating surfaces of the implant. To reduce the chances of aseptic loosening, the generation of wear particles must be low and osseointegration around the implant or cement must be achieved.

The purpose of this project was to investigate the potential use of carbon nanofilaments to address some of these issues in bone repair devices. In order to understand the possibilities of using nanofilaments as biomaterials, the following section discusses current research into carbon nanofilaments.

2.2. Carbon Nanofilaments

Since the discovery of Buckminster fullerene, much interest has gone into the synthesis and formation of other carbon nanostructures, such as graphitic nanofibres and carbon nanotubes. These nanofilaments have been shown to exhibit superior properties, especially electrical and mechanical properties, when compared to their larger counterparts, carbon fibres (microfibres).

Scientific understanding of carbon nanofilaments has accelerated over the last 20 years due to advances in electron microscopy techniques.^{50,51} Carbon nanotubes (CNT) were characterised for the first time in 1991, although there were references to them decades before.¹ The nanotubes were discovered in the soot at the negative electrode using an arc discharge evaporation technique similar to that used for fullerene synthesis. The CNTs discovered were multi-walled carbon nanotubes (MWNT) comprising of coaxial tubes of graphite sheets, ranging from 2 to 50 sheets. The diameter of the

MWNTs discovered ranged from 3-10 nm and lengths of up to 1 μm .⁵² This discovery has prompted much research into the properties and potential applications of these nanostructured materials.

2.2.1. Nanofilament structure and synthesis

Carbon nanofilaments, such as carbon nanotubes (CNT) and graphitic nanofibres (GNF), are based on the structure of graphite. In graphite, each carbon atom is attached to three other carbons in a plane forming a hexagonal lattice, creating a near ideal sp^2 carbon structure (figure 2.9). Hexagonal planes are held together by van der Waal's forces (d-spacing of 0.34 nm). The C-C bonds in the plane are very strong, exhibiting bond lengths shorter than in diamond (0.141 nm compared to 0.154 nm respectively), but the interplanar van der Waal's interactions are relatively weak, therefore graphite exhibits anisotropy. So there are 3 carbon atoms covalently bonded to each carbon atom, hence leaving a spare electron in the π -orbital (in between planes) that enables conductivity parallel to the graphite plane.

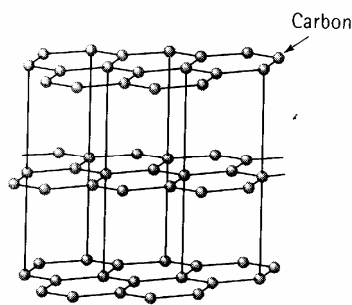


Figure 2.9: Crystal structure of graphite⁵³

It will be beneficial at this point to clarify what is meant by 'nanotube' and 'nanofibre'. Carbon nanotubes are composed of a cylindrical graphite

tubule, called single walled carbon nanotubes (SWNT), or several concentric cylindrical graphite tubules (MWNT). Each tubule has the structure of a rolled up graphite sheet. The interlayer spacing between these sheets is between 0.34 - 0.36 nm, comparable to that of graphite.⁵⁴ The tubular structure of CNT can be orientated in one of three ways; armchair, zigzag or chiral (in between armchair and zigzag).⁵⁵⁻⁵⁷ These orientations are illustrated in figure 2.10.

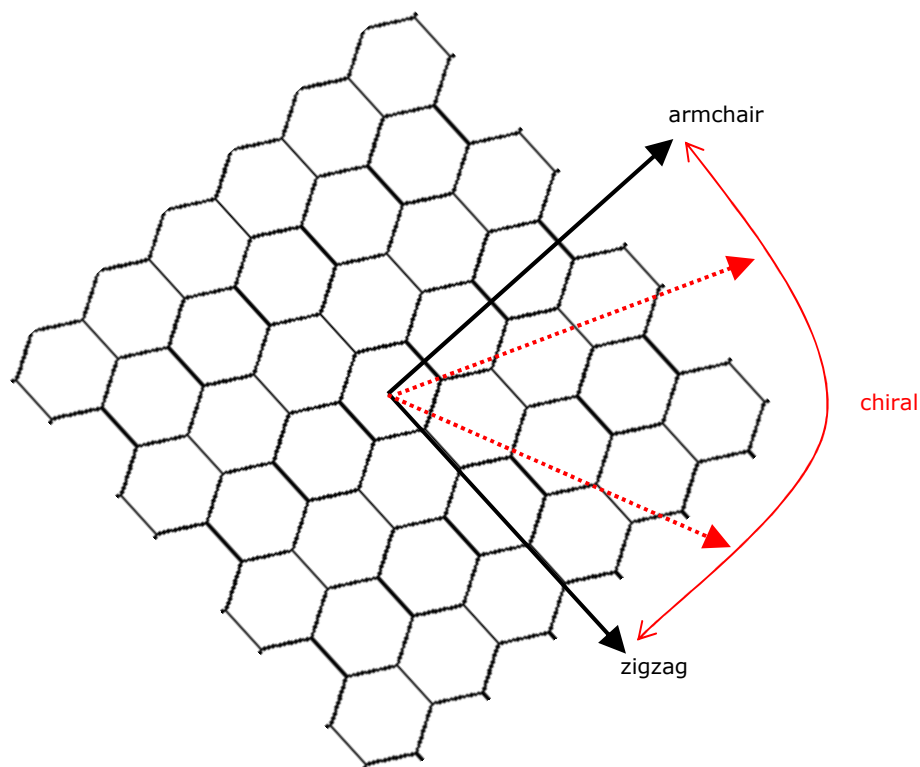


Figure 2.10: Classification of the orientation of graphite sheets in carbon single-walled and multi-walled nanotubes. Hexagonal lattice represents the graphene plane and the arrows indicate the direction of the filament axis for zig-zag, armchair and chiral nanotubes.

Graphitic nanofibres, however, exhibit a very different structure. The graphite planes in GNF are stacked in the form of a platelet structure (perpendicular to the fibre-axis) or in a herringbone structure (at an angle to the fibre-axis). The orientation of these planes is believed to be determined by the shape of the metal catalyst particles (figure 2.11).^{51,58}

There are currently three main synthesis routes that produce a reasonable yield of CNTs and/or GNFs; electric arc discharge (EAD), laser ablation (LA) and chemical vapour deposition (CVD). All of these methods employ a carbon-containing gas or vapour to produce the nanostructures.⁵⁵

Electric arc deposition employs carbon electrodes, placed a few millimetres apart. A current of ~ 100 A vaporises the carbon into a hot plasma, some of which condenses into nanotubes. This method produces a yield of up to 30 wt% of CNT, with diameters between 2 and 20 nm and maximum lengths of ~ 50 nm. Addition of a transition metal catalyst favours the growth of SWNT.⁵⁴

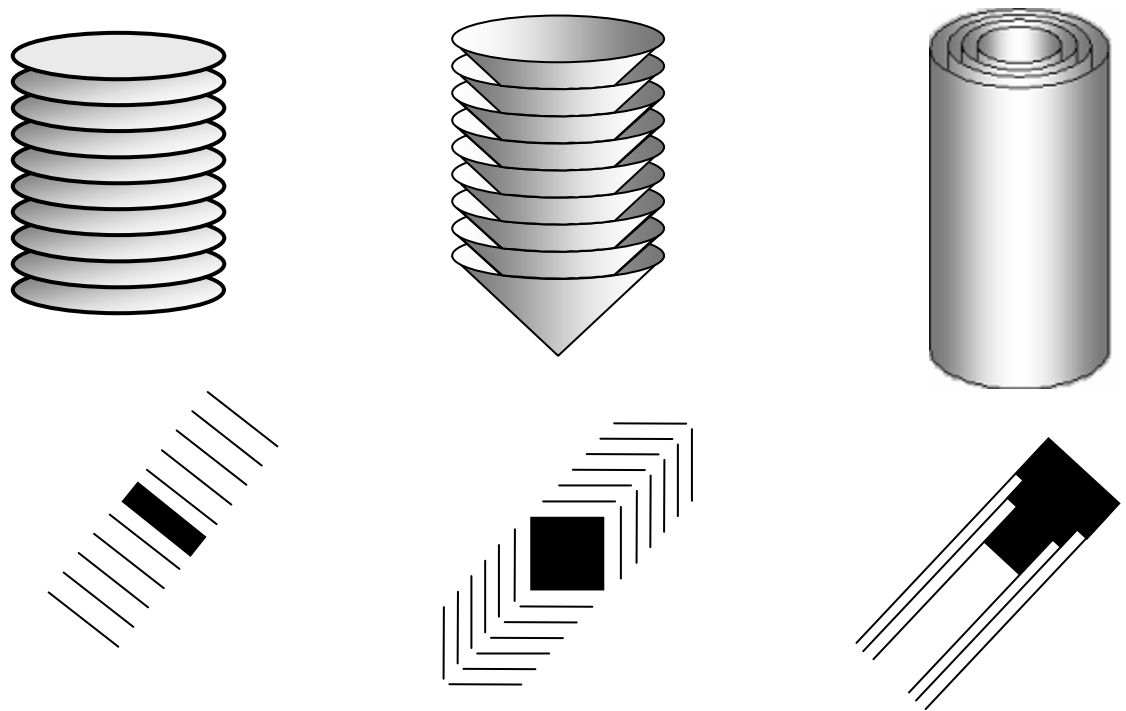


Figure 2.11: Three-dimensional and cross-sectional structures of platelet nanofibres (left), herringbone nanofibres (middle) and multi-walled nanotubes (right)⁵⁹

Laser ablation of a graphite rod has been implemented to produce SWNT. This method produced aligned bundles of nanotubes, predominantly of the armchair type. This method of producing aligned bundles of nanotubes was performed in a furnace at 1100-1200 °C. Again, a metal catalyst (e.g. Co-Ni) has been shown to assist nanotube growth, as it is thought to prevent ends of nanotubes from being capped. This method provides better control of growth conditions. The reaction temperature can be controlled to manipulate the diameter of the nanotubes produced.

The last synthesis process mentioned here is chemical vapour deposition (CVD). This process is performed at lower temperatures (400-1000 °C), and nanofilaments are grown by catalytic decomposition of a hydrocarbon over small metal catalyst particles, such as iron, cobalt or nickel.⁵⁰ CVD was used in this study and is discussed in more detail below.

CVD produces nanofilaments with a lower amount of unwanted soot or encapsulated carbon and a higher yield of nanofilaments^{51,60} compared to other routes. GNFs and CNTs can be grown at the same time under similar conditions, so work is continuing to optimise the selectivity of the synthesis process.

Generally, there are three or four different gases used to aid the growth of nanofilaments; one or more carbon-containing gases (usually hydrocarbons), hydrogen and an inert gas. There is a wide range of carbon-containing gases used, such as methane,^{61,62} ethane,^{62,63} ethylene,^{58,64,65} benzene,^{66,67} acetylene,^{65,68-71} kerosene⁷² and carbon monoxide.⁵⁸ One or more of these carbon-containing gases are mixed with other gases, especially hydrogen, to promote the production of CNTs or GNFs.⁵⁰ The inert gases used

are usually helium or argon, but nitrogen is sometimes used as a substitute especially for CNT production.^{64-66,68,69,71,72}

There are four commonly used catalysts employed for the growth of carbon nanofilaments; nickel, iron, cobalt and sometimes copper. These catalysts can also be used together as bimetallic catalysts, such as copper-nickel,⁵⁰ copper-iron,⁵⁸ cobalt-iron^{69,71} or nickel-iron.⁷³ The addition of a second metal can also play an important part in the nature of the filaments grown.⁷⁴ Different catalysts will produce different yields and produce yields containing different types of carbon structures.

Supports can be used to produce aligned nanofilaments. The choice of catalyst and catalyst support need special consideration when synthesising carbon nanofilaments, especially nanotubes. The alignment, thickness and length of the nanotubes, in particular, are altered by the choice of catalyst and support. For large-scale nanotube production, it is best to anchor the metal catalyst into a support to impede the formation of large catalyst clusters.⁷⁵ Common support-materials include silica,^{58,60-63,68,69,76} alumina,^{62,64,65,76} zeolites^{69,71} and carbon microfibres.⁶³

Porous substrates, especially silica, have been shown to be more beneficial for growing self-orientated nanotubes on large surfaces, than fully dense silica. The nanotubes grow faster, are well aligned and grow perpendicular to the substrate.⁵⁴ The aligned nanotubes obtained on porous supports are thought to grow parallel to each other because of the catalyst-surface interaction and the van der Waal's forces acting between the nanotubes. As carbon nanotubes tend to grow out of the pores, aligned pores aid the growth of well-aligned nanotubes.^{54,68} One possible growth model was put forward by Li *et al.*⁶⁸ (figure 2.12), which puts forward the idea that with

a uniform mesoporous support, aligned nanotubes can be obtained as the MWNT grow out from the embedded iron catalyst particles and are constrained by the pores.

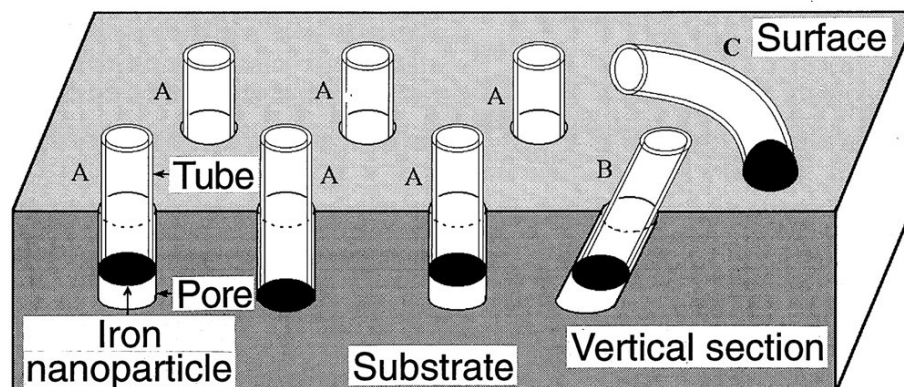


Figure 2.12: Possible model for growth of carbon nanotubes from an iron-impregnated silica substrate. Li *et al.*⁶⁸ suggest that carbon nanotubes will grow dependent on the position of the iron nanoparticle catalyst, where particles embedded in the vertical pores support nanotube growth perpendicular to the surface (A), particles embedded in inclined pores support tilted nanotube growth (B) and nanotubes grow freely from nanoparticles exposed at the surface of the silica substrate (C)⁶⁸

There are two mechanisms for the growth of CNT; root- or tip-growth (illustrated in figure 2.13). Li *et al.* assume that it is likely that both root and tip growth occur. MWNTs that are synthesised by the tip growth mechanism are more likely to be non-aligned as the decomposition of the hydrocarbon and the diffusion rate of the dissolved carbon on the catalyst would determine the direction of MWNT growth. Root growth would allow the catalyst nanoparticle to remain in the pore of the support and, as it is porous, would provide access for the carbon-containing gas. Therefore, the mechanism proposed by Li *et al.* assumes root growth to dominate (as illustrated in figure 2.12) and therefore producing an aligned batch of MWNTs. Many studies have used a silica support embedded with iron catalyst particles and observed a high density and purity of nanotubes.^{68,77}

When choosing an adequate support, three things must be taken into account as they will influence the growth of carbon filaments; the degree of

dispersion and nature of impregnated catalyst, the chemical properties of the substrate surface and the nature of interaction between the catalyst and support.⁵⁰

The proposed mechanism of graphite formation on catalyst particles to produce GNF is believed to occur from decomposition of hydrocarbon molecules on a free-metal surface forming carbon atoms and desorbing hydrogen simultaneously. Carbon dissolves and diffuses through the bulk of the catalyst particle and forms graphitic carbon on the opposite side of the particle.⁵¹ It is generally believed that diffusion of carbon through the catalyst particle is the rate determining step in the growth of carbon nanostructures. There is generally a correlation between the activation energies for growth and the diffusion of carbon through the corresponding metals.⁵⁰ The concentration gradient of carbon is believed to be the origin of carbon diffusion through the metal catalyst.⁷⁸

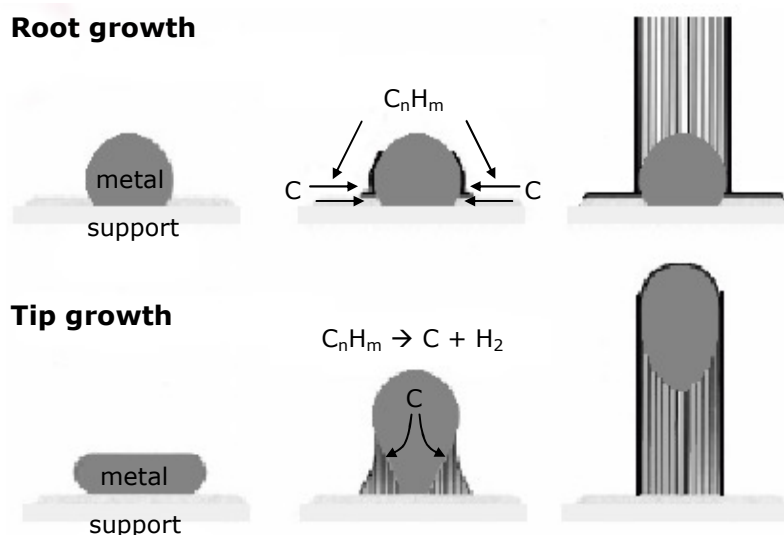


Figure 2.13: Schematic of growth mechanisms of nanotubes growth; root growth and tip growth⁷⁹

The growth in GNF is usually bidirectional growing at identical rates symmetrically away from the catalyst particle. Hence the facets of the particle

govern the type of GNF produced. Bimetallic catalysts and metal catalysts with non-metallic additions have shown bidirectional growth forming twisted nanofibres, helical nanofibres and branched nanofibres. Twisted and helical nanofibres were formed by catalyst particles exhibiting 'rotary motion'. Branched nanofibres were produced when a catalyst particle located at the end of a growing fibre suddenly dispersed into numerous smaller particles. The orientation of the catalyst particle has effects on its activity. Therefore the chemical nature of the gas has to be taken into consideration as this will affect the crystallographic characteristics of the catalyst particle. For instance, the presence of hydrogen can induce reconstruction of the exposed metal faces, which in turn changes the catalytic action in the system.⁵⁰

It has been observed that Fe and Co have more potential to fabricate nanotubes while Ni tends to predominantly produce nanofibres.⁶⁷ Ni catalysts have also mainly been observed to produce herringbone nanofibres and iron produces more platelet nanofibres.⁵¹ Particles with a diameter less than 25 nm would tend to produce CNT.⁶⁷ Having said this, different trends in parameters used to synthesise specific nanostructured nanofilaments have been reported by different groups. However, it is clear that the synthesis parameters affect the shape of catalyst particle and hence determine the nanofilament structure.⁵⁹

The ratio of hydrogen to hydrocarbon is a key parameter for the high yield production of nanofilaments. The amount of hydrogen in contact with the metal particle whilst the filament is growing has been shown to regulate the flow of carbon dissolving into the metal catalyst. The morphological characteristics, the degree of crystallinity and the orientation of the graphite crystals can be tailored by the choice of catalyst, the ratio of hydrocarbon-hydrogen reaction mixture and the reaction temperature.^{50,59,80}

2.2.2. Nanofilament properties

As mentioned previously, carbon nanostructures can produce some properties that are superior to alternative carbon materials but on a smaller scale. Properties, such as high electrical conductivity, thermal conductivity and mechanical strength occur along the graphite planes.⁷⁵ The most interesting physical property of carbon nanofilaments is their electronic structure, which is only affected by its geometry. The electrical properties of CNTs especially, are greatly affected by their diameter and chirality.⁵⁶ As seen in the anisotropy of graphite, electrical properties are best in the direction of the graphite sheets and poor perpendicular to the sheets. Electrical conductivity will be better in nanotubes, compared to nanofibres due to the orientation of the graphene plane. There will also be differences in conductivity due to the orientation of the planes in relation to the fibre axis, especially in nanotubes. Conductance will vary between nanotube types (see previous section), from semi-conductive zig-zag nanotubes to conductive armchair nanotubes.²⁰

Table 2.1: Table listing properties of common composite fillers, graphite and carbon nanofilaments. References to data are displayed in brackets. * indicates data not available

	Young's modulus	Resistivity	Diameter ranges
Conventional carbon fibre	250-800 GPa (81)	$1.5 \times 10^{-5} \Omega.m$ (46)	10-150 μm (53)
Glass fibre	$\sim 35-90$ GPa (53)	$10^6-10^{10} \Omega.m$ (46)	10-150 μm (53)
Graphite	1060 GPa (81)	$1.5 \times 10^{-5} \Omega.m$ (50)	N/A
SWNTs	1000 GPa (20,82,83)	$10^{-6} \Omega.m$ (75)	1.4-20 nm (83)
MWNTs	1000-1800 GPa (20,83,84) ⁷⁵	$10^{-6} \Omega.m$ (85)	2-100 nm (86)
GNFs	400 GPa (50)	$2.5 \times 10^{-5} \Omega.m$ (58)	5-500 nm (50)
VGNFs	*	$2 \times 10^{-5} \Omega.m$ (87)	70-200 nm (88)

Carbon nanofibres have been shown to exhibit beneficial elastic properties as well as superior strength along their fibre axis. Elastically, carbon nanofibres have been extended up to three times their original length and plastically, up to 4.5 times their original length.⁸⁹ Carbon nanotubes have also shown significant flexibility depending on synthesis technique used⁹⁰ and yield strength have also been shown to change with differing nanotube symmetry.^{54,91} Atomic Force Microscopy (AFM) has been employed to manipulate pinned carbon nanotubes to try to obtain some kind of values for mechanical properties.⁹¹ They exhibited an interesting buckling process to avoid fracture and were 2 times stiffer than silicon carbide nanorods.^{54,84} Values for Young's modulus tend to vary from 0.5-1.8 TPa depending on the synthesis technique used.^{2,5} A comparison of Young's modulus, electrical resistivity and diameter ranges of carbon nanofilaments, graphite and other common fibrous composite fillers are listed in table 2.1.

The measurement of length and diameter of nanofilament samples are commonly restricted to electron microscopy techniques, which involves lengthy analysis and measurement to minimise error. It has been suggested that photon correlation spectroscopy (PCS) or dynamic light scattering (DLS) can be used to determine the diameter and length of nanofilament samples.⁹² This technique is often used for particle-size analysis of spherical particles as it is rapid and requires little sample preparation. It has been suggested that this technique can be used for specific length and diameter particle analysis. However, it is clear that the aspect ratio can only be determined.⁹³

In brief, PCS uses a laser beam which is scattered by the sample particles in suspension.⁹³⁻⁹⁶ The model for spherical particles uses the theory that the particles will move according to Brownian motion, so if the particles

are small, they move faster through the solution by diffusion and larger particles will travel slower. The hydrodynamic diameter of the particles ($d(H)$) is therefore dependant on the diffusion coefficient (D) according to the equation below:

$$D = \frac{kT}{3\pi\eta d(H)} \quad \text{Equation 2.1}$$

Where k is the Boltzmann constant, T is absolute temperature and η is the viscosity of the solution. Some groups have adapted this spherical model to allow for particles which are shaped like a rigid rod (hence named the rigid rod model).^{92,97} Since the dimensions of the rod are now not equal, there has to be translational and rotational diffusion coefficients to account for the length (L) and diameter (d) of the rod. The equations for the translational diffusion coefficient (D_t^{\parallel} parallel to the rod axis and D_t^{\perp} perpendicular to the rod axis) and rotational (D_r) diffusion coefficient are stated below:

$$D_t^{\parallel} = \frac{k_B T}{2\pi\eta_0 L} (\sigma - \gamma_{\parallel}) \quad \text{Equation 2.2}$$

$$D_t^{\perp} = \frac{k_B T}{4\pi\eta_0 L} (\sigma - \gamma_{\perp}) \quad \text{Equation 2.3}$$

$$D_r = \frac{3k_B T}{\pi\eta_0 L^3} (\sigma - \delta_{\perp}) \quad \text{Equation 2.4}$$

where:

$$\sigma = \ln\left(\frac{2L}{d}\right) \quad \text{Equation 2.5}$$

$$\gamma_{\parallel} = 0.807 + \frac{0.15}{\sigma} + \frac{13.5}{\sigma^2} - \frac{37}{\sigma^3} + \frac{22}{\sigma^4} \quad \text{Equation 2.6}$$

$$\gamma_{\perp} = -0.193 + \frac{0.15}{\sigma} + \frac{8.1}{\sigma^2} + \frac{18}{\sigma^3} + \frac{9}{\sigma^4} \quad \text{Equation 2.7}$$

$$\delta_{\perp} = 1.14 + \frac{0.2}{\sigma} + \frac{16}{\sigma^2} - \frac{63}{\sigma^3} + \frac{62}{\sigma^4} \quad \text{Equation 2.8}$$

D_t^{\parallel} and D_t^{\perp} combine to form the translational diffusion coefficient, D_t :

$$D_t = \frac{k_B T}{3\pi\eta_0 L} (\sigma - \gamma) \quad \text{Equation 2.9}$$

where:

$$\gamma = \frac{\gamma_{\parallel} + \gamma_{\perp}}{2} \quad \text{Equation 2.10}$$

This model can then be used to produce a range of particle sizes related to the diffusion coefficients of the particles.

Some groups have used the rigid rod model to analyse nanofilament samples^{2,5} and another group has used the technique for analysing nanofilament agglomerates but also individual nanofilament dimensions.⁹² Although the sample preparation and analysis is very straight forward, the theory used for rod-like structures needs careful consideration. Branca *et al.*^{3,8,10,98} used PCS in conjunction with static light scattering (SLS), which uses the scatter of laser light in relation to time at a constant scatter angle. They used PCS to deduce length to diameter ratio (p) and used the radius of gyration (R_g) obtained from SLS to calculate length (L) using the following equation:

$$R_g = L \sqrt{\frac{1}{12} + \frac{1}{8p^2}} \quad \text{Equation 2.11}$$

PCS can only be used to measure the aspect ratio, but cannot be used alone to determine length and/or diameter values as suggested by some researchers because γ is a function of both length and diameter. It can be

used along side other techniques such as SLS or TEM but not as an additional technique.

Since nanofilament samples cannot always be assumed to be rigid rod-like structures and since the theory relies on determination of length, diameter or radius of gyration, this technique is only reviewed and was not employed in this study.

2.3. The Potential of Carbon Nanofilaments in Bone Repair

Carbon has been used clinically in biomedical applications, especially in orthopaedic applications (table 2.2). Aside from orthopaedic use, carbon nanotubes and nanofibres have been investigated for other potential applications, such as neural implants,⁹⁹ cartilage repair¹⁰⁰ and muscle actuators.³ Research into neural devices has indicated that carbon nanotubes (as compacted discs) have encouraged neural cell growth^{3,10} and decreased astrocyte growth,¹⁰¹ which competes to form non-conductive glial scar tissue instead of desired nerve tissue.^{10,98} Further reductions in astrocyte growth were seen in nanotubes with smaller diameters and higher surface energies (obtained by pyrolytically stripping as-grown fibres).¹⁰²⁻¹⁰⁴ When it comes to detailing the advantages of nanofilaments in bone repair applications, there are three areas that they could potentially be used in; surface modification of biomaterials taking advantage of their shape and size, improvement of surface topography and bulk mechanical properties of polymer composites using nanofilaments as a filler, and exploring their electrical properties in stimulating osteogenesis around an electrically stimulated composite. These three areas are detailed below with respect to current understanding in biomedical materials and in relation to carbon nanofilaments.

2.3.1. Surface modification of biomaterials

Surface modification encompasses a wide range of surface techniques that can enhance or discourage cell attachment around the implant material. Some examples of modifying biomaterial surfaces include altering the surface roughness,¹⁰⁵⁻¹⁰⁷ topography^{9,107}, chemistry,^{2,108} and energy¹⁰⁹ of an implant.

Table 2.2: Examples of Carbon Biomaterials^{adapted from 17,105}

Type of material	Function	Type of implant	Area of medicine
Carbon-carbon composites	Bone fixation	Screws, plates, nails, stems of endoprosthesis	Bone surgery
Braided carbon fibres	Tissue knitting, reconstruction of joint ligaments and tendons	Surgical sutures, ligament and tendon prosthesis	Orthopaedics
Unwoven carbon fabric	Filling bone and cartilage losses	Disks and rings	Bone surgery
Coatings of diamond-like carbon	Coating of metal implants-corrosion protection	Joint endoprosthesis, screws	Bone surgery
Glassy carbon	Blood flow regulation	Heart valves	Cardiology
Polymer-carbon composites	Bone fixation	Screws, plates, nails, stems of endoprosthesis	Bone surgery

Cells respond to objects as small as 5 nm,^{2,105,106,110} and many groups have shown an enhanced response of cells to features in the region of 100 nm compared to features above 100 nm or in the micron-scale.¹¹⁰ For example, Webster *et al.*¹⁰³ demonstrated enhanced adhesion of osteoblasts on alumina, titania and hydroxyapatite with nanoscale grain sizes (<100 nm) compared to those above 100 nm. Surface roughness and texture also play an important role in cell adhesion, proliferation and differentiation. Linez-Bataillon *et al.*¹⁰³ investigated the effect of surface roughness of a titanium, aluminium, vanadium (Ti6Al4V) alloy on a mouse osteoblast-like cell line (MC3T3-E1) adhesion and proliferation during 3 days of culture. Roughness was controlled using sandblasting and a series of polishing grades down to mirror-finished

samples. Actin filaments were more organised around the cells with regular focal adhesions on the polished surfaces compared to the sandblasted surfaces. The proliferation rate decreased as the roughness of the samples increased.¹⁰⁴ Washburn *et al.*¹⁰⁴ also observed an increase in proliferation of the same cells (MC3T3-E1) on smoother regions of poly(L-lactic acid) surfaces, but with no differences in cell adhesion.¹¹¹ Roughness can be attributed to regular or irregular features on a surface, one group studied the gene expression and cell mineralisation of rat calvarial osteoblasts on grooved and roughened titanium surfaces. They suggest that the topography of the surface (i.e. roughened as opposed to regular grooved surfaces) alter the expression of the rat calvarial osteoblasts.^{105,106,112} So there are clearly differences between roughnesses attributed to regular (grooves, pits, hills) or irregularly shaped features.

Curtis *et al.* have invested much research into looking at the effects of regular surface features on cell activity in the nano-scale and micron scale.¹¹³ Nanotopographies, such as 95 nm high islands produced from polymer-demixing of polystyrene and polybromostyrene, have been shown to inhibit fibroblast spreading over a period of 3 weeks, hence affecting cell proliferation and progression to differentiation.¹¹³ Nano-island diameters were stated to be $0.99\ \mu\text{m} \pm 0.69\ \mu\text{m}$ but had a bimodal distribution (at approximately 0.4 and 1.5 μm) and were separated by $1.67\ \mu\text{m} \pm 0.66\ \mu\text{m}$. Fibroblasts were shown to interact with the surrounding nanopatterned surface, especially with filopodia extensions (figure 2.14). The group found that the morphology of the attached fibroblast cells was important in their progression to proliferation and differentiation. Cells attached and spread on the nanopatterned surfaces, but did not spread enough to encourage proliferation, which in turn would affect differentiation. Cells attached to the flat surfaces in lower number, but

spread enough to proceed to proliferation and many more cells spread on the surfaces to confluency compared to the nano-island surfaces.¹¹⁴

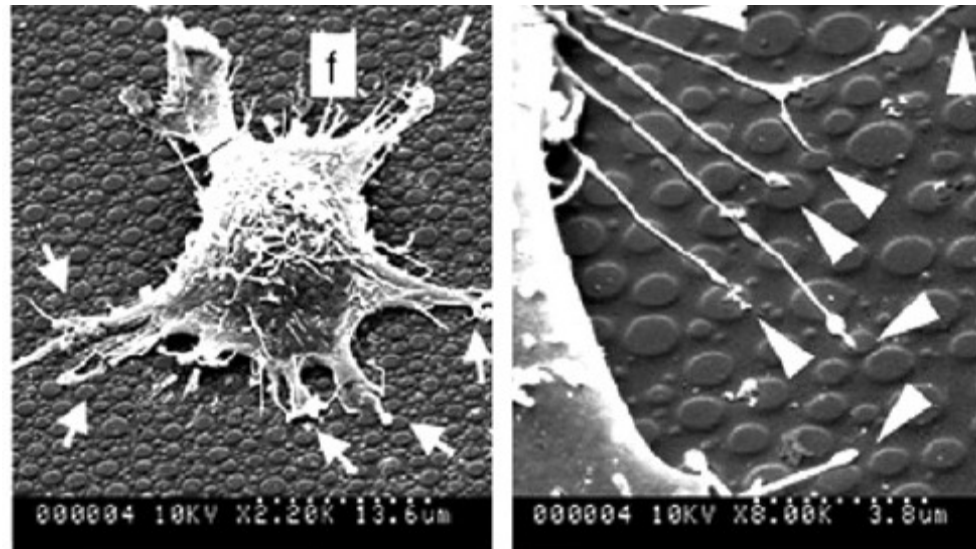


Figure 2.14: Human fibroblast interacting with 95 nm high nano-islands after 24 hours of culture. Arrows and arrowheads highlight the cells pseudopodia and filopodia respectively.^{113,115}

Cell attachment of human osteoblasts has been shown to be affected by regular topographies.¹¹² Osteoblasts spread to more of an extent with increased adhesion formation on poly(carbonate) surfaces with a random pits (of 120 nm diameter and 100 nm depth), compared to regular arrays of the same sized pits (300 nm spacings in a square conformation). Reduced spreading and adhesion does not necessarily mean that the osteoblasts will not differentiate. Dalby *et al.*¹¹² studied the effects of regular embossed surface pits of 30 μm and 40 μm in width with depths of 310 nm and 362 nm respectively, and grooves of 5 μm and 50 μm in width with depths of 510 nm and 327 nm respectively, on PMMA surfaces compared to an unembossed control. Human mesenchymal bone marrow stromal cells (HBMSCs) were used to study their osteogenic potential on these surfaces. Cells spread more on the surfaces with embossed pits, but showed more sign of differentiation into osteoblasts on grooved surfaces indicated by staining osteocalcin and

osteopontin marker proteins. The group postulate that cytoskeleton organisation along the grooved surface may decrease the elongated cell area, but the topography encourages differentiation.¹¹³

Regular nanopatterned surfaces have been shown to encourage cell motility and migration. Filopodia clearly have great importance in the attachment and further cell function and appear to influence cell behaviour after gathering information from the cells environment.^{105,116} A grooved topography has been shown to not only affect cell spreading but encourage migration along the aligned topography. Cells become aligned after seeding onto a grooved substrate¹¹⁷ and migrate along the grooves.¹⁰⁵ This kind of cell behaviour could be due to the way cells act *in vivo* along collagen nanofeatures, such as banding on collagen fibres.¹¹⁸

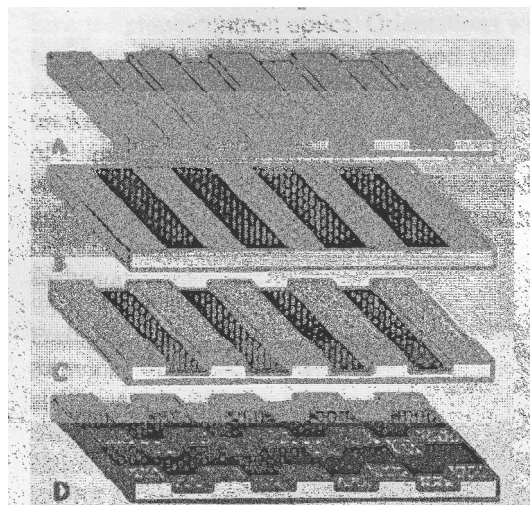


Figure 2.15: Substrates microfabricated with aligned topographical grooves (A), chemically-patterned tracks (B), aligned grooves and tracks (C), and grooves and chemical tracks aligned perpendicularly (D)¹⁰⁷

Cells also respond to different chemistries. Zreiqat *et al.*⁷⁻⁹ modified the surface of a titanium alloy (Ti-6Al-4V) with zinc, magnesium or alkoxide-derived hydroxyl carbonate apatite (CHAP). Western blotting analysis of

human osteoblasts cultured on the surfaces indicated magnesium or CHAP-modified Ti-6Al-4V modulated key intracellular signalling processes. Functionalisation of surfaces is a way of altering the chemistry of a surface to enhance cell response. Carbon nanofilaments have successfully been functionalised, inducing differences in cell response,¹¹⁹ which is discussed in more detail later in this section. It is understood that osteoblasts generally attach to material surfaces with higher surface energy. Zhao *et al.*¹⁰⁷ demonstrated that there was an effect of high surface energy and micron-scale roughness, which encouraged osteoblasts to exhibit a more differentiated phenotype on titanium surfaces acid etched and sandblasted to regulate roughness and rinsed under nitrogen protection to prevent exposure to air and increase surface energy due to reduction in carbon contamination. Osteoblast-like (MG63) cells attached less to the rough, high energy substrates but with significantly more sign of osteoblast differentiation.

So the question is not whether topography or chemistry has an affect on the cellular response, but which has a more positive effect. Britland *et al.*^{2,6} investigated the effects of desired neurite growth along chemically modified tracks in comparison to topographical grooves on the same surfaces (figure 2.15). Topographical grooves were etched into microscope slides with 100, 50, 25 and 12 μm -wide grooves and ridges with depths of 50, 100 and 500 nm. Chemically-modified, laminin tracks were laid down using the same sized grating. Neurite extensions aligned to chemically modified tracks when topographical grooves were shallow (less than 500 nm), but would preferentially align to grooves deeper than 500 nm, and therefore responded to topographical features.

Graphitic nanofibres and nanotubes have dimensions that are comparable with constituents in the first two nano-sized levels of organisation

in bone-tissue (figure 2.16). Nanofilaments can be prepared to form pressed compacts,¹²⁰ cross-linked networks,¹²¹⁻¹²⁴ or incorporated into polymer composites.^{108,125,126} These surfaces that are made up completely or partially of nanofilaments could be used to mimic the matrix of bone. The texture of the nanofilament surfaces could be tailored to match the collagen-mineral composite surfaces of bone.

Few studies have investigated the growth of osteoblasts on nanostructured carbon filaments. One research group (Price *et al.*¹⁰⁸) has seen promising results of osteoblast activity on carbon nanotube compacts in comparison to Ti6Al4V, CoCrMo and etched glass samples.^{3,108} They concluded that smaller scale carbon nanotubes promoted osteoblast adhesion but did not promote other cell lines (such as chondrocyte and fibroblast activity).² This could be desired for certain orthopaedic applications where competition from other cell lines could impede bone growth. A longer term *in vitro* study showed increased osteoblast activity over a 7 day period.² Elias *et al.*¹⁰⁸ demonstrated that human osteoblast cells responded to nanofilaments with diameters of 60 nm and 100 nm with greater proliferation, alkaline phosphatase activity and extracellular calcium compared to larger diameters (125 nm and 200 nm) despite differences in surface energy (due to nanofilament stripping of the pyrolytic outer layer) between the samples. The same group showed a preference for as-grown nanofilaments (with a pyrolytic outer layer) in terms of proliferation using other cells (bovine bladder smooth muscle cells, mouse skin fibroblasts and human articular chondrocytes) compared to pyrolytically stripped nanofilaments, but human osteoblasts responded to diameter instead of surface energy (same trends as Elias *et al.*).^{127,128} George *et al.* studied the response of human lung epithelial cells (A549), osteoblast-like cells (MG63) and primary foetal osteoblast cells on multi-walled carbon nanotube arrays.¹²⁷ It is evident from their results that

cells proliferated on the nanotube surfaces over 7 days of culture. The rate of proliferation, however, decreased in comparison to flat glass control surfaces. Through observation of cell spreading and morphology, in particular, there was a difference in focal contact adhesion and cell morphology on the MWNT arrays when compared to flat control surfaces.¹²⁹ Reduced proliferation may be preferred in some biomedical devices and tailoring the presentation of nanofilaments at the surface of an implant could be used to impart different cell responses.

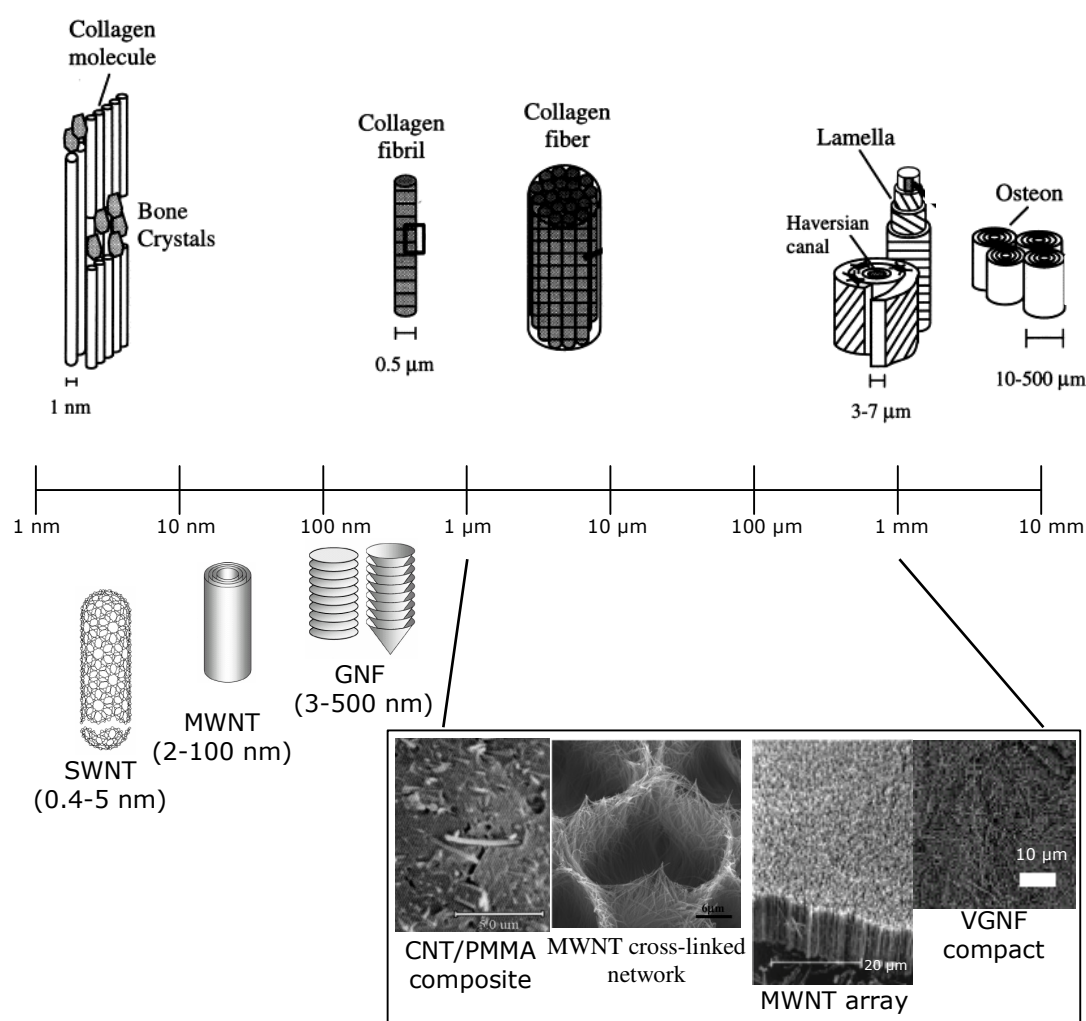


Figure 2.16: Comparison of diameters of bone constituents⁵⁹ and carbon nanotubes, graphitic nanofibres,¹²³ and larger scale nanofilament materials that maintain nanoscale features including a nanotube-methacrylate composite,¹²⁰ MWNT network,¹⁰⁰ nanofilament arrays,¹⁰⁸ and nanofilament compact⁹

When biomaterials are exposed to biological environments, extracellular matrix (ECM) proteins are adsorbed onto the surface of the implant, then neighbouring cells indirectly interact with the surface of the biomaterial through this adsorbed protein layer.¹³⁰ Biomaterial surfaces can be modified with bioactive molecules to render them biomimetic. Biomimesis may be achieved by incorporating cell-binding peptides into the structure of materials to enhance cell attachment and biomaterial integration into the body. In early work on biomimetic materials, ECM proteins such as fibronectin, vitronectin and laminin were used to modify biomaterial surfaces to promote cell adhesion and proliferation.³⁷ These proteins all contain the tripeptide, Arginine-Glycine-Aspartic acid (RGD), which has been shown to promote cell adhesion if accessible to arriving cells as discussed in section 2.2.1.^{29,36,38} Integrins are thought to be the dominant mechanism by which cells communicate with noncellular surroundings,^{128,131} therefore by maximising the probability of displaying the RGD sequence to arriving cells will give the implant a better chance of being integrated into the body.

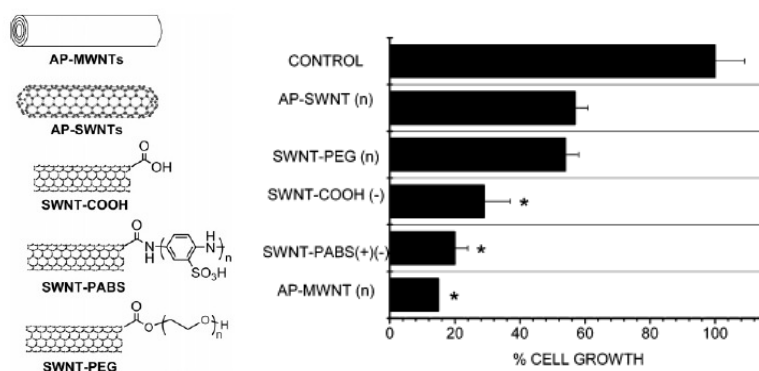


Figure 2.17: Chemical structures of functionalised single-walled nanotubes and quantification of cell proliferation on SWNT sprayed substrates⁸

Nanofilaments can also be functionalised to promote enhanced cell or tissue response. Nanotubes, especially, have been studied to enhance or control cell activity, especially for neural and orthopaedic applications. One of the first indications of functionalising carbon nanotubes for neural growth was reported by Mattson *et al.*⁹ Their findings suggested that neurite outgrowth was observed on unmodified nanotube surfaces but neurite branching was not observed, contrary to the neurons grown on the 4-hydroxynonenal (4-HNE) coated nanotubes. More recently Zanello *et al.*⁷ published work on single-walled and multi-walled nanotubes functionalised with a neutral, negative or zwitterionic net charge. SWNTs were functionalised with carboxyl groups (SWNT-COOH; negative charge), poly-(m-amino-benzene sulphonic acid) (SWNT-PABS; zwitterionic charge), and poly (ethylene glycol) (SWNT-PEG; neutral) as illustrated in figure 2.17. The group found a greater degree of rat osteosarcoma cell growth on the neutral SWNTs compared to functionalised SWNTs with any electronic charge. The same group discovered that functionalisation with positively charged groups encouraged neurite outgrowth of hippocampal neurons isolated from Sprague-Dawley rats.⁹ This may indicate that different cell types may respond differently to specifically charged functionalised groups, but a positively charged functionalised group was not investigated with rat osteosarcoma cells.^{132,133} Nanotubes have also been functionalised with hydrophilic polymers,¹³³ biological and bioactive groups including proteins,¹³⁴ amines and enzymes.¹² These functionalised nanotubes have yet to be investigated with respect to their cytocompatibility.

2.3.2. Improvement of bulk properties of implants

One way to combat the modulus mismatch between bone and metal implants is to use materials with an elastic modulus closer to that of bone. Examples of other materials that are used in orthopaedic devices include

ceramics, glasses, polymers and composites. Ceramics and glasses have been used in biomedical devices, especially hard tissue repair or replacement which require adequate adhesion between the tissue and biomaterial.¹² Such examples include synthetic hydroxyapatite and bioactive glasses which encourage direct attachment to bone, tricalcium phosphate which eventually gets replaced by bone tissue, and ceramic coatings which support mechanical attachment between bone and implant.¹³⁵

When designing orthopaedic devices, the concern is not only whether the implant will get accepted into the body, but also what tissue response is required. Permanent devices require osseointegration in order to be successful, such as permanent fixation plates, femoral stems of TJR and bone cements. Temporary biomaterials, such as fixation plates or screws, need minimal bone bonding as the device would need to be removed without trauma.¹³⁶

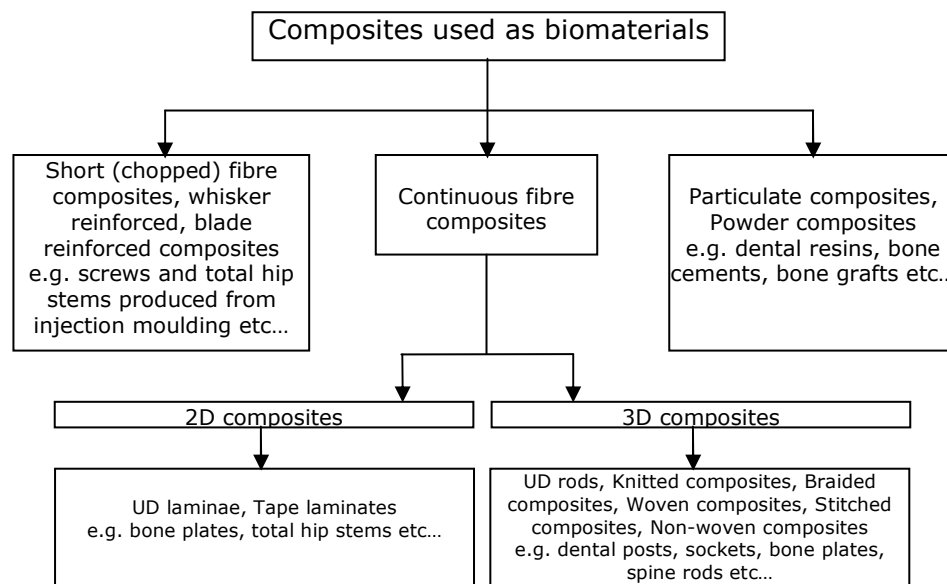


Figure 2.18: Classification of reinforced composites¹³⁶

The bulk properties of orthopaedic materials can be improved by choosing or tailoring the bulk mechanical properties of a biomaterial nearer to that of bone. Polymers and polymer composites are examples of materials that could improve biomaterial function as orthopaedic implants. Specifically, polymer composites could be used as bone cements or porous polymeric scaffolds, both of which require osseointegration or a strong implant/tissue interface.

As there are large differences in strength and stiffness between bone and most orthopaedic devices, some reinforced polymers have also been investigated as potential substitutes as their strength to weight ratio is nearer that of bone. Bone itself is a composite of collagen fibrils and inorganic calcified phase; this producing a lightweight, high-strength structure. Therefore, to mimic the composition of bone, many reinforced composites employ a high stiffness fibrous or particulate material incorporated into a polymer to produce a lightweight implant with increased stiffness and fatigue life.

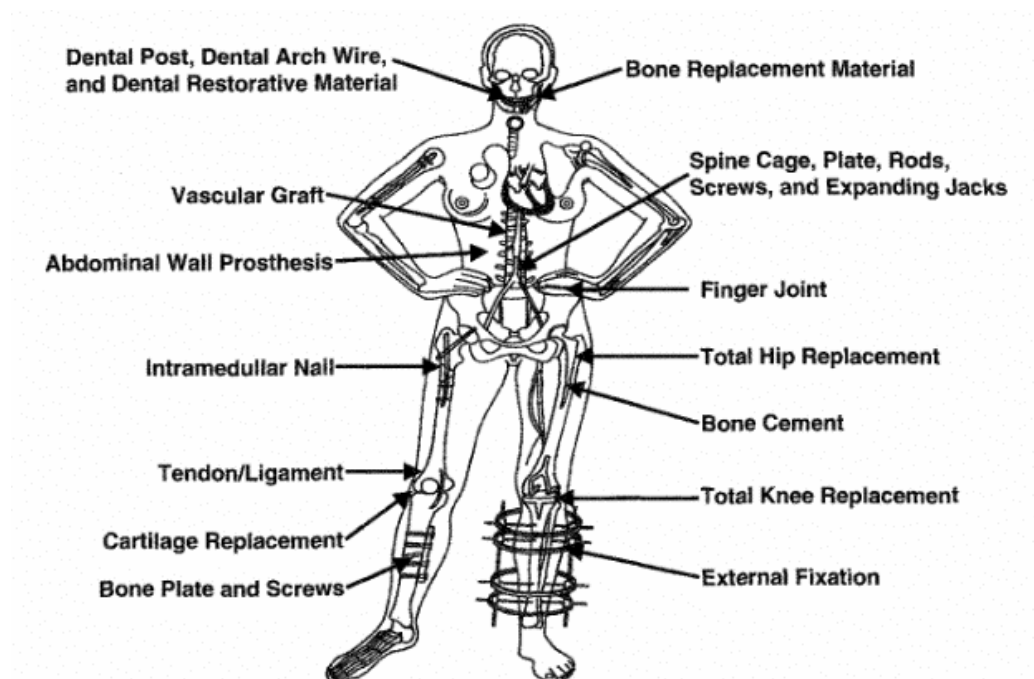


Figure 2.19: Medical devices fabricated from composite materials¹³⁷⁻¹³⁹

Micron-size carbon fibres have been used to reinforce UHMWPE, poly(ether ether ketone) (PEEK),¹² poly(methyl methacrylate) (PMMA), high density polyethylene (HDPE) and poly(tetrafluoroethylene) (PTFE).¹⁹ These reinforced polymers have been used for prosthetic hip stems, fracture fixation devices, artificial joint bearing surfaces and bone cements. Figure 2.18 summarises different types of composite materials depending on their reinforcing phase, and their biomedical applications. Potential composite applications are illustrated in figure 2.19 including soft and hard tissue devices. PEEK-OPTIMA® is a clinical bioinert polymer, based on PEEK that can be reinforced with short carbon fibres (microfibres). The addition of 30 wt% carbon fibres raises the flexural modulus of the material (from 4 to 19 GPa) nearer to that of cortical bone (19 GPa).¹⁹ Endolign®, another carbon fibre-reinforced PEEK composite, uses unidirectionally-aligned continuous carbon fibres that raises the modulus to a greater extent (from 4 GPa with no reinforcement to 150 GPa).¹³

Methacrylate polymers are used frequently in medical devices, especially in clinical bone cements. Poly(methyl methacrylate) (PMMA) is the most commonly used methacrylate, but there are other methacrylate polymers being used and researched. These include poly(hydroxyethyl methacrylate) (PHEMA), a hydrogel, and poly(ethyl methacrylate) (PEMA). All commercial bone cements are made from methyl methacrylate (MMA)¹³, which is an ester of methacrylic acid (MA). For clinical applications, polymerisation from MMA monomer would take too much time, would produce too high a shrinkage (21%) and generate heat that would be too high for biomedical use (100 °C). Therefore, pre-polymerised PMMA, in the form of tiny balls is used to aid polymerisation as it easily dissolves in the monomer MMA solution. This greatly reduces the polymerisation time, reduces shrinkage and greatly reduces the temperature of polymerisation.¹⁴⁰⁻¹⁴⁵

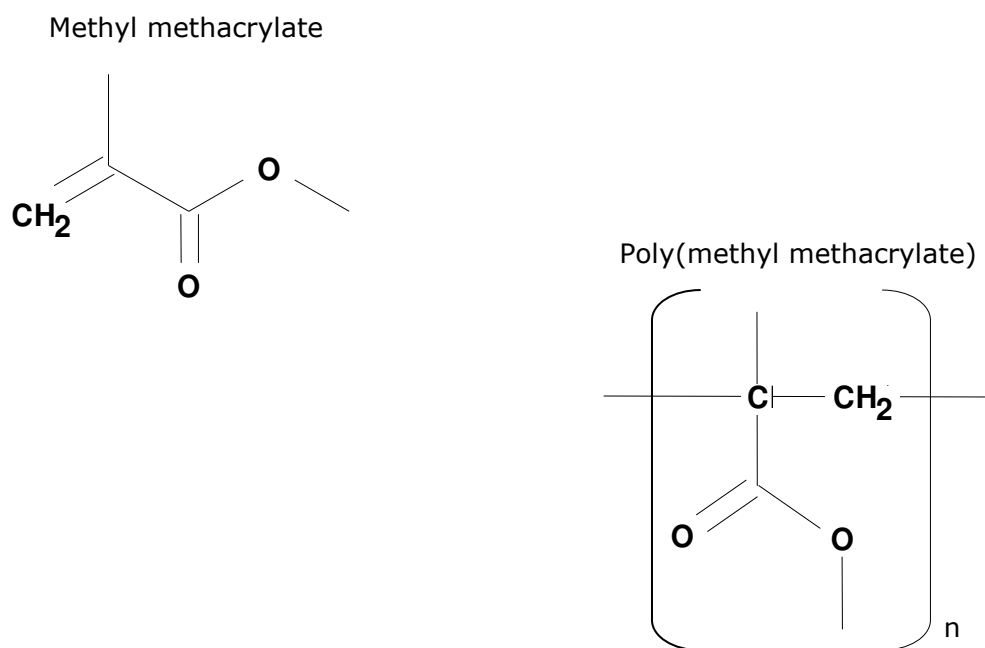


Figure 2.20: Chemical formulae of methyl methacrylate (MMA) and poly(methyl methacrylate) (PMMA)¹⁴⁶

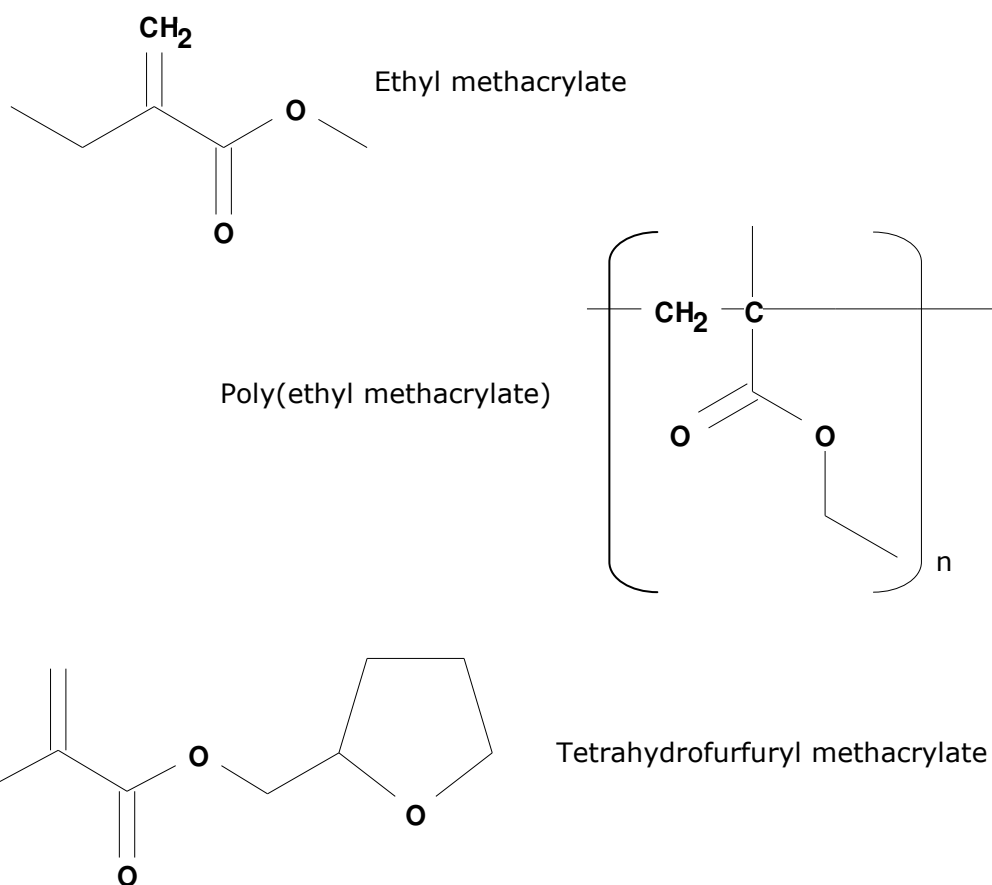


Figure 2.21: Chemical formulae of ethyl methacrylate (EMA), poly(ethyl methacrylate) (PEMA) and tetrahydrofurfuryl methacrylate (THFMA)

Other methacrylate polymers can be produced by a similar method. Poly(ethyl methacrylate)/tetrahydrofurfuryl methacrylate (PEMA/THFMA) has shown potential in cartilage repair and bone contacting applications.¹³ PEMA/THFMA is polymerised in a similar fashion to PMMA. The final co-polymer is polymerised from a THFMA monomer liquid, a PEMA polymer powder and N,N-dimethyl-p-toluidine (DmpT) as the initiator. The chemical formula of PEMA/THFMA is shown in figure 2.21.

The polymerisation process in methacrylate bone cements is a free-radical polymerisation. Free-radical polymerisation is a chain polymerisation in which each polymer molecule grows by addition of monomer to a terminal free-radical reactive site known as an active centre. To generate free-radicals, an initiator is required, dibenzoyl peroxide (BPO) in the case of producing PMMA. PMMA bone cement can also be polymerised using an additional initiator, N,N dimethyl-p-toluidine (DmpT), which can work together with BPO to form free-radicals (figure 2.22). BPO is premixed with the PMMA powder component and DmpT premixed with the MMA liquid component. Therefore, the components required for the free-radical chain polymerisation are a monomer liquid, a polymer powder and an initiator system. The initiator system produces free radicals when the liquid and powder components are mixed together. DmpT breaks the BPO initiator at room temperature (figure 2.22), which in turn attacks the double bond of the MMA (for example) increasing the polymer chain (figure 2.23). The growing polymer chains encapsulate the polymer beads within the solid matrix.¹⁴⁶ There are three stages in free-radical chain polymerisation: initiation, propagation and termination.

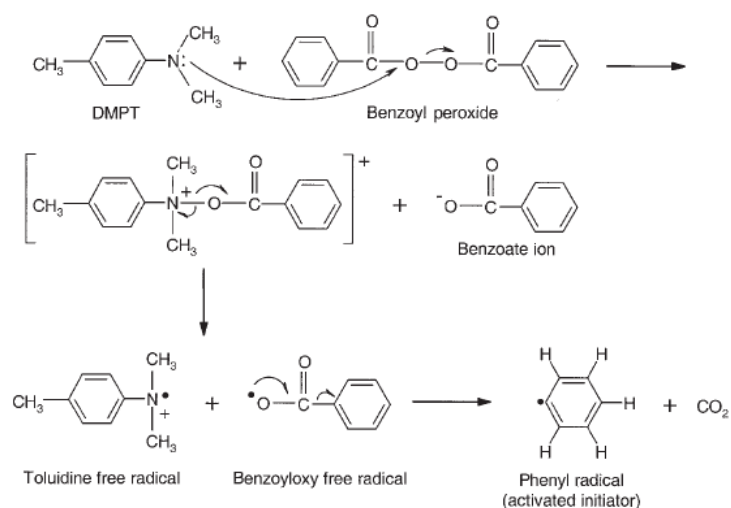


Figure 2.22: Free radical production using dibenzoyl peroxide, BPO, (in the polymer powder) and N,N dimethyl-p-toluidine, DmpT, (in the liquid monomer) of bone cements¹⁴⁶

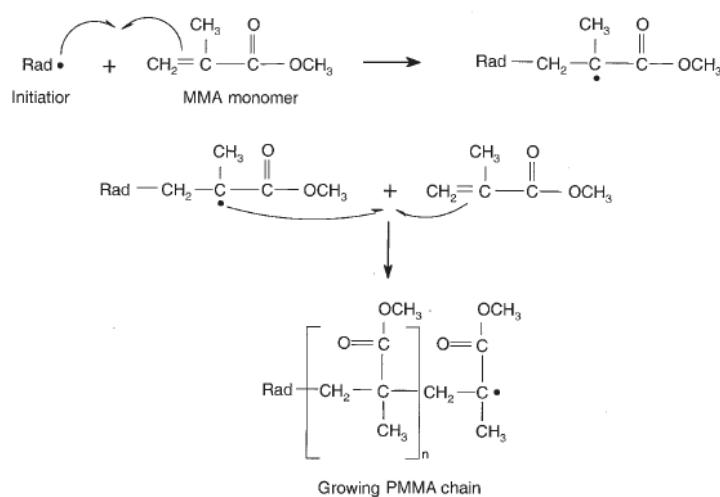


Figure 2.23: Polymer growth initiated by free radical interaction with the monomer (methyl methacrylate in this example)¹³

Initiation occurs in two steps. Initially, the formation of free radicals must occur from the initiator, and then the addition of the free radicals to a molecule or monomer. Free radicals are generated by homolysis of a single bond or single electron transfer to or from an ion or molecule (redox). Homolysis can be affected by heat (thermolysis) or the application of radiation (photolysis). Redox reactions are often used because they operate at lower temperatures. The free radicals are then required to produce active centres,

by attacking the π -bond of a molecule or monomer. This will be achieved by one of the two modes illustrated in figure 2.24.

Secondly, propagation of the polymer chain occurs by rapid sequential addition of the monomer to the active centres. Head-to-tail addition is more likely as the methylene carbon (highlighted in figure 2.24) is less sterically hindered and produces a more stable molecule. Finally, termination of the polymerisation process occurs by two growing chains reacting together either by combination or disproportionation.

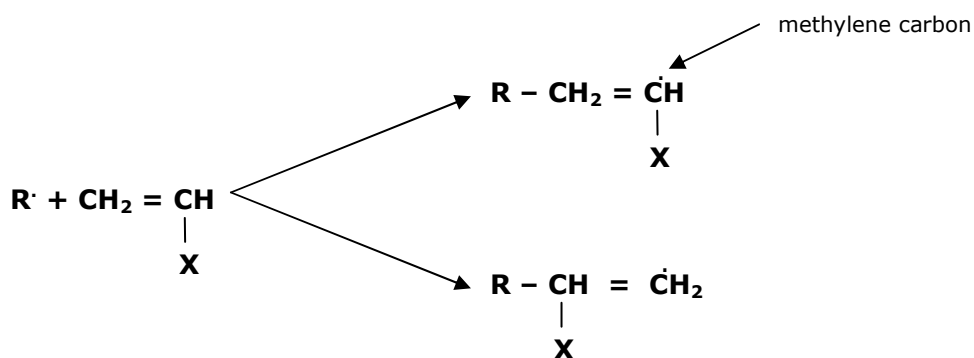


Figure 2.24: Two modes of addition where free radicals attack the π -bond of a molecule or monomer

The polymerisation of these methacrylate polymers is characterised in four steps: mixing phase, waiting phase, working phase and hardening phase.¹⁵ The mixing phase of the polymerisation process provides a low-viscous solution where the monomer liquid and polymer powder are mixed. When the waiting phase occurs and the solution starts to increase in viscosity, there is a limited amount of time to add a filler (if not already incorporated), until chain propagation (working phase). This still provides time in the working phase to mould the curing composite for its purpose. The setting phase then occurs until polymerisation is complete.

Porous scaffolds offer a 3-dimensional structure that will allow mechanical stability whilst encouraging tissue ingrowth and potentially restore bone form and function. Cancellous bone is a 3-dimensional porous scaffold which contributes to its form and function. Scaffolds provide a volume fill, mechanical integrity and can be designed to enhance tissue regeneration by chemical and architectural guidance.¹⁴² Polymers are the most common materials, which can be made into scaffolds by fibre bonding, particulate leaching, emulsion freeze drying, phase separation, rapid prototyping and supercritical foaming.¹⁴⁷ In the case of bone repair, a scaffold must have an interconnected pore network of certain pore size to aid cell migration and an adequate flow of nutrient and removal of waste, with mechanical properties near to that of bone and it must exhibit suitable surface chemistry to promote osteoblast attachment, proliferation and differentiation.^{121,124,148}

The addition of carbon nanofilaments into polymeric matrices can enhance the surface characteristics and bulk mechanical properties of the polymer. These properties can be tailored and exploited in biomedical devices. Various polymers have been investigated as matrices for carbon nanofilaments, primarily nanotubes. Such polymers include polycarbonate (PC),¹⁰ polycarbonate urethane,^{149,150} polyethylene,¹²⁴ polypropylene,¹⁵¹ epoxy resins,^{122,123,152-155} and methacrylates.¹²¹ Many of these polymers could be used or are clinically used as biomaterials. Reinforcing properties have been observed when incorporating nanofilaments into polymer matrices. Nanotubes especially have been shown to improve mechanical properties compared to unfilled polymer. For example, Carneiro *et al.*¹²¹ observed a 39% increase in elastic modulus and 17% increase in yield stress when incorporating 20 wt% vapour-grown nanofibres (Pyrograf[®] III) into a poly(carbonate) matrix.¹⁵⁶ Other groups have seen improvements at much lower loadings. Shi *et al.*,¹²² for example, used 0.05 wt% SWNT in a poly(propylene fumarate) matrix and

observed an increase of 74% in compression modulus and 69% in flexural modulus. Another potential application of carbon nanofilaments in bone repair applications is in low-wear implants, such as the wear surface of an acetabular cup. One group¹⁵⁷ investigated the tribological properties of PMMA-CNT composites and noticed that the optimum properties were at a 1 wt% loading of nanotubes. Microhardness increased from approximately 26 to 37 HV, the coefficient of friction decreased from approximately 0.45 to 0.32 and wear rate decreased from approximately 2.5×10^{-4} to $1 \times 10^{-4} \text{ mm}^3 \text{N}^{-1} \text{m}^{-1}$.

One of the problems with carbon nanofilaments as fillers is that they tend to agglomerate, which limits the efficiency of the composite, producing defect sites.¹⁵⁸ Dispersion techniques, such as optimum physical blending, *in situ* polymerisation and chemical functionalisation, are designed to minimise filament bundling and entanglement.¹⁵⁷ Sonication and high speed shearing are two examples of optimising physical blending. These techniques are still the most convenient and practical way of dispersing nanofilaments in a polymer matrix. Qian *et al.*¹⁵⁸ used a high energy sonication technique to disperse nanotubes in a polystyrene matrix dissolved in toluene. *In situ* polymerisation is perhaps the easiest way to incorporate filler into a polymer matrix due to the low viscosity of the monomer.

Melt mixing and ball milling are also used to disperse nanofilaments in polymer matrices. Surfactants can also be used to aid dispersion. Melt mixing is commonly achieved by extrusion or injection moulding, where the polymer is usually in the form of pellets or powder to aid melting. The polymer is loaded through a hopper and heated to melting point whilst being forced by a rotating screw into a mould (injection moulding) or as extrudate (extrusion). Extrudate can then be moulded using one of several methods such as blow moulding, rotational moulding or calendaring.

Anisotropic properties can be achieved in a composite by aligning the filler. For example, electrical and mechanical properties of carbon nanofilament-polymer composites will be affected by the orientation of the carbon. It is important in some applications to achieve anisotropy. Various *ex situ* alignment syntheses can be used before introducing them to the polymer, such as filtration, plasma-enhanced CVD and catalyst templates.⁴⁴

2.3.3. Electrical stimulation of osteogenesis

A method for enhancing bone repair in orthopaedic devices is through electrical stimulation. Although the mechanism is not yet known, electrical stimulation of osteogenesis (production of new bone) has been used clinically for the enhancement and stimulation of bone growth especially in non-union or delayed union of fractures.²¹ It can also be used to accelerate repair and remodel, especially in sports fractures where time is more critical.^{33,44,159,160} This section concentrates on the biophysical principles of regenerating bone tissue with particular respect to the electromechanical stimulation of bone growth.

2.3.3.1. Mechanisms of electrical stimulation

Bone is believed to use electrical energy to stimulate its continual growth in response to mechanical forces applied,³³ hence termed electromechanical stimulation. It is thought that when a load is applied to bone, the mechanical energy is converted into electrical signals and changes the bioelectric environment that may control the mitotic and functional activity of bone or mesenchymal cells.^{33,160,161}

The mechanisms of the electrical stimulation of bone regeneration are still poorly understood, but it is thought that the cause is mainly due to the piezoelectric properties or streaming potentials in the bone tissue environment.¹⁶¹ Piezoelectricity is caused in crystalline materials when the deformation of the crystal results in a flow of electric current as electrons are displaced from one part of the lattice to another.^{33,162-164} Piezoelectric effects in bone would result from the stresses applied as mechanical forces are exerted on the crystalline constituents in the bone matrix especially hydroxyapatite crystals and collagen fibres.^{33,162} Streaming potentials result from cells, ions or charged bodies flowing past stationary charged components, such as endothelial cells or biopolymers in the vascular wall. Streaming potentials would largely be caused by blood flow or the flow of interstitial fluid past bone tissue (as a result of mechanical forces).³³ Other possible causes of bioelectric effects could be due to pyroelectricity produced from polarisation in certain crystalline substances as a function of temperature change or ferroelectricity/ferroelasticity from crystals which exhibit a spontaneous electric dipole moment.¹⁶⁴ There is not much literature investigating the effects of pyroelectricity or ferroelectricity on osteogenesis as piezoelectricity and streaming potentials are understood to be the predominant mechanisms.

To study the effects of electrical stimulation of bone or bone-forming cells, it is clear that you can either deliver a direct or indirect electrical current through a material, or perhaps develop a biomaterial that possesses piezoelectric properties.¹⁶⁴ Miara *et al.*²⁵ have proposed a biomaterial made from an inert perforated piezoelectric matrix that could be filled with osteoblasts. The group tried to mimic natural bone, by producing a potentially bioactive material that would produce small local electric currents (by

piezoelectric effects) nearby osteoblast cells. Unfortunately, this work is in its initial stages and at this time is only a theoretical model.

With respect to studying the response of bone tissue or osteoblasts to electrical current, there seem to be clearer conclusions drawn from *in vivo* studies rather than *in vitro* investigations. This may be due to the bioelectric effects in the bone matrix contributing to the cellular response rather than the direct application of a current to stimulate cells *in vitro*. Nevertheless, electrical stimulation of osteoblasts has been shown to create enhanced responses *in vitro*. One possible explanation for this is that an electric current or an electromagnetic field causes a charge around the cell membrane, which would influence ion channels. Calcium ion channels, in particular, affect osteoblast proliferation. Zhuang *et al.*²⁵ studied the effects of pulsed capacitively-coupled electric stimulation on the proliferation of osteoblast-like cells (MC3T3-E1) and the levels of TGF- β 1 mRNA, an important growth factor in inducing bone formation. The observed increase in TGF- β 1 was accounted to a rise in cytosolic calcium (Ca^{2+}), which would activate calmodulin (intracellular calcium-binding protein which is involved in cell proliferation) and give rise to TGF- β 1. Although it was noted that TGF- β 1 was not strictly involved in the mechanism of electrically-induced proliferation of osteoblast cells but gave evidence for the increase in cytosolic calcium.^{44,162,163}

2.3.3.2. Methods of electrical stimulation *in vitro* and *in vivo*

There are three methods used to promote the growth of new bone that can be used *in vitro* or *in vivo*; Faradic, inductive and capacitive electrical signals.^{162,165,166}

In Faradic stimulation, electricity is delivered directly to the sample (*in vitro*) or bone (*in vivo*) utilising electrodes. The inserted electrodes and electrochemical reaction products obtained are likely to initiate cellular responses.¹⁶⁷ Faradic stimulation of bone has been shown to promote bone formation at the negatively charged electrode, and accelerated healing of osteotomies has also been observed *in vivo*.^{168,169}

Inductive stimulation offers an indirect approach, without the need for implanting electrodes. This method is usually performed using an electromagnetic coil that is placed around the culture plate (*in vitro*)^{162,166,170,171} or bone tissue (*in vivo*)^{169,171} and an electromagnetic field produced in the desired area. A common inductive stimulation method is called pulsed electromagnetic field (PEMF) stimulation and has been used for over 25 years on patients with delayed fracture healing.¹⁶⁶ One of its advantages is that it is a non-invasive method and also that it may be enhanced by using it along side conductive prosthetic materials after implantation. Yonemori *et al.*¹⁶⁶ showed differences in bone growth *in vivo* between the Faradic direct current (d.c.) stimulation method, the PEMF stimulation method and an unstimulated and PEMF-stimulated Kirshner-wire (orthopaedic fixation device) alongside the PEMF technique. A Kirshner-wire was inserted into a rabbit humerus to understand the inflammatory response to the electrode as well as the electrical mechanisms. Figure 2.25 illustrates the difference in new bone formation along the humerus of rabbits. The largest tissue response was observed around the cathode stimulated with direct current. There was a milder response from the Kirshner-wire stimulated with PEMF induction, but uniform over the length of the wire.¹⁶⁶

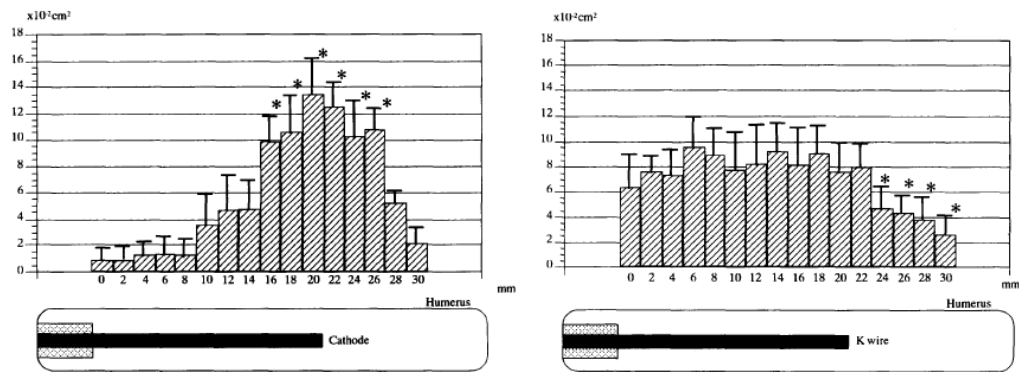


Figure 2.25: New bone formation along the humerus of a rabbit with the insertion of a cathode stimulated by a direct current (left), and a Kirshner-wire stimulated by PEMF electromagnetic induction (right). The vertical y-axis indicates cross-sectional area of new bone growth.¹⁶²

Lastly, the capacitive technique stimulates bone by transferring electric charge from one conducting material to another resulting in a potential difference between them.^{22,42} This has been demonstrated *in vitro* by using two stainless steel electrode plates attached to the top and bottom of a cell culture dish. Electric charge can then be transferred from one plate to the other through the culture dish,⁴ usually utilised in a pulsed fashion. It can also be used semi-capacitively *in vitro* by placing one of the capacitive plates into the culture media and using the sample as the other plate.¹⁷² *In vivo*, this method could be manipulated by placing bone in between the two plates.¹⁶⁵

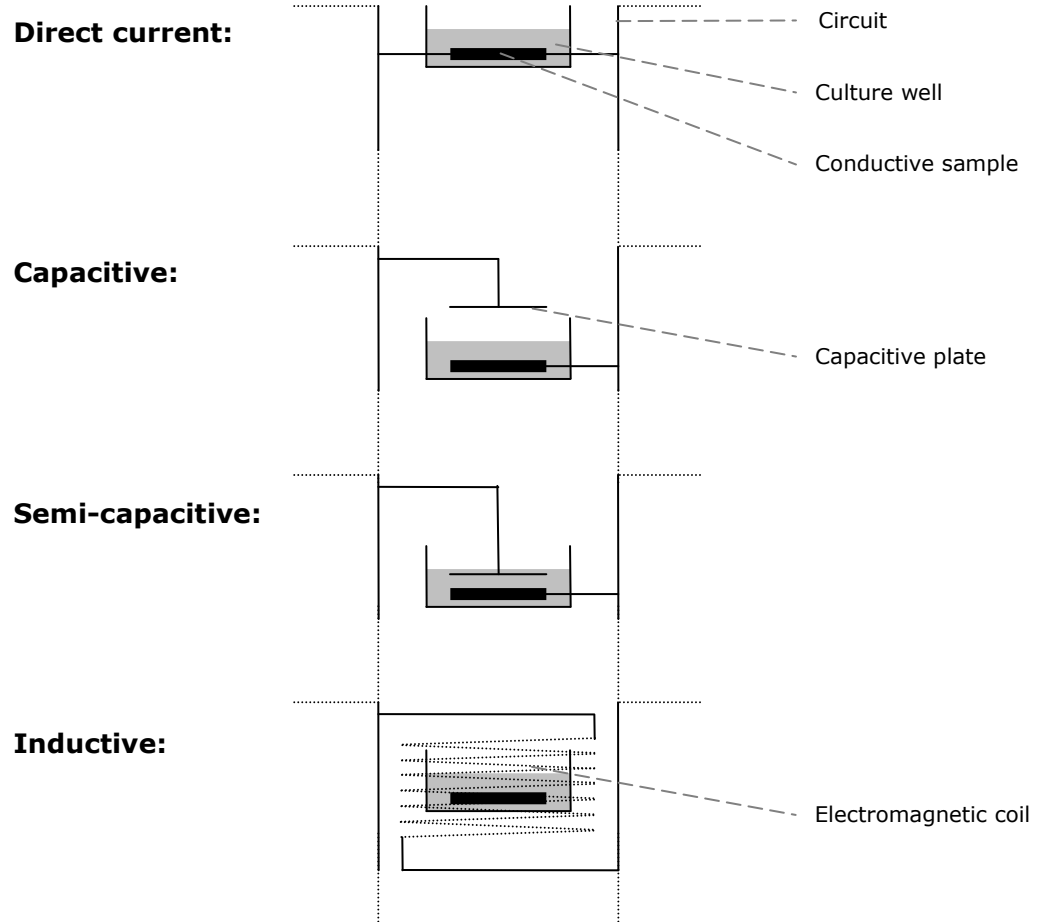


Figure 2.26: Basic schematic of different experimental set-ups for *in vitro* electrical stimulation of osteoblast cells.

In vitro investigations have centred on these three methods to electrically stimulate osteoblasts. Figure 2.26 shows a summary of different set-ups to achieve this. Direct current simply applies a current through electrodes to the conductive sample in culture.^{4,22,25,42} There will be effects of electric field, effects at the anode and cathode, and also effects of current and frequency on the exposed cells. The capacitive and semi-capacitive experiments use a capacitive plate to discharge pulses of current to the anode sample.⁴² The capacitive plate is located above the culture media in capacitive induction and in the media for semi-capacitive induction. Finally, inductive stimulation uses an electromagnetic coil to provide an electric field.²² This electric field will then cause current in the conductive sample in culture. All

three methods of stimulation have shown enhanced growth of osteoblasts or osteoblast-like cells *in vitro*. For example, capacitively-coupled fields have been shown to induce an increase in extracellular calcium after 10 days to 21 days of culture compared to unstimulated controls in osteoblast-like cells.¹⁶⁸ Tang *et al.*¹⁶⁸ used PEMF to stimulate mouse osteoblasts to investigate the effects of pulsed frequency on cell proliferation, proliferative activity of the cells after exposure and magnitude of pulsed current on intracellular calcium concentration. Any frequency of pulsed current (200 mV cm^{-1}) up to 1000 Hz induced an increase in the number of cultured cells after 36 hours with initial 20 minutes of exposure to electromagnetic field. The ratio of cells in the S-phase was measured by flow cytometry and was higher on cells exposed to PEMF than on the control. The concentration of intracellular calcium was also shown to be higher on cells that had been exposed to PEMF.^{25,168} This agrees with the idea that the charge on a cell membrane may cause calcium channels to open and encourage further cell signalling and function.⁴

Polymers can exhibit electrical conductivity by incorporation of conductive carbon nanofilaments. Supronowicz *et al.*⁴ used polylactic acid blended with CNT to investigate the effects of electrical current on osteoblast activity. As detailed previously, the presence of an electric field through bone can induce bone reformation or growth. Carbon nanotubes conduct electricity along their fibre axis, providing an alternative to metal implants to conduct electricity *in situ* when implanted into bone. One study has investigated the cellular response to the application of an alternating electrical current through a carbon nanocomposite.⁴ The research looked at polylactic acid reinforced with carbon nanotubes (80% PLA/20% CNT) and indicated that osteoblast function increased with electrical stimulation. An increase in osteoblast proliferation, their expression of collagenous and noncollagenous proteins and calcium deposition in their extracellular matrix was observed compared to a

non-electrically stimulated reference sample.¹⁷³ Nanotubes have also been incorporated into a three-dimensional porous PLA structure, similar to that of cancellous bone that conducted electrical current. The composite scaffold showed increased osteoblast proliferation when exposed to a semi-capacitive electrical current.¹⁷⁴⁻¹⁸⁰

2.3.4. Biomedical concerns of carbon nanofilaments

Interest in carbon nanofilaments for biomedical use is rapidly increasing. Not surprisingly, the concern over the toxic response of cells and tissues to the exposure of carbon nanofilament or other nanoparticulates is also increasing.¹⁷⁷ The majority of studies into the toxicity of nanoparticulates focus on lung response, as the main concern is from the inhalation of particles from the atmosphere, especially carbon products from exhaust fumes. Of particular interest is whether, when inhaled, particulate matter (PM) passes through the air: blood barrier in the alveoli of the lungs. Therefore, the work is either directed at the lung response if the PM does not pass through the lungs or the effects of PM on other organs in the body if permitted to pass into the blood circulation.

PM is separated into three categories in order to determine the effects of different sized particles:

- 'Coarse' particles (PM_{10}): Particles 2.5-10 μm
- 'Fine' particles ($PM_{2.5}$): Particles 0.1-2.5 μm
- 'Ultrafine' particles (nanoparticles): Particles less than 0.1 μm

As this investigation is related to structures in the nanoscale it is the 'ultrafine' particles that we are concerned with. These are often termed as

nanoparticles and for the purposes of this study the term nanoparticles will be used.

One study by Nemmar *et al.*¹⁷⁷, used radio-labelled carbon nanoparticles (^{99m}Technetium-labelled carbon particles <100 nm) to assess how rapidly nanoparticulate matter passes into the systemic circulation and to what extent nanoparticulate matter passes through the air: blood barrier. Five healthy, male, non-smoking volunteers inhaled an aerosol suspension of ^{99m}Technetium-labelled carbon nanoparticles. A gamma camera was used to examine where the nanoparticles went and a gamma counter was used to assess what relative concentration of nanoparticles reached the liver and bladder compared to the lungs. The gamma counter showed that the radioactivity in the blood from the radiolabelled carbon nanoparticles plateaued after 20 minutes. The lungs had the greatest intensity of gamma counts, but the liver and increasingly with time, the bladder, also showed presence of the nanoparticles.^{179,180}

Lung cells, such as human alveolar cell lines and alveolar macrophages are often used to try to understand the lung response to nanoparticulate matter. When considering the movement of particles into the blood circulation, there are a number of obstacles to encounter before they can cross the air: blood barrier. In order to reach the alveolus, the particles have to pass through the airway from the bronchia avoiding the cilia. The cilia are epithelial cellular extensions that remove the particles by propelling the particles through the mucus away from the alveolus. The last obstacle before reaching the air: blood barrier is to avoid alveolar macrophages. These macrophages remove unwanted particles by phagocytosis. A problem with excessive amounts of nanoparticulate matter in the lungs is overloading the macrophages, inhibiting their response. Carbon black and especially silica

have shown increased macrophage clearance time with relatively small concentrations of nanoparticles compared to other nanoparticles.¹⁷⁸ An *in vivo* investigation¹⁷⁸ administered CNTs intratracheally into Sprague-Dawley rats. Carbon nanotubes were not rapidly eliminated and still present after 60 days (biopersistent). Ground nanotubes created a larger response with respect to TNF α concentrations and lactate dehydrogenase (LDH) activity than acid washed nanotubes *in vitro*, although unground samples showed a greater biopersistence in the rat lung *in vivo*.¹⁷⁵

With respect to this project, the problem of any free carbon nanofilaments in the body is not concerned with the lungs, but concentrated in the bone and surrounding tissues. If nanofilaments get into the blood, they will circulate around the body and possibly affect other tissues. The response of immunological cells is important as they will be the major source of removal from the affected tissues and may cause inflammatory response. For this reason there have been other studies into the response of cells to loose carbon nanofilaments. For instance, Bottini *et al.*¹⁷⁵ used human T lymphocyte cells cultured in media containing pristine (untreated) nanotubes compared to acid treated nanotubes. Their findings suggest that oxidised (acid treated) nanotubes provoked more of a response than pristine nanotubes. This may have been due to the pristine nanotubes being hydrophobic and not as well dispersed in the media. Bottini *et al.* did not see a significant reaction with oxidised nanotubes below 40 $\mu\text{g/ml}$ and the group suggest that in use, CNTs have concentrations well below this level.^{3,4,108} Having said this, it cannot be assumed that nanotubes with different surface chemistries will act in a similar way.

2.4. Summary

The structure and function of bone is very complex. Its composition, structure and cellular organisation cause many obstacles when considering solutions for bone repair devices. As a three-dimensional structure, the environment of bone tissue has dimensional, configurational, compositional and mechanical factors that can be simulated by biomaterials to instigate bone tissue growth in and around an implant.

Carbon nanofilaments offer potential in bone repair devices due to their dimensional parameters with particular respect to their diameters compared to collagen fibrils in bone tissue. The diversity of nanofilament sizes and structures also offer reinforcing capabilities,³ as well as producing nanoscale surface textures when incorporated into polymer composites.⁴ The electrical conductivity of carbon nanofilaments⁴ also offer opportunity to utilise nanofilament incorporated composites as conductive scaffolds to electrically stimulate bone regeneration.^{2,3,6,108}

At present, there is limited information reported in the literature concerning the role of carbon nanofilaments in biomaterials, especially with respect to nanofilaments of differing structure. Size effects of vapour-grown nanofibres (VGNFs), which are essentially MWNTs with an amorphous carbon outer layer, have been investigated somewhat by Price *et al.*,²⁰ but with little respect to nanofilament structure. The size and structure of nanofilaments is critical in understanding their role in surface modification, mechanical reinforcement of polymers and increasing conductivity in polymers. Surface modification using nanofilament compacts or nanofilament textured composites can be used to assess bone growth around such biomaterials. This study investigates, for the first time, the effects of both diameter and

structure on pressed nanofilament surfaces and nanofilament-composite surfaces with particular respect to osteoblast response on the resultant surface topographies, as well as the effects of nanofilament nature on reinforcing and increasing conductivity of poly(ethyl methacrylate)/tetra hydrofurfuryl methacrylate (PEMA/THFMA) polymers. Subsequently, the effects of electrical stimulation of osteoblasts, with pulsed current, grown on nanotube-PEMA/THFMA composites were investigated in terms of proliferation and differentiation.

3. Carbon Nanofilament Preparation and Characterisation

3.1. Introduction

This chapter is concerned with the production and characterisation of the nanofilaments used in this investigation. In order to assess the potential role of carbon nanofilaments in bone repair devices discussed in later chapters, it was critical to understand the nature and characteristics of the material involved. The surface textures formed after pressing nanofilament substrates (chapter 4) will depend on the shape and size of the nanofilaments. In the case of incorporating nanofilaments into polymer composites (chapter 5), the size and structure of the nanofilaments will affect their reinforcing capabilities, especially the adhesion between the nanofilament filler and polymer matrix. The surface properties will be affected by the form of nanofilaments. The electrical properties of a nanofilament-polymer composite (chapter 6) will also be influenced by the orientation of graphene in the nanofilaments⁵⁰ and the connectivity between the nanofilament filler so nanofilament length and dispersion will be an important factor.

The external surface of carbon nanofilaments are different depending on the orientation of the graphene planes in the filaments.¹⁸¹ Where GNFs have terminated graphene sheets at an angle or perpendicular to the filament axis, nanotubes have graphitic planes parallel to the filament axis, and vapour-grown nanofibres have a MWNT core with an exterior surface of amorphous carbon. Since the structure of the nanofilaments are determined by the orientation of the graphene planes, and given that cells have been shown to respond to different crystal surfaces,^{182,183} this also may affect

osteoblast response to compacted nanofilament surfaces or nanofilament composite surfaces.

Therefore, the intention of this part of the project was to obtain a variety of characterised carbon nanofilament samples with a range of structures and diameters and to then go on to characterise pressed nanofilament surfaces and polymer composites and progress onto investigating osteoblast attachment and proliferation to such features.

CVD was employed as it produces high yields with a low amount of sooty carbon but at the cost of crystallinity (see section 2.2.1).^{50,51,182} The literature suggests that there are several factors that affect the size and structure of the nanofilaments produced.^{59,80} Since the conditions of CVD affect the nature of the synthesised nanofilaments, different conditions (i.e. catalyst, temperature, reaction gas mix and duration of synthesis) were experimented with to acquire a range of nanofilament samples. For example, the choice of catalyst will be a major factor on the synthesised nanofilaments. Iron and nickel catalysts, in particular, have been shown to control nanofilament diameter and structure, but are co-dependent on temperature and state of the catalyst.⁶⁸ Catalyst supports can control the structure of nanofilaments, especially nanotubes. Porous silica impregnated with catalyst, for example, contains embedded catalyst particles into pores so the pore size contributes to the nanofilaments produced.¹⁸⁴

Removal of the remnant catalyst and support, if used, also needs to be considered as metal nanoparticles can be detrimental to cells and tissues. Acid treatment is an easy and common procedure used to dissolve away catalyst particles and has been shown to be effective in nanofibres,⁶⁰ but encapsulation of catalyst in nanotubes can hinder catalyst removal.⁸⁷

Nanofilaments were therefore characterised before and after acid treatments using electron microscopy techniques (TEM and SEM), BET surface area measurements, and powder X-ray diffraction (XRD).

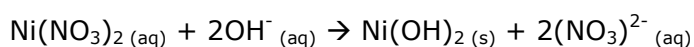
The aim of the work in this chapter, therefore, was to produce and characterise nanofilaments with varying structure and diameter, with minimal remnant metal catalyst for further investigation on their role in pressed compacts and polymer composites for use as biomaterials in bone repair applications.

3.2. Materials and Methods

3.2.1. Catalyst Preparation

3.2.1.1. *Nickel catalyst preparation*

An unsupported nickel catalyst was used to synthesise GNFs. The catalyst was prepared by reacting nickel nitrate hexahydrate ($\text{Ni}(\text{NO}_3)_2 \cdot 6\text{H}_2\text{O}$) with 12 M ammonia (NH_3) solution at 100 °C, conforming to the equation below:



Equation 3.1

The catalyst was then decomposed from nickel hydroxide to nickel oxide (NiO) after further application of heat. A colour change from green to dark green, to a black nickel oxide was seen at each stage of the decomposition process.

3.2.1.2. Supported iron catalyst preparation

A silica supported iron catalyst was used to synthesise a MWNT sample. Silica (Sigma-Aldrich) was impregnated with iron nitrate ($\text{Fe}(\text{NO}_3)_3$) by a wet impregnation route. A suitable iron nitrate solution was made up to produce a specific loading of iron in the final catalyst. Several concentrations of iron in the support were investigated until a suitable composition was successful in producing MWNT in sufficient yield and purity. The catalyst support to be used in this investigation was prepared with 10 wt% of iron. The catalyst support was prepared in bulk (10 grams) by impregnation of 8.038 g iron nitrate in distilled water and left overnight at 130 °C. This support was then thermally degraded in 10% hydrogen (in Argon) at 400 °C for 4 hours ready to be used as the catalyst support to synthesise MWNT.

3.2.2. Chemical vapour deposition

Chemical vapour deposition (CVD) was used to synthesise the carbon nanofilaments. The apparatus that was used is illustrated in figure 3.1. A ceramic boat containing 0.05 g of unsupported nickel catalyst or 3 g of silica supported iron (10 wt%) catalyst was used to synthesise GNF or MWNT respectively. The boat was placed in a quartz tube furnace and the temperature and gas compositions were controlled as outlined in figure 3.2.

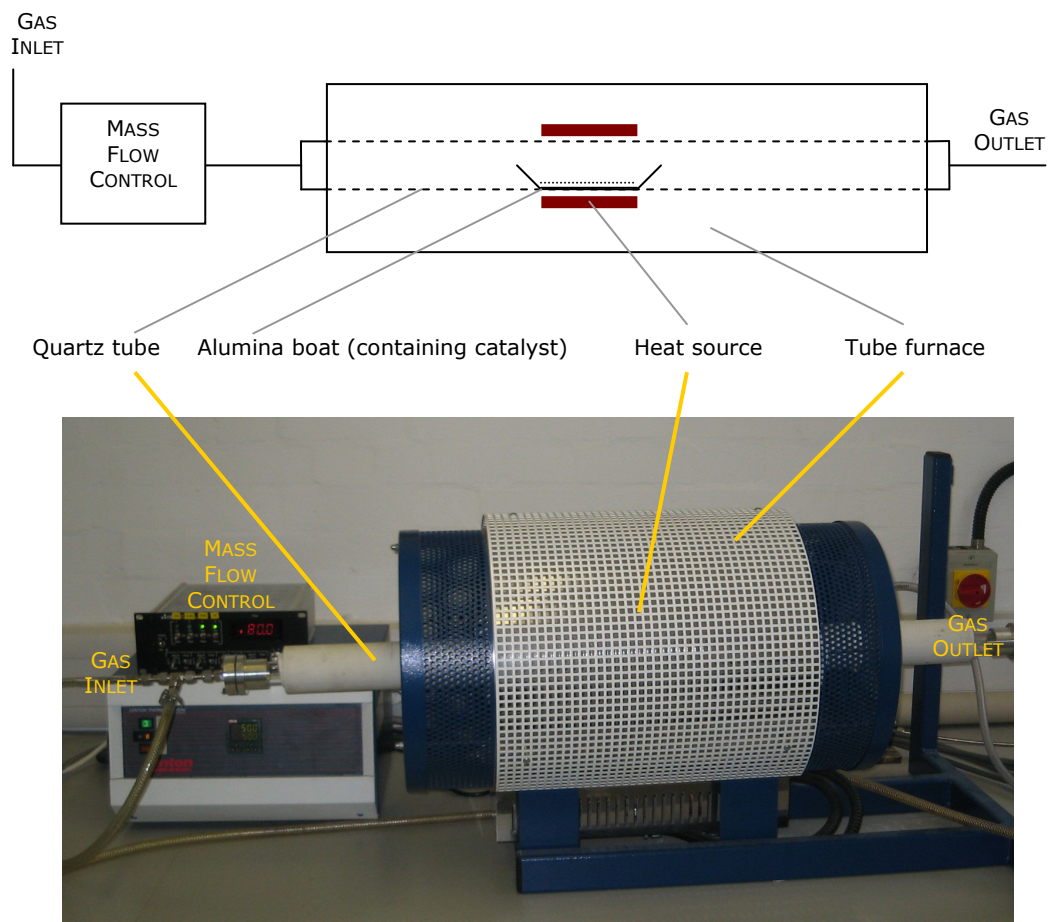


Figure 3.1: Schematic diagram and photograph illustrating the CVD synthesis process

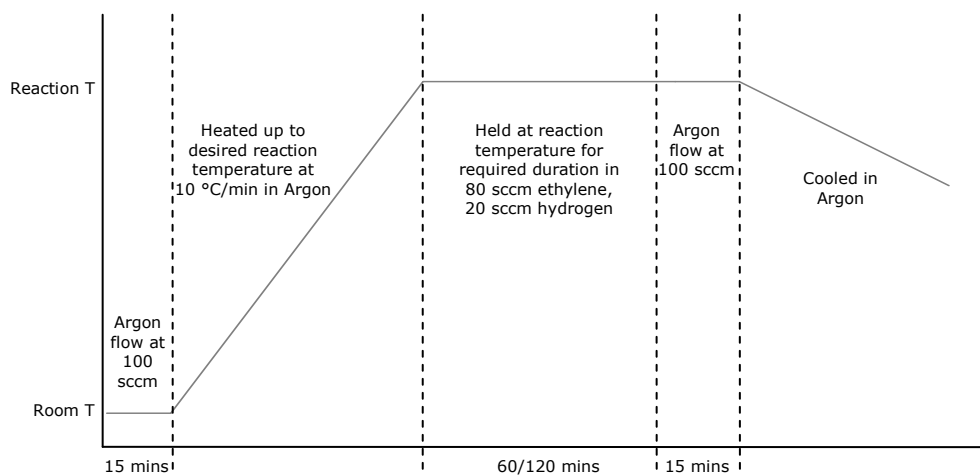


Figure 3.2: Temperature programme for carbon nanofilament synthesis

3.2.3. Pyrograf® III sample

The other sample investigated was not synthesised in Nottingham. A Pyrograf® III sample (PR19PS) was kindly donated by Applied Sciences, Cedarville, USA.^{60,69} Pyrograf® III was synthesised using CVD by decomposing methane, ethane, other aliphatic hydrocarbons, or coal gas in the presence of an iron catalyst, hydrogen sulfide and ammonia. The sample, PR19PS in this case, was stripped of any polyaromatic hydrocarbons from the surface of the nanotubes. Applied Sciences state these nanostructures as nanotubes with extra deposited amorphous carbon, which increases their diameter. For this reason, Applied Sciences term these structures as nanofibres. These types of nanofilaments are often termed vapour-grown carbon nanofibres (VGNFs), but are essentially MWNTs that have an external layer of amorphous carbon.

3.2.4. Summary of samples

The samples used in this study are summarised in table 3.1. GNF1, GNF3, MWNT9 were synthesised in Nottingham, and PR19PS supplied by Applied Sciences. The synthesis conditions of the nanofilaments produced varied and are outlined table 3.1.

Table 3.1: Summary of origin and synthesis of samples used in this study (+silica supported and *not supplied)

Sample (Source)	Catalyst	Synthesis Temperature (°C)	Duration of reaction (mins)
GNF1 (Nottingham)	Nickel	500	120
GNF3 (Nottingham)	Nickel	600	120
MWNT9 (Nottingham)	Iron ⁺	600	60
PR19PS (Applied Sciences)	Iron	-*	-*

3.2.5. Purification techniques

Nitric acid was used to remove the metal catalyst from GNF1, GNF3 and PRI9PS samples. Concentrated nitric acid was diluted to a 12 M concentration with distilled water, added to the carbon sample and stirred at room temperature for 18 hours. The sample was then filtered using a Buchner funnel and washed with excess distilled water and acetone. The sample was then left in a drying cupboard at 80 °C until dry.

Hydrofluoric acid (HF) was used to remove the silica and iron from the silica supported iron sample (MWNT9). The sample was exposed to 20% hydrofluoric acid in three, 30 minute periods, with thorough filtering and washing in distilled water and ethanol.

3.2.6. Characterisation techniques

Nanofilament powders were characterised and analysed using TEM, SEM, BET and XRD.

3.2.6.1. *Transmission electron microscopy*

TEM was analysed using a Jeol 2000fx low resolution TEM (TEM) and some samples using a Jeol 4000fx high resolution TEM (HRTEM). Samples were prepared by sonicating a small amount of sample for 3 minutes in isopropanol or acetone, then dropping a few drops of the solution onto a holey carbon TEM grid (Fisher). The samples were viewed using an accelerating voltage of 200 kV (low-res TEM) or 400 kV (HRTEM). Images were obtained in bright field (direct beam) and dark field (deflected beam) to analyse the structures of the nanofilaments. Selected area diffraction (SAD) patterns were also obtained using the TEM by detecting electrons deflected by the specimen.

SAD patterns indicate the crystal structure of graphene in nanofilaments, which is discussed later in this chapter. Quantitative analysis could then be performed using the data obtained.

3.2.6.2. Scanning electron microscopy

Nanofilament powders were prepared for SEM by simply grinding and mounting on a carbon sticky tab. Since the nanofilaments are conductive, no sputtering was required. The samples were analysed using a Philips XL-30 SEM and was performed using a secondary electron or backscattered electron detector at varying accelerating voltage and spot size.

3.2.6.3. BET surface area measurements

BET surface area measurements were performed on an Quantachrome Autosorb-1 and analysed using Quantachrome software. Samples were prepared by weighing out between 0.1 and 0.2 g of ground carbon nanofilament sample. The sample was outgassed at 300 °C for 2 hours and left to cool down before performing surface area measurements using 7-point BET method. Each sample was analysed three times to reduce any anomalies.

3.2.6.4. Powder x-ray diffraction

Powder x-ray diffraction was performed on a Siemens D500 diffractometer. A copper anode ($\text{CuK}\alpha$, $\lambda=0.154$) was used as the radiation source in the Siemens D500 with an operating voltage of 40 kV. The XRD was performed in step mode with a step interval of 0.02° over a 2θ range of $15-90^\circ$ with a dwell time of 7 seconds. Powder samples, before and after acid treatment, were prepared for XRD by grinding and mounting onto a sticky tab on a custom-made sample holder.

3.3.Results

3.3.1. CVD yields

The yields of carbon nanofilaments synthesised using CVD are summarised in table 3.2. The yields of carbon were measured before any acid treatments and hence still contain the metal catalyst.

Sample (catalyst)	Table 3.2: Average catalytic yields				Yield (%) $= \frac{m_c}{m_{cat}} \times 100$
	Mass (g)		Synthesis conditions		
	Catalyst (m_{cat})	Product (m_c)	T (°C)	Duration (mins)	
GNF1 (Ni)	0.025	4.68	500	120	18620
GNF3 (Ni)	0.025	5.00	600	120	19900
MWNT9 (Si-Fe)	0.132	2.20	600	60	1567

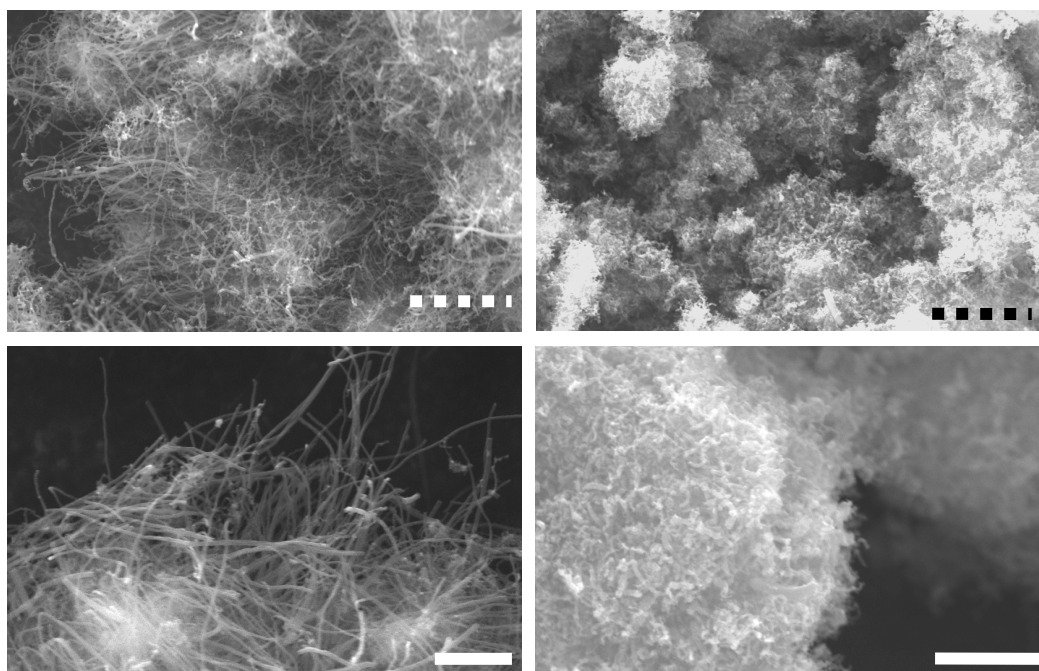


Figure 3.3: SEM images showing typical topography of graphitic nanofibre powders: GNF1 (left) and GNF3 (right). Scale bars: Dashed line = 10 μm; Solid line = 5 μm

3.3.2. Nanofilament characterisation

3.3.2.1. Morphology and nanostructure

SEM and TEM were used to analyse the nanofilament samples. The morphology of the GNF samples using SEM is shown in figure 3.3. Figure 3.4a is a micrograph of the unimpregnated silica particles. After impregnation, reduction of the iron catalyst and chemical vapour deposition, the nanotubes were shown to be successfully synthesised using a mesoporous silica support (figure 3.4b).

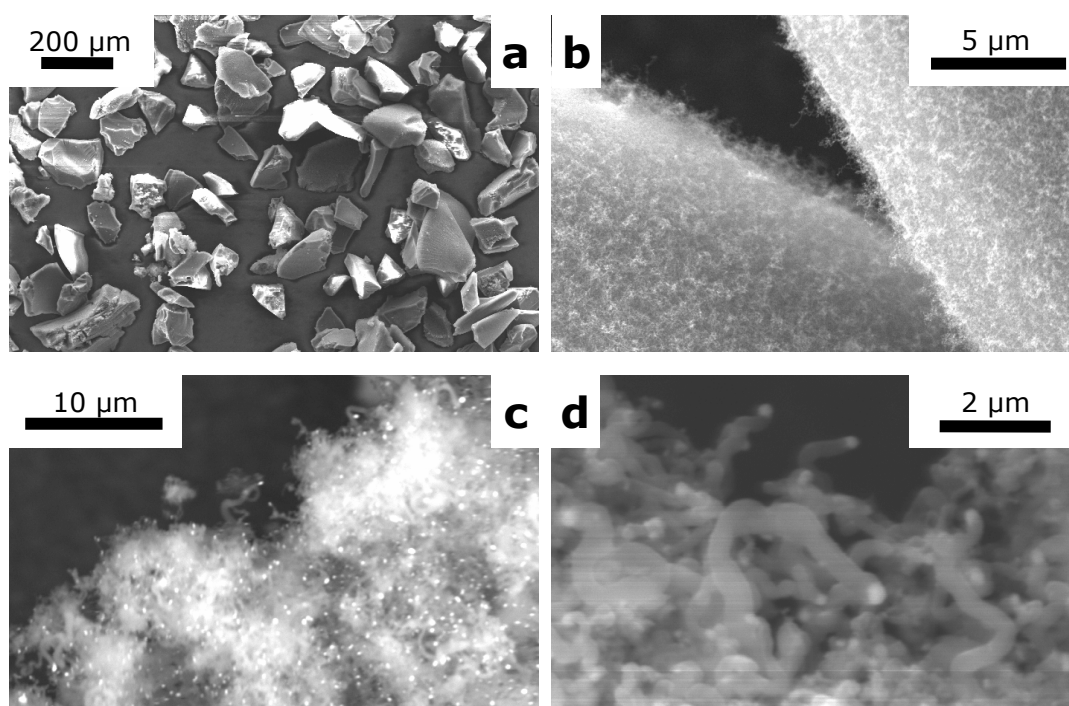


Figure 3.4: SEM micrographs of silica and MWNT9 nanotube samples. a) silica particles; b) nanotubes synthesised using silica supported iron catalyst; c) back-scattered image of nanotubes highlighting catalyst location; d) secondary electron image of nanotubes

Average diameters were determined from TEM micrographs. The number of nanofilament diameters used was decided using the cumulative average method. GNF1 was used to determine the number of nanofilament samples required for a precise average measurement (figure 3.5), but all

nanofilament samples were calculated in this way. Average diameters were recorded until the fluctuations levelled out at a certain value (within 5% percentage error). Percentage error was calculated using:

$$\text{Percentage error} = \frac{\text{Average}}{\text{Average}(n = 75)} \times 100 \quad \text{Equation 3.2}$$

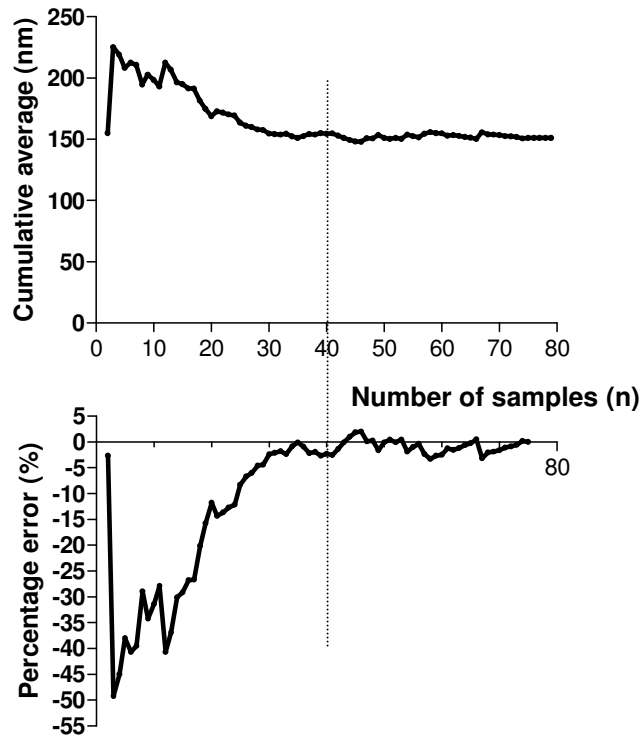


Figure 3.5: Determination of number of samples used to acquire average diameters for the GNF1 sample using the cumulative average method (above) and percentage error (below) over 75 measured nanofilaments. The average diameter at n=40 was within 5% of the average diameter at n=75 (indicated by dashed line)

The percentage error using the final average value (at n=75), was then determined to confirm that the value at n=40 was within 5% of the value at n=75.

Figure 3.6 summarises the TEM micrographs taken of each sample. Arcs observed on the selected area diffraction (SAD) patterns obtained from the samples indicated the orientation of graphene planes relative to the

filament axis. SAD patterns were taken of 75 randomly selected nanofilaments from each sample and the type and composition of each nanostructure noted and tabulated in table 3.3. A typical SAD pattern from sample GNF1 is shown figure 3.6a, and shows diffraction arcs from graphene planes perpendicular to the fibre axis. GNF1 was made up of predominantly platelet structure (table 3.3). Similarly, four arcs are observed from the angled graphene planes in herringbone-structured GNFs (figure 3.6b). GNF3 was confirmed to be a mixture of both platelet and herringbone structured GNFs.

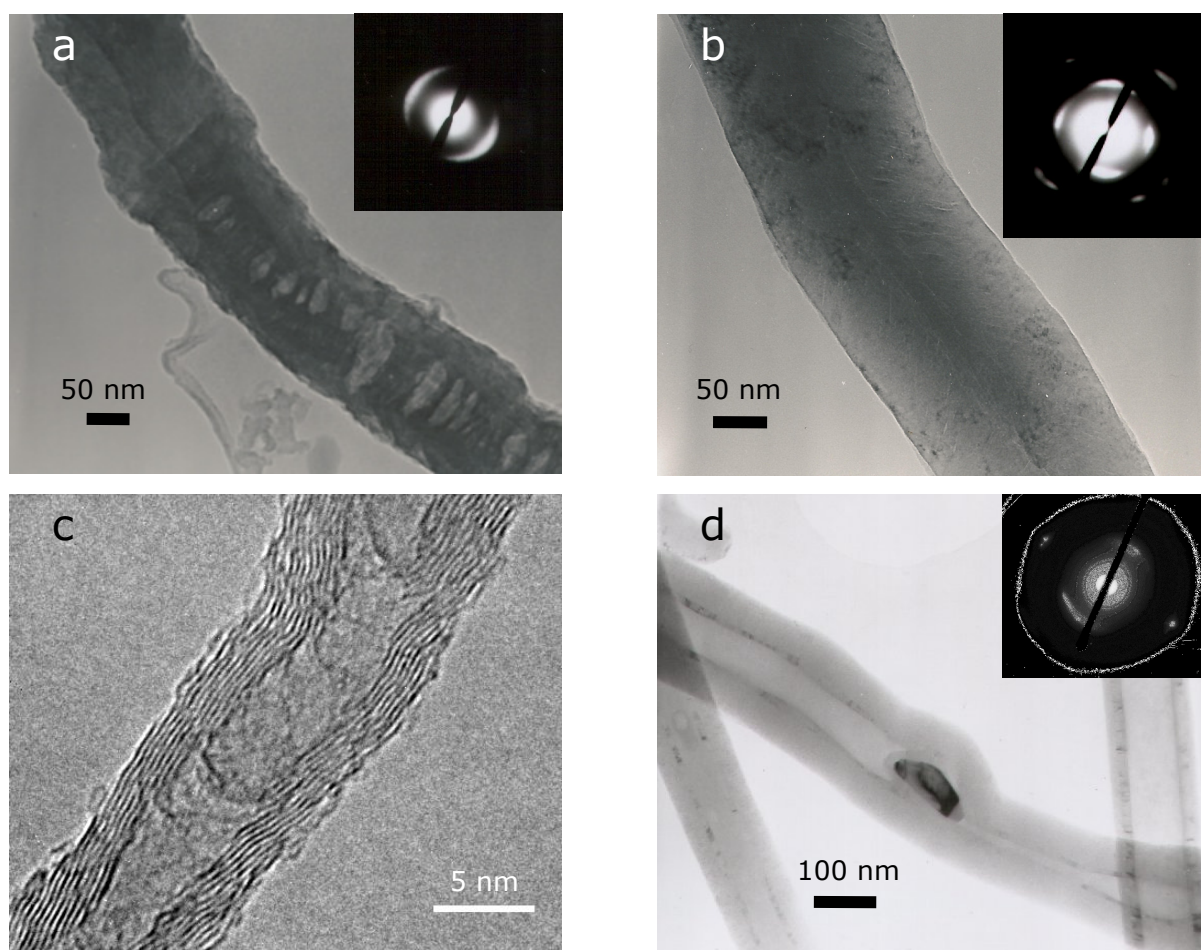


Figure 3.6: Typical morphology and structure of carbon nanofilaments taken from TEM micrographs and selected area diffraction patterns of individual nanofilaments or high-resolution TEM (HRTEM): a) GNF1; b) GNF3; c) MWNT9 (HRTEM); and d) PR19PS

Table 3.3: Table detailing the nanostructure and composition of the nanofilament samples, where H=Herringbone GNF, P=Platelet GNF and NT=carbon nanotube

Sample (catalyst)	Predominant nanostructure present	Composition in sample (%; n=75)		
		H	P	NT
GNF1 (Ni)	P	5	87	8
GNF3 (Ni)	H & P	35	58	7
MWNT9 (Si-Fe)	NT	-	-	100
PR19PS	NT	-	-	100

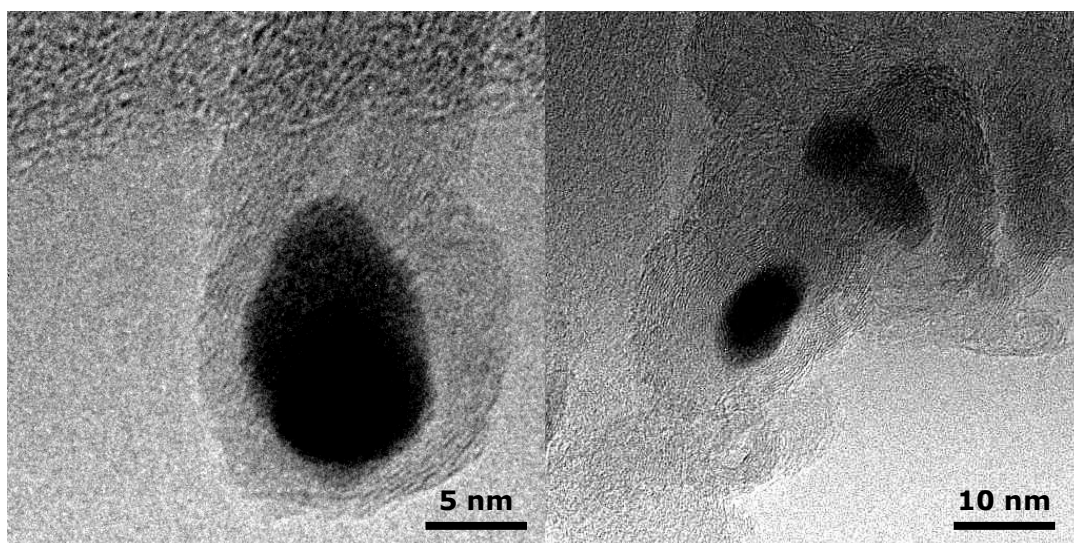


Figure 3.7: High-resolution TEM micrograph of iron catalyst nanoparticles encapsulated in MWNT9 nanotubes

MWNT9 and PR19PS consisted only of multiwalled nanotubes. The MWNT9 nanotube sample viewed using the high resolution TEM (figure 3.6c) showed the lattice fringes of the nanotube. The angle between the fibre axis and lattice fringes appears to change through the length of the nanotube. The majority of the nanotubes had a typical nanotube structure, but occasionally, the orientation of the planes would converge into a cone structure (similar to herringbone nanofibre structure). This was typical of the MWNT9 sample. It was also common to find encapsulated iron catalyst nanoparticles usually found at the end of the nanotubes (figure 3.7).

The PR19PS sample was analysed using TEM. SAD patterns showed the structure of the graphene planes to be perpendicular to the fibre axis (figure 3.6d). In figure 3.8, the bright field image looks as if there is an ordered carbon layer (MWNT) and an amorphous carbon layer on the exterior as explained. The dark field images obtained from different diffraction spots are highlighted as shown. The dark field images confirm that there was a difference in structure between the inner and outer layers.

TEM was also used to determine the length of the nanofilament samples (table 3.4). The four nanofilament samples synthesised had varying diameters and diameter ranges. At first glance, the mean diameters of GNF1, GNF3 and the commercial PR19PS sample were similar, as were their range of diameters. When viewing these samples and taking the standard error into consideration, the GNF samples had a wider range of nanofilament diameters, whereas the commercial sample possessed a tighter array of nanofilament diameters. The thinner MWNT9 sample was the most consistent sample with respect to the range of nanofilament diameters.

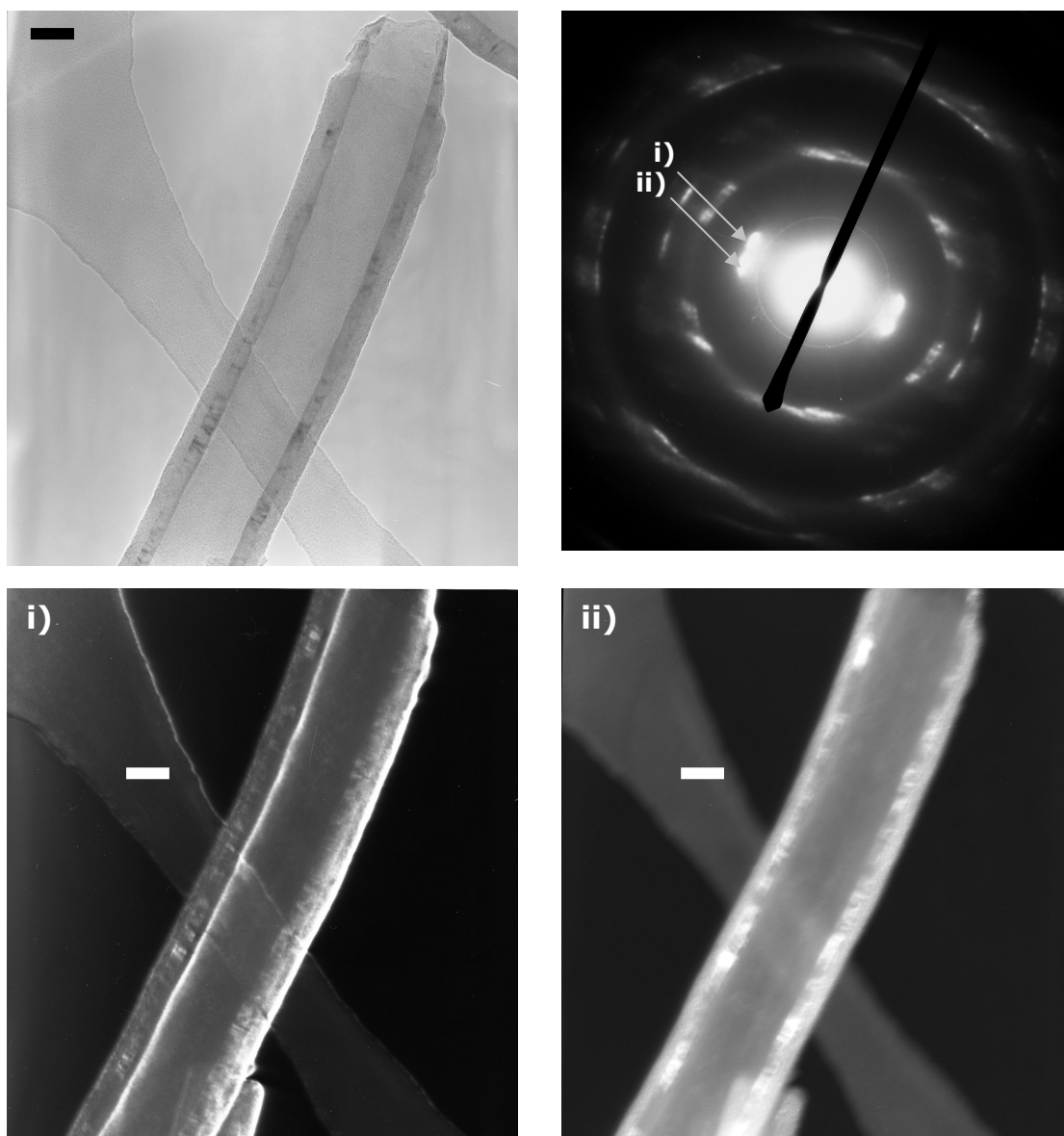


Figure 3.8: TEM micrographs of a single PR19PS nanotube: Clockwise from top-left image: Bright field image; Selected area diffraction pattern; Dark field images. Scale bars = 50 nm

Table 3.4: Table illustrating nanofilament structure, diameter and length obtained from TEM analysis.

Sample	Mean diameter \pm sem (nm)	Diameter range (nm)	Mean length \pm sem (μ m)
GNF1	155 \pm 13	50 - 250	2.20 \pm 0.28
GNF3	142 \pm 12	50 - 200	2.40 \pm 0.67
MWNT9	13 \pm 1	15 - 20	-*
PR19PS	134 \pm 7	50 - 200	8.21 \pm 0.87

*nanotubes were too twisted and entangled to determine length

The surface area measurements of the carbon samples are shown in figure 3.9. PR19PS had the lowest surface area. There was no significant difference in average diameters between GNF1, GNF3 and PR19PS. Since PR19PS is significantly longer, the surface area is less. As the nanotubes in the MWNT9 sample were significantly thinner in diameter than the other nanofilaments, their surface area is significantly higher.

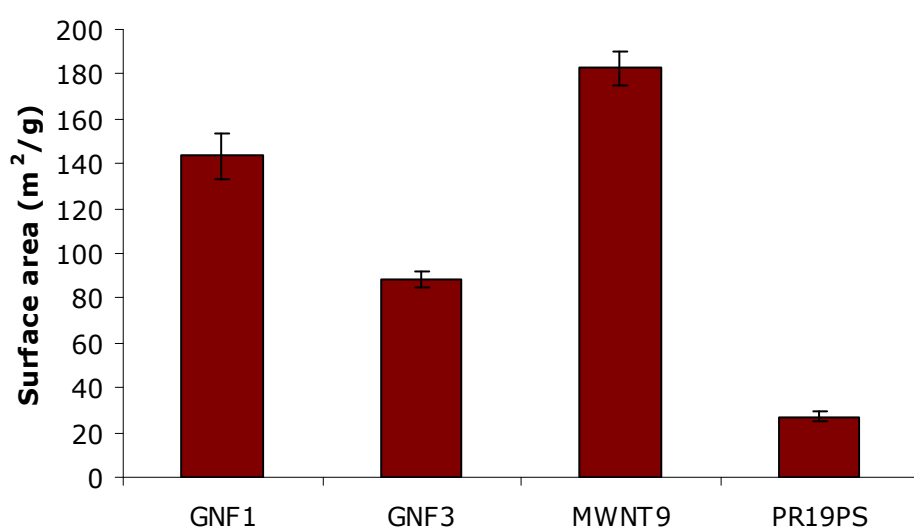


Figure 3.9: BET surface area measurements for carbon nanofilaments (Mean \pm SEM; n=3)

Samples were sonicated for 3 minutes in isopropanol before being analysed using TEM. As the graphene layer in the GNF samples was orientated perpendicular to the fibre axis, the nanofibres are more likely to break than nanotube samples. For this reason, the effect of sonication time on GNF1 sample was recorded using the cumulative average method. The results are summarised in figure 3.10.

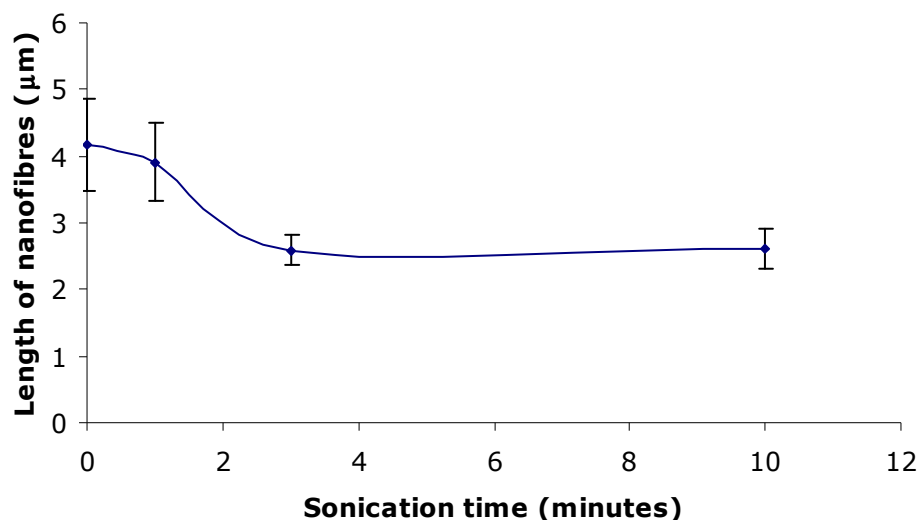


Figure 3.10: Effect of duration of sonication on nanofibre (GNF1) length (Mean \pm SEM; $n > 48$)

Figure 3.10 shows that nanofibres do break and reduce in length when sonicated. This reached a plateau after approximately 3 minutes. Hence 3 minutes sonication was used for TEM preparation so as to disperse the sample as much as possible for viewing.

3.3.2.2. Nanofilament composition

XRD and TEM were performed on the samples to analyse the state of the catalyst and synthesised carbon before and after synthesis and after acid treatments. Figure 3.11 shows the XRD patterns for the two synthesised GNF samples. Reflections are shown for the nickel oxide (NiO) catalyst used for CVD synthesis and both carbon products are shown to reflect at the characteristic graphite carbon peak.

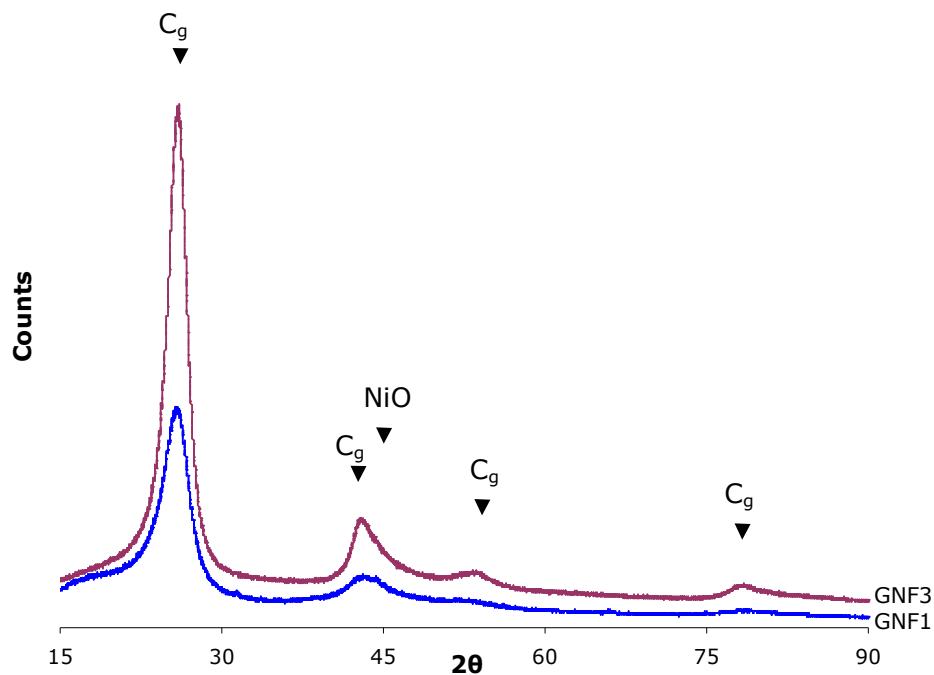


Figure 3.11: XRD patterns for GNF samples before acid treatment

Similarly, the silica supported iron catalyst used to synthesise MWNTs was analysed using XRD and the pattern is shown in figure 3.12. The figure highlights the diffraction patterns at the stages through which the silica supported iron catalyst was prepared. Initially, an XRD pattern was obtained for the silica support. There was an amorphous hump observed in the presence of silica. After the silica was impregnated with iron nitrate, the XRD pattern indicated no new reflections. However, after the support was thermally degraded at 400 °C in 10 % hydrogen for 4 hours, there were clear iron oxide (Fe_2O_3 and Fe_3O_4) peaks within the XRD pattern.

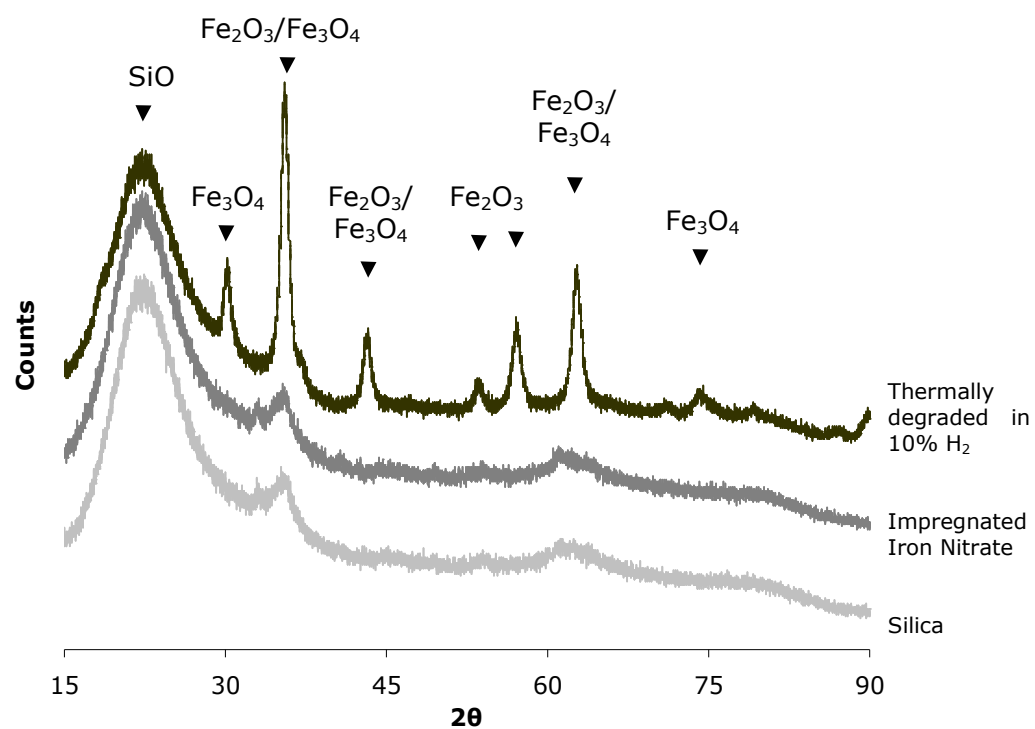


Figure 3.12: XRD patterns for silica, silica impregnated with iron nitrate and then thermally degraded in 10% hydrogen

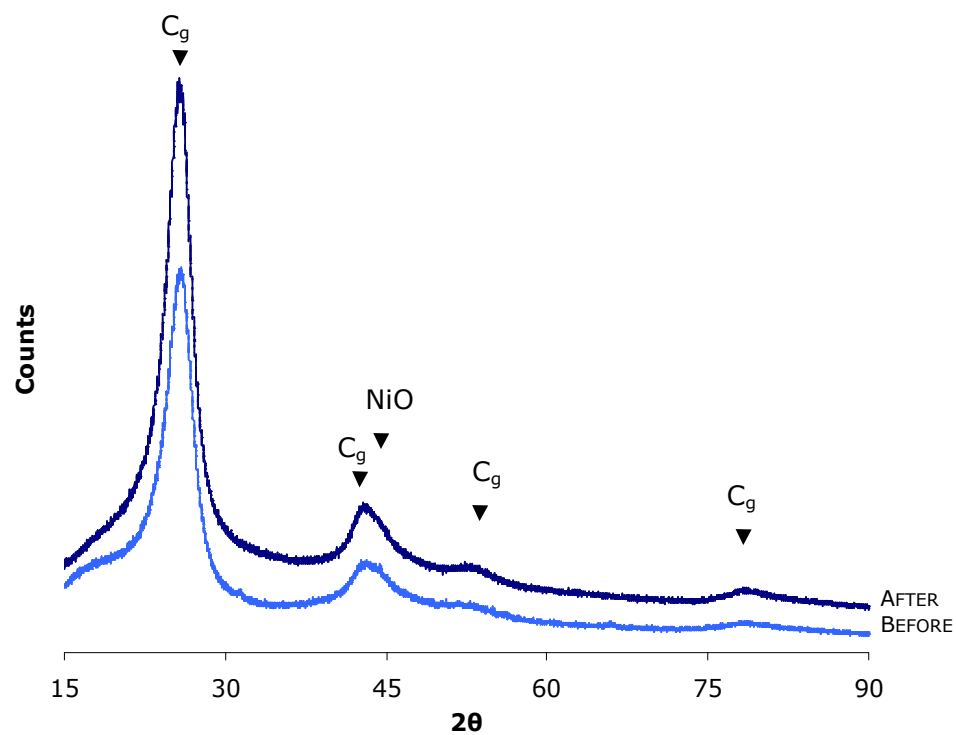


Figure 3.13: XRD patterns of GNF1 before and after nitric acid treatment

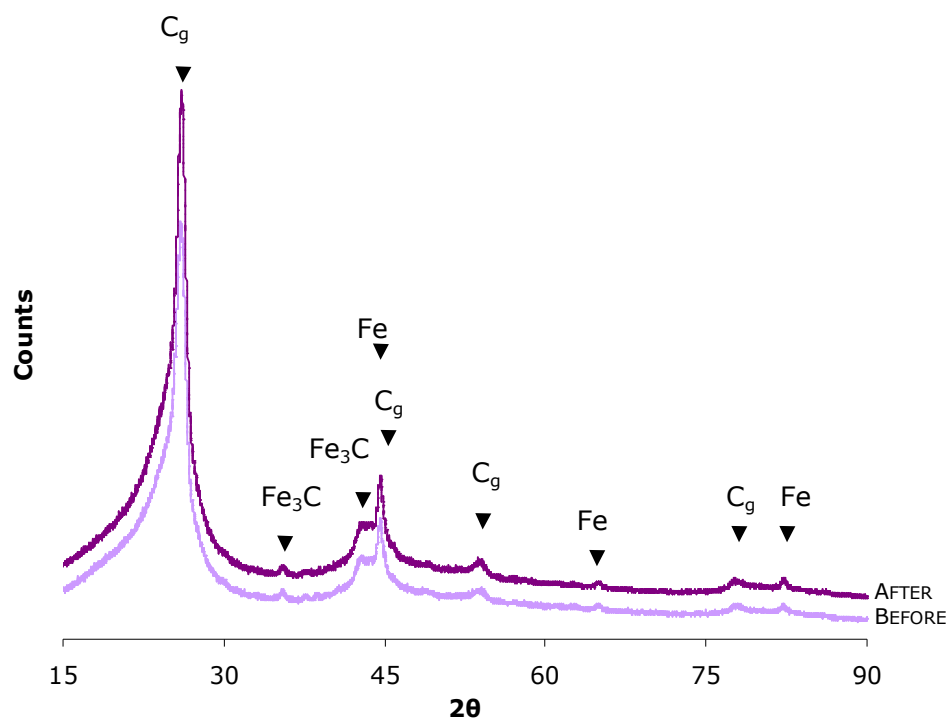


Figure 3.14: XRD patterns of PR19PS before (as-received) and after nitric acid treatment

XRD was also used to detect any amount of catalyst that remained in the samples after acid treatment. The XRD pattern shown in figure 3.13 shows the characteristic X-ray reflections for nickel oxide and graphitic carbon.

The XRD patterns obtained from the as-received and post-acid washed PR19PS samples are shown in figure 3.14. The patterns for the as-received sample showed the sample to be made up of iron carbide (Fe_3C), iron and graphitic carbon. The XRD pattern for PR19PS after acid treatment does not seem to change compared to before treatment.

After CVD synthesis using this silica supported iron catalyst, the problem was then how to remove the catalyst – both the silica support and

the iron nanoparticles. Figure 3.15 is a powder XRD pattern of the silica supported iron sample after CVD synthesis, and then after two different acid treatments to attempt to remove the silica and iron catalyst. Hydrofluoric acid was used initially, as it has been reported to be successful in dissolving silica supported catalysts in the literature.⁸⁰ The powder XRD pattern (figure 3.15) showed no silica peak but still showed iron carbide catalyst peaks after HF treatment. Therefore, concentrated nitric acid was used as it was successful in removing unsupported nickel catalyst as described earlier. However, the iron carbide peaks were still present after this further acid treatment.

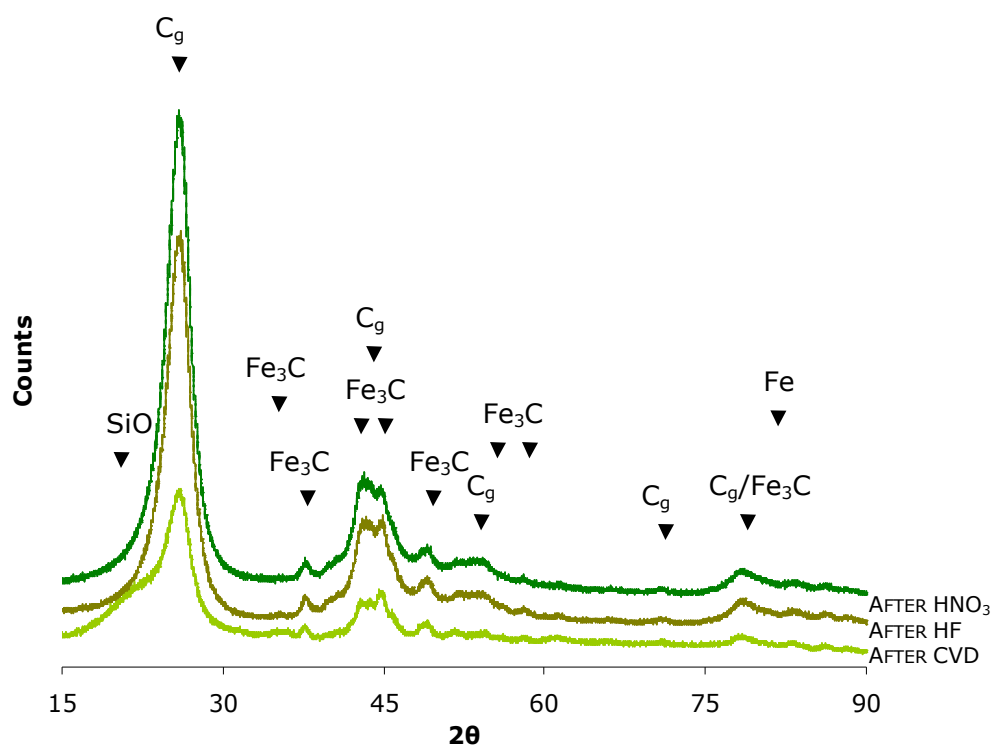


Figure 3.15: XRD patterns of MWNT9 before any acid treatment (i.e. after CVD), after hydrofluoric acid treatment and after nitric acid treatment

3.4. Discussion

The nanofilaments characterised in this chapter were used as samples in the work studied in the subsequent chapters. Since CVD provides a comparatively large yield with little unwanted carbon products compared to

other routes, it was used to synthesise two different GNF samples (GNF1 and GNF3) and a MWNT sample (MWNT9). CVD was also used commercially by the suppliers of the Pyrograf[®] III sample (PR19PS). The differences in nanofilament structure and size would be important in understanding the surface properties and bulk properties of the samples used in the following chapters. The nanofilament size and morphology would affect the topography of pressed nanofilament substrates and nanofilament-polymer composites, which would be important in assessing their potential to form a strong adhesion to bone. The bulk properties of polymer composites will be dependent on the length and agglomeration of nanofilaments in the matrix as well as nanofilament structure.

The parameters used in CVD to produce nanofilaments did affect their size and structure. The metal catalyst and its form contributed to the yield, size and structure of the synthesised nanofilaments. The yield of carbon nanofibres produced from the nickel catalyst (table 3.2) was similar to the yields produced previously in the laboratory by Bououdina *et al.*,⁷⁹ although GNF3, which was synthesised at a slightly higher temperature (600 °C), was produced with a 7 % higher yield in this investigation with the same conditions. The yield of nanotubes synthesised by CVD over a silica-supported iron catalyst are not referred to enough in other publications to be able to compare. The yields obtained from a silica supported iron catalyst were lower than the nickel catalyst.

A silica supported iron catalyst produced a more consistently sized and structured nanofilament sample compared to the unsupported nickel catalyst. It was apparent that the mechanism of the nanotube growth was tip growth (section 2.2.1).⁶⁸ This was because the catalyst particles (before purification) were located at the ends of the nanotubes (figure 3.4c & d). Li *et al.*⁵⁹

proposed that the mechanism of nanotube growth from an iron impregnated mesoporous silica support would be a mixture of tip growth and root growth but predominantly root growth. Backscattered and secondary images (figure 3.4c and d respectively) of synthesised nanotubes using silica supported iron catalyst showed that catalyst particles were located at the exposed ends of the nanotubes. As tip-growth means that the catalyst would be more exposed to the ethylene (or other carbon-containing gas) than if it were in the silica support, this mechanism is more favourable than root-growth. This may also explain why the nanotubes were twisted and entangled, as the catalyst particle would not remain supported in the silica and hence would be more mobile during nanotube synthesis.

The morphology and structure of the nanofibres and nanotubes was observed by TEM and SAD patterns (figure 3.6). It was observed that platelet nanofibres were successfully produced by CVD using a nickel nanoparticulate catalyst at 500 °C with an ethylene/hydrogen (80/20) gas flow (GNF1). By raising the temperature to 600 °C, a mixture of platelet and herringbone structures were observed (GNF3). These results were shown to be repeatable. The effect of temperature has been shown to be a factor in the synthesised structures of nanofibres using an unsupported iron catalyst where herringbone nanofibres were produced at low temperature (500 °C) and platelet structures were seen at a higher temperature (600 °C).^{2,3,5,108,123,125,126}

Much of the literature describes Pyrograf® III as nanofibres^{185,186} or vapour-grown nanofibres (VGNFs).⁸⁷ This is because CVD is used to synthesise the carbon filament and then a disordered carbon layer is vapour-deposited (hence the term vapour-grown nanofibres). These VGNFs could be widened to the micron scale with vapour deposited carbon. Due to the nature of the SAD patterns highlighted in figure 3.8, the PR19PS sample was

essentially a nanotube sample with an external surface of amorphous carbon. Since the PR19PS sample was obtained from a commercial source, information on the state of the pre-synthesised catalyst was only obtained from Applied Sciences.¹⁸ Using XRD, the catalyst was confirmed to be iron and iron carbide (figure 3.14), but XRD reflections before and after did not show signs of removal of the iron catalyst. On further inspection using TEM micrographs before and after the treatment, the majority of iron catalyst was encapsulated within the nanotubes (figure 3.6d), therefore being shielded from the acid during treatment. This was also seen in MWNT9 (figure 3.7). Since the graphene sheets are formed into cylinders, they tend to encapsulate the catalyst particle more easily and therefore leave some iron catalyst behind. HR-TEM analysis confirmed that there was a remnant of encapsulated catalyst after acid treatment on the MWNT9 sample (figure 3.7). This provided more evidence that it was encapsulated iron catalyst remaining in the purified sample.

Acid treatments look to have been more successful in removing the catalyst from the nanofibre samples (figure 3.13). There was a slight difference in the NiO reflection between the XRD patterns before and after acid treatment. The nickel peak looks to have almost disappeared after acid treatment in both GNF samples. The reason why there was only a slight difference is partly due to the graphite carbon characteristic reflection being so close to the nickel oxide and also the fact that there was a high ratio of synthesised carbon to catalyst so the that the nickel oxide catalyst reflection was not so prominent.

This chapter outlined the carbon nanofilament samples required to investigate the potential of carbon nanofilaments in surface modification of implants or as fillers in biocompatible polymer composites. A range of carbon

nanofilament diameters (13 nm, 134 nm, 142 nm, and 155 nm) and structures (platelet, platelet and herringbone, multi-walled nanotubes and vapour-grown nanofibres) were synthesised or acquired, then purified to remove metal catalyst nanoparticles. Therefore, the effect of diameter on surface properties of nanofilament substrates and composites, as well as bulk properties of nanofilament composites could be assessed by comparing nanofilament samples with average diameters of 134-155 nm (GNF1, GNF3 and PR19PS) to 13 nm (MWNT9), and also the comparing the effects of graphitic structure of GNFs, MWNTs and VGNFs. The possible remnants of iron and nickel catalyst nanoparticles are thought to be encapsulated within the nanofilaments, but may cause an additional factor when culturing osteoblasts on these materials depending on if the catalyst particles would leach out into culture media and to what extent.

4. Investigation of Osteoblast Response to Pressed Nanofilament Substrates

4.1. Introduction

Carbon nanofilaments show potential for use in biomaterials for bone repair to create a nanotextured surface that mimics the matrix of natural bone.¹²⁰ Since nanofilaments can be synthesised with diameters similar to that of collagen fibrils in bone, a nanofilament substrate can potentially simulate the texture of a collagen matrix. Carbon nanofilaments can be synthesised or prepared to produce various textured substrates, including cross-linked nanotube networks,^{100,187,188} aligned regular nanotube arrays,^{2,108} and nanofilament compacts.^{106,119,189-191} These nanofilament surfaces could be used to modify surfaces of biomaterial implants, especially in total joint replacement components. In this application, a strong bond between the prosthesis and bone is required and this could be encouraged by using a material similar in texture to that of the components of the bone matrix.

The topography and texture of a surface has been shown to be an important factor in the attachment and proliferation of cells, especially in the nano-scale.¹⁰⁸ With particular respect to nanofilaments, Price *et al.*² successfully produced carbon nanofilament compacts of Pyrograf® III and cultured osteoblasts on them. They found that nanofilament diameters below 100 nm encouraged greater cell attachment, proliferation² and differentiation⁶ on the substrates compared to larger diameter filaments, which may be due to the surface texture of carbon nanofilament compacts compared to collagen matrix in bone. The replication of the dimensional tissue environment on biomaterial surfaces is thought to be a critical factor in different cell responses. For example, fibroblasts have been shown to attach less to smaller nanoscale nanofilaments (<100 nm) than those above 100 nm, whilst smaller

nanofilament compacts were shown to increase osteoblast attachment thus encouraging bone matrix formation rather than soft tissue formation.^{3,5,18} It is possible that osteoblast function may be encouraged by simulating the dimensions of extracellular matrix components.¹⁹²

Another factor to consider with human osteoblast responses to different carbon nanofilament substrates is their interaction with different graphene structures. The orientation of graphene planes within the carbon nanofilaments will result in different crystal orientations at the exposed surface, which have equivalent chemistry to each other, but varying structural organisation. Different crystal surfaces have shown to affect epithelial (kidney A6 cell line) cell adhesion. Epithelial cells adhered rapidly to {011} faces of calcium (R,R) tartrate, compared to tissue culture plastic surfaces and attached even slower on the ¹³⁹ crystal surfaces. The attachment of the epithelial cells to the {011} crystal faces was shown to be independent of the presence of RGD peptides or serum proteins, but on the ¹³⁹ faces were promoted in the presence of serum proteins and inhibited by RGD peptides.¹⁸¹ It was thought that the protein adhesion and cell attachment were determined by the chemical nature of the surface or by its specific structural organisation.^{193,194}

The aim of this particular part of the project was to investigate the effect of nanofilament diameter and structure on the surface properties of compacted carbon nanofilament substrates and assess the osteoblast responses to these nanofilament substrates. Therefore, the synthesised carbon nanofilament powder samples characterised in chapter 3 (GNF1, GNF3, MWNT9 and PR19PS) were compacted onto PEEK discs. The substrate topography and chemistry was assessed as well as investigating the attachment, proliferation and differentiation of human osteoblasts cultured on

the nanofilament surfaces. Particular attention was paid to the structure and diameter of the nanofilament samples to explore the production of suitable surfaces using nanofilaments to promote osteoblast growth.

4.2. Materials and Methods

4.2.1. Nanofilament Pressing

Samples were prepared as outlined in section 3.2 by CVD and purified using acid treatments. Four samples were used; GNF1, GNF3, MWNT9 and PR19PS as outlined and characterised in chapter 3. The nanofilament powder samples were pressed onto poly(ether ether ketone) (PEEK) discs (diameter:11 mm; thickness:2 mm, RS Components, UK) using a hydraulic press at 150-200 MPa three times to produce a substrate of carbon nanofilaments. The nanofibre and nanotube samples were pressed at 150 and 200 MPa respectively as these loads provided adequate nanofilament substrates that remained stable in solution.

Discs were sterilised by either ultra violet (UV) light (for attachment studies) or by industrial methylated spirits (IMS) (for proliferation studies). Samples sterilised by ultra-violet light were exposed to UV light for 1 hour per side and samples sterilised by IMS were soaked in IMS over at least 2 days and then left to evaporate under sterile conditions.

Grafoil, a commercially available graphite sheet, was obtained from GrafTech International Ltd (Ohio, USA) to be used as a control as the surface chemistry is similar to the nanofilament samples, but had a different surface topography. Grafoil is a flexible graphite sheet that can be used as a packing

or gasket material. Sterilisation of Grafoil was performed in the same way as the pressed carbon discs detailed above.

4.2.2. Nanofilament disc characterisation

SEM, energy dispersive x-ray (EDX) analysis (Philips XL-30) and pulse-force atomic force microscopy (Topometrix PF-AFM) were used to characterise the pressed sample surfaces. Roughness analyses were performed using a Leica TCS 4D confocal laser scanning microscope (CLSM) to assess the micron-scale roughness of the pressed surface and AFM to analyse the roughness at the nanoscale.

SEM was undertaken as outlined in section 3.2.6.2. EDX spot scans were performed using an Oxford Instruments ISIS 300 series machine fitted with a Si (Li) crystal spectrometer that was controlled by the reference spaced ZAF correction program. Spot scans were performed alongside SEM investigations using an electron beam with a spot size of 6 and accelerating voltage of 20 kV over 20 random areas of each sample surface. This provided quantitative data on the degree of residual catalyst or catalyst support left in the samples. AFM was used in tapping mode to analyse the pressed nanofilament substrates. The surfaces were soft and so contact mode produced noisy and inadequate data to analyse the surfaces. Scans were performed of $10\ \mu\text{m}^2$ areas of random regions of the sample and a scanning rate of $10\ \mu\text{m.s}^{-1}$ was used. CLSM was performed in reflectance mode with appropriate objective magnification to account for the features. Roughness analyses were performed from CLSM and AFM data using the Leica or Topometrix software respectively.

4.2.3. Osteoblast attachment studies

Primary derived human osteoblasts (HOBs) isolated from femoral head trabecular bone were used in this study. HOBs were seeded onto samples at a seeding density of $32,000 \text{ cells.cm}^{-2}$, cultured in Dulbecco's Modified Eagles Medium (DMEM) supplemented with 10% foetal bovine serum (FBS), 2% Hepes buffer, 1% non-essential amino acids (NEAA), 1% L-Glutamine (L-Glut) (all Gibco, Invitrogen, UK), 0.85 mM ascorbic acid (Sigma-Aldrich, UK), and 2% penicillin/streptomycin (pen/strep), and incubated in standard cell culture conditions for 90 minutes (37°C in a humidified atmosphere with 5% CO_2). Glass rings (inner diameter: 10 mm) were used so that cells were subjected to the same areas on each sample. The experiment was repeated on separate occasions ($n=8$).

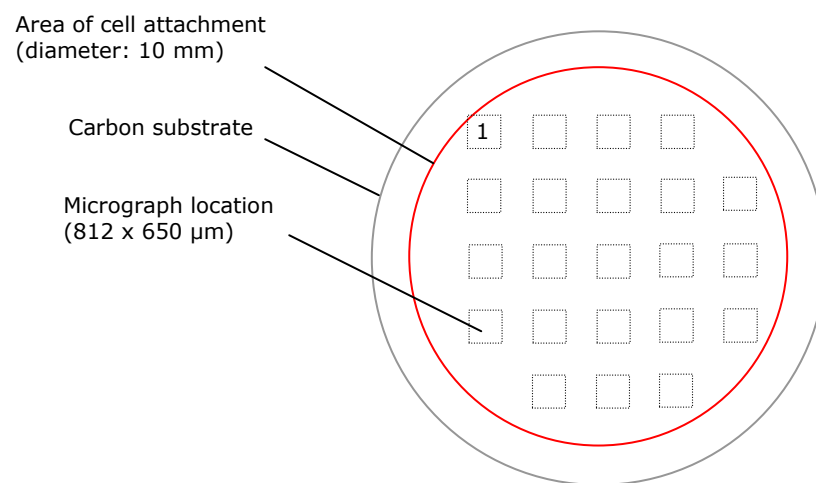


Figure 4.1: Schematic diagram of the method used to count the number of viable cells attached to the exposed carbon substrate

4.2.3.1. Cell counting using propidium iodide staining

After cell seeding, the culture media from the samples was removed and the samples thoroughly washed in sterile, phosphate buffered saline

(sPBS). They were then fixed with 4% paraformaldehyde (in PBS) for 10 minutes at 4 °C. Following this, the samples were thoroughly washed with phosphate buffered saline solution (PBS), and exposed to permibilising solution (containing 0.48 g hepes, 10.27 g sucrose, 0.29 g NaCl, 0.06 g MgCl, 0.5 ml Triton X-100 and 100 ml PBS) at -15 °C for 5 minutes. The samples were again thoroughly washed with PBS and stained with 0.05 wt% propidium iodide (in PBS) for 2 seconds and then washed a further three times in PBS. The samples were mounted on a glass slide with a drop of glycerol containing 10% DABCO/PBS (2 mg/ml 1,4-diazabicyclo[2.2.2]octane in PBS) (Sigma-Aldrich, UK) and a cover slip, ready to be viewed on a fluorescence microscope (Leica DM LB). Cell counts were performed from micrographs of 22 systematically chosen areas on the samples and counted using Image Pro Plus software. Cells were counted from the micrographs which were taken systematically across the sample as shown in figure 4.1 starting from the position labelled "1". The number of cells counted using the software could then be divided by the area of the combined micrographs and cell density on the carbon surface could be measured.

4.2.3.2. SEM sample preparation

HOBs seeded onto duplicate sample substrates were washed three times in sPBS and then fixed in 3% glutaraldehyde (in 0.1 M sodium cacodylate buffer) for at least 30 minutes. After initial fixation, the samples were thoroughly washed with 0.1 M sodium cacodylate buffer (with 7 % sucrose) and then post-fixed in 1% osmium tetroxide for 30 minutes. A graded series of ethanol was subsequently used to dehydrate the cells; 5 x 1 minute in distilled water, 2 x 5 minutes in 50% ethanol, 2 x 5 minutes in 70% ethanol, 2 x 5 minutes in 90% ethanol, 3 x 10 minutes in 100% ethanol, and finally the samples were transferred to hexamethyldisilazone (HMDS) (twice

for two minutes) and left to dry. Samples were sputtered with gold prior to analysis by SEM to avoid charging of the substrate. Cell areas were measured from 25 SEM micrographs of individual osteoblasts using Image Pro Plus software. The number of micrographs required was determined using the cumulative averaging method discussed in section 3.3.2.1.

4.2.4. Proliferation and differentiation of human osteoblasts

To assess their proliferation and differentiation, HOBs were seeded onto the nanofilament samples, grafoil and TCPS. Alamar Blue (AB; Serotec, UK), DNA (Hoechst 33258) and alkaline phosphatase (ALP; Randox, UK) assays were used to assess the activity, proliferation and differentiation of the cells after 7 and 14 days of culture. Samples were also prepared for SEM analysis as detailed in section 4.2.3.2. HOBs were cultured in DMEM supplemented with 10% foetal bovine serum (as detailed in section 4.2.3). Media was changed on all samples every 2-3 days. The experiment was run twice on separate occasions (n=4).

4.2.4.1. Alamar blue assay

Alamar blue assay (AB) was used to measure the activity of HOBs on the samples after the time periods outlined above. The assay uses a fluorometric activity indicator based on the detection of metabolic activity. A chemical reduction of resazurin (blue and nonfluorescent) to resorufin (pink and highly fluorescent) is thought to be caused by mitochondrial or cytosolic enzymatic activity detected intracellularly.¹⁹⁵

After the relevant time period, the culture media was discarded from the samples and washed in sterile phosphate buffered saline solution (SPBS).

The samples were then incubated in 1 ml of 10% AB (in Hanks' Balanced Salt Solution (HBSS)) solution for 90 minutes. After 90 minutes, 100 µl of the AB solution from each well was transferred to a 96-well plate and the fluorescence measured on a fluorescence plate reader (Bio-Tek FLx800) using 530 nm excitation and 590 nm emission filters.

4.2.4.2. DNA (Hoechst 33258) and Alkaline Phosphatase assays

After the AB assay was performed as outlined above, the samples were washed thoroughly in sPBS and lysed in 1 ml sterile distilled water by 3 freeze/thaw cycles (frozen at -20 °C and thawed to 37 °C).

The concentration of DNA in the cell lysates was determined by comparing the fluorescence of Hoechst 33258 stain on the samples to that of a standard curve generated using a calf thymus stock solution (Sigma, UK) of known DNA concentrations. Before analysis of the samples, a 100 ml solution of buffer was made from 0.156 g tris(hydroxymethyl) methylamine, 11.72 g sodium chloride and 0.0372 g ethylene diamine tetraacetic acid (EDTA) in 100 ml distilled water (TNE buffer).

To measure the DNA content in the cell lysates, a quantity of 100 µl of each was placed into individual wells of a 96-well plate with 100 µl Hoechst 33258 solution (20 mg/ml Hoechst in TNE buffer). These solutions were then read using a fluorescence plate reader (Bio-Tek FLx800) using wavelengths of 360 nm excitation and 460 nm emission.

Alkaline phosphatase (ALP) is an enzyme that peaks early on in bone mineralisation¹⁹⁶ and is a good indication of osteoblast differentiation *in vitro*.⁵⁰ The ALP assay (Randox Alkaline Phosphatase kit, AP 307) is used to

determine the relative activity of ALP in the samples tested. The assay was catalysed by ALP in the reaction of 4-nitrophenylphosphate and water producing phosphate and 4-nitrophenolate. The rate of production of 4-nitrophenolate was therefore determined using a colorimeter.

In order to quantify ALP activity, 100 μ l of the cell lysate was placed in wells of a 96-well plate. After 100 μ l of the reaction solution (4-nitrophenylphosphate in diethanolamine buffer) was added to each well, the plate was read on a colorimetric plate reader (Bio-Tek ELx800) using 405 measurement and 620 nm reference filters and the rate was calculated over 12 minutes in order to compare with other samples. Values were normalised using DNA data to account for quantity of cells on the substrates.

4.2.5. Statistical analysis

Statistical analysis was performed using Graphpad Prism[®] 4 software. One-way analysis of variance (One-way ANOVA) with Tukey's post test was used as a multi comparison post test. Statistical significance was taken to be $P \leq 0.05$.

4.3. Results

4.3.1. Surface composition, morphology and topography

Figure 4.2, figure 4.3 and figure 4.4 illustrate the morphology and topography of pressed nanofilament substrates using SEM, CLSM and AFM respectively. The surfaces viewed at low magnification using SEM (figure 4.2) illustrate the morphology of the pressed surfaces. The surfaces do not appear to be very different using these images alone. CLSM reflectance data (figure 4.3), however, show that the MWNT9 and PR19PS pressed samples were

rougher than the two GNF samples. GNF samples had a smaller roughness in the region of 0.5-2.0 μm compared to the nanotube samples (3.0-4.0 μm).

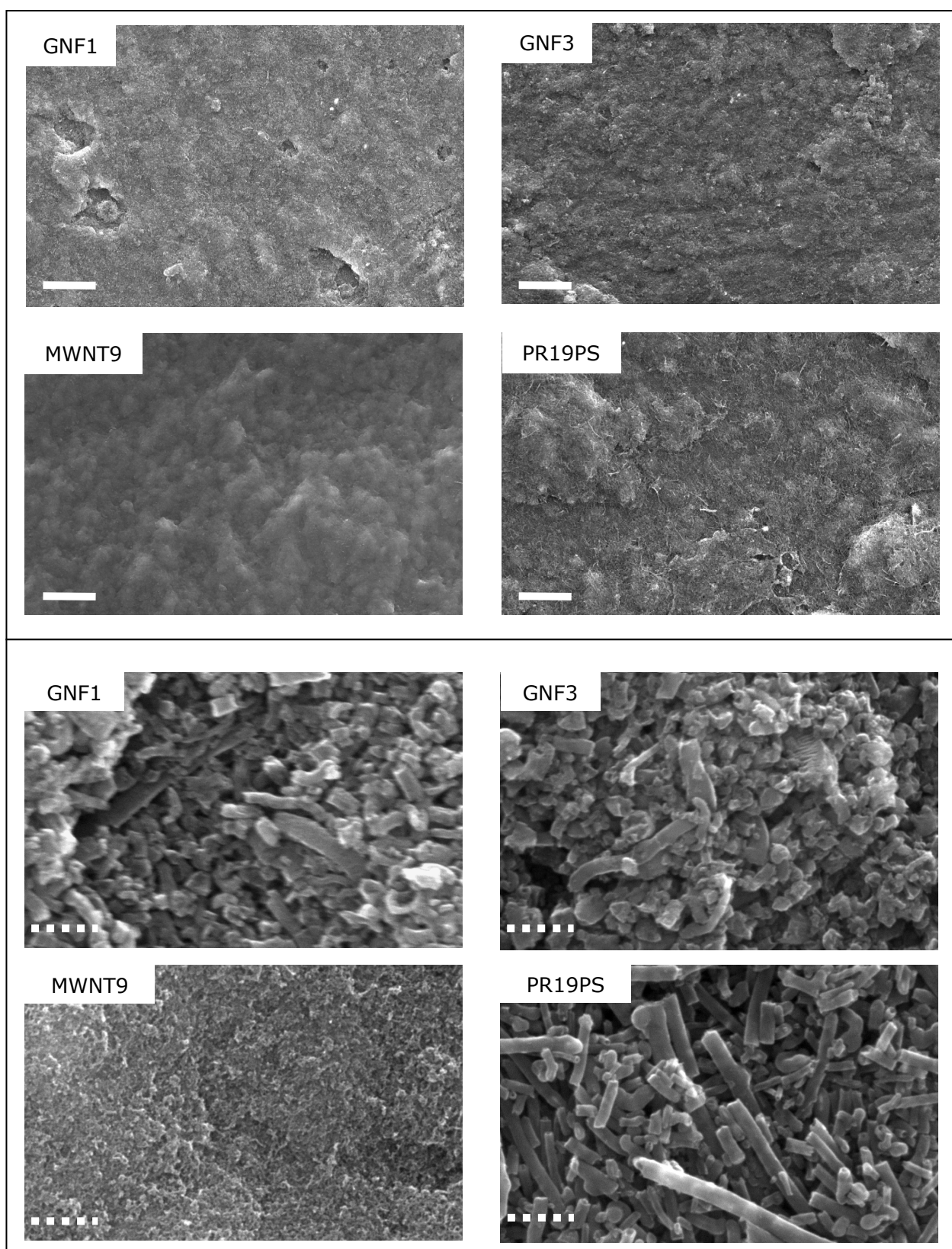


Figure 4.2: Morphology of pressed nanofilament substrate surfaces using SEM.
Scale bars: Solid=500 μm , and Dashed=1 μm

Higher magnification images of the samples using SEM are illustrated in figure 4.2. GNFs and MWNTs can be clearly seen on the GNF1, GNF3 and PR19PS samples. The nanofilaments tended to appear shorter after pressing especially in the GNF samples, which are more likely to break across their fibre axis. The MWNTs on the MWNT9 sample are too small to be shown on the SEM. Similar results were found from the AFM data. AFM scans illustrate the topography of the pressed nanofilament substrates. The nanofilament topography was shown especially in the PR19PS sample but can also be seen, but to a lesser extent, in the GNF substrates. Nanoscale roughness, analysed from AFM data, was mainly affected by the nanofilament size and shape, and did not show a significant difference between any of the samples (figure 4.4).

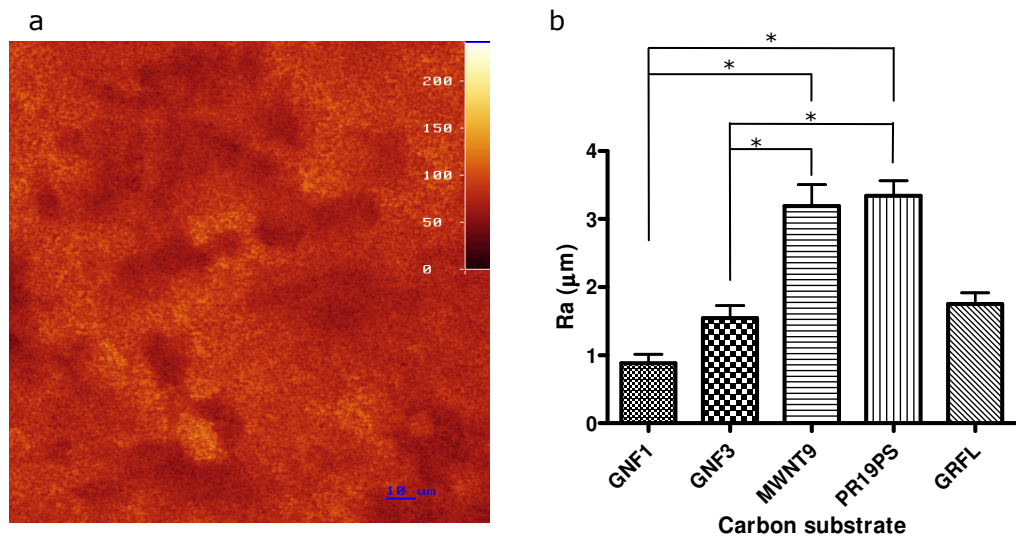


Figure 4.3: a) Example of Reflectance CLSM image highlighting features in the GNF1 substrate; b) Micron-scale roughness values (R_a) of the carbon substrates analysed using CLSM. Values are mean \pm Standard error (n=5).

***Significant difference ($P < 0.05$)**

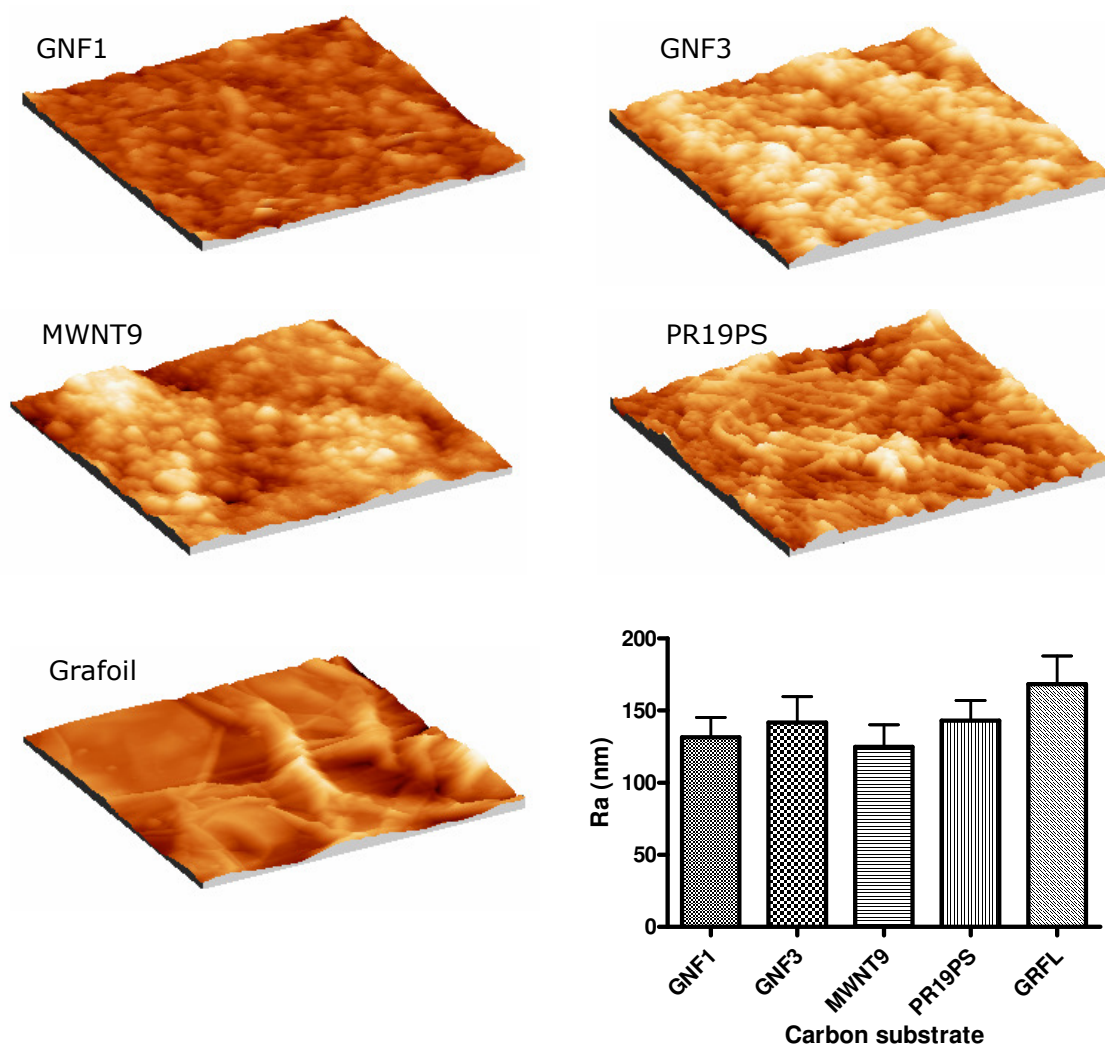


Figure 4.4: Topography of substrates from AFM. $10\ \mu\text{m}^2$ scans are illustrated above for all pressed nanofilament samples and the Grafoil control. Nanoscale roughness (R_a) is also shown, calculated from AFM data. R_a values are mean \pm sem ($n=4$). No significant differences were observed ($P \leq 0.05$)

The nanofilaments were treated with differing acid treatments depending on their catalyst as previously described in section 3.2. EDX was used to determine the percentage of catalyst and support remaining in the sample after acid treatment and pressing onto the PEEK discs. The atomic percentages of carbon, oxygen, and the remaining catalyst from the samples (nickel in GNF1 and GNF3; iron in PR19PS; iron and silica in MWNT9) are summarised in figure 4.5. The composition of carbon and oxygen were similar

(no significant difference) between the samples being measured in the region of 80 at% and 20 at % for carbon and oxygen respectively.

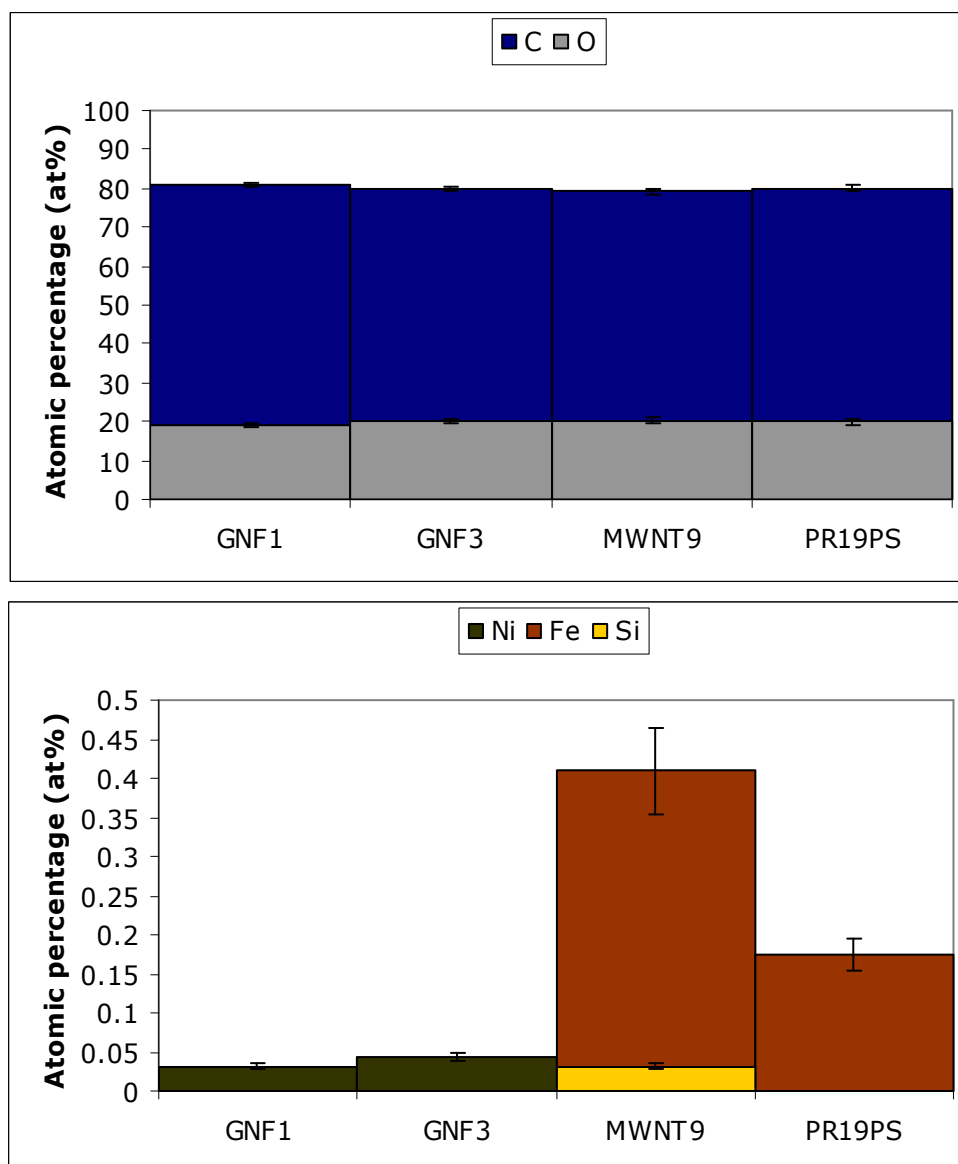


Figure 4.5: EDX analysis of pressed carbon nanofilament surfaces. Atomic percentages were analysed using a spot size of 6 and an accelerating voltage of 20 kV (Mean \pm sem; n=20)

The GNF samples showed very little remnant catalyst (<0.05 at%) and the PR19PS sample had little catalyst remaining (0.17 at%). MWNT9 was synthesised from a silica supported sample and the data suggest that both silica and iron were almost removed (0.41 at% Fe and 0.03 at% Si).

4.3.2. Osteoblast attachment results

A high proportion of the seeded cells attached to the GNF1, GNF3 and PR19PS substrates compared to the initial seeding density ($32,000 \text{ cells.cm}^{-2}$). HOBs attached to a lower degree on the MWNT9 sample and grafoil control (figure 4.6). The number of cells attached to the nanofibre and commercial PR19PS surfaces was 3-4 times greater than those on MWNT9 and the grafoil control (figure 4.6). Cells on the substrates with greatest cell attachment (GNF1, GNF3 and PR19PS) appear to have attached and spread rapidly after 90 minutes with many filopodia or lamellipodia (figure 4.7). The MWNT9 sample showed the least cell attachment and their morphology was rounded with very little sign of spreading.

Although the number of cells that attached to the nanofibre and commercial nanotube samples was similar, the morphology of the HOBs was different (figure 4.7). Figure 4.7a illustrates the morphology of a typical cell on the GNF1 substrate. The body of the cell is still round in shape, but has filipodia extended more than $5 \mu\text{m}$ in this example. This was common in the cells on the GNF3 sample as well, although there were also signs of elongated cells with short lamellipodia as shown in figure 4.7b. The commercial sample, PR19PS, exhibited cells that were elongated in morphology. The cells spread in a different fashion to HOBs on the other samples as it showed a greater degree of lamellipodia extensions.

The area of the cells on the commercial surface were therefore the greatest as the wide lamellipodia caused higher area measurements compared to the cells on other samples with thin filopodia. The areas

measured for cells attached to MWNT9 sample were the smallest as the cells had not spread.

A higher magnification image showing the interaction of an osteoblast with a pressed PR19PS surface is given in figure 4.9. The cell in this micrograph has spread over the nanotextured surface and filopodia have extended along the nanotube surface.

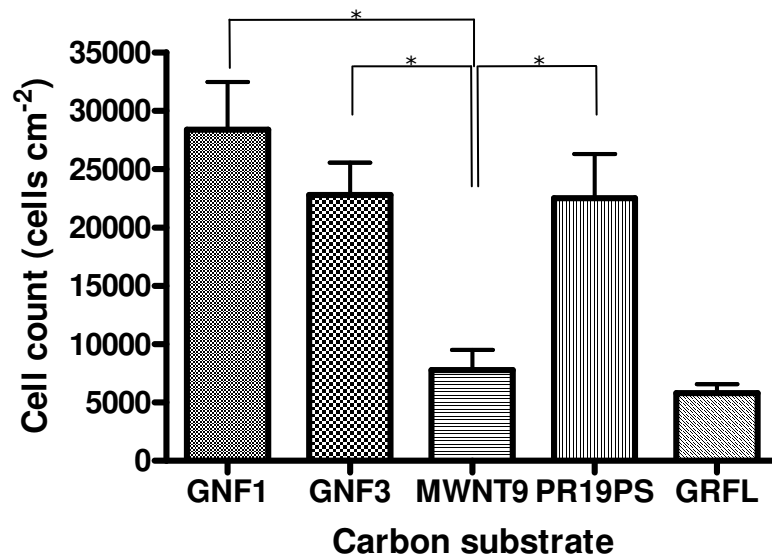


Figure 4.6: Average number of viable HOBs on carbon substrates taken from cell counts obtained from propidium iodide staining (Mean \pm sem; n=8). * Significantly different ($P < 0.05$).

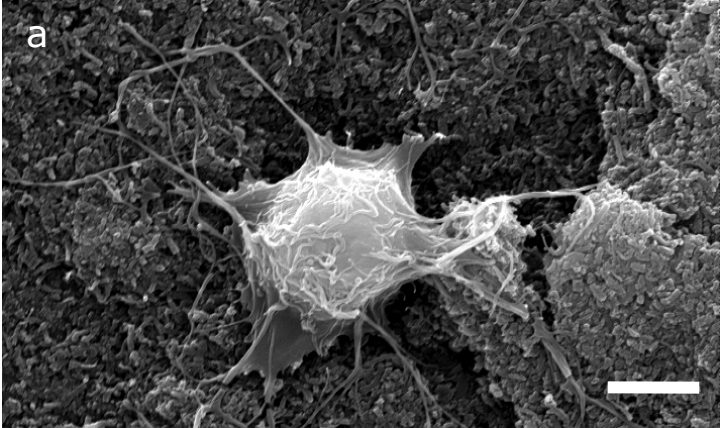
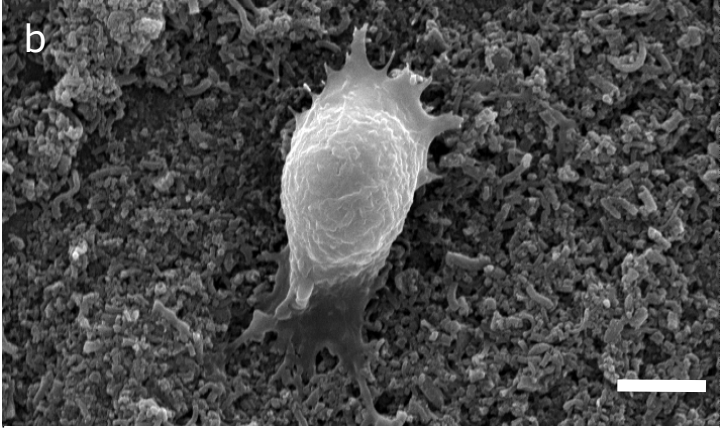
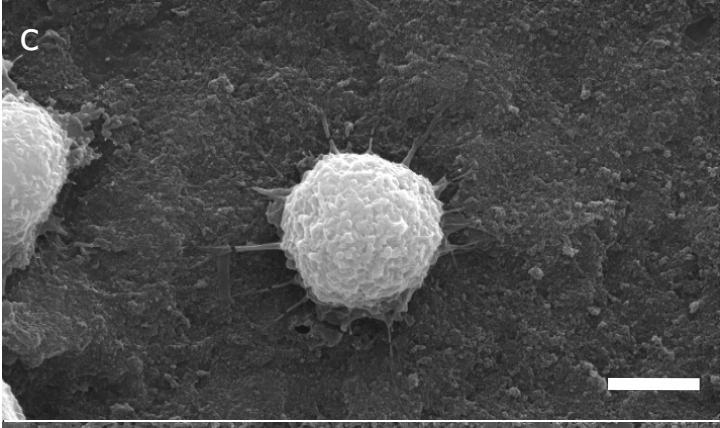
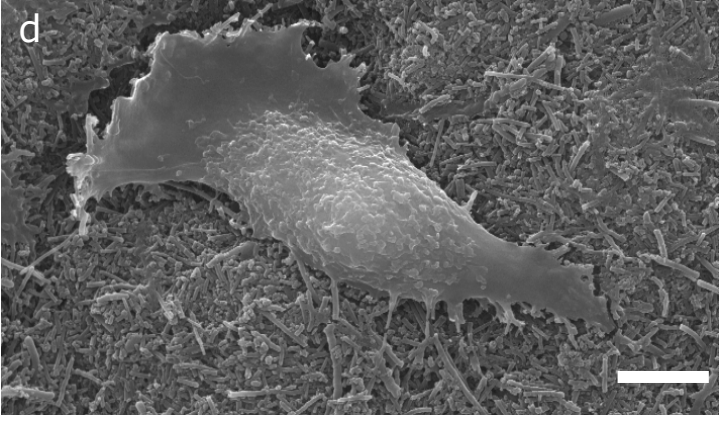
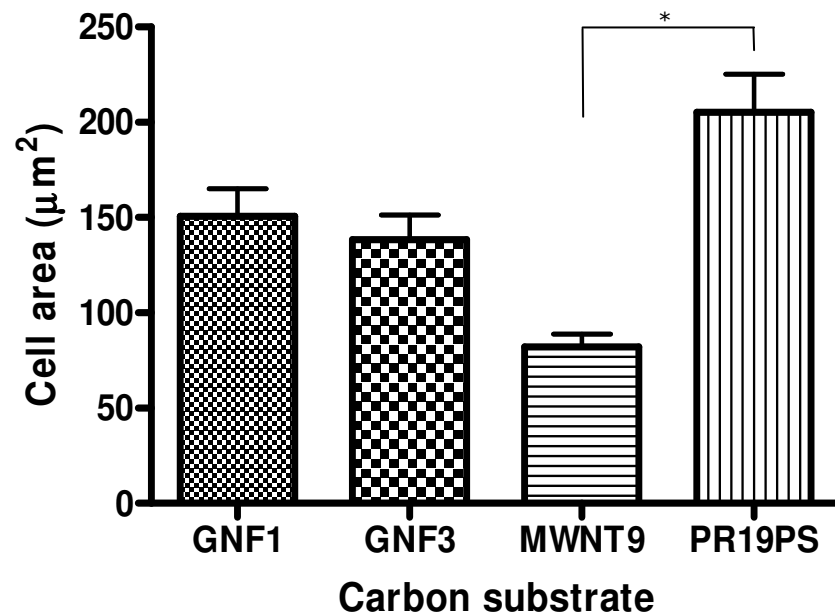
SEM micrograph	Average diameter (nm)	Roughness, R_a (μm) (nm)	
a 	155 ± 13	0.9 ± 0.2	131 ± 14
b 	142 ± 12	1.5 ± 0.3	150 ± 19
c 	13 ± 1	3.2 ± 0.5	125 ± 15
d 	137 ± 7	3.3 ± 0.3	143 ± 14

Figure 4.7: Appearance of HOBs on pressed carbon nanofilament samples; a) GNf1, b) GNf3, c) MWNT9, and d) PR19PS, after 90 minutes in standard cell culture conditions, as well as their corresponding average nanofilament diameters and surface roughness values. Values are mean \pm sem. Scale bar: 5 μm



**Figure 4.8: Cell areas measured from SEM micrographs using Image Pro Plus software (Mean \pm sem; n=25).
* Significantly different (P < 0.05)**

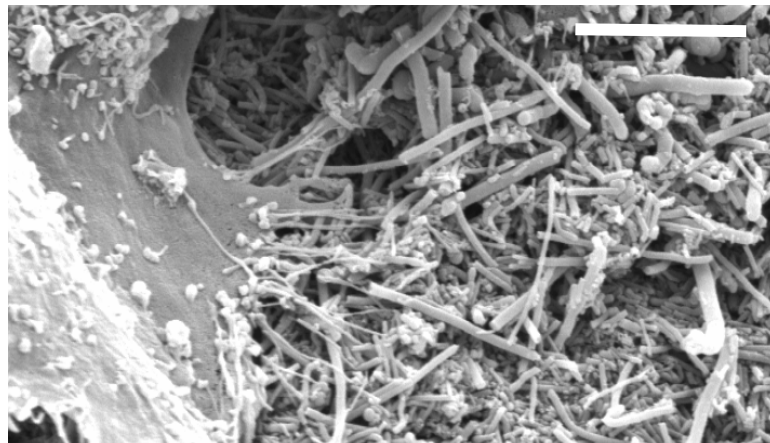


Figure 4.9: SEM micrograph illustrating the interaction of osteoblast filopodia with pressed PR19PS carbon nanotubes after 90 minutes of attachment. Sample was tilted by 30°. Scale bar: 5 μm

4.3.3. Osteoblast proliferation results

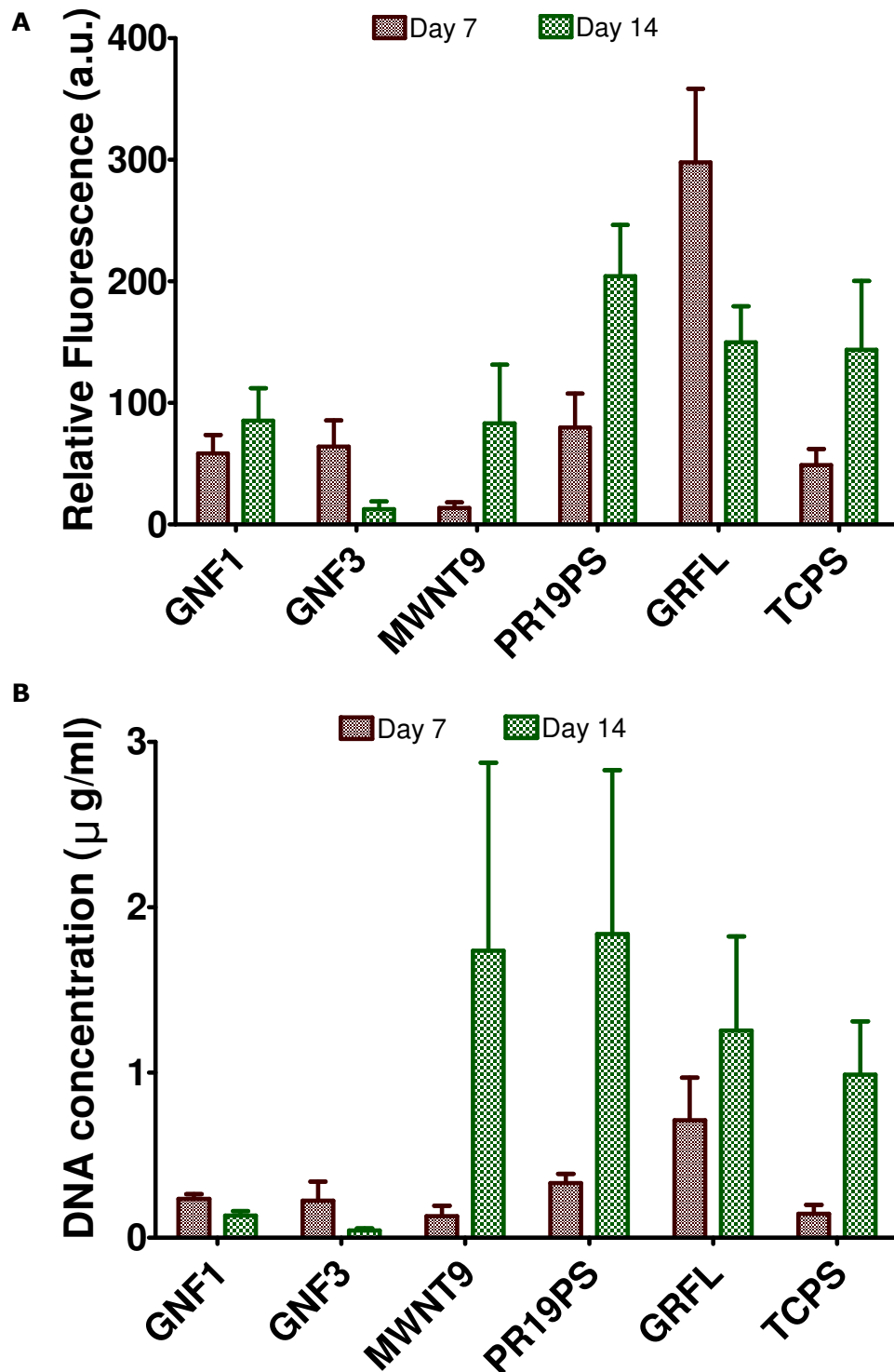


Figure 4.10: Human osteoblast proliferation using Alamar blue (A) and DNA assays (B) on pressed carbon nanofilament samples (GNF1, GNF3, MWNT9, PR19PS), grafoil (GRFL) and tissue culture polystyrene (TCPS). (Mean \pm sem, n=4)

The cellular activity on the substrates, assessed using the alamar blue assay, is represented in figure 4.10a. There was a similar activity on the

samples, aside from MWNT9 and grafoil, after 7 days of culture. The activity of GNF1, PR19PS and TCPS were found to increase from day 7 as well as the MWNT9 sample, which increased from a lower activity. GNF3 and GRFL showed decreased levels of cellular activity after 14 days.

DNA concentrations, quantifying the number of cells on the samples, are illustrated in figure 4.10b. All of the samples, excluding the nanofibre samples, showed proliferation between day 7 and 14. The levels of cellular activity and number of cells indicated similar trends on each sample, apart from the grafoil control. According to the alamar blue data, the activity of the cells decreased, whereas the number of cells increased over the 14 days.

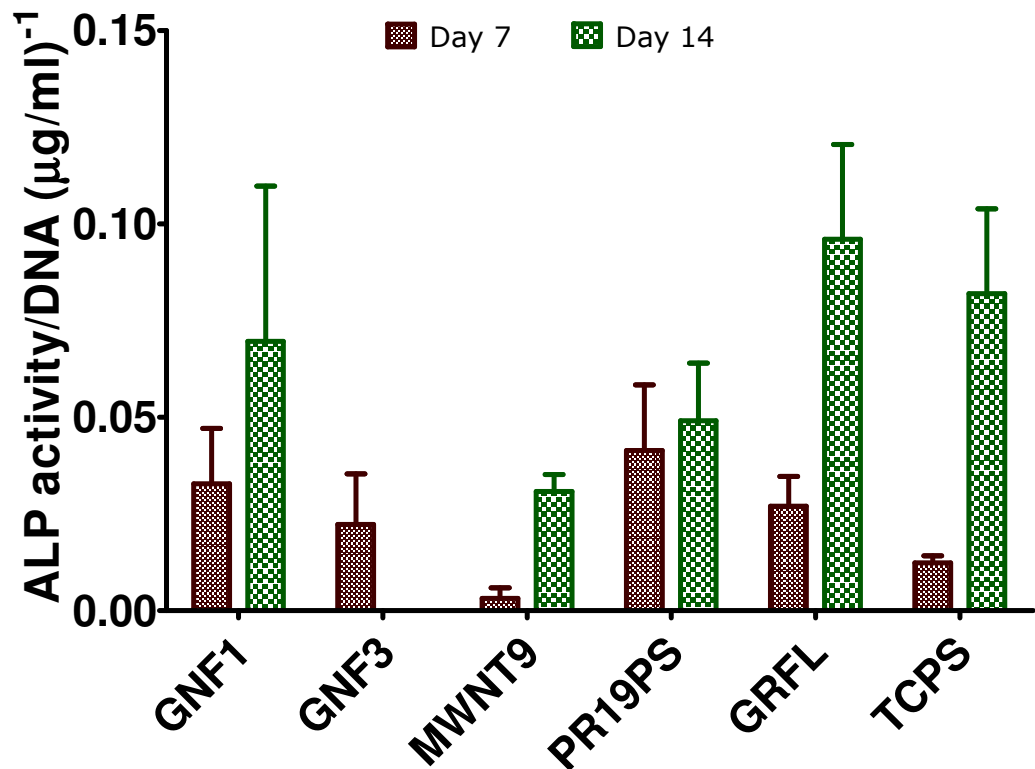


Figure 4.11: Alkaline phosphatase activity per μg DNA of human osteoblasts cultured on pressed carbon nanofilament samples (GNF1, GNF3, MWNT9, PR19PS), grafoil (GRFL) and tissue culture polystyrene (TCPS) over 14 days. (Mean \pm sem, $n=4$)

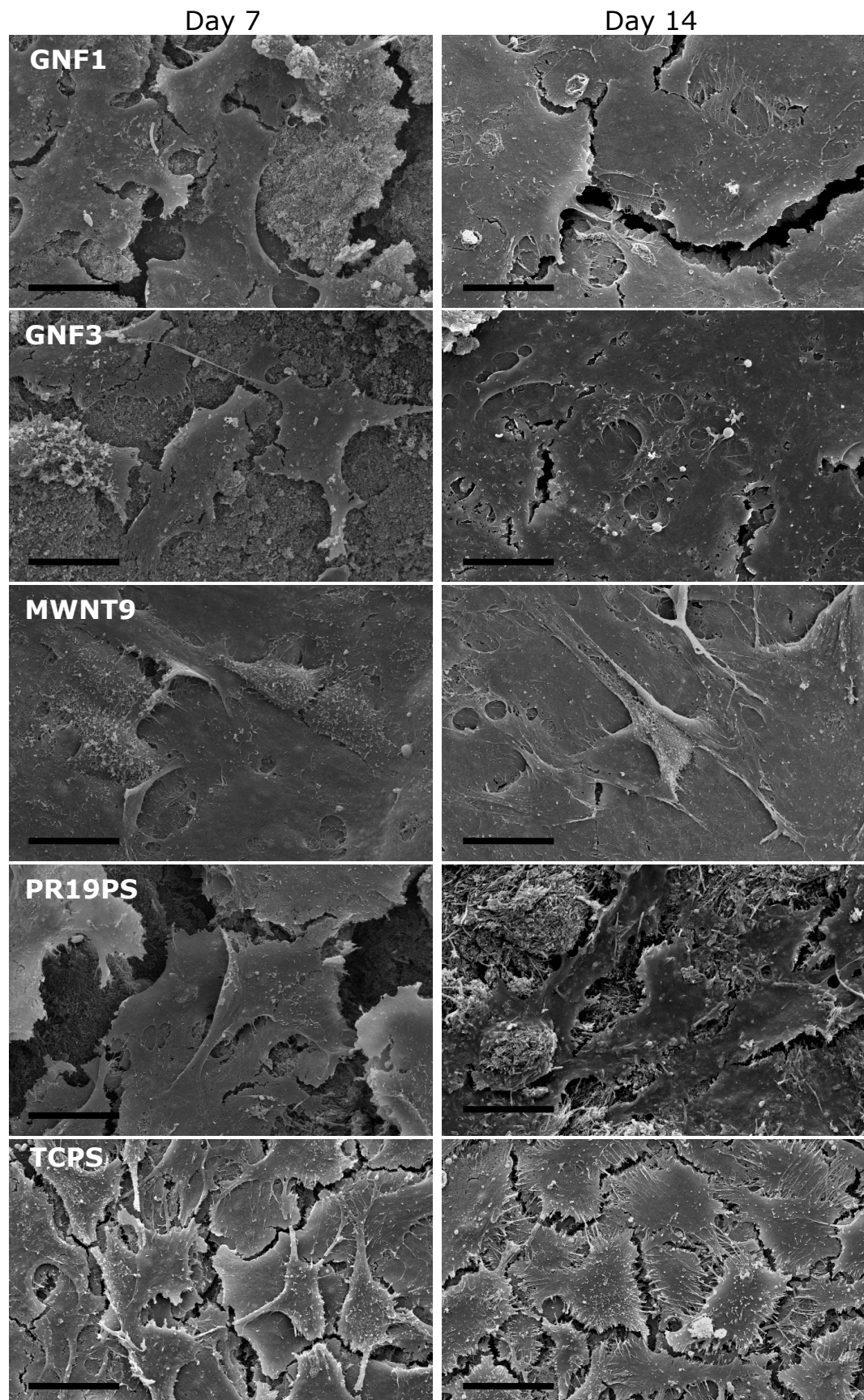


Figure 4.12: SEM micrographs of human osteoblasts cultured on pressed carbon nanofilament surfaces (GNF1, GNF3, MWNT9 & PR19PS) and tissue culture polystyrene (TCPS) for 7 and 14 days

Alkaline phosphatase activity detected on the samples over 14 days is represented in figure 4.11. Cells on all surfaces, excluding GNF3, showed an increase in alkaline phosphatase activity per cell over 14 days. The extent of multi-layering of cells was assessed using SEM (figure 4.12). Cells had proliferated and were multi-layering on GNF1, GNF3 and MWNT9 after 14 days. The osteoblasts on the PR19PS sample were not confluent over the surface to the same extent as the other nanofilament samples. Osteoblasts cultured on the TCPS surface were multi-layering by day 7.

4.4. Discussion

The structure and size of carbon nanofilaments altered the topography of the pressed substrates prepared. SEM analysis (figure 4.2) confirmed that the nanofilaments were successfully pressed onto the PEEK discs and that the nature of the nanofilaments affected the morphology of the substrates. The MWNT9 nanotubes, for example, were much thinner than the other samples and produced a surface with smaller features, whereas the GNF1, GNF3 and PR19PS samples had larger diameters and produced larger features. The nanofibre samples (GNF1 and GNF3) look to have broken during pressing, especially compared with the PR19PS nanofilaments, which were more than three times longer. As the interplanar interactions between graphene sheets will be weaker than the covalent bonding along planes, nanofibres are more likely to break as the graphene planes are orientated perpendicular to the fibre axis.⁶ Therefore the shape and form of the nanofilament samples were all different, where the GNF samples consisted of short individual nanofibres of different structure, the MWNT9 sample consisted of entangled curly nanotubes and the commercial PR19PS sample consisted of agglomerated long straight nanofilaments.

CLSM and AFM data (figure 4.3 and figure 4.4), used to assess the topography of the substrates, showed a difference in micron-scale roughness in terms of R_a (using CLSM analysis), but no significant difference in nano-scale roughness (using AFM R_a data). The micron-scale roughness of the nanotube samples (MWNT9 and PR19PS), thought to be attributed to the degree of compaction of the pressed nanofilaments, was double ($\sim 3\text{-}4\text{ }\mu\text{m}$) that of the R_a values for the nanofibres ($\sim 0.5\text{-}2\text{ }\mu\text{m}$). This may be due to the better compaction of the shorter nanofibres. The commercial PR19PS sample, which did not show breakage, had longer nanofilaments than the GNF samples and the MWNT9 sample was very curly in nature and tended to cluster and entangle. These clusters and the long length of the PR19PS nanotubes are likely to be harder to pack together during pressing, compared to the shorter nanofibres. The roughness of the GNF substrates in the micron-scale, therefore, was lower than the nanotube samples. The nano-scale roughnesses, accredited to the size and shape of the individual nanofilaments, were not significantly different between the samples. Since the diameter of the MWNT9 sample was very thin, the resultant nanoscale roughness of these samples was therefore attributed to clusters with smaller nanotube features (in contrast to other nanofilament samples).

Surface chemistry of the substrates was assessed by EDX (figure 4.5). Complimentary to the XRD data on the unpressed powder samples (chapter 3), EDX data provided further quantitative evidence of the removal of residual catalyst from the samples. There was a higher proportion of iron in the MWNT samples (MWNT9 and PR19PS) as it was more likely to get encapsulated within the nanotube samples than the nanofibre samples (as explained previously in section 3.3.2). The amount of iron catalyst remaining in the nanotube samples (0.41 at% in MWNT9 and 0.17 at% in PR19PS) was

unlikely to affect the osteoblast response in this study as the catalyst particles remain encapsulated within the nanofilaments. The acid treatments proved to remove a very high proportion of the catalyst from the samples, especially from the nanofibre samples, but not entirely (<0.05 at% of remnant nickel).

The topography and chemistry of surfaces was important in understanding osteoblast responses to carbon nanofilaments. The pressed nanofilament substrates produced surfaces that varied in micron-scale roughness and surface morphology due to the shape of the nanofilaments and graphitic nano-structure. HOBs responded differently to the different carbon substrates. Propidium iodide staining (figure 4.6) showed that a high percentage of cells attached to the samples with average diameters of 134-155 nm (GNF1, GNF3 and PR19PS). SEM observations showed evidence of rapid cell spreading on the same surfaces (figure 4.7). The results of another study¹⁰⁸ indicate that osteoblasts attached in higher quantity to VGNF compacts with higher nano-scale roughness containing VGNFs with average diameters of 100 nm or less. In this study, cells attached to substrates with higher diameters (i.e. GNF1, GNF3 and PR19PS) in the region of 134-155 nm rather than substrates with higher micron-scale roughness (figure 4.6). Earlier work of Price *et al.*,^{104,105} also indicated that osteoblasts attach in greater number to substrates with nanofilaments below 100 nm. There may be an optimal nanofilament diameter that encourages early osteoblast attachment (after 90 minutes), which is higher than 13 nm (the diameter of MWNT9) but lower than 100 nm.

The morphology of the cells on the different samples was slightly different after 90 minutes (figure 4.7). Cells that attached to the GNF1 sample extended predominantly with filopodia (figure 4.7a) at this set time point, as opposed to the many cells on the PR19PS sample that spread using

lamellipodia (figure 4.7d). All three samples showed some degree of extended filopodia and lamellipodia. This was reflected in the cell area measurements (figure 4.8) where there was a higher cell area on the PR19PS sample than the other samples as lamellipodia will produce an increased cell area compared to thin filopodia. The cells on the MWNT9 sample showed the smallest degree of spreading and exhibited the lowest cell area. The area of spread cells compared to the rounded cells on MWNT9 was not high enough to produce statistically significant differences. The morphology of the substrate seemed to have an impact on the morphology of attached cells.

It appears that cells responded rapidly on the nanofilament surfaces with an average diameter of 134-155 nm and that this may be due to the cells responding to the substrate topography. Since the cells will see the nanoscale surface of the substrates,³⁶ it is likely that the cells responded to nanofilament diameters or shape, and that the MWNT9 nanotubes were too small or too entangled for the cells to respond to at early stages of cell attachment. The attachment of cells on biomaterials is influential on the long term responses *in vitro*,¹¹³ but an initial positive response, i.e. high attachment and spreading, does not necessarily lead to a positive long-term proliferation and differentiation.¹⁹⁷ The morphology of cells has been closely associated with cell growth.¹⁹⁷ Folkman and Moscona varied tissue culture plastic surfaces with poly(2-hydroxyethyl methacrylate) to induce differences in fibroblast morphology and found that cell growth (determined by measuring DNA synthesis) was highly dependent on cell shape.¹¹⁹ The osteoblasts that attached to the GNF samples in this study remained rounded with many filopodia extensions (figure 4.7), whereas osteoblasts on the PR19PS sample spread to a greater extent were more elongated and promoted both filopodia and lamellipodia.

Considering the response of osteoblasts over a longer period of time, MWNT9 and PR19PS indicated an increase in cell activity, proliferation and differentiation over two weeks compared to the GNF samples (figure 4.10 and figure 4.11). The alamar blue and DNA assays do not show much osteoblast proliferation on the GNF samples, although there were signs of proliferation from the SEM micrographs taken 14 days after cell seeding. This may suggest that the osteoblasts responded to a difference in nanofilament structure, i.e. MWNT structure, during this proliferation and differentiation period. However, as the MWNT samples (MWNT9 and PR19PS) themselves had a different structure to each other (the PR19PS sample had an amorphous carbon layer on the exterior of the nanotubes (see section 3.3.2.1)), it is more likely that the cells responded to a difference in micron-scale topography. The MWNT9 and PR19PS samples had a rougher micron-scale topography ($R_a \sim 3\text{-}4\text{ }\mu\text{m}$) compared to the GNF samples ($R_a \sim 0.5\text{-}2\text{ }\mu\text{m}$) as shown in figure 4.3. The MWNT9 substrate did not show any sign of osteoblast spreading after 90 minutes, but these cells progressed on to proliferate on these surfaces. This suggests that cells were slower to attach on the nanotube surface, but did eventually spread on the surface enough to promote cell proliferation. An increase in micron-scale surface roughness has been shown to reduce osteoblast-like (MG63) attachment on titanium surfaces, but with increased signs of differentiation by increased osteocalcin levels¹⁹⁸ and alkaline phosphatase activity levels.² This correlates particularly with the cells cultured on the MWNT9 substrate in this study, where there was little sign of osteoblast attachment, but increased levels of alkaline phosphatase activity over 14 days compared to the GNF samples. This trend was not shown in osteoblasts on the PR19PS substrate, which had attached and spread rapidly (figure 4.6 and figure 4.7) as well as showing signs of proliferation and differentiation (figure 4.10 and figure 4.11).

These results add further understanding with the few studies that have been performed with these materials. Elias *et al.*² illustrated an improved osteoblast proliferation and differentiation on nanofilaments that were 60 nm and 100 nm in diameter compared to samples with 125 nm and 200 nm respectively. The samples used by Elias were similar in surface chemistry to the commercial PR19PS sample used in this study. Since the nanofilament structure and chemistry of the samples was slightly different from each other, it created an additional factor. The surface of the MWNT9 nanotube sample was made up of a graphene plane, whereas the PR19PS nanotube sample had an amorphous carbon external layer. The proliferation and differentiation of osteoblasts on the nanofilaments here indicated that the nanotube samples show enhanced cell function compared to the graphitic nanofibres, unrelated to nanofilament dimension. These results do not compliment the results obtained from Elias *et al.*,^{199,200} which indicate that there was an optimum nanofilament diameter for osteoblast response below 100 nm. It appears from this current investigation that nanofilaments with diameters below 100 nm (i.e. MWNT9 with average diameter of 13 nm) do encourage osteoblast proliferation and differentiation, but also was observed in nanofilaments with larger diameters (i.e. PR19PS with average diameter of 134 nm). Alternatively, the osteoblasts may have attached preferentially to proteins adhered to the nanofilaments spaced at a particular distance from each other. RGD-containing cyclic peptide sequences have been used to investigate the role of distance between integrin ligands on cell adhesion using various cells including MC3T3 osteoblasts and B16 melanocytes.¹¹² Surfaces were organised in hexagonal patterns with RGD peptides attached to gold nanoparticles spaced at constant distances of 28-110 nm from each other. The group found that a separation of between 58-73 nm between RGD peptides encouraged cell spreading and stable integrin-mediated adhesion compared to spacing of less than 58 nm and more than 73 nm. It is possible

that through protein adsorption on the nanofilament surfaces from the culture media, osteoblasts attached preferentially to substrates displaying proteins at certain distances from each other. The spacings of the adhered proteins would be dependent on the spacings between nanofilaments or between clusters of nanotubes (i.e. MWNT9 sample). This would happen in the extracellular matrix of bone as extracellular proteins that adhere to collagen fibrils encourage osteoblast attachment and growth.

Alternatively, the difference in osteoblast proliferation on the substrates may have been due to their different morphologies. The GNF samples tended to be broken up, whereas the other two samples maintained their form after compaction. The thin MWNT9 nanotubes entangled and twisted together due to their curly nature and PR19PS filaments were long, stiff and straight. The differences in the final topography of the pressed nanofilaments may have contributed to the proliferation and differentiation of osteoblasts on the MWNT9 and PR19PS substrates. This may have been due to their resultant micron-scale roughness, but alternatively may have been a result of nanofilament surface features on the substrates. The topography of the MWNT9 and PR19PS substrates, compared to the GNF substrates, may have encouraged proliferation and differentiation because of cytoskeletal organisation in response to the nanofilament topography, which has been reported by Dalby *et al.*¹¹² The group used human bone marrow stromal cells (HBMSCs) on PMMA surface patterned with pits and grooves. Grooves of 50 μm width and 327 nm depth induced reduced cell spreading after 4 days, but increased actin and vinculin organisation after 4 days, as well as increased detection of osteocalcin and osteopontin marker proteins after 21 days of culture. This suggested that the reduction in cell spreading was due to elongated spreading along the grooves, which also promoted cytoskeletal organisation orientated with the surface features. The elongated cells were

thought to have promoted differentiation in the osteogenic cells. Cytoskeletal organisation of osteoblasts were not investigated in this study, but the elongated morphology of cells on the PR19PS substrate suggest that cells had responded to the surface features of the PR19PS substrate. This kind of cell morphology was not observed in the osteoblasts attached to the MWNT9 substrate, but cells may have taken a longer time to attach to these surfaces.

There was a difference in the trends seen in cell attachment and spreading compared to the proliferation and differentiation results. It has been shown that positive signs of attachment do not necessarily lead to enhanced proliferation and differentiation.¹⁹⁷ Folkman *et al.* explain that if a cell (fibroblasts in their investigation) starts to spread quickly but does not spread enough, it will hinder cell growth, hence potentially showing good signs of attachment but little sign of proliferation and consequently differentiation.²⁰¹ This has been shown in this study. Osteoblasts on both nanofibre samples, GNF1 and GNF3, attached in high number and exhibited rapid cell spreading (figure 4.6 and figure 4.7), but had limited cell proliferation and differentiation (figure 4.10 and figure 4.11). The body of the cells were still rounded and despite a large number of extended filopodia, it was likely that the cells did not spread enough to promote proliferation.

Another possible explanation for the differences in proliferation between the GNF samples and the MWNT9 and PR19PS samples was that the amount of remnant catalyst may have influenced osteoblast function. Although there was a smaller amount of remnant catalyst in the nanofibres synthesised with nickel (figure 4.5), it was possible that the nickel nanoparticles would have had a more detrimental effect on osteoblast growth compared to the effects of iron catalyst nanoparticles, which have been shown to have little cytotoxic effects on human monocyte-macrophages²⁰² and rat

liver cells²⁰³ *in vitro*. Nickel ions have been shown to be carcinogenic,²⁰⁴ binding to DNA and inhibiting its replication and transcription.⁶ Therefore, it was possible that although there was less than 0.05 at% of nickel catalyst in the nanofibre samples, it hindered proliferation of the osteoblasts. The remnant catalyst was not observed in the GNF samples by TEM, which may indicate that the catalyst may have been dispersed as smaller nanoparticles during processing. Although this remnant catalyst was likely to have been encapsulated, it was possible that it could have leached during the 14 days of the experiment and affected osteoblast growth.

In order to modify biomaterial implants with carbon nanofilaments, it is critical to understand the role of their structure and diameter on promoting osseointegration. It seems that if nanofilaments do indeed approximate to the collagen extracellular matrix, there is an optimal diameter that would encourage osteoblast attachment.¹⁰⁵ The longer term responses of osteoblasts were attributed to micron-scale roughness, but it is possible that cells also responded to the shape and form of the nanofilaments. Since cells have been shown to respond to features in the range of 5 nm,^{2,108} it is possible that the small MWNT9 nanotubes (13 nm in diameter), may have promoted osteoblast proliferation and differentiation due to their size in comparison to collagen molecules (1 nm in diameter). Similarly, the longer, wider PR19PS nanofilaments (134 nm in diameter), which were close in diameter to the size of collagen fibrils (up to 500 nm), did also promote osteoblast proliferation and differentiation. This study indicates that there may not only be one optimal range of filament diameters that encourage osteoblast growth in the region of 100 nm, suggested by Price *et al.*,^{122,123,153} that are close to the diameters of collagen fibrils. There may be another range closer to that of collagen molecules (of 1 nm in diameter), which was closer to the filament diameter of the MWNT9 substrate (13 nm in diameter). The MWNT9 substrate

also had larger nanoscale features formed from nanofilament clustering, that were observed on the SEM and AFM scans, which may have contributed to osteoblast growth due to micron-scale features. The GNF samples of similar average diameters to the PR19PS sample (142 nm and 155 nm) may have hindered osteoblast growth due to their nanofibre structure or the effects of the small amount of remnant nickel catalyst.

5. Investigation Osteoblast responses to Carbon Nanofilament- Methacrylate Composites

5.1.Introduction

Carbon nanofilaments can be incorporated into polymer matrices and they have been shown to affect the mechanical, thermal, electrical and surface properties of the polymers. Examples include PMMA,¹²⁴ polypropylene,¹²¹ polycarbonate¹⁵⁰ and UHMWPE^{12,205} in various forms. Such nanofilament-filled composites could be used in place of clinically used polymers, such as those mentioned above, to improve their bulk and surface properties in bone repair applications, in polymeric bone cements or tissue engineered scaffolds, for example. In both of these examples, the bulk and surface properties of the composite are critical to support the healing tissue and promote bone tissue growth around the implant.

Micron-sized fibres have been used primarily to reinforce polymers for clinical applications, especially carbon fibres used for spinal cages, fracture fixation devices, intramedullary pins and rods and in total joint replacement components.^{154,206} Conventional carbon fibres have diameters in the region of 1-10 μm and exhibit a Young's modulus reported to be up to 750 MPa,^{54,84,206} whereas carbon nanofilaments have been reported to have a Young's modulus of 0.5-1.8 TPa (although this range is uncertain).²⁰⁶ This does not necessarily mean that nanofilaments will induce superior mechanical properties in a composite as this would be dependent on the nanofilament-polymer interface.¹⁸ Carbon nanofilaments could also provide topographical features in the scale of the extracellular matrix and if present at the composite surface, potentially encourage tissue growth as described in chapter 4.¹⁴⁰

PEMA/THFMA is a copolymer system that has shown potential surface and bulk characteristics beneficial to bone repair devices. McFarland *et al.*^{141,142,145} have observed that the surface of the PEMA/THFMA appears to favourably present adsorbed fibronectin that may contribute to promoting cell attachment and potentially matrix formation. The polymer has also shown to maintain chondrocyte phenotype *in vitro*²⁰⁷ and cartilage growth *in vivo*.¹⁵⁸ PEMA/THFMA was chosen in this study as a model to investigate the interaction of carbon nanofilaments with a polymer matrix, as well as their effects on promoting osteoblast responses on such surfaces.

This chapter is concerned with the effects of incorporating carbon nanofilaments into PEMA/THFMA, with particular respect to their reinforcing capabilities and effects on thermal and surface properties. The dispersion of nanofilaments in the matrix and the bonding between filler and matrix are two important factors to consider in the reinforcement of polymers. Nanofilaments can easily agglomerate and bundle together, which may produce poorly dispersed composites that would restrict their reinforcing capabilities.^{122,150,157} However, there are techniques that can encourage dispersion, such as optimal physical blending,^{122,153} *in situ* polymerisation¹⁵⁶ or chemical functionalisation.³

Carbon nanofilaments could also be used in polymer composites to produce a textured surface that would encourage osteoblast adhesion. This has been demonstrated by Webster *et al.*³ who used poly(carbonate urethane) reinforced with VGNFs at various loadings from 0-100 % (100 % was a VGNF compact). The group demonstrated decreased fibroblast adhesion, but increased osteoblast adhesion on composites with higher compositions of carbon nanofilaments.^{140,141,145} This could have been due to the size and shape of the nanofilaments present on the surface of the composite.

This chapter, therefore, focuses on investigating the use of nanofilaments described in chapter 3 as fillers in poly(ethyl methacrylate)/tetra hydro furfuryl methacrylate (PEMA/THFMA) co-polymer. The effects of nanofilament size and structure are assessed with respect to mechanical, thermal and surface properties of the composites. Human osteoblasts were seeded onto the samples for 90 minutes and for up to 2 weeks to assess their *in vitro* responses in light of the surface texture of the composites with varying nanofilament concentrations.

5.2.Methods

5.2.1. PEMA/THFMA preparation

PEMA/THFMA copolymer was polymerised by mixing 5 g PEMA powder (Sigma Aldrich, UK) and 3 ml THFMA monomer liquid (Sigma Aldrich, UK).²⁰⁸ An initiator system of benzoyl peroxide (BPO; Sigma Aldrich, UK) and dimethyl-p-toluidine (DmpT; Sigma Aldrich, UK) was used to create free radicals to aid polymerisation as shown in section 2.5.1. BPO (0.6 wt%) was added to the PEMA powder and DmpT (2.5 v/v%) was added to the liquid THFMA monomer prior to polymerisation. After thoroughly mixing the liquid and powder components, the mixture was left to cure in a custom-built PTFE mould clamped between two stainless steel plates to maintain the shape of the mould. The copolymer was cured into either discs of 12 mm diameter and 3 mm thickness or 60 mm x 15 mm x 1 mm plaques. The copolymer was left to polymerise overnight at 70 °C.

5.2.2. Nanofilament incorporation

Carbon nanofilament incorporation was achieved using *in situ* polymerisation by mixing the carbon nanofilament powder with the powder

polymer component before polymerisation. After thoroughly mixing the liquid monomer (with 2.5 v/v% DmpT initiator) with the polymer/nanofilament powder, composites were left to polymerise in a 70 °C drying oven overnight. Three nanofilament samples were used in this part of the project; GNF1 (hereafter termed GNF), MWNT9 and PR19PS.

Samples were sterilised for cytocompatibility work by exposing their surfaces to ultra-violet light for at least one hour.

5.2.3. Composite characterisation

5.2.3.1. Bulk analysis of composites

Dynamic Mechanical Analysis (DMA) was used to determine the flexural properties of the methacrylate polymer and carbon-methacrylate composites.

Storage modulus, loss modulus, $\tan \delta$ and glass-transition temperature were analysed using a TA DMA Q800. A temperature sweep was performed using a 20 mm 3-point bending clamp, by ramping the sample from 25 to 130 °C at 3 °C/min with a constant strain amplitude (4.0 μm) under a continual frequency of 1 Hz. Samples for three-point bending were cut during polymerisation from rectangular plaques into smaller plaques of approximately 30 mm x 7.5 mm x 1 mm and precisely measured after polymerisation.

Differential scanning calorimetry (TA DSC Q10) was used to characterise the thermal behaviour of the curing and thermal transitions in the co-polymer and carbon composites. Samples were subjected to a ramping temperature of 5 °C/min from 0 °C to 130 °C. Heat flow verses temperature

was used to determine glass transition temperatures and onset of polymerisation activated by heat.

Micro-computerised tomography (μ -CT 40, Scanco Medical) was used to assess the porosity of PR19PS –PEMA/THFMA composite. Medium resolution (16 μ m voxel resolution) was used to scan the composite samples with an integration time of 300 ms. Images and porosity measurements were constructed using the Scanco software.

5.2.3.2. Surface analysis of composites

Composite surfaces were characterised using SEM, and topographical analysis using profilometry and AFM as described in section 4.2.2. Samples analysed by SEM were simply mounted on a stub and analysis was carried out using an accelerating voltage of 10 eV and a spot size of 4. Composite samples and polymer samples were freeze fractured in liquid nitrogen and then mounted on sticky carbon tabs so that their surfaces and cross-sections could be viewed. Polymer samples were gold-coated, but the composites were not, as they had sufficient conductivity. Profilometry was performed using Mitutoyo Surftest SV-600 and scanning 5 mm line scans at 0.1 mm.s⁻¹. Atomic force microscopy was used in contact mode using a PF-AFM Explorer as detailed in section 4.2.2.

5.2.4. Osteoblast Attachment studies

Primary derived HOBs were isolated from femoral head trabecular bone¹⁴⁰ and seeded onto the co-polymer and composite samples with 5 and 15 wt% of GNF1, MWNT9 and PR19PS samples. Cells were seeded at a density of 32,000 cells.cm⁻², cultured in DMEM supplemented with 10% FBS

and cultured in standard cell culture conditions for 90 minutes. Assays were performed on two separate occasions in triplicate (n=6).

Propidium iodide staining was performed as stated in section 4.2.3.1. As the polymer and composite samples would degrade in ethanol (which would usually be used to dehydrate cells after fixation as in section 4.2.3.2), environmental scanning electron microscopy using a field emission gun (XL-30 FEG ESEM) was used to view osteoblasts when assessing their morphology for signs of attachment and proliferation. After the appropriate time period in culture, samples were washed with sterile PBS three times, then fixed with 3% glutaraldehyde in 0.1 M sodium cacodylate. After at least 30 minutes, the glutaraldehyde was thoroughly washed off with 7% sucrose in sodium cacodylate buffer solution and transferred to distilled water shortly before viewing on ESEM. ESEM was performed in wet mode (so as not to dehydrate the cells), using a gaseous secondary electron detector (GSE) to view the cells on the sample surfaces.

5.2.5. Proliferation and differentiation of HOBs

HOBs were seeded onto composite samples at a density of 32,000 cells.cm⁻². Alamar blue, DNA (Hoechst 33258) and alkaline phosphatase assays were performed after 2, 7 and 14 days as outlined in section 4.2.4. Cell assays were performed on two separate occasions in quadruplicate (n=8).

5.2.6. Statistical analysis

Statistical analysis was performed using Graphpad Prism® 4 software. One-way analysis of variance (One-way ANOVA) with Tukey's post test was

used as a multi comparison post test. Statistical significance was taken to be $P \leq 0.05$.

5.3.Results

5.3.1. Carbon incorporation into carbon-composites

GNF incorporation above 1 wt%, into the PEMA/THFMA system with only DmpT initiator produced very rubbery and low strength composites. The appearance and rheology of the sample did not change without the DmpT initiator. The commercial PR19PS sample also produced rubbery or flaky samples at compositions above 5 wt%. Composites were polymerised with and without DmpT initiator and would only harden over a period of a few days. It was therefore assumed that nanofilament incorporation into the copolymer was hindering the initiator during polymerisation.

Initially, only DmpT initiator was used to manufacture the composites as used by McFarland *et al.*²⁰⁹ This proved sufficient for carbon nanofilament incorporation below 1 wt%. However, graphitic nanofibre fillers and high percentages of nanotube incorporation caused a reduction in the polymerisation rate and often produced rubbery samples. For this reason, different percentages of initiator and heat treatments were experimented with to improve the polymerisation process.

DSC was performed on the co-polymer immediately after initial mixing of the liquid monomer and powder polymer (figure 5.1). The polymer and monomer constituents were mixed, with and without DmpT and DmpT-BPO initiators, to explore their effect on the onset of polymerisation induced by heat. A reduction in the onset temperature of polymerisation (93.7 to

56.1 °C) was observed when DmpT initiator was added to the polymerising system (figure 5.1). Further reduction was seen when BPO was added as well as DmpT.

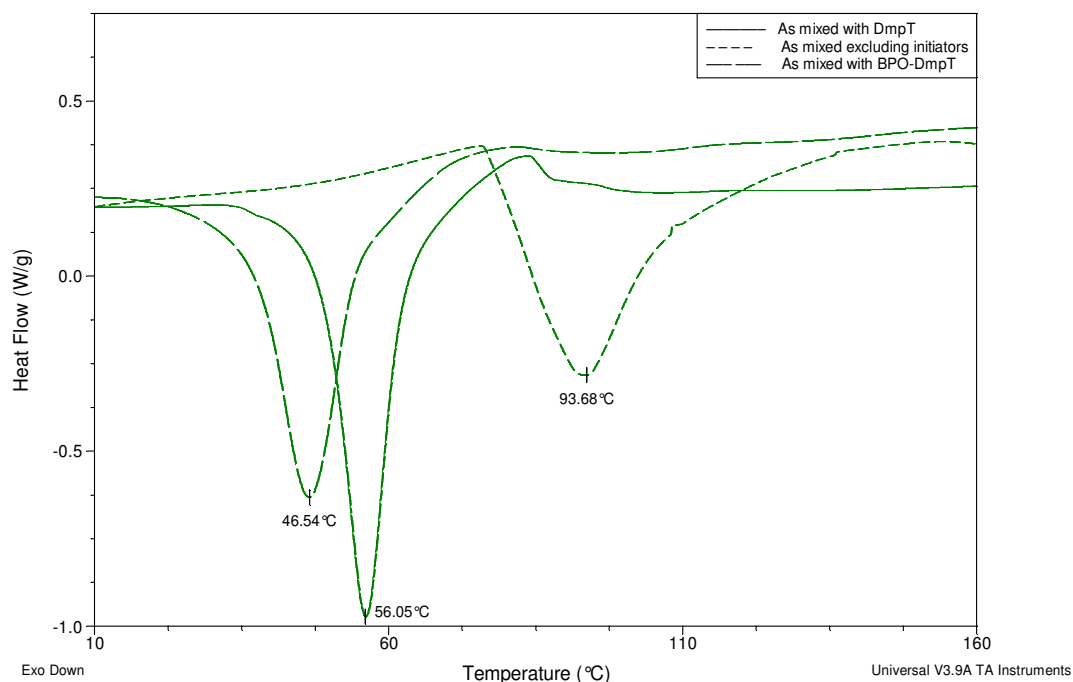


Figure 5.1: DSC plot for PEMA/THFMA without initiator and with dimethyl-*p*-toluidine and with benzoyl peroxide and dimethyl-*p*-toluidine initiators, immediately after the constituents were mixed together

DSC results (figure 5.1) indicated that the addition of BPO to the polymer system reduced the temperature onset of polymerisation by heat. Therefore, to aid maximum polymerisation, BPO was included in the polymerisation process and samples were heated at 70 °C to encourage polymerisation.

5.3.2. Dynamic mechanical analysis of composites

DMA was used to investigate the mechanical properties of the co-polymer and nanofilament composites. Figure 5.2 illustrates an example of a temperature sweep on a 15 wt% GNF composite sample. Such experiments

give information on storage modulus at specific temperatures, glass transition temperature (T_g) using the temperature transition in storage modulus (+) or tan delta peak (x), and also tan delta values. As is shown in figure 5.2, there is a difference in T_g measurements using the storage modulus transition and tan δ peak.

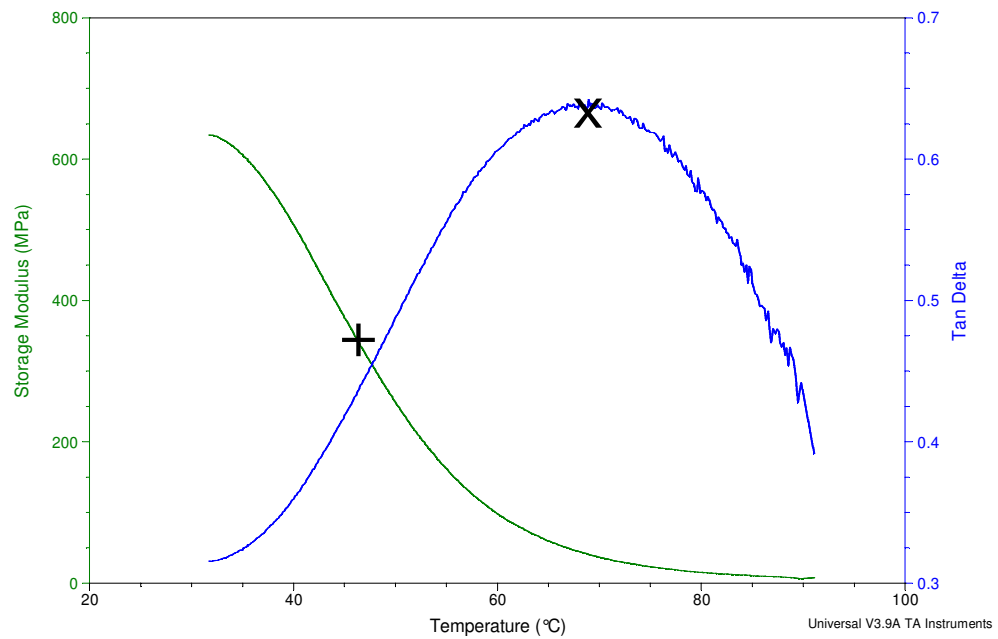


Figure 5.2: Example of a DMA temperature sweep on a 15 wt% GNF composite sample, where T_g can be measured by tan delta peak, labelled "x", or storage modulus transition, labelled "+".

The measured glass transition temperatures from tan δ peaks and the drop in storage modulus are summarised in figure 5.3. All tan δ peak values and storage moduli transitions followed the same trends. Statistical analysis only showed a significant difference between PEMA/THFMA polymer and the composites for tan δ measurements, apart from the polymer and 5 wt% or 15 wt% PR19PS containing composites, and for storage modulus transition, apart from 5 wt% MWNT9 and 15 wt% PR19PS. There was a drop in T_g in all samples after 5 wt% of carbon nanofilament incorporation. However, both GNF and PR19PS composites possessed an increase in T_g above 10 wt%, whereas the MWNT sample showed a constant decay in T_g

with further addition of nanotubes. The T_g was always lower using the storage modulus transition rather than the $\tan \delta$ peak.

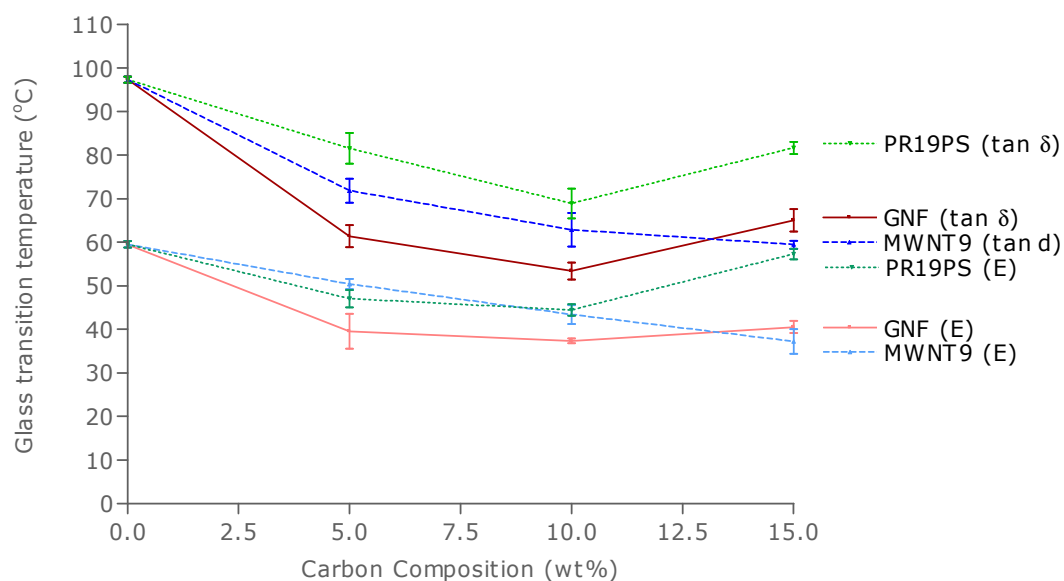


Figure 5.3: Glass transition temperatures measured from storage moduli (E) and loss tangent ($\tan \delta$) graphs (Mean \pm sem; $n=4$)

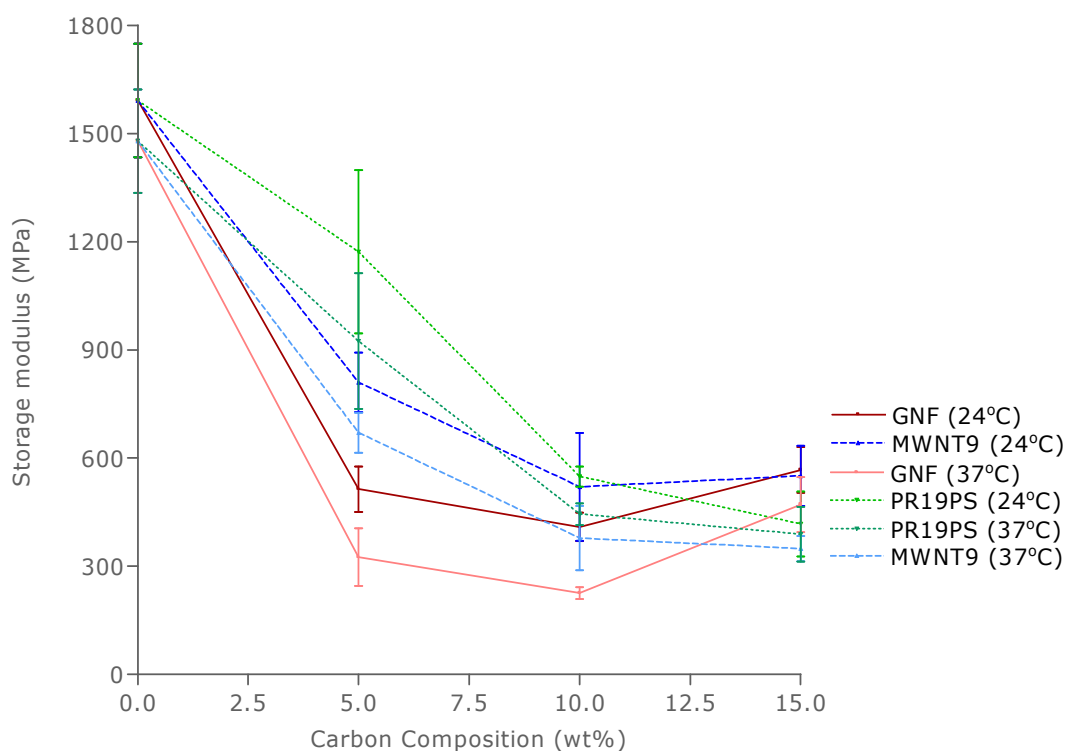


Figure 5.4: Storage modulus measured from DMA data at 24°C and 37°C (Mean \pm sem; $n=4$)

Storage moduli decreased with any carbon nanofilament incorporation (see figure 5.4). The co-polymer was significantly different from all compositions of carbon nanofilaments at both 24 °C and 37 °C (apart from 5 wt% MWNT9 at 24 °C, 5 wt% PR19PS at 24 °C and 37 °C). As with T_g trends, there was a sign of an increase in the storage modulus after 10 wt% of nanofibres in the GNF composite samples at both 24 and 37 °C. There was a drop in storage modulus when raising the samples from room temperature (24 °C) to body temperature (37 °C) in all samples.

All composites again showed a decrease in $\tan \delta$ values as shown in figure 5.5. Polymer measurements were significantly different ($P < 0.05$) from the composite measurements. Other statistical differences were noted between 5 wt% and 15 wt% GNF and MWNT9 and all PR19PS composites.

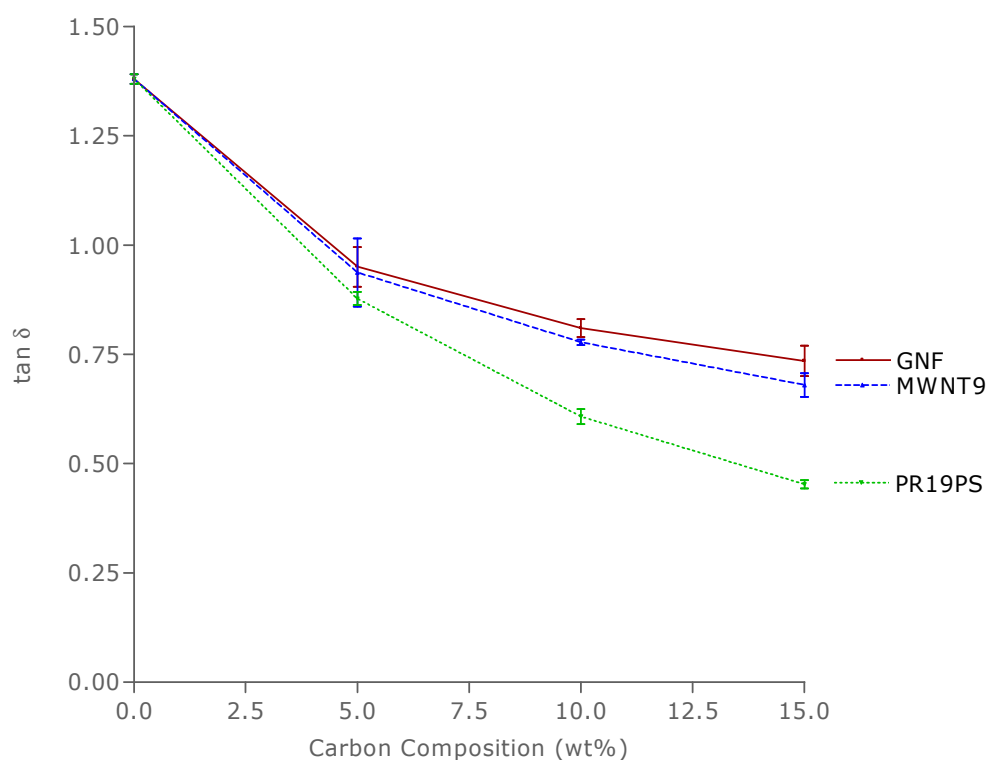


Figure 5.5: Graph of the difference in loss tangent ($\tan \delta$) peak values measured using a temperature sweep at rate of 3 °C/min and a frequency of 1 Hz against increasing composite carbon content (Mean \pm sem; n=4)

5.3.3. Temperature Transitions in the composites

DSC was also used to assess T_g in the co-polymer and composite samples. Figure 5.6 illustrates a temperature sweep of a 5 wt% PR19PS sample whilst monitoring heat flow in the sample. Figure 5.7 shows that the glass transition temperature varied with carbon composition according to DSC results. The T_g of the composites drop off agreeing with the DMA glass transition measurements in section 5.3.2 and show an increase after 10 wt% in GNF and PR19PS samples. A comparison of the glass transition temperatures measured from DMA and DSC thermal analysis techniques is summarised in table 5.1.

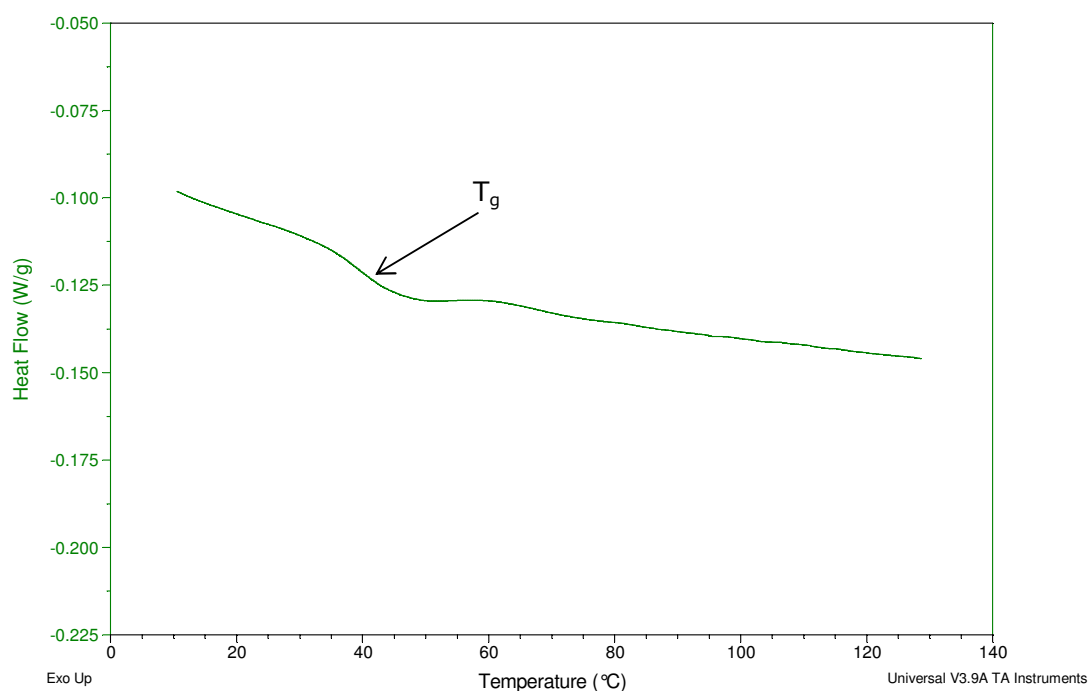


Figure 5.6: DSC of 5 wt% PR19PS-PEMA/THFMA sample illustrating the glass transition temperature (T_g)

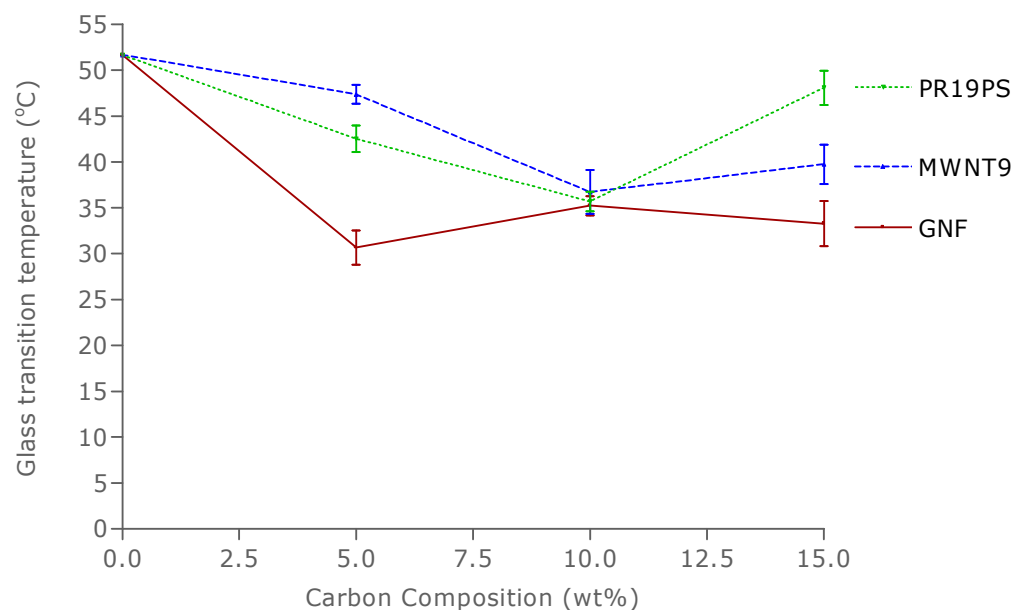


Figure 5.7: Glass transition temperatures of various fractions of carbon nanofilaments (GNF, MWNT9 and PR19PS) into PEMA/THFMA co-polymer system (Mean \pm sem; n=3)

Table 5.1: Comparison of glass transition temperature measurements made from $\tan \delta$ peaks, storage moduli drop (E') and heat flow drops. Values are stated degrees Celsius ($^{\circ}\text{C}$)

	PEMA/ THFMA	GNF			MWNT9			PR19PS		
		5 wt%	10 wt%	15 wt%	5 wt%	10 wt%	15 wt%	5 wt%	10 wt%	15 wt%
DMA ($\tan \delta$)	97.3 \pm 0.7	61.4 \pm 2.5	53.4 \pm 2.0	65.0 \pm 2.6	71.8 \pm 2.7	62.9 \pm 3.9	59.4 \pm 0.9	81.5 \pm 3.5	68.9 \pm 3.4	81.6 \pm 1.4
DMA (E')	59.5 \pm 0.7	39.6 \pm 4.0	37.3 \pm 0.5	40.5 \pm 1.4	50.4 \pm 1.2	43.4 \pm 2.2	37.2 \pm 2.8	47.0 \pm 2.0	44.4 \pm 1.3	57.3 \pm 1.2
DSC (Heat flow)	51.6 \pm 0.1	30.7 \pm 1.9	35.2 \pm 1.0	33.3 \pm 2.5	47.4 \pm 1.0	36.7 \pm 2.4	39.7 \pm 2.1	42.5 \pm 1.4	35.7 \pm 1.1	48.1 \pm 1.9

5.3.4. Morphology and topography of the composites

The morphology of the composite surfaces are summarised in figure 5.8, figure 5.9 and figure 5.10 and polymer surface is shown in figure 5.11. There was charging from parts of all the composite surfaces (labelled with solid arrowheads) at lower magnification. This was not observed on the

PEMA/THFMA copolymer surface, which was coated prior to SEM analysis. The appearance of the GNF-PEMA/THFMA and MWNT-PEMA/THFMA surfaces with all carbon compositions show the composites to be relatively flat with occasional bubbles up to 100 μm in size. GNFs were detected in the 5 wt% and 15 wt% GNF-PEMA/THFMA surface micrographs with little sign of clustering (figure 5.8). Nanotubes in the MWNT9 were not individually detected from SEM micrographs, but there are signs of clumping of the nanotubes into clusters of varying sizes, giving a cloudy appearance.

The surface of the PR19PS-PEMA/THFMA composites, however, had a different morphology to the other carbon composites. The 5 wt% PR19PS composite sample shows nanotubes within the polymer matrix but the surface does not appear to be as smooth as the other carbon composites. The PR19PS nanotubes appear to cluster together in both compositions. As the composition of PR19PS in the sample increases, the surface of the consequent composite gets rougher and in turn appears to be porous. There appears to be clusters of nanotubes that form larger particles, of the size of tens of microns, which are held together with the polymer matrix (which charges under the electron beam).

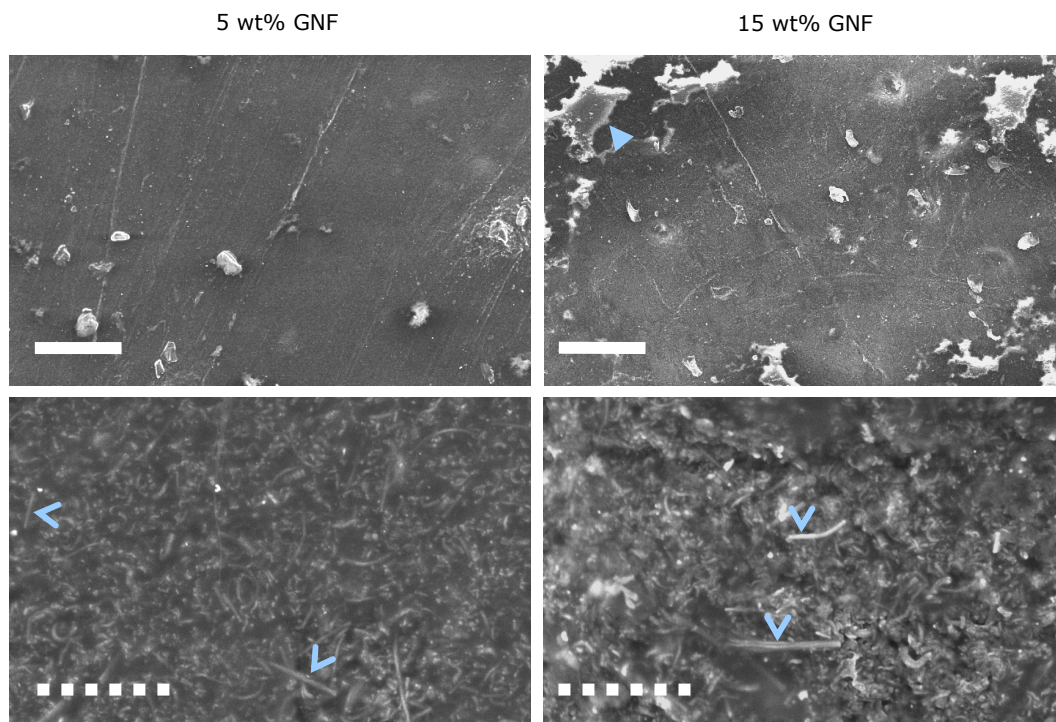


Figure 5.8: SEM micrographs of GNF-PEMA/THFMA composites with 5 and 15 wt% GNF1 at low magnification (top) and high magnification (bottom). Solid arrowheads point out examples of charged particles on the composite surface and hollow arrowheads point out examples of nanofilaments detected. Scale bars: solid = 100 μm ; dashed = 10 μm

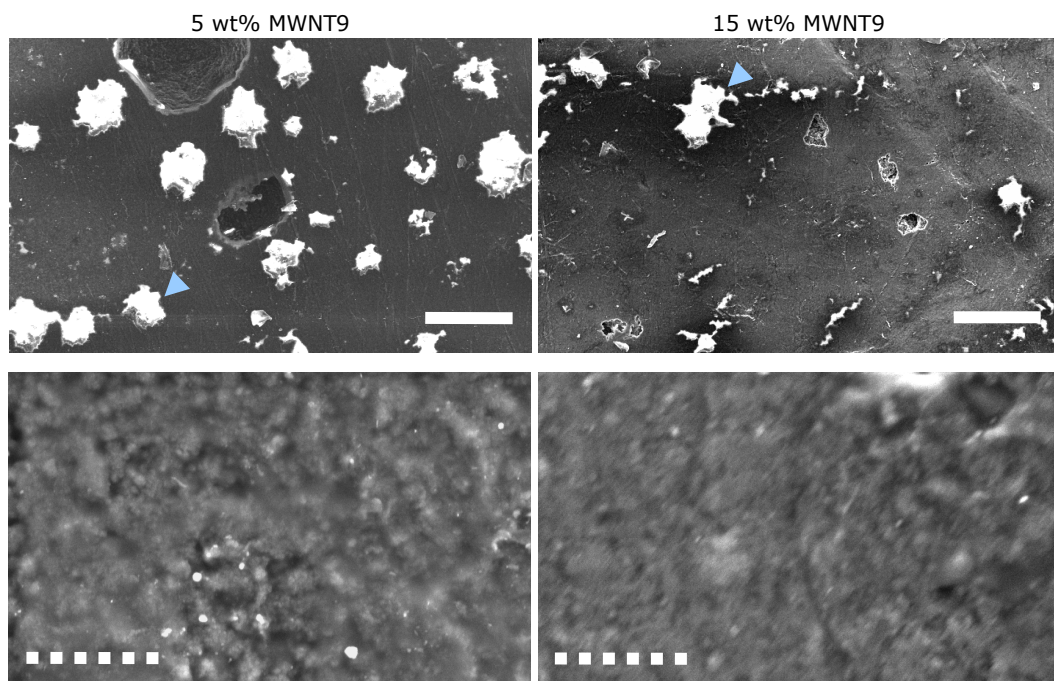


Figure 5.9: SEM micrographs of MWNT9-PEMA/THFMA composites with 5 and 15 wt% MWNT9 at low magnification (top) and high magnification (bottom). Solid arrowheads point out examples of charged particles on the composite surface and hollow arrowheads point out examples of nanofilaments detected. Scale bars: solid = 100 μm ; dashed = 10 μm

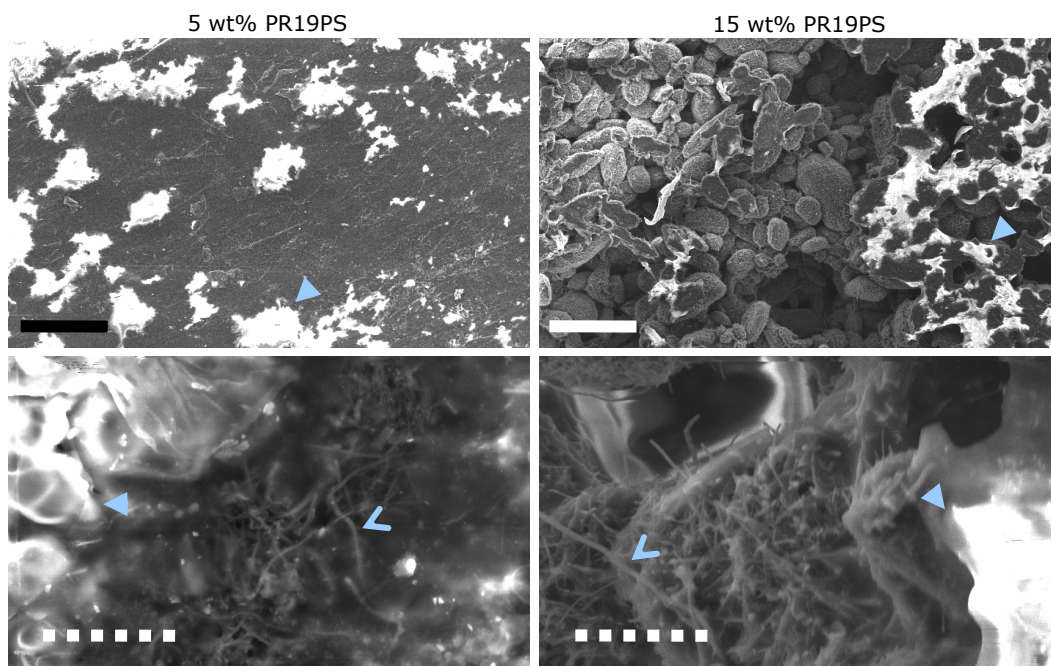


Figure 5.10: SEM micrographs of PR19PS-PEMA/THFMA composites with 5 and 15 wt% PR19PS at low magnification (top) and high magnification (bottom). Solid arrowheads point out examples of charged particles on the composite surface and hollow arrowheads point out examples of nanofilaments detected.
Scale bars: solid = 100 μ m; dashed = 10 μ m

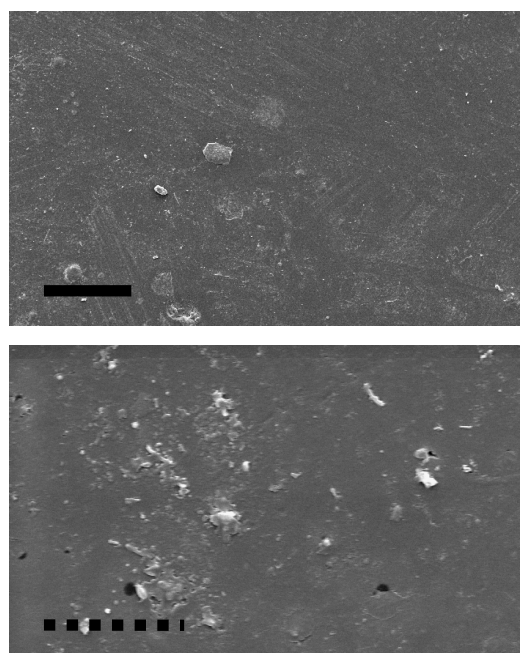


Figure 5.11: SEM micrographs of PEMA/THFMA copolymer at low magnification (top) and high magnification (bottom).
Scale bars: solid = 100 μ m; dashed = 10 μ m

On the freeze-fractured cross-sectional surfaces (figure 5.12), nanofilaments were detected in the cross-sections of the GNF and PR19PS

samples at 5 wt% and to more of an extent of the 15 wt% samples (labelled with arrowheads). The 5 wt% MWNT9 sample had a smooth texture after freeze-fracture and again, no nanotubes were observed as they were too small to be detected. Nanotube clumping may cause the cloudy appearance of the 15 wt% MWNT9 cross-section, which was not seen on the PEMA/THFMA cross-sectional surface.

The micron-scale surface roughnesses, acquired by profilometry, are illustrated in figure 5.13. The only significant differences observed were between 10 wt% PR19PS and 15 wt% PR19PS compared to the rest of the samples evaluated. The difference in roughness values was due to the increased porosity in the structure of the PR19PS composites as shown in the SEM micrographs of the samples (figure 5.10). Another point to be noted from the profilometry results is that the roughness of the PTFE mould was lower than the PEMA/THFMA pure co-polymer samples. The roughness of the composite samples are shown to be in between the roughness of the PTFE mould and the PEMA/THFMA polymer values (excluding the 10 wt% and 15 wt% PR19PS discussed previously). As the majority of samples had a smoother surface than the PEMA/THFMA pure copolymer, the addition of nanofilaments appears to reduce the roughness of the resultant composite (apart from PR19PS above 5 wt% as explained previously).

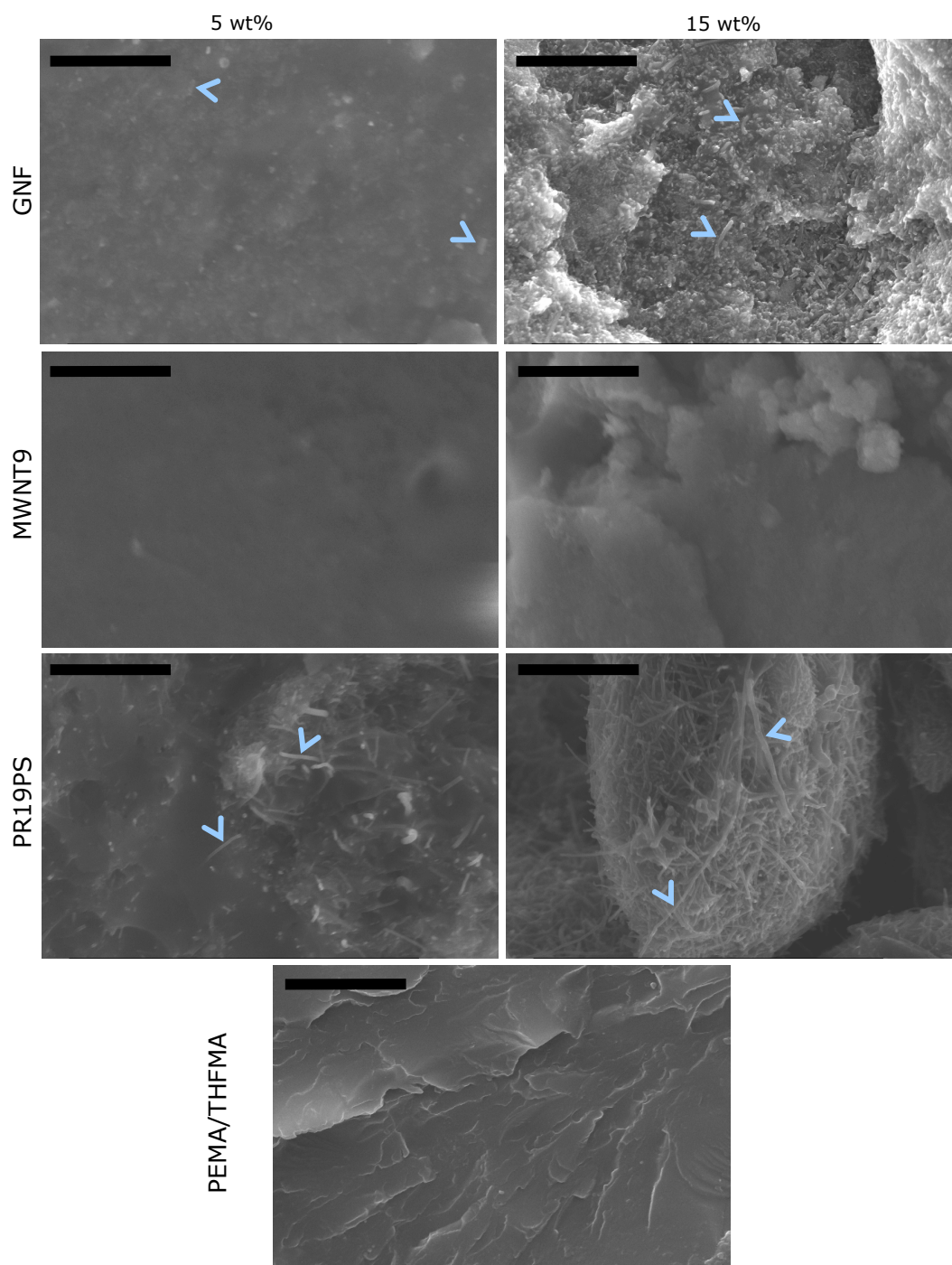


Figure 5.12: SEM micrographs of freeze-fractured composites (GNF, MWNT9, PR19PS) at 5 and 15 wt%, and pure PEMA/THFMA copolymer. Hollow arrowheads identify examples of nanofilaments located in the cross-section of the composites. Scale bar = 10 μ m

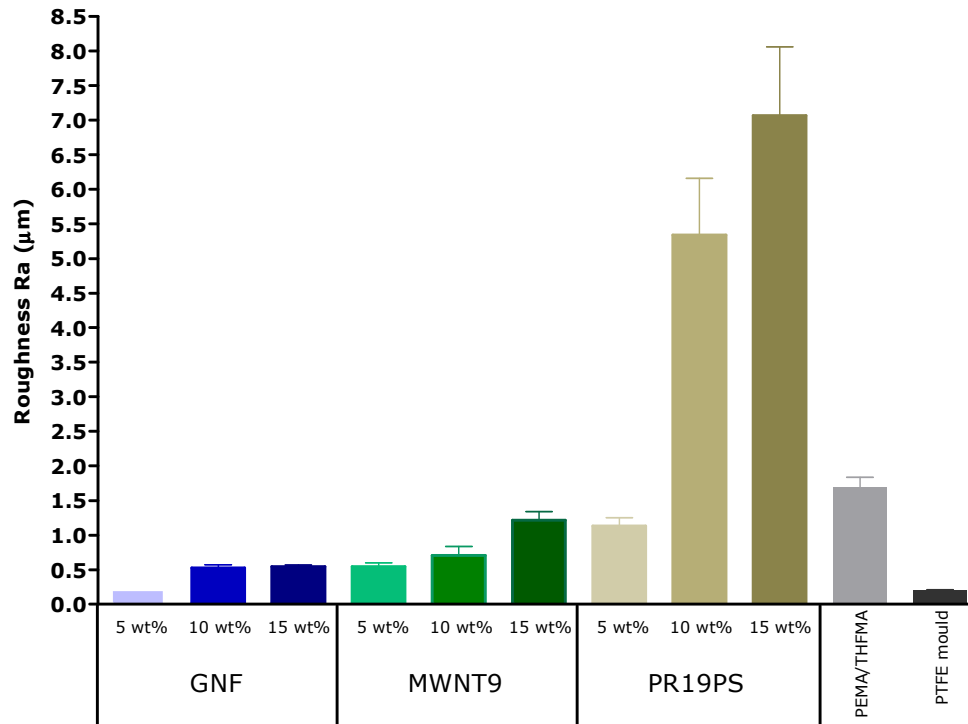
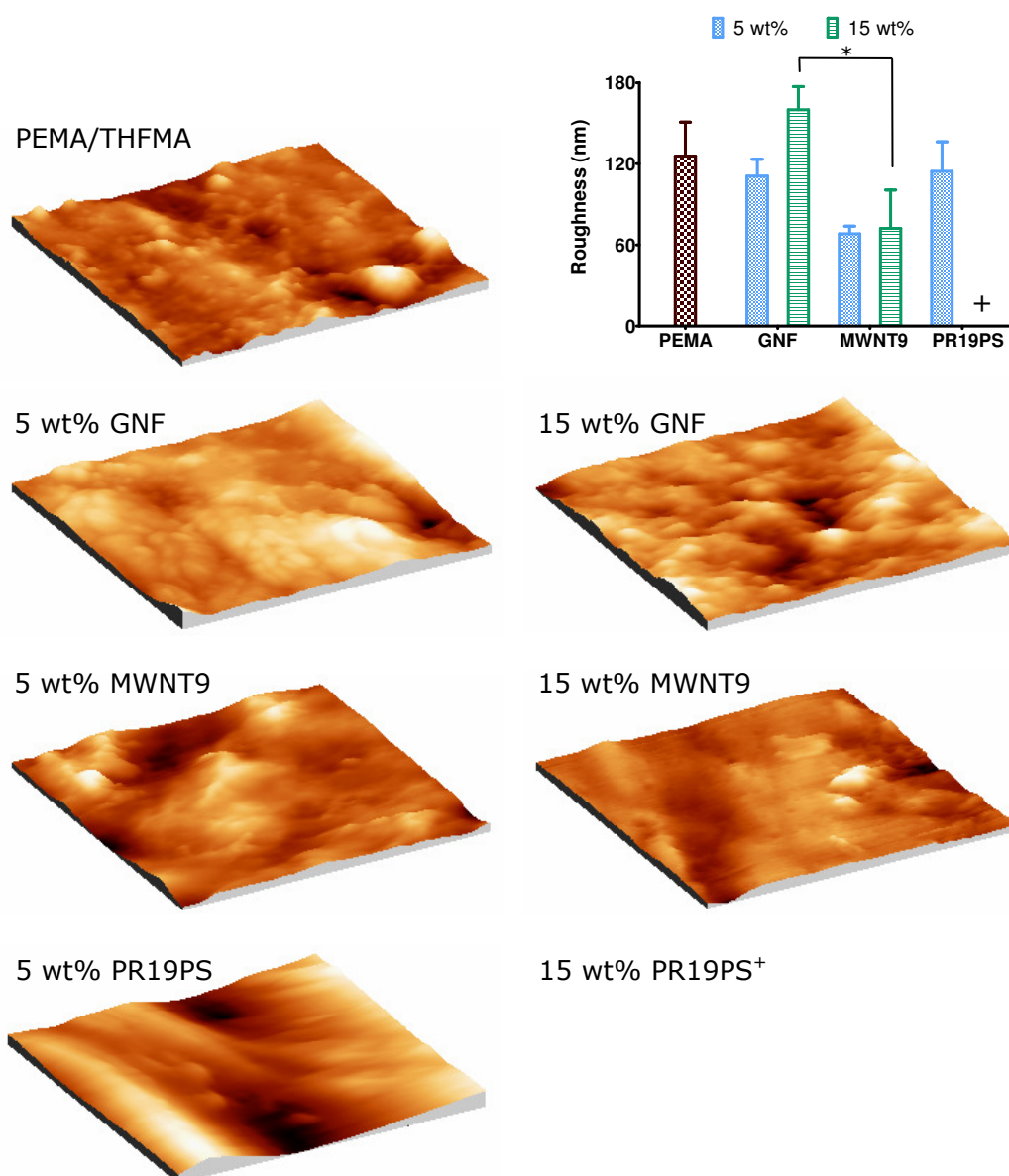


Figure 5.13: Roughness (R_a) analysis on carbon- PEMA/THFMA composites. There were significant differences between 10 wt% and 15 wt% PR19PS compared to all other composites ($P < 0.05$). R_a values are mean \pm sem ($n=4$)

AFM was also employed to characterise the topography of the composite surfaces (figure 5.14). All surfaces were scanned except 15 wt% PR19PS which was too rough to gain accurate data, even in non-contact mode. The data acquired from the other samples provided details of topography and roughness values in the nano-scale. The notable difference in roughness was in the MWNT9 composite samples. The average roughness of the MWNT9 samples was just over half the average roughness of pure PEMA/THFMA surface. This would suggest that the addition of MWNT9 nanotubes decreases the surface roughness of carbon composites at the nano and micron scale. There were features observed on the surface topographies of all samples.



**Figure 5.14: Topographies of PEMA/THFMA polymer and carbon nanofilemant composite surfaces using AFM. 10 μm^2 areas were scanned and nano-scale roughness calculated and displayed in bar graph above. R_a values are mean \pm sem.
⁺15 wt% PR19PS was too rough to acquire accurate data
^{*}Significantly different ($P < 0.05$)**

Figure 5.15 is another representation of the results presented in figure 5.13 and figure 5.14. In all of the roughness measurements at the micron-scale and nano-scale, the roughness decreased on addition of carbon nanofilaments after 5 wt% and then increased with further addition. This was the most notable in PR19PS sample, where the roughness increased as the composite became porous after 10 wt% of PR19PS.

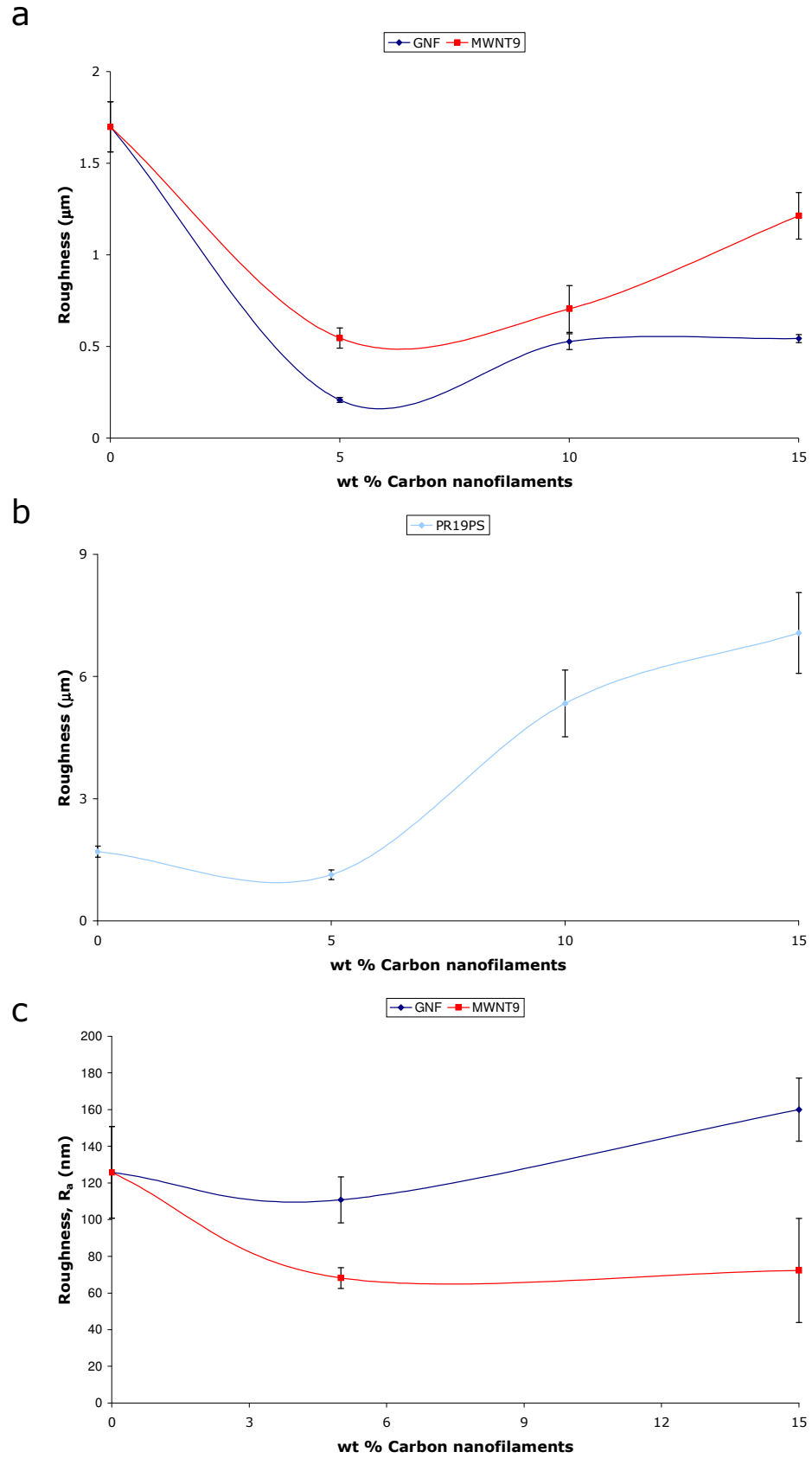


Figure 5.15: Trends in surface roughness with respect to nanofilament incorporation into PEMA/THFMA composites. Roughness analysed from profilometry at the micron scale (a & b) and AFM at the nanoscale(c). Values are mean \pm sem.

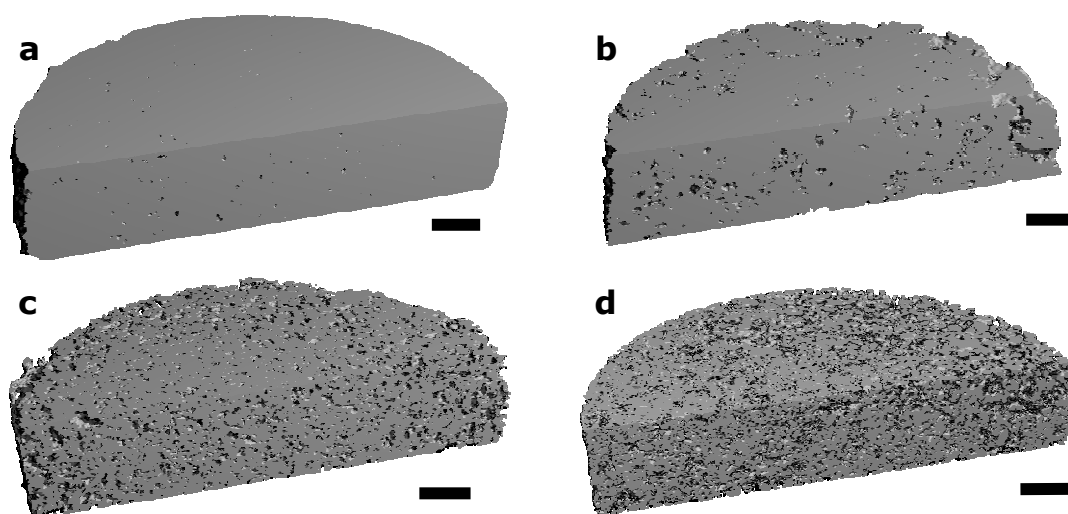


Figure 5.16: Micro-CT of PR19PS-PEMA/THFMA composites; a) 5 wt%; b) 10 wt%; c) 15 wt%; and d) 20 wt%

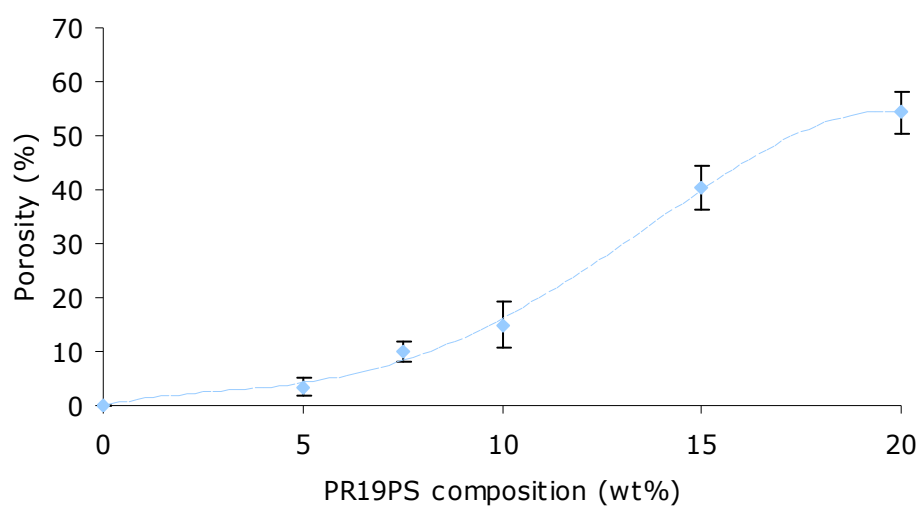


Figure 5.17: Overall porosity of PR19PS-PEMA/THFMA composites. Values are mean \pm sem.

Micro computerised tomography (μ -CT) was used to analyse the porosity of the PR19PS samples. Figure 5.16 shows the cross-sections of the porous structures. The pores within the composites are irregular and of varying sizes. These results compliment the SEM and profilometry data

presented previously. The greater amount of PR19PS filler within the polymer matrix, the greater the porosity of the samples (figure 5.17). The size and position of the pores in the sample with highest porosity (20 wt% PR19PS) was very irregular with limited connectivity.

5.3.5. Osteoblast attachment results

Osteoblasts were seeded onto PEMA/THFMA and carbon nanofilament-PEMA/THFMA composites at a density of $32,000 \text{ cells.cm}^{-2}$. The numbers of cells counted on the surfaces are illustrated in figure 5.18. The number of cells that attached to the PEMA/THFMA sample was not significantly different from any of the composite samples. It was neither better nor worse with respect to the degree of cell attachment than the composite samples. The amount of cells that attached to the composite surfaces was different in comparison to the PEMA/THFMA co-polymer after 90 minutes of culture. There looks to be a decrease in cell number on 5 wt% GNF and 5 wt% PR19PS samples, when compared to the pure copolymer cell count. On both GNF and PR19PS samples, there was an increase in cell number on 15 wt% GNF and 15 wt% PR19PS composites compared to 5 wt% GNF and 5 wt% PR19PS respectively. This was not seen on the MWNT9 composite samples. There was no significant difference between the two MWNT9 samples (5 wt% and 15 wt%).

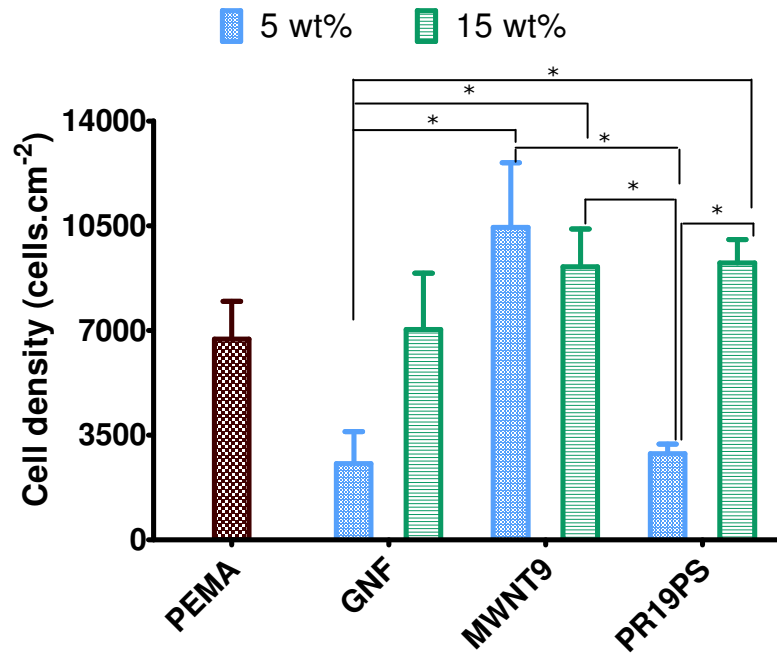


Figure 5.18: Osteoblast attachment to carbon nanofilament-PEMA/THFMA composites (Mean \pm sem; n=6). *Significant difference ($P<0.05$)

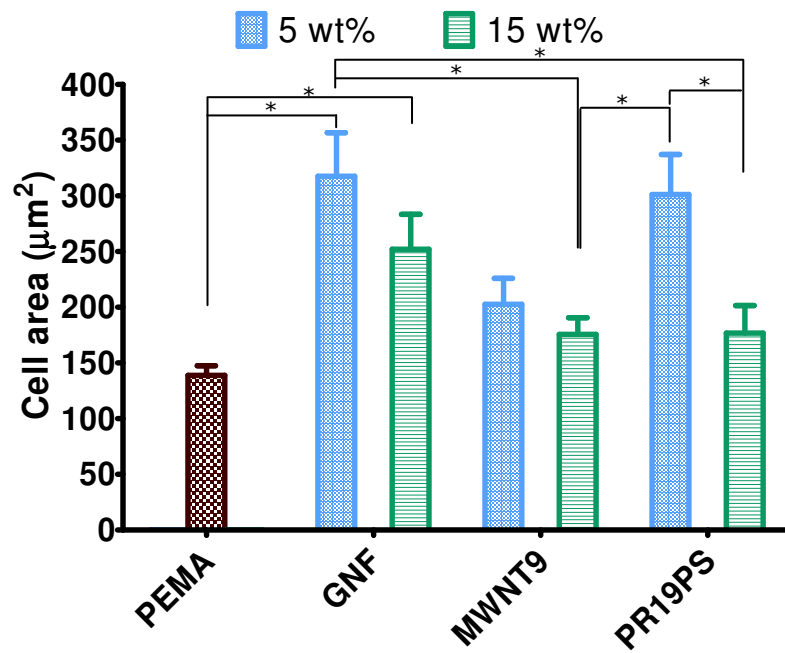


Figure 5.19: Osteoblast areas on carbon nanofilament- PEMA/THFMA composites after 90 minutes of culture, measured from SEM micrographs (Mean \pm SEM; n=10). *Significant difference ($P<0.05$)

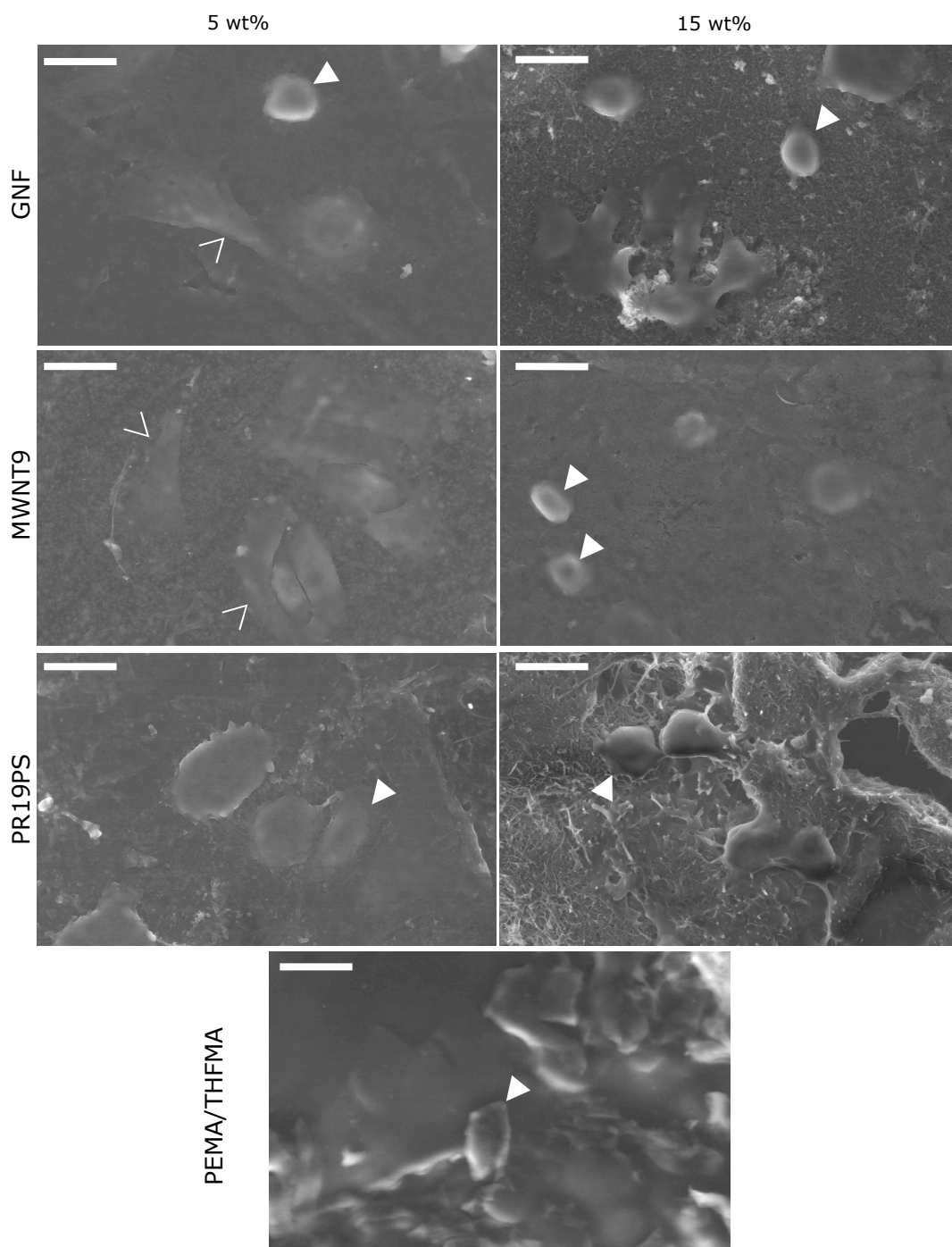


Figure 5.20: General morphology of osteoblasts cultured for 90 minutes on 5 wt% and 15 wt% composites (GNF, MWNT9 and PR19PS) and pure PEMA/THFMA viewed in wet mode on an ESEM (at 1.5-4 Torr). Solid arrowheads highlight examples of rounded attached cells and hollow arrowheads highlight examples of spread cells. Scale bars = 50 μ m

The trends for osteoblast spreading quantified by cell area (figure 5.19) from micrographs of the cells cultured on the polymer and composite samples after 90 minutes (examples of cell micrographs are shown in figure

5.20) were different to those observed in the amount of cells that attached to the same samples (figure 5.18). Osteoblasts on the PEMA/THFMA surfaces were rounded and had the lowest cell area of all the samples. Cells had spread more on the composite surfaces compared to the PEMA/THFMA surfaces. The cell area decreased with increasing amount of carbon nanofilaments in the samples, in contrast to increasing cell numbers with increasing nanofilament composition. Cells generally appeared to have spread more on the 5 wt% surfaces compared to the 15 wt% samples. There were some signs of membrane blebbing on approximately 38 % of the cells cultured on the 5 wt% PR19PS sample (figure 5.21).

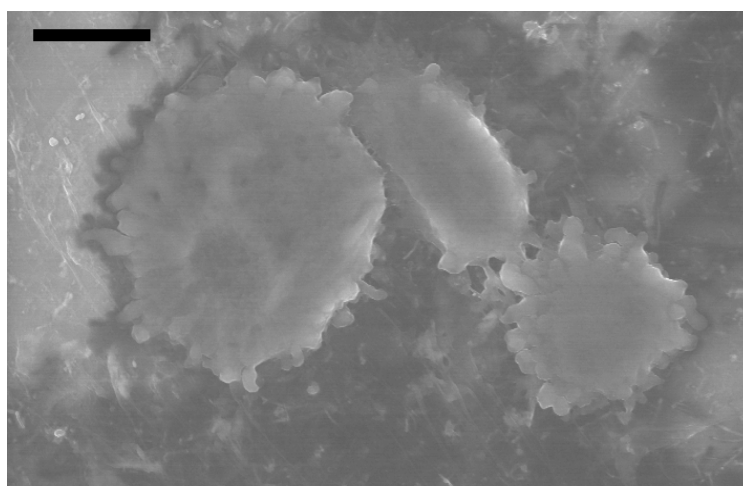


Figure 5.21: General example of membrane blebbing observed on 5 wt% PR19PS PEMA/THFMA composites, viewed in wet mode on an ESEM at 1.5 Torr. Scale bar = 10 μ m

5.3.6. Osteoblast proliferation and differentiation results

Results acquired from alamar blue, DNA and alkaline phosphatase activity assays are presented in figure 5.22, figure 5.23 and figure 5.24 respectively. Metabolic activity (figure 5.22) and levels of DNA (figure 5.23) suggest some signs of cell proliferation on 15 wt% PR19PS, but predominantly on 5 wt% MWNT9. Other samples show cell activity during the 14 days of the experiment but do not appear to show increased cell activity or proliferation,

especially from day 7 to day 14. Similarly, ALP activity (figure 5.24) was only shown in osteoblasts on the 5 wt% MWNT9 sample over 14 days and not to the same extent as tissue culture polystyrene, but significantly more than the other polymeric samples. There were signs of alkaline phosphatase activity per cell (per μg DNA) on the samples over 14 days but increases in ALP were only shown on 5 wt% MWNT9 composite and TCPS.

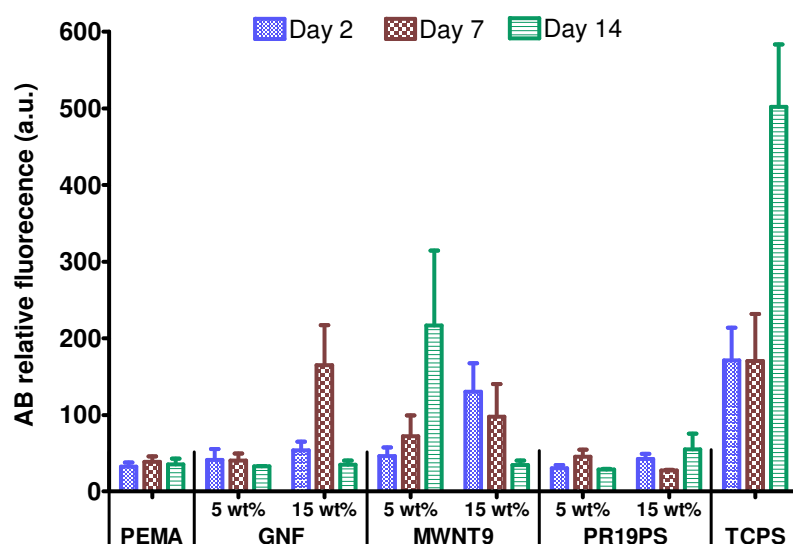


Figure 5.22: Relative fluorescence of alamar blue indicating metabolic activity of osteoblasts grown on PEMA/THFMA polymer, GNF, MWNT9 and PR19PS composites (5 wt & 15 wt%), and tissue culture plastic (TCPS) after 2, 7 and 14 days (Mean \pm sem; n=8)

The ESEM micrographs taken after 14 days of culture are shown in figure 5.25. The 5 wt% MWNT9 composite sample was the only sample that had a confluent layer of cells on after 7 days and looked to have multi-layers of cells after 14 days (figure 5.26). Cells cultured on the other samples were not confluent over their surfaces and cells were often found in small inconsistently-sized colonies around the samples.

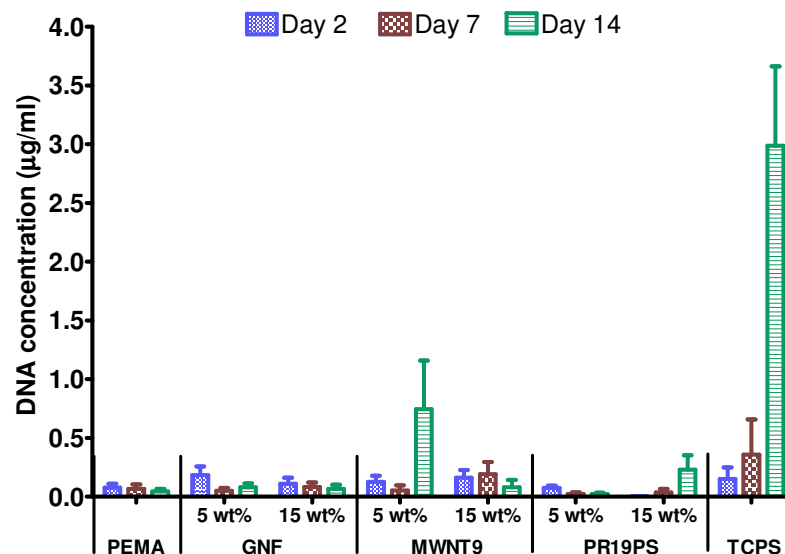


Figure 5.23: DNA concentration of osteoblasts on PEMA/THFMA polymer, nanofilament composites (5 & 15 wt% GNF, MWNT9 and PR19PS) and tissue culture plastic (TCPS) after 2, 7 and 14 days (Mean \pm sem; n=8)

The morphology of cells on the different samples was different. Osteoblasts spread over the 5 wt% GNF and PR19PS surfaces, especially, had cell debris over much of the surfaces. Cells on 15 wt% GNF surface were fairly well spread and were visible over much of the substrate but were not confluent. Many of the cells extended across the composite surface to other cells. There was not much sign of cells on 15 wt% MWNT9, 5 wt% PR19PS and PEMA/THFMA surfaces. Osteoblasts on the 15 wt% MWNT9 surface were not spread to much of an extent and there were some signs of cells spreading on the 5 wt% PR19PS but the cells looked to have collapsed. This may have been due to the processing treatments before ESEM analysis.

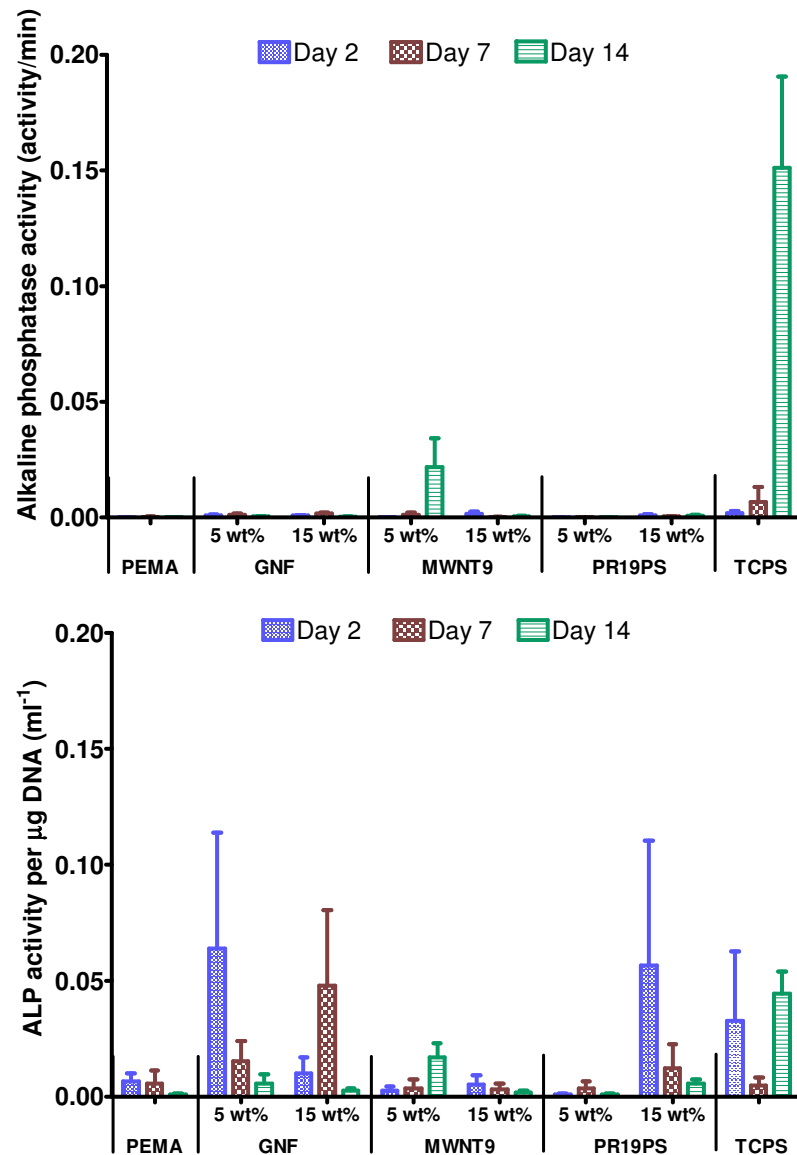


Figure 5.24: Activity of alkaline phosphatase (top) and ALP per µg DNA (bottom) produced by osteoblasts on PEMA/THFMA polymer, nanofilament composites (5 & 15 wt% GNf, MWNT9 and PR19PS) and tissue culture plastic (TCPS) after 2, 7 and 14 days (Mean ± sem; n=8)

Osteoblasts were found on the 15 wt% PR19PS composite sample. The cells were rounded in morphology and were only found in certain areas of the sample. As the composite sample was porous, some cells may have migrated to the bottom of pores and thus could not be viewed by ESEM. There was some sign of spreading across polymer constituent (indicated from arrowhead

in figure 5.25). Clusters of rounded cells were generally seen on the 15 wt% sample.

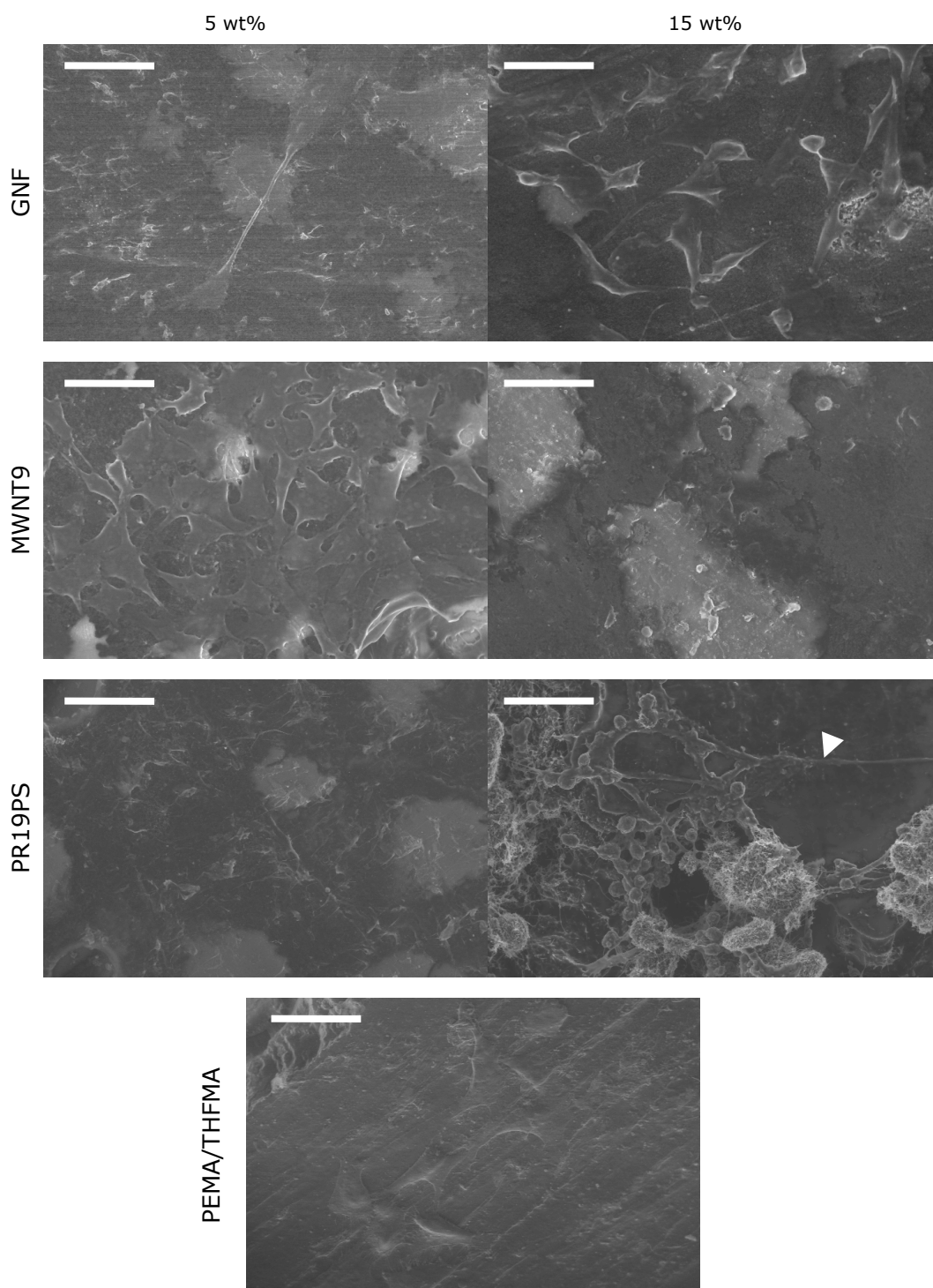


Figure 5.25: Environmental SEM of human osteoblasts cultured on PEMA/THFMA and composite samples after 14 days viewed in wet-mode at 1.5-4 Torr. Scale bar = 50 μ m. Arrow-head highlights spreading on 15 wt% PR19PS composite surface

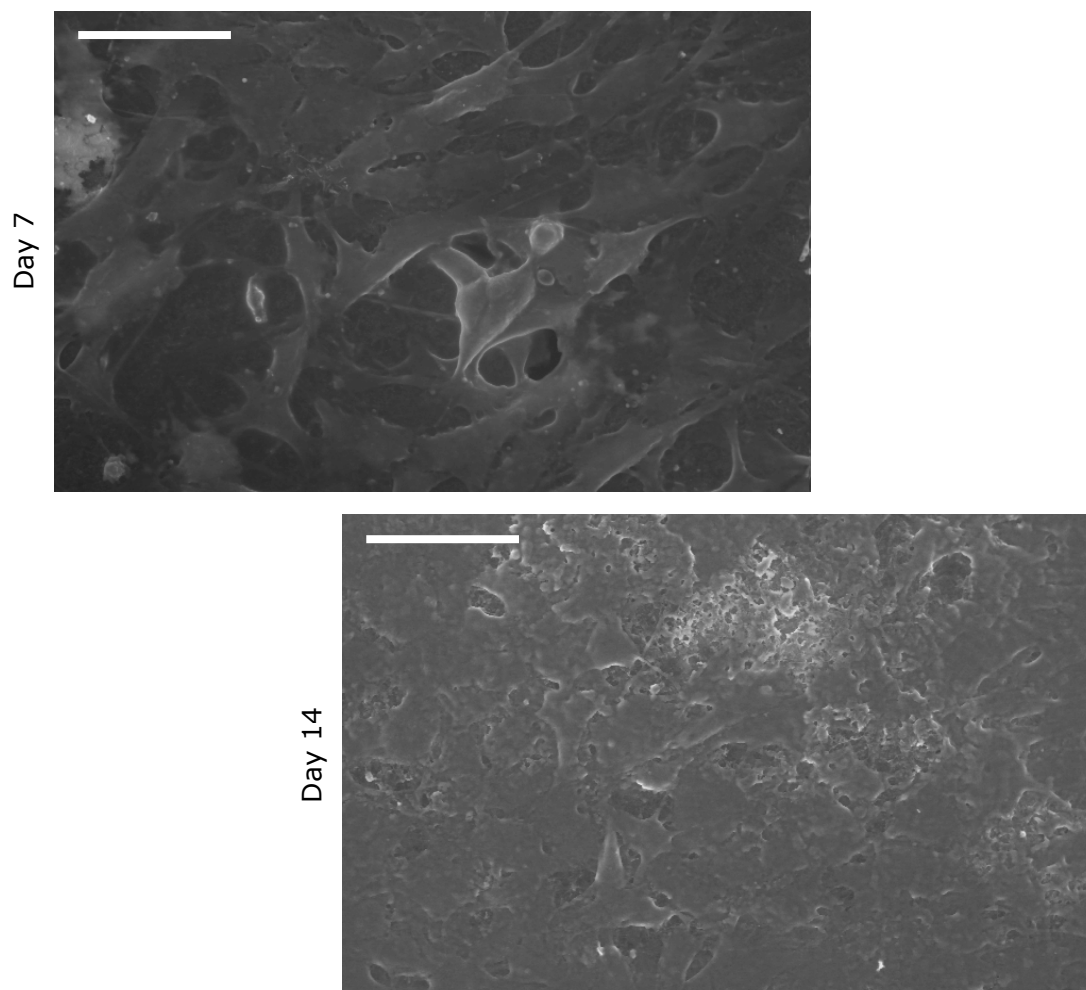


Figure 5.26: Cell morphology and extent of multi-layering of osteoblasts cultured on 5 wt% MWNT9 composite after 7 and 14 days of culture. Scale bar = 50 μm

5.4. Discussion

It was found that carbon nanofilaments were easily incorporated into PEMA/THFMA *in situ* during the polymerisation procedure by incorporating them into the polymer powder before mixing. The addition of BPO as an initiator and the application of heat were used to promote polymerisation. However, the incorporation of nanofilaments into this particular polymer system inhibited polymerisation compared to unfilled PEMA/THFMA. The cured composites took longer to polymerise and produced more flexible samples than the unfilled polymer. This may have been due to nanofilament hindrance

of the initiator. The hindrance of polymerisation may have been due to reaction of the initiator with the nanofilaments, which would have depended on their nanostructure. The large drop in the T_g of GNF composites (table 5.1), especially, could have been due to nanofibres being more reactive due to graphene plane edges at the surface of the nanofibres, which are more likely to react with the initiator or growing polymer chains. The nature of the graphene planes arranged in the MWNT9 and PR19PS samples could have reacted with the initiator or polymer chains but not to the same extent as the GNF sample because of the number of exposed graphene plane end groups. Alternatively, the nanofilaments may have caused extra nucleation sites for polymerisation and consequently produced shorter polymer chains and a drop in mechanical and thermal properties. There was some improvement in storage modulus after incorporation of approximately 10 wt% of nanofilament (figure 5.4). It is possible that this was due to the reinforcing properties of the nanofilaments overriding any inhibition of polymerisation.

The storage modulus of all samples dropped when increasing the measurement temperature from room temperature (24 °C) to body temperature (37 °C) as shown in figure 5.4. This was because the temperature was approaching the T_g of the samples, hence causing a drop in storage modulus. Lozano *et al.*⁸⁷ investigated commercial PR24AG, an as-grown nanotube sample with an amorphous carbon outer layer obtained from Applied Sciences,²⁰⁹ incorporated into high-density polyethylene. The group observed an increase in storage modulus, but a reduction in $\tan \delta$ with addition of PR24AG. It was believed that the vapour-grown nanofibers reinforced the HDPE matrix and the improvement in damping was due to restriction of the polymer molecules by the nanofilaments.²⁰⁹ It is possible in this current investigation that although there were no signs of reinforcement

of the nanofilaments, there was a reduction of damping in the composites, with increasing nanofilaments (figure 5.5). This reduction in damping ($\tan \delta$) will be due to restriction of the polymer chains by the VGNFs.²¹⁰ The largest drop in loss tangent was observed in the PR19PS composite sample. This was likely to be due to the longer filaments restricting polymer chain movement, compared to the shorter nanofibre (GNF) and small curly clumped nanotubes (MWNT9), which were less likely to hinder chain movement. There was still a decrease in loss tangent on the GNF and MWNT9 composites. The restriction of polymer chain movement could also indicate effective interfacial bonding between the nanofilament filler and polymer matrix.

The change in storage modulus on application of nanofilaments may be beneficial in tailoring a biocompatible composite to match that of bone. Guedes *et al.*²¹⁰ studied the storage moduli of bovine cancellous bone cut from sections of the femur. Their studies were performed at room temperature over a range of frequencies using a similar method to the DMA procedure explained earlier in this chapter. At 1 Hz (the frequency used in this investigation), the storage moduli of their samples ranged from approximately 150 - 1400 MPa. As the storage modulus (at room temperature) of the PEMA/THFMA tested here was 1591 MPa (± 157) and was reduced to a minimum of 410 MPa (± 37) with addition of 10 wt% GNF, any of these samples would have been in the range of the spongiosa studied by Guedes *et al.*²¹¹ This was only representational of the storage modulus of the samples compared to that of bone, indicating the response of these composites to oscillated loads. However, other mechanical properties have to also be considered, especially elastic modulus, flexural strength and fatigue life, as the applied forces to bone would sometimes be under prolonged stresses, high stresses and be subjected to hundreds of thousands of loading cycles.²¹²

The nanofilaments were well dispersed in the GNF composites (figure 5.8), but were observed to be clumping in the MWNT9 and PR19PS composites giving a cloudy appearance of MWNT9 and visible PR19PS nanofilament clumps in the SEM high magnification micrographs (figure 5.9 and figure 5.10 respectively). The form and dispersion of the nanofilaments in the polymer matrix would have affected their mechanical properties, especially the agglomerated MWNT9 and PR19PS nanofilaments. The storage modulus of the GNF composites improved the most between 10 wt% and 15 wt% compared to the other composites (figure 5.4). This may have been due to the dispersion of the GNFs in the bulk of the sample, but was more likely to be caused by the effect of increasing T_g . Both storage modulus and T_g of the GNF composite decreased from 0 to 10 wt% GNF and then increased after 10 wt% (figure 5.3 and figure 5.4). The lower T_g would have produced a lower storage modulus as the T_g was close to the temperature the composites were tested at. The storage modulus did not increase with any amount of MWNT9 or PR19PS incorporation into the composites. The composites, again followed the trends in T_g , apart from 15 wt% PR19PS, which lost mechanical properties due to the porous structure of the composite (as shown in figure 5.16). The PR19PS –PEMA/THFMA composite had the highest storage modulus at 5 wt%, compared to the other composites, but was lower than the other composites at 15 wt% (figure 5.4). If the porosity of the PR19PS composite was minimised, the storage modulus would be higher than the GNF and MWNT9 composites. The reduction in storage modulus in all the nanofilament composites would have been affected by different factors. The GNF composites would have only been affected by the interaction of the nanofilament filler with the initiator or growing polymer chains. The agglomeration of the MWNT9 and PR19PS nanofilaments as well as their

interaction with polymerisation would have also affected the structure and mechanical properties of the filled composite. The additional factor of the PR19PS composite porosity would have also affected the properties of the commercial nanofilament composite.

There are many techniques used to determine thermal transitions, especially in polymeric materials. Because DMA shows a dramatic decrease in storage modulus when the temperature is taken above the T_g , it is considered to be the most sensitive technique for measurement of the T_g . This means that detection of T_g in highly crystalline or crosslinked polymers can also be achieved.²¹² There was a difference in T_g measured by DMA (by $\tan \delta$ peak and storage modulus transition) and DSC as shown in table 5.1. It is believed that onset of glass transition temperature is at the initial decrease in the storage modulus slope as it is at this point that a materials' mechanical properties decrease and the material becomes easier to deform.^{212,213} The midpoint of the drop in storage modulus indicates the temperature when the polymer has maximum mobility and can also be characterised by a peak in loss modulus (not presented here). Glass transition temperatures gained from DSC results were generally lower than the other glass transition temperatures measured using DMA. Glass transition temperatures measured using DSC would have been dependent on the heating rate used and higher heating rates produced results with greater sensitivity in heat flow. Generally a higher heating rate would increase the measured T_g of the sample.²¹⁴ The rate of heating used in this investigation was 5 °C/min. A higher heating rate (such as 10 °C/min) may have produced a clearer T_g transition. DMA is considered to be the most sensitive technique because the dramatic decrease in storage modulus at the materials' T_g during heating.

The addition of carbon nanofilaments to PEMA/THFMA also caused a difference in composite topography. In all of the roughness measurements at the micron-scale and nano-scale, the roughness decreased on addition of carbon nanofilaments to the PEMA/THFMA polymer and then increased with further addition after 5 wt% (figure 5.15). This was the most notable in the PR19PS sample, where the roughness increased as the composite became porous after 10 wt% of PR19PS. The slight increase in roughness after 5 wt% on the GNF and MWNT9 composites at the micron and nano-scale (figure 5.15a & c), was likely to have been due to an increase in nanofilaments at the composite surface. The addition of any type of carbon nanofilaments did reduce the surface roughness of this polymer system. This phenomenon has not been well documented, but it is clear that nanofilaments were present at the surface of the composite due to change in topography. Due to the large difference between the roughness of the PTFE mould and the polymer and composite surfaces, it was likely that the polymer and composites shrunk during polymerisation. The polymer system has been reported to be a low shrinkage material,²¹⁵ but any degree of shrinkage will affect the surface of the curing composite. Long, stiff, PR19PS nanofilaments showed the smallest reduction in surface roughness (figure 5.13). This would have been because the filaments were more susceptible to protrusion out of the polymer surface, thus producing a surface of either exposed nanofilaments or protruded nanofilaments coated in polymer matrix. Shorter GNF nanofilaments were more likely to produce a smoother surface due to easier packing density, whereas the curly nature of the MWNT9 samples would encourage the nanotubes to loop in and out of the composite or produce a nanotube topography coated with polymer matrix. This idea of the nature of nanofilaments affecting composite topography is inferred by Colbert.¹⁵ Although there were surface effects on application of nanofilaments to the polymer matrix, it is unclear whether these effects are from exposed

nanofilaments at the surface or a change in the polymer surface, which would have had an affect on osteoblast response to the surfaces.

The addition of PR19PS nanofilaments into the PEMA/THFMA polymer was observed to produce a porous composite (figure 5.16). In tissue engineering in particular, a porous scaffold designed for chemical and architectural guidance of cells¹²³ can be used to encourage tissue ingrowth. The pores in the PR19PS –PEMA/THFMA structures were not interconnecting and exhibited irregular random pore sizes that would not be beneficial for a scaffold for use in tissue engineering. Therefore, an alternative processing route would be preferred to minimise porosity, such as melt mixing of methacrylate polymers.¹²³ Zeng *et al.*¹⁴² produced composite rods using other Pyrograf® III nanofilaments (PR21PS and PR24PS) incorporated into PMMA rods implementing rotating twin screw extrusion. The pressure involved in melt mixing and extrusion would avoid formation of pores and encourage dispersion of the filaments. Control of porosity in PEMA/THFMA copolymers has been performed using supercritical carbon dioxide foaming, which would be more favourable for producing porous nanofilament composites.¹⁰³ This would be performed after melt-mixing of pre-polymerised polymer and carbon nanofilaments to minimise interaction of the nanofilaments with the curing matrix.

The number of attached osteoblasts (figure 5.18) generally looked to have responded to rougher substrates (figure 5.15). This was true, particularly with GNF and PR19PS samples, where the rougher 15 wt% samples (in the micron and nano-scale) had a higher number of cells. However, the smoother 5 wt% MWNT9 composite did not follow the same trends as it had a high number of cells attached after 90 minutes indicating that the comparatively high cell attachment on the 5 wt% MWNT9 sample was

independent of surface roughness. The 5 wt% MWNT9 sample showed the highest cell attachment (figure 5.18) and showed significantly higher cell attachment compared to the other 5 wt% carbon composites (GNF and PR19PS). The degree of osteoblast spreading generally showed a different trend to the cell attachment data. As the composition of carbon nanofilaments in the composites increased, the area of osteoblasts on the surfaces decreased (figure 5.19). There was a correlation between the roughness (figure 5.13 and figure 5.14) of the samples and the degree of cell spreading (figure 5.19). Cells attached more to the rougher surfaces, which has been shown with human fibroblasts¹¹¹ and osteoblasts.¹⁰³ Although the number of cells attached to the surfaces increased with increasing roughness, the cells spread more on the surfaces that were smoother.

There was cell activity on the other samples throughout the 14 days, but the only convincing sign of proliferation was shown on the 5 wt% MWNT9 composite (figure 5.22 and figure 5.23). It may be that proliferation was hindered or slowed down on these samples because of the morphology of the cells observed after 90 minutes. Cells, especially on the 15 wt% GNF and pure polymer samples, were well spread after 14 days and may have gone on to proliferate if the experiment had progressed for a longer duration (figure 5.25). The lack of proliferation could have been due to the morphology of attached cells. Osteoblasts had proliferated on 5 wt% MWNT9 composite which exhibited a smoother surface. This has been observed by Linez-Bataillon *et al.*,^{142,143,216,217} who saw a greater proliferation of mouse osteoblasts on smooth Ti6Al4V surfaces compared to rougher unpolished surfaces of the same material. However, cells did not respond to the smoother 5 wt% GNF composite. One reason for the enhanced proliferation on the 5 wt% MWNT9 surface is that nanotubes may have contributed to a topography that encouraged cell growth. However, the cells did not respond in the same

way to the 15 wt% MWNT9 surface, which may have been because cells also responded to the smoother surface of the 5 wt% MWNT9 composite. Alkaline phosphatase was detected in the cells on the 5 wt% MWNT9 sample (figure 5.24). This was the only sample that showed conclusive signs of proliferation and cell multi-layering and the detection of alkaline phosphatase activity from cells on this sample indicated that cells were differentiating towards extracellular matrix maturation.

PEMA/THFMA has been shown to support maintained chondrocyte phenotype over 28 days,¹⁴⁵ and positive signs of osteoblast adhesion over 24 hours.^{140,218} It is thought that osteoblast adhesion on PEMA/THFMA after 90 minutes was largely due to the absorption of cell adhesion proteins, such as fibronectin, in an active formation.¹⁴⁰ Hutcheon *et al.* studied the attachment of osteoblasts after 24 hours to PEMA/THFMA and saw similar attachment of cells compared to tissue culture polystyrene (~90% DNA content, ~60% alamar blue fluorescence compared with tissue culture polystyrene).²¹⁸ In this investigation, DNA content of the cells on the PEMA/THFMA was approximately 50% of the value measured from cells on the TCPS control and did not proliferate over 14 days. Although the PEMA/THFMA copolymer system has shown positive potential in bone and cartilage applications mainly due to maintained chondrocyte phenotype over 28 days and osteoblast adhesion over 24 hours, the results here suggest that the polymer does not support osteoblast growth over 14 days.

There may have been a residual amount of unreacted THFMA monomer in the composite systems due to hindered polymerisation, which has been shown to be toxic to cells.¹⁴² Barry¹⁴² investigated the effect of THFMA leaching from foamed PEMA/THFMA polymer on 3T3 mouse fibroblast cells *in vitro*. The PEMA/THFMA was polymerised using the same method described in

this study but without BPO initiator and with additional treatment using supercritical carbon dioxide fluid foaming to produce a porous scaffold. Barry reported that 2 mM of THFMA monomer leached out of foamed PEMA/THFMA scaffolds into media after 72 hours. There may be more monomer in the composite samples used in this current investigation due to hindered polymerisation by the carbon nanofilaments. Using 3T3 fibroblasts, Barry determined the IC_{50} (concentration of a compound required to reduce a population of cells by 50 % *in vitro*) as 9.8 mM of THFMA monomer.²¹¹ It is possible in this current investigation that due to hindered polymerisation, there may have been increased concentrations of THFMA monomer than the 2 mM observed by Barry and possibly high enough to induce decreased cell viability. The concentrations of THFMA monomer in the samples were not investigated here and would need to be studied in order to determine its toxicity on the cultured human osteoblasts. The difference in polymerisation between the unrestricted PEMA/THFMA copolymer and the hindered polymerisation of the nanofilament-filled PEMA/THFMA composites was not a fair comparison as the effects of varying amounts of monomer in the samples would override the topographical effects of the polymer and composites on the cultured osteoblasts. It is possible that the cells responded to different degrees of monomer concentration rather than the topography of the polymer or composites. Conversely, osteoblasts responded more positively to the 5 wt% MWNT9 composite compared to the unfilled polymer, which may indicate a response to the agglomerated MWNT9 nanotubes at the composite surface.

As the nanofilaments hindered the polymerisation of the PEMA/THFMA, it is difficult to understand their reinforcing capabilities. However, the effect of nanofilament addition did reduce damping properties of the PEMA/THFMA (figure 5.5), perhaps indicating adhesion between the filler and matrix and there were some signs of reinforcement at higher loadings. The 5 wt%

MWNT9 composite, especially, showed signs of encouraging osteoblast attachment and growth (figure 5.18 and figure 5.23). The surface effects of nanofilament incorporation did indicate that nanofilaments altered the roughness of the composite surface and textured the surfaces at higher loadings (figure 5.15). For these reasons, it seems that the 5 wt% MWNT9 composite offers the most potential as a candidate for a bone repair device which requires osseointegration. It is inconclusive with these results to understand whether this was because of the topography of the MWNT9 nanotubes either individually or due to their agglomeration compared to the GNF and PR19PS composites, or alternatively due to the orientation of the graphene in the nanotubes affecting the degree of polymerisation and concentration of monomer in the composite system compared to the GNF and PR19PS composites. More work is needed to understand the response of the osteoblasts on these surfaces.

Nanofilament textured surfaces could be used in bone cements and scaffolds to encourage osseointegration and stability of the implant and healing tissue. It is critical that the mechanical properties are close to that of bone to reduce stress shielding from the bone tissue when it has healed sufficiently to bear load.²¹¹ As with the nanofilament-PEMA/THFMA composites used in this study, non-degradable load-supporting implants will struggle to either bear load (leading to failure of the implant) or transfer load to bone at the appropriate time to encourage healthy tissue regeneration (which will lead to osteoporosis and higher susceptibility to fracture).¹⁶ It is for these reasons that osseointegration is necessary for long term stability of the implant and regenerated bone tissue. The texture of the 5 wt% MWNT-PEMA/THFMA composite indicated potential for supporting osteoblast growth and differentiation on their surfaces, which may induce osseointegration *in vivo*,

but the mechanical properties are not sufficient enough to provide support during bone regeneration.

Another possible application of nanofilament-polymer composites in orthopaedic devices is in tissue engineering of synthetic bone grafts. Again, both mechanical compatibility of bone and the composite, as well as osseointegration is essential. The size and shape of carbon nanofilaments can simulate the texture of the collagen matrix in bone, but also provide reinforcing capabilities that collagen does not offer.¹⁴² The PEMA/THFMA polymer has been foamed using a supercritical carbon dioxide technique to produce porous scaffolds of controlled diameter, which has shown chondrocyte migration into the centre of one scaffold with interconnected average pore sizes of 358 μm .¹²¹ This could be investigated further with porous nanofilament-PEMA/THFMA composites used here, but due to the reduction in mechanical properties observed, an alternative incorporation of nanofilaments into a pre-polymerised matrix is necessary. Nanofilaments have been successfully incorporated into poly(carbonate),¹⁵⁰ UHMWPE¹²² and PMMA^{4,24,25} with observed reinforcement.

6. Electrical Stimulation of Human Osteoblasts Using Carbon Nanofilament Composites

6.1. Introduction

Electrical stimulation has been used to enhance²¹⁻²³ and accelerate¹⁴² bone tissue regeneration. As carbon nanofilaments are conductive to varying degrees, depending on the orientation of the graphene plane, they have been used to fill composites to provide conductivity across polymers. Carbon nanofilament-polymer composites could, therefore, potentially be implemented as devices that enhance tissue regeneration by electrical stimulation. The nanofilament-PEMA/THFMA composite, detailed in the previous chapter, could be developed into a scaffold to be used in tissue engineering as has been shown previously with unfilled PEMA/THFMA.¹⁴⁷ A tissue engineering scaffold must have a high porosity with an interconnected pore network for cell integration and transport of nutrients and metabolic waste.¹⁷ As demonstrated in chapter 5, nanofilaments affect the topography of PEMA/THFMA surfaces. Therefore, by incorporating nanofilaments into a microporous scaffold with nanoscale features will potentially enhance osseointegration.²¹⁹ If this material was also to show enhanced osteoblast growth by electrical stimulation, it would also provide further potential in instigating osseointegration around and into the material. This chapter details the effects of pulsed current through conductive nanofilament-PEMA/THFMA unfoamed composites in order to investigate the potential for enhanced osteoblast growth.

The effect of carbon nanofilaments on the electrical properties of polymer composites will depend on the graphene of the nanofilaments²¹⁵ and the dispersion and connectivity of nanofilaments in the polymer matrix.²¹⁹ The structure and dispersion of the different nanofilament samples has been

discussed previously in chapter 3 and 5 respectively. The GNF sample was well dispersed in the PEMA/THFMA matrix, but would have been less conductive in nature to the MWNT9 nanotubes as the conductivity of the nanofilaments run in the direction of the graphene planes (which were perpendicular and parallel to the filament axis in GNF and MWNT9 respectively).²¹⁵ The structure of PR19PS, however, was also different as it exhibited amorphous carbon on the exterior of the nanotubes, which is less conductive than ordered graphene. Both MWNT9 and PR19PS also showed inefficient dispersion in the PEMA/THFMA composites as the nanofilaments in these samples clustered together. This would also reduce the conductive properties of the composites due to limited connectivity between the nanofilaments.^{71,148} The literature tends to indicate that electrical resistivity of nanofilament-polymer matrices tends to drop at around 2 wt% of nanotubes^{124,220} and between 5 – 15 wt% of VGNF (such as Pyrograf® III).^{71,148} At these loadings the resistivity is in order of 10^{-1} – 10^{-2} $\Omega\cdot\text{m}$ in nanotube composites^{124,220} and 10^3 $\Omega\cdot\text{m}$ in VGNF composites.^{4,22,23,165,168,169}

Electrical stimulation of osteoblasts can be investigated using Faradic, capacitive or inductive stimulation and all three methods have been shown to promote enhanced cellular and tissue response *in vitro*^{24,166} and *in vivo*.¹⁶⁶ Faradic stimulation, which was used in this investigation, delivers a current directly via electrodes or via a conductive biomaterial to bone *in vivo* or osteoblasts *in vitro*. Faradic stimulation has been shown to promote new bone formation *in vivo* around a cathode inserted into a rabbit humerus after 14 days²⁴ and stimulation of osteogenesis during healing of osteotomy in the mandible of goats over 10 days (stimulated for first 3 days).⁴ Faradic stimulation was employed in this study as it has been shown to promote new bone formation and is useful to instigate understanding into the mechanisms of electrical stimulation of osteogenesis.

There is very limited documentation on the electrical stimulation of osteoblasts through nanofilament composites. Supronowicz *et al.*⁵⁰ investigated the effects of semi-capacitive stimulation of rat osteoblasts on carbon nanotube-poly(lactic acid) (CNT/PLA) composites. The group used a pulsed alternating current and passed it semi-capacitively using the PLA/CNT composites (20 wt% CNT) by immersing a stainless steel electrode into the culture media and using the sample as the positive electrode. Their results suggested that passing a small pulsed current of 10 μ A at 10 Hz for 6 hours daily produced a significantly greater proliferation after 2 days and a greater amount of differentiation after 21 days.

Therefore, the study outlined in this chapter aims to investigate the potential of carbon nanofilament-PEMA/THFMA composites to stimulate osteoblasts by Faradic stimulation *in vitro*, especially with respect to the potential improvement of osteoblast response to nanofilament-PEMA/THFMA composites. The electrical resistivity of the composite samples was characterised with varied nanofilament structure and composition and an apparatus was specifically designed, tested and used to study the osteoblast response to electrically stimulated carbon nanofilament -PEMA/THFMA composites. The study used one composite sample, 5 wt% MWNT - PEMA/THFMA, to test the rig after construction and explore the use of these composites in stimulating osteogenesis. The 5 wt% MWNT sample was selected as it produced the best cytocompatibility results (presented in chapter 5).

6.2.Methods

6.2.1. Composite preparation

Composites were prepared as detailed in section 5.2.2. Samples were prepared differently for resistivity tests and electrical stimulation. With both preparation procedures, the polymer was cured at 70 °C for approximately 5-10 minutes enclosed within the mould to produce part-cured composite discs (diameter of 12 mm and thickness of 3 mm). Before the composites were fully cured and viscous enough to implant, gold-plated terminal pins (Surtech distribution, Andover, UK) were inserted into the discs. Four pins were inserted into the samples undergoing resistivity measurements and two pins inserted for evaluation of osteoblast response to electrical pulses through the conductive composites. The location of the pins in the composite samples are illustrated in figure 6.1.

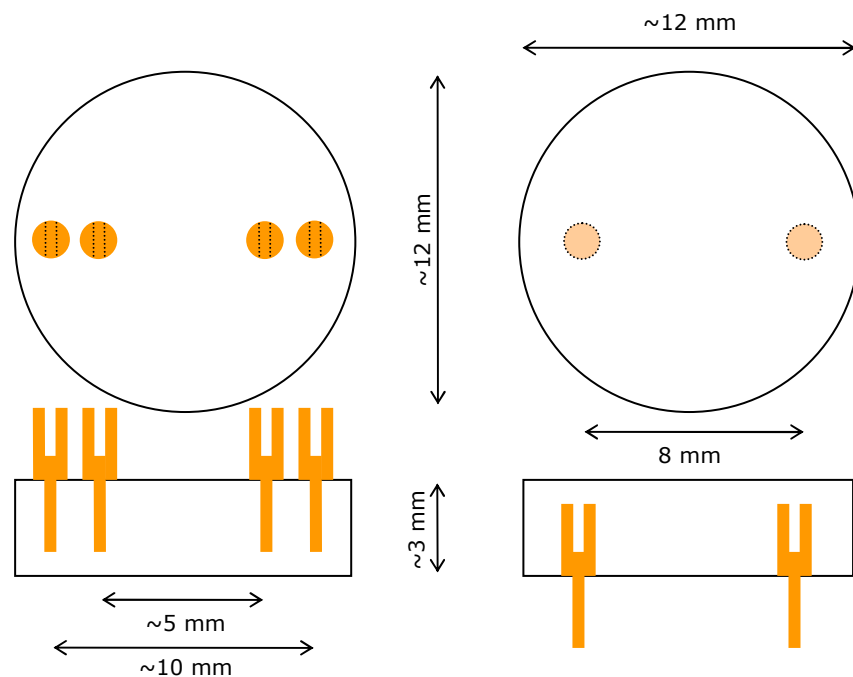


Figure 6.1: Location of the inserted terminal pins into samples used for four-point probe resistivity measurements (left) and electrical stimulation testing (right)

6.2.2. Four-point probe resistivity measurements

Resistivity measurements were performed using the four-point probe technique. This method uses an ohm-meter which was connected to the tested sample as in figure 6.2. A current is passed through the sample using the terminals labelled 'C' and 'C₁'. The potential difference of the composite can then be measured across the 'P' and 'P₁' terminals and resistivity calculated.

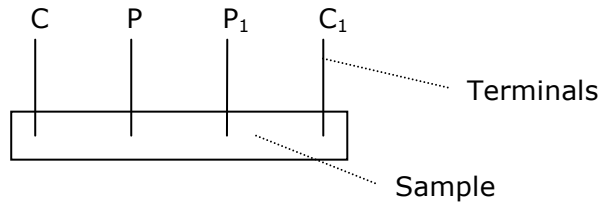


Figure 6.2: Schematic diagram illustrating the terminals used to pass a current (C and C₁) and measure the potential (P and P₁) through and across the composite sample

By knowing the current through the sample (I), between C and C₁, and the potential across the volume between the potential terminals, between P and P₁ (V), the resistance (R) can be calculated as in Equation 6.1:

$$R = \frac{V}{I}$$

Equation 6.1

The area (A) and length (l) of the sample between the two potential terminals was calculated using digital callipers. Thus, the resistivity (ρ) of the individual samples was calculated using Equation 6.2 (where l = length, and A = area):

$$\rho = \frac{R.A}{l}$$

Equation 6.2

6.2.3. Rig assembly for stimulation of osteoblasts

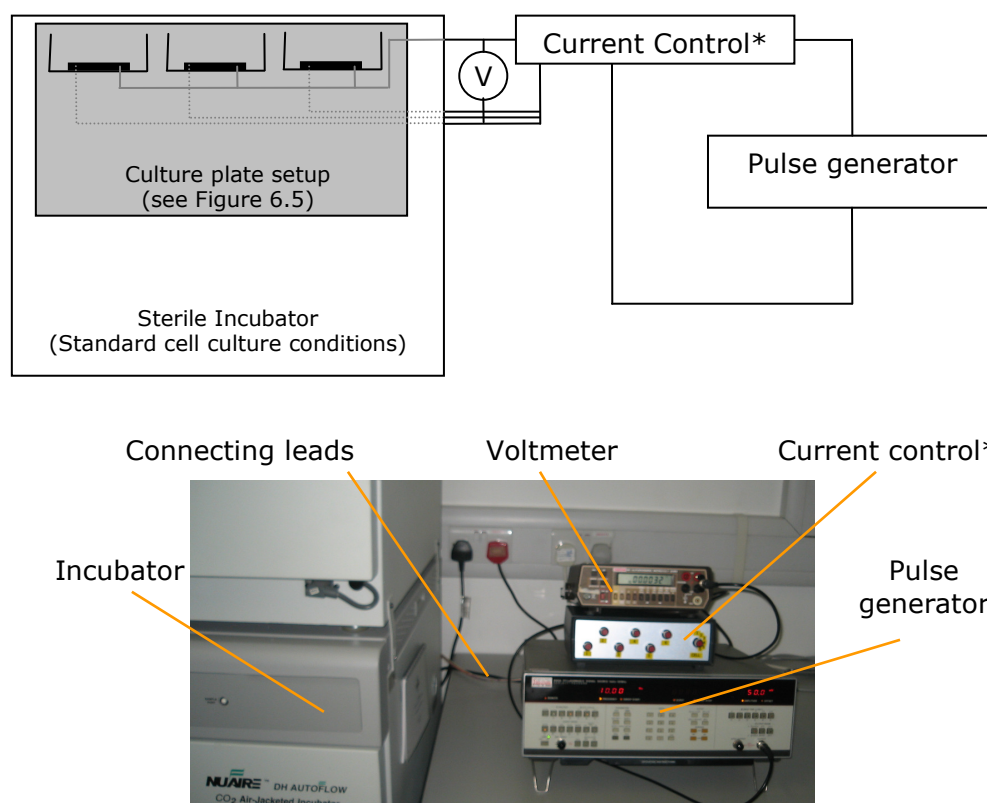


Figure 6.3: Circuit diagram and photograph of setup used to electrically stimulate human osteoblasts using carbon nanofilament-methacrylate composites. *See figure 6.4

The general assembly used to investigate the electrical stimulation of cells on carbon nanofilament-PEMA/THFMA composites was designed and assembled as illustrated in figure 6.3. A HP-Agilent 8165A pulse generator was used to generate a current with specific wave function and frequency. The current was set to control specific current passing through each sample. The current through a particular sample was monitored by measuring the

input and specific output current of a given sample using the voltmeter and be adjusted using the variable resistors in the 'Current Control' (figure 6.4).

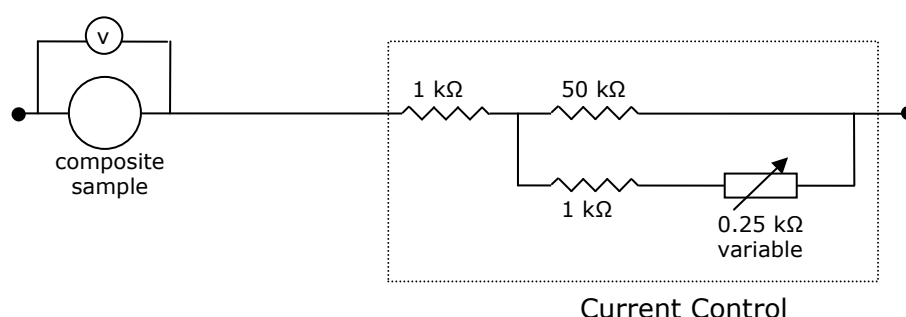


Figure 6.4: Electrical circuit of the 'Current Control' used to manipulate accurate flow of current through each sample.

A PC board was manufactured with tracks to deliver a current to a series of three samples and three individual outputs (figure 6.5). This means that samples could be used in triplicate when investigating electrical stimulation of the cells. For multiple sample-types, the system was duplicated so that 24 samples could be used. The PC board setup was designed so that a 24-well culture plate could simply be plugged in (figure 6.6). This also meant that it provided easy removal in order to replace culture media or exchange culture plates.

The apparatus is versatile and can be used for other conductive samples. The holes drilled in the culture plates for the connector pins need to be sealed. With these samples, the composites were finally cured in the culture plates, thus forming a seal around the electrodes.

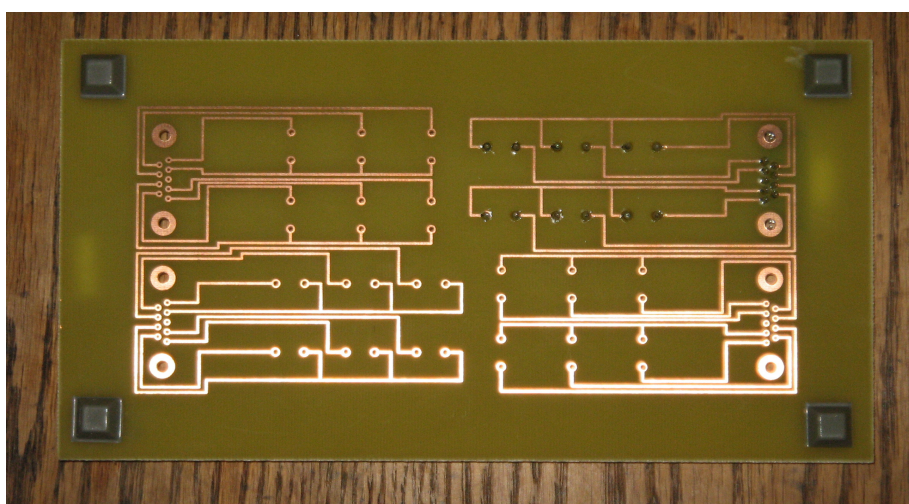
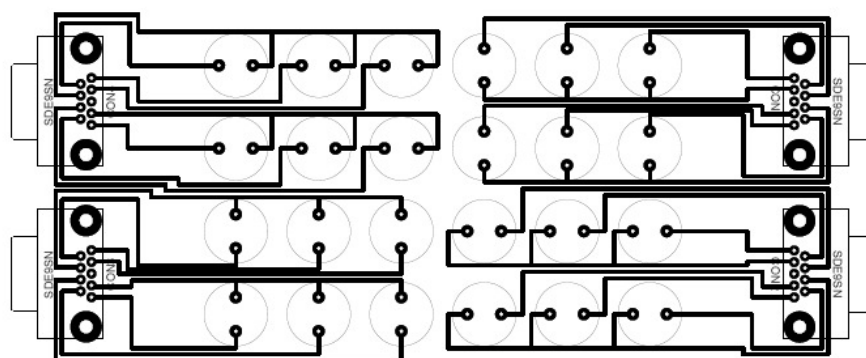


Figure 6.5: Circuit diagram and photograph of the underside of the PC board used to deliver current to the conductive samples. N.B. The circuit diagram is the inverse of the tracks produced as the track are on the underside of the PC board



Figure 6.6: Photograph of a 24-well plate plugged into the top of the PC board manufactured to deliver current to conductive composite samples

6.2.4. Electrical stimulation of osteoblasts

The novelty of the setup designed and assembled here has the versatility of the pluggable culture plate into the PC board. It enables the ability to monitor and adjust the current of multiple cells.

Human osteoblasts, isolated from femoral head trabecular bone, were used in this study and seeded onto the samples in triplicate at a cell density of 32,000 cells.cm⁻². The cells were left for 24 hours before any kind of stimulation and alamar blue, DNA and alkaline phosphatase assays were used (as described in section 4.2.4) after 2, 7 and 14 days. An alternating current of 10 μ A was applied to each sample at a frequency of 10 Hz and a duty cycle of 50 % (i.e. the current was applied for 50 % in one direction, then 50 % in the opposite direction during one cycle) every day (except the initial 24 hours) before the assays were performed.

These conditions were applied to the samples for 6 hours daily for a 14 day period. In order to compare with the conditions set out in the previous chapter (chapter 5), the alamar blue and DNA assays were used to compare the activity and quantity of cells on the electrically stimulated samples compared to unstimulated controls. To study the effects of electrical current on human osteoblasts, the most conductive and cytocompatible sample was used, which was the 5 wt% MWNT9 -PEMA/THFMA composite.

6.2.5. Statistical analysis

Statistical analysis was performed using Graphpad Prism[®] 4 software. One-way analysis of variance (One-way ANOVA) with Tukey's post test was used as a multi comparison post test. Statistical significance was taken to be $P \leq 0.05$.

6.3.Results

6.3.1. Resistivity of carbon nanofilament-composites

Resistivity of the conductive composites was measured using the four-point probe technique. The resistivity of the composites with differing carbon compositions is shown below in figure 6.7 and figure 6.8.

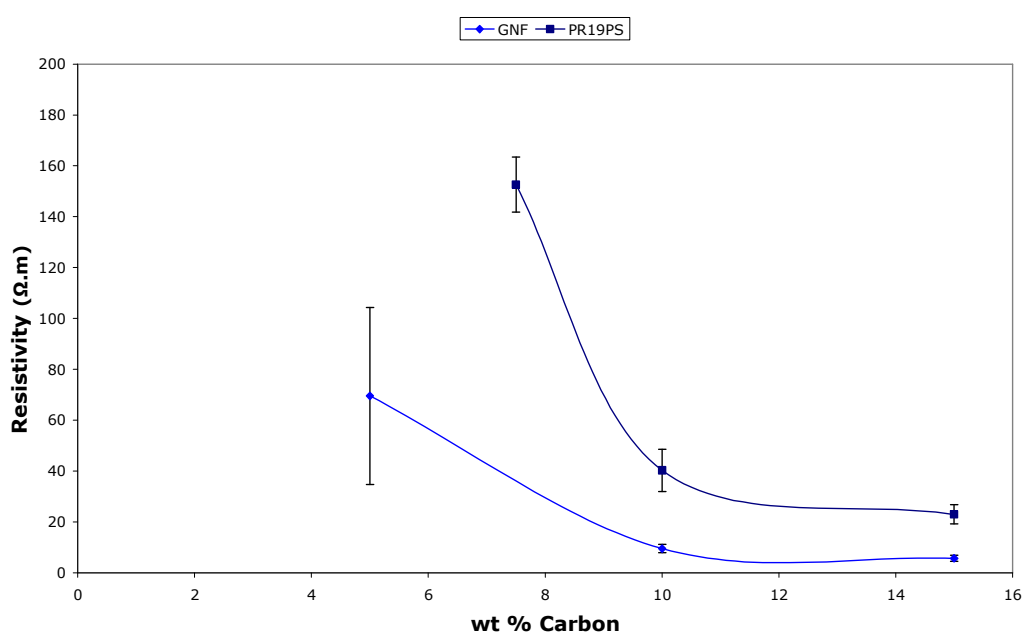


Figure 6.7: Graph illustrating the effects of carbon nanofilament (GNF and PR19PS) incorporation into PEMA/THFMA composites with respect to electrical resistivity (Mean \pm sem; n=4)

The GNF, MWNT9 and PR19PS composites were all tested to measure their resistivities with respect to the amount of carbon nanofibres or nanotubes. The measured resistivities plateaued above 10 wt% of carbon nanofilament incorporation. The resistivities are more consistent as illustrated in the standard error at and above 10 wt%.

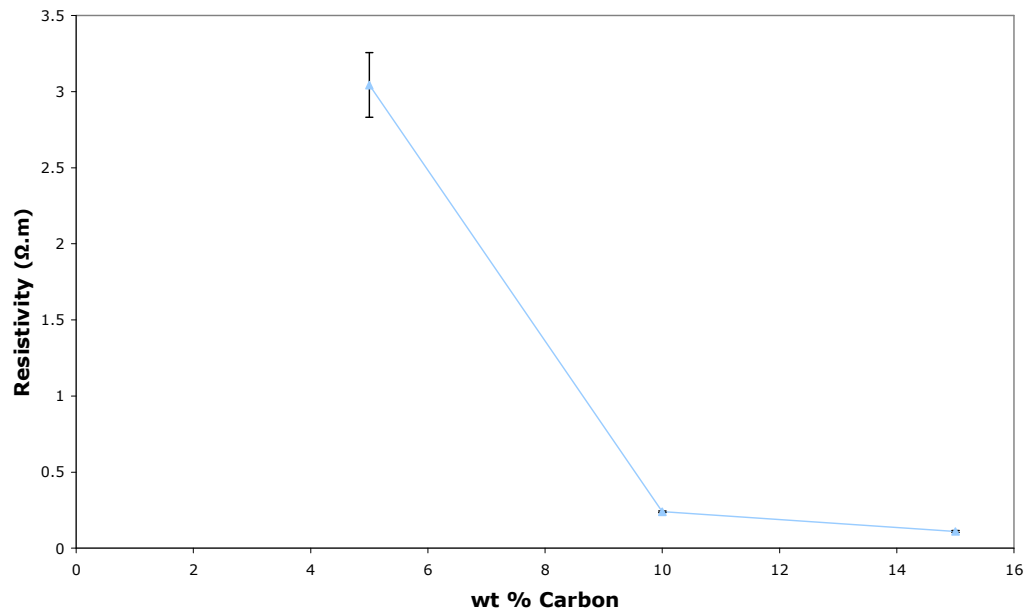


Figure 6.8: Graph illustrating the effects of MWNT9 incorporation into PEMA/THFMA composites with respect to electrical resistivity (Mean \pm sem; n=4)

6.3.2. Human osteoblast response to electrically stimulated composites

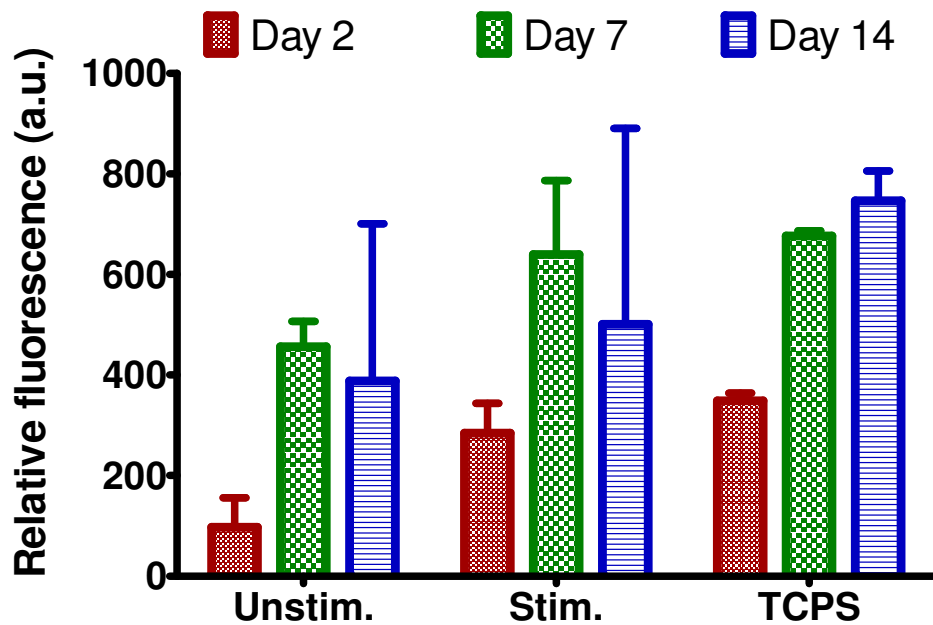


Figure 6.9: Relative fluorescence of alamar blue indicating metabolic activity of osteoblasts grown on 5 wt% MWNT9 alone (Unstim.), 5 wt% MWNT9 electrically stimulated by pulsed current (Stim.) and tissue culture plastic (TCPS) (Mean \pm sem; n=6).

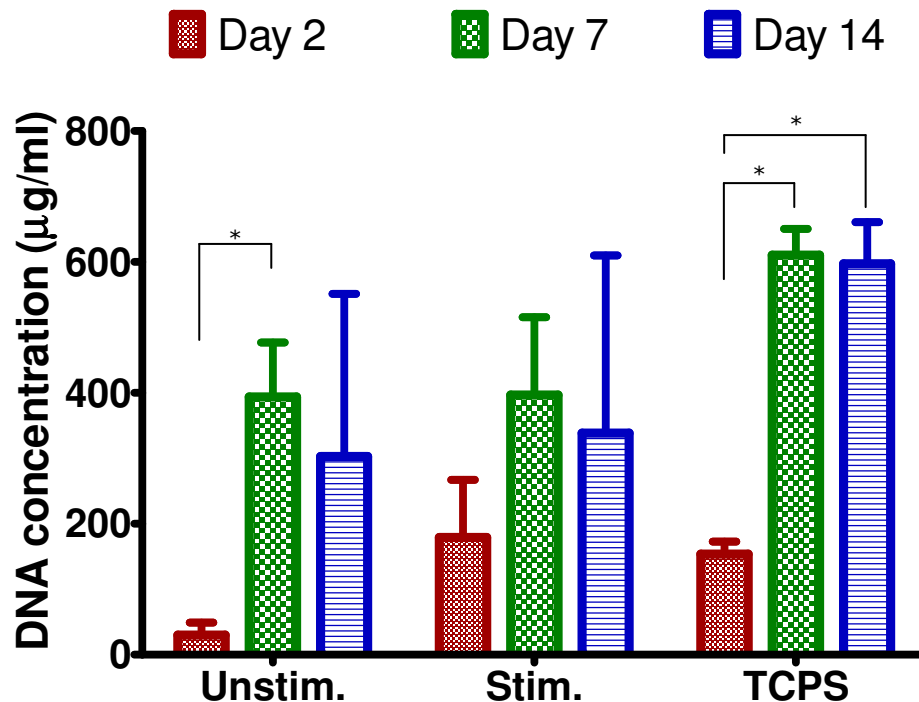


Figure 6.10: DNA concentrations quantifying the amount of osteoblasts on 5 wt% MWNT9 alone (Unstim.), 5 wt% MWNT9 electrically stimulated by pulsed current (Stim.) and tissue culture plastic (TCPS) (Mean \pm sem; n=6). * Significantly different ($P < 0.05$)

The activity and DNA concentrations of cell cultures on stimulated and unstimulated 5 wt% MWNT9 composites is illustrated in figure 6.9 and figure 6.10 respectively. Osteoblast activity and number was higher on the stimulated samples after 2 days and higher in activity after 7 days of culture compared to the unstimulated composite sample. Tissue culture plastic showed the most proliferation over all three samples in relation to cell activity and DNA concentrations of cells on the cultures. Both stimulated and unstimulated samples showed proliferation over 14 days of culture, but had large inconsistencies in activity and number as highlighted by the comparatively large error bars at day 14. The amount of alkaline phosphatase activity on the stimulated cultures was higher over 7 and 14 days, but when normalised per μg DNA (per cell) showed higher alkaline phosphatase activity on the unstimulated cells (figure 6.11).

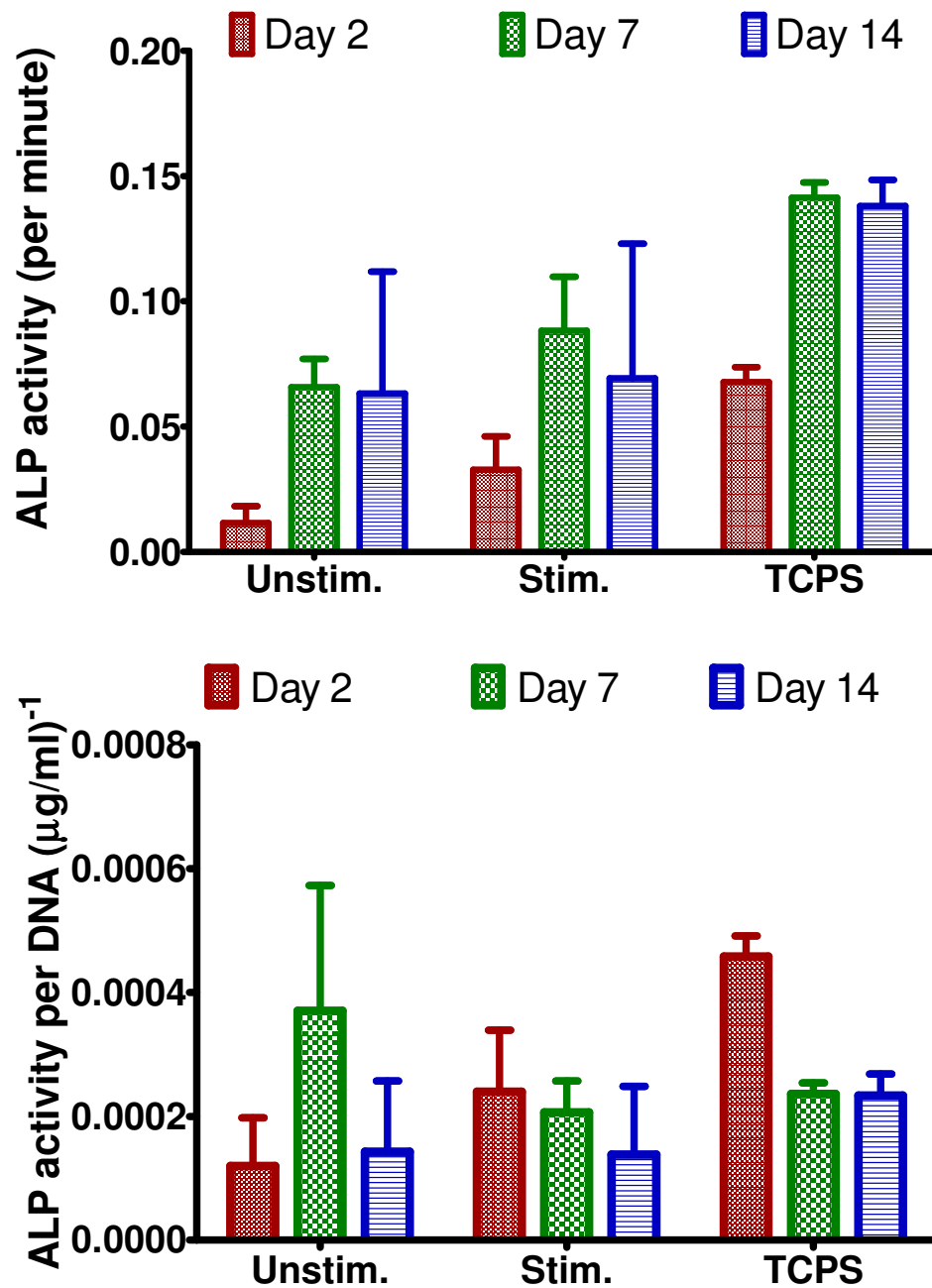


Figure 6.11: ALP activity (top) and ALP activity per μg DNA (bottom) from cells on 5 wt% MWNT9 alone (Unstim.), 5 wt% MWNT9 electrically stimulated by pulsed current (Stim.) and tissue culture polystyrene (TCPS) (Mean \pm sem; $n=6$). * Significantly different ($P < 0.05$)

6.4. Discussion

Three types of nanofilaments were assessed in this part of the study for their electrical resistivity (figure 6.7 and figure 6.8). All three nanofilament composite samples indicated decreased resistivity with increasing amounts of

carbon nanofilaments and all looked to be approaching their optimum conductivity slightly above 10 wt%. The MWNT9 sample proved to have the greatest conductivity compared to the other nanofilament samples because the graphene planes were orientated along the fibre axis, hence exhibiting greater conductivity than the GNF sample, which were composed of graphene planes perpendicular to the fibre axis.²²¹ The PR19PS sample showed the least conductivity in comparison to the other samples. This was likely to have been due to the amorphous carbon layer on the exterior of the PR19PS nanotubes,^{71,148} which would hinder the flow of current through the nanofilaments. The MWNT9 nanotube composites did not reach minimal resistivity until approximately 10 wt% (figure 6.8). This is much higher than the 2 wt% percolation point reported in the literature,^{71,148} but the measured resistivity at percolation shown in the 10 wt% MWNT9 composite in this study ($10^{-2} \Omega \cdot \text{cm}$) was comparable with that for the 2 wt% MWNT composites reported.²¹⁵ This was most likely due to the dispersion of the nanotubes in the PEMA/THFMA matrix.

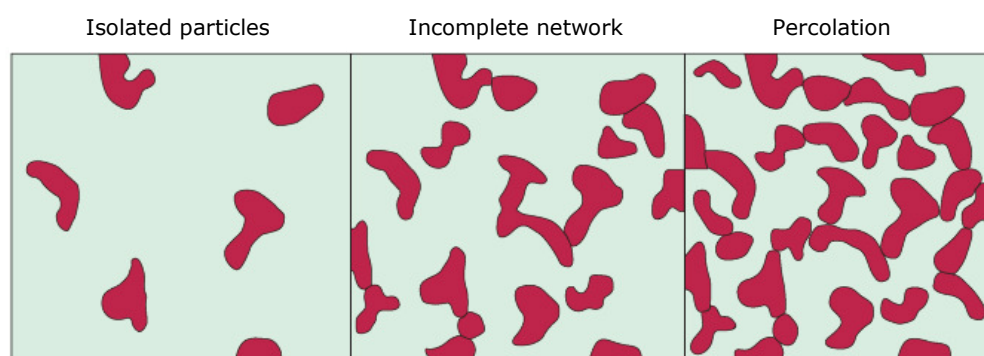


Figure 6.12: Illustration of connectivity of nanofilament clusters in a polymer matrix, which will affect electrical resistivity of the composite⁴

As the MWNT9 nanotubes formed clusters, their connectivity would have been hindered, but as an increased amount of nanotube clusters would provide higher connection between the nanotubes or nanotube clusters

forming composites with lower resistivity. Figure 6.12 illustrates how clustering of nanofilaments can increase connectivity between nanofilaments, which would, in turn, decrease electrical resistivity of the composite. The GNF composites were more uniformly dispersed in the matrix (figure 5.8), but the nanofibres were less conductive due to the orientation of the graphene planes being perpendicular to the fibre axis producing less conductive filaments. The amorphous carbon outer layer of the PR19PS nanofilaments would have hindered the flow of electrons in their composites as well as the clustering, reducing the connectivity of the filler.

The apparatus used here was designed, assembled and tested as part of the project. There are a number of electrical parameters that could be investigated in another investigation, such as pulse frequency, current amplitude, time of exposure, as well as versatility to test multiple triplicated samples simultaneously. The setup was used to assess 5 wt% MWNT9 – PEMA/THFMA. There was a small indication of higher proliferation on the electrically stimulated composite compared to the unstimulated composite, due to higher osteoblast activity (figure 6.9) and DNA concentrations (figure 6.10) after 2 days of osteoblast culture. Supronowicz *et al.*⁴ used an alternating current of 10 μ A, but by semi-capacitive means, to enhance the response of osteoblasts on CNT/PLA composites. The group observed a significant increase of proliferation of osteoblasts after 2 days of stimulation and a large increase of extracellular calcium from the cells after 21 days. These large differences were not observed in this investigation.

The flow of current through the composite was dependent on the conduction through the nanotube filler. Since the MWNT9 nanotubes were clustered and entangled together, the resultant current density would have been greater around the areas of concentrated nanotubes and smaller

through individual nanotubes. In addition to this, the current density would have decreased as the lateral distance away from the electrodes increased. This was because the resistance of the conduction pathways would have increased as the distance increased from one electrode to the other. According to Ohm's law, the current would have decreased as a result. The variability of the current throughout the surface of the composite would have therefore affected the electromagnetic field that the osteoblasts would have been exposed to. There would have been a significant decrease in the current at the surface and at the edges of the composite surface than the delivered 10 μ A between the electrodes through the entire composite sample.

Assuming that there was a current being delivered through the surface of the composite, the electromagnetic field would have exerted a force on the surrounding charges (i.e. cell membrane charges). A magnetic field would have been produced by electric current flow through the nanotubes within the composite. As MWNT9 nanotubes were used in this investigation, there would have been increased localised magnetic fields produced from the nano-sized coils created from the curly nanotubes. Since magnetic and electric fields are very closely related to each other, the changing magnetic field (due to the pulsed current) would also produce an electric field perpendicular to it. The combination of the forces exerted on charged cell membranes from magnetic and electric fields could potentially stimulate osteoblast growth if the electric current is large enough.

This means that cells ultimately did not experience the same kind of electric field that would have been induced using capacitive stimulation employed by Supronowicz *et al.*⁴ Although Supronowicz *et al.* used the same pulsatile frequency and delivered current of 10 μ A as in this investigation, the capacitive technique used by Supronowicz would have produced a uniform

electric field across the sample for each half cycle and then a uniform electric field in the opposite direction for the other half (depending on the direction of current flow). A similar pulsed nature was used here but the applied electric field for each half cycle was non-uniform due to the geometry of the electrode pins. This would have led to an electric field gradient and a lower electric field on the surface of the samples than the exposed field across the samples used by Supronowicz with the same applied 10 μ A of current as shown in figure 6.13. Since the position of the pins in this study were not located at the edge of the sample, the cells attached near the edge of the sample would have experienced little or no electric field compared to higher fields experienced by cells at the centre of the sample. The Supronowicz group saw a larger increase in cellular proliferation, upregulation of osteocalcin, osteonectin and collagen type I gene expression and extracellular deposition of calcium after 21 days.⁴ The electric field induced by the same 10 μ A current as Supronowicz *et al.*,¹⁰⁸ but induced Faradically, did not appear to be appropriate enough to stimulate osteoblast proliferation and differentiation to the same degree.

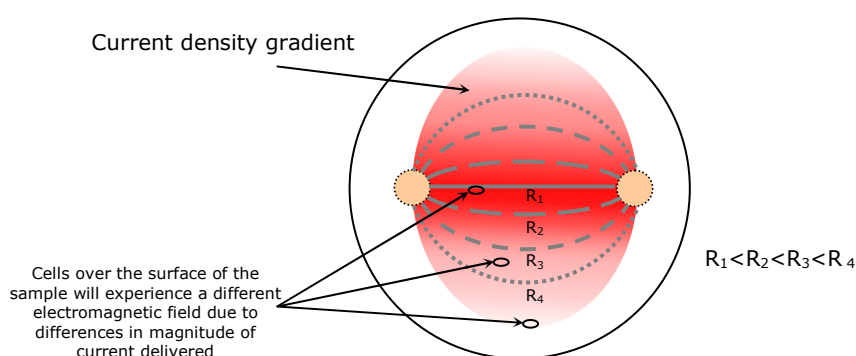


Figure 6.13: Figure illustrating the reduction of current (due to increased resistance) with distance from the electrodes. Current density will also decrease as a consequence (indicated by colour gradient away from the electrodes)

There were some signs of increased osteoblast response on the electrically stimulated nanotube -PEMA/THFMA composite in this investigation. This could have been due to the electric field experienced by the cells in the middle of the samples, but not by the cells on the edges of the samples. The maximum electric field experienced directly between the two pins was calculated to be $\sim 6.7 \text{ V.m}^{-1}$ (where the resistivity of the sample was $3 \text{ }\Omega\text{.m}$, the delivered current was $10 \text{ }\mu\text{A}$, the distance between the electrodes was 8 mm , and the cross-sectional area between the pins was $3 \text{ mm} \times 1.5 \text{ mm}$). This magnitude of electric field has been shown to effect the proliferation of osteoblasts using capacitive or pulsed electromagnetic field methods.^{42,169,222} It is possible that the osteoblasts used in this study were affected by the electric fields produced, but that it was only cells in the middle of the samples that experienced a field high enough to enhance their proliferation. Carbon nanofilaments have shown some potential to support electrical stimulation of osteogenesis, which could particularly be used to enhance osseointegration around scaffolds used in tissue engineering. Thus with further investigation, carbon nanofilaments could hold possibilities to reinforce, texture and electrically stimulate osteogenesis around biocompatible polymeric scaffolds to provide mechanical stability and enhanced osseointegration.

Scaled up investigations could also be performed with the apparatus designed and tested in this study to understand whether there are differences associated with varying nanofilament structures and compositions in biocompatible polymers when it comes to stimulating osteoblasts. This setup detailed here could be further improved by modifying the amount of electrical current delivered to the surface of the composite. This could be done by experimenting with various degrees of delivered current or alternatively modifying the shape and position of the electrodes as illustrated in figure

6.14. Alternatively the setup could be modified to provide a capacitive or inductive current around the composites so that the electric and magnetic fields are consistent to the samples.

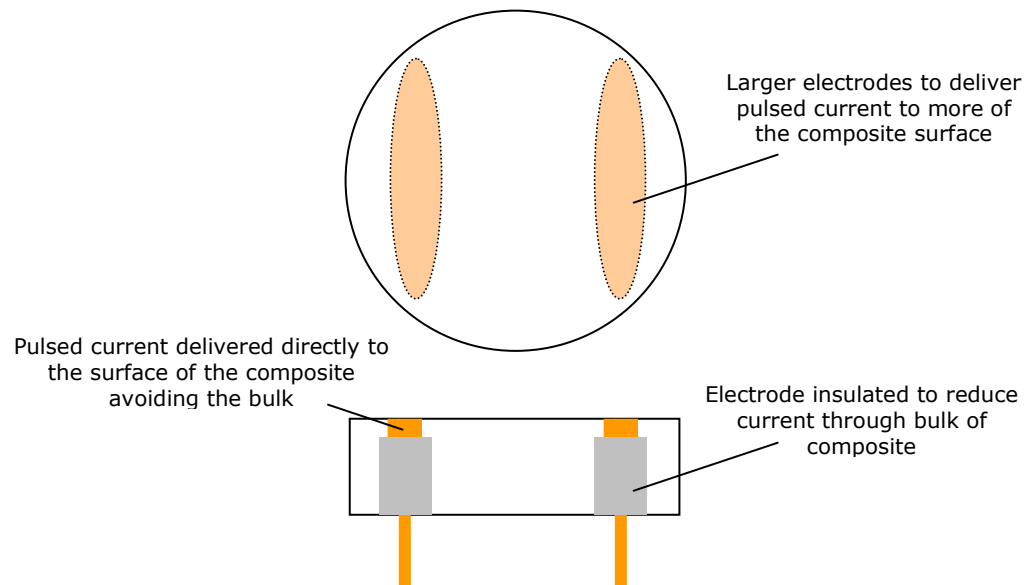


Figure 6.14: Suggested modifications of electrodes used to maximise delivered pulsed current using Faradic stimulation in future investigations

7. General Discussion

The surface characteristics of pressed nanofilament substrates and nanofilament -PEMA/THFMA composites were affected by the size and nature of the carbon nanofilaments. There were significant differences in micron-scale roughness in the MWNT9 and PR19PS pressed substrates (figure 4.3) and the PR19PS-incorporated composites (figure 5.13). The increase in roughness on the PR19PS composite surface was attributed to the porous structure formed by clusters of PR19PS nanofilaments. The cloudy appearance on the MWNT9 composite substrates was thought to be entangled MWNT9 clusters (figure 5.9), which were much smaller in size than the PR19PS clusters (figure 5.10). The clustering of the MWNT9 and PR19PS nanofilaments may have contributed to the increase in micron-scale roughness in the pressed substrates. The clusters would have formed micron-sized particles that in turn would have formed micron-sized features on the substrates after pressing. The nano-scale roughness was not significantly different as it was only affected by the nanofilaments themselves.

The nano-scale roughness of the composites increased (after 5 wt%) due to increased concentrations of nanofilaments at the substrate surface (figure 5.14). This meant that nanofilaments were contributing to the surface texture of the composites. The texture of the pressed and composite surfaces would have been affected differently by the nanofilaments at their surfaces. The pressed nanofilament surfaces had a rougher texture as the nanofilaments were pressed onto one another, whereas the composite surface textures were dependent upon the amount of nanofilaments present and their effects on the surface of the polymer matrix. The change in topography would have been due to the nature of the nanofilaments at the composite surfaces.

The packing density (long, stiff PR19PS nanofilaments compared to short GNFs for example) and morphology (e.g. curly nature of the thin MWNT9 nanotubes) of nanofilaments at the surfaces of the composites would have affected the topography, but it is unclear whether these surface differences were caused by coated nanofilaments or a combination of exposed and polymer coated nanofilaments present at the composite surface.

The chemistry of the PEMA/THFMA will also contribute to the cells response on the nanofilament-textured surfaces. An increase in nanofilaments at the surface of the composite, however, did increase cell attachment compared to the unfilled PEMA/THFMA surface (figure 5.18). This suggests that the osteoblasts attached to nanofilament shaped features, which was also shown on the pressed nanofilament substrates that attached and spread specifically to substrates with nanofilament diameters between 134-155 nm (figure 4.6 and figure 4.7).

The dispersion and structure of the nanofilaments also affected the resultant composite structure and properties. The mechanical and electrical properties depended on the porosity of the PR19PS composites, the structure and the dispersion of the nanofilaments and their effects on the degree of polymerisation of the PEMA/THFMA polymer. GNF dispersed the most in the polymer matrices, but their structure would have contributed the least to mechanical and electrical properties due to its anisotropic properties. This was because they were more liable to break, had poor conductivity compared to the MWNT9 samples and had more reactive end groups which would have hindered polymerisation. The graphene planes in GNFs were perpendicular to the filament axis (or at an angle in herringbone nanofibres); van der Waals interactions (much weaker than covalent bonding) held the planes together and hence held the filaments together. The conductivity of the GNFs was also

compromised as current flow would run in the direction of the graphene planes perpendicular to the fibre axis. The structure of the nanofilaments also affected the pressed substrate topography. Both GNF samples were shown to break forming shorter nanofilaments on the pressed substrate (figure 4.2), whereas the PR19PS and MWNT9, covalently bonded along the filament axis did not break. However, clustering of the PR19PS and MWNT9 samples hindered the magnitude of storage modulus and electrical resistivity of the composites as it reduced the connectivity between filaments through the composite structure and, in the case of PR19PS, formed a less mechanically stable porous structure at higher loadings (figure 5.16).

The length of the nanofilaments (table 3.4) will have contributed to the topography of the pressed substrates as well as the mechanical, thermal and electrical properties of the composites. PR19PS nanofilaments were far longer than the GNF samples (~ 4 times longer, table 3.4), which would have inhibited polymer chain movement during DMA, increasing the storage modulus and narrowing the storage modulus inflexion at its T_g . The length of nanofilaments would also affect connectivity between the nanofilaments, therefore affecting their electrical conductivity. Again, this would have been hindered by clustering of the PR19PS nanofilaments, resulting in poor connectivity.

Osteoblasts attached and spread on pressed nanofilament substrates with average nanofilament diameters in the region of 134-155 nm (figure 4.6), but tended to respond to surface roughness over longer time points on the pressed substrates and nanofilament polymer composites (figure 4.10 and figure 5.23). Price *et al.* observed that osteoblasts attached to carbon nanofilament compacts dependent on nano-scale roughness^{108,125,126} and nanofilament of diameters below 100 nm.¹⁰⁸ The same group also showed

higher cell attachment to polycarbonate urethane composites with higher nanofilament loadings.⁶ The current study indicated that although the osteoblasts attached preferentially to pressed nanofilament substrates with specific average diameters (134 – 155 nm), longer term osteoblast activity was dependent on surface roughness. Similar to the results of Price *et al.*¹¹³ there may have been a balance between nanofilament diameter and surface roughness as cell proliferation and differentiation depended on attached cell morphology. Cells responded more rapidly to PR19PS substrate, but spread enough to encourage proliferation,²²³ whereas the cells on the MWNT9 substrate did not respond as quickly but promoted proliferation on the substrate over 2 weeks.

Osteoblasts cultured on the nanofilament composites, however, attached in higher numbers to rougher surfaces but with less spreading (figure 5.18 and figure 5.19). The only sample to markedly show longer term activity of osteoblasts was 5 wt% MWNT9 –PEMA/THFMA composite, which showed high attachment and spreading regardless of substrate roughness. Considering all of this, osteoblasts did show a more favourable interaction on substrates with nanoscale dimensions (i.e. 13 nm diameter of MWNT9 nanotubes) with a certain concentration at the surface (5 wt% bulk concentration). The size and structure of the MWNT9 nanotube sample clearly encouraged osteoblast growth on the MWNT9 pressed and composite surfaces. The size and structure of the clustered MWNT9 nanotubes also affected the bulk properties of PEMA/THFMA polymer system, especially exhibiting the lowest resistivity of all the nanofilament samples. This sample showed the most promise, in terms of structure and dimension, to stimulate osseointegration or provide a conductive filler in a biocompatible polymer to electrically stimulate osteogenesis. This nanofilament sample, incorporated

into another polymer matrix, such as PMMA,¹⁸⁰ could also potentially produce reinforcing capabilities to stabilise bone during healing.

The roughness and texture of pressed and composite surfaces was modified using carbon nanofilaments of varying structures and diameters. The *in vitro* results obtained using HOBs, indicated that MWNT9 nanotubes formed surfaces that promoted osteoblast function, whether that be from the texture of the nanotubes or their effect of the polymerisation of PEMA/THFMA.

If nanofilaments are to be used for surface modification or in bulk prostheses, the potential release of wear particles could induce inflammation and ultimately discourage acceptance of the implant into the body and severely damage the local tissue environment. The release of individual nanofilaments pressed or from composite surfaces could produce inflammation around the device. The toxicological response of the body to these nanomaterials has been researched by Brown *et al.* (Appendix). It was found that phagocytosis of nanofilaments *in vitro* was more prevalent on the short GNF1 and GNF3 nanofibre samples and the curly MWNT9 sample than the stiffer nanotube samples. Frustrated phagocytosis was observed on the straighter PR19PS sample, which was hard to engulf by the macrophages and could cause an inflammatory response because of inhibition of nanofilament removal. If nanofilaments cannot be removed away easily by phagocytosis, they will persist in the tissue and cause inflammation, fibrosis and possibly tumour production.⁵ Price *et al.*⁵ observed osteoblast viability exposed to media with small concentrations of VGNF (similar to PR19PS in this investigation) at 0.005 – 0.5 µg/ml. The group found that nanofilaments with diameters in the range of those used in this investigation did not show much decreased osteoblast viability until concentrations of 0.005 µg/ml and above compared to a control up to 24 hours.⁴ At higher concentrations (15.625 –

125 µg/ml) used by Brown *et al.*, the degree of phagocytosis of human macrophages (THP-1) and release of pro-inflammatory cytokine TNF- α and reactive oxygen species (ROS) in human mononuclear cells was dependent on nanofilament structure and size. Smaller GNF samples and entangled MWNT9 samples were phagocytosed more readily than the longer, stiffer PR19PS nanofilaments. There was also a lower production of TNF- α and ROS release from cells exposed to the GNF and MWNT9 samples compared to the stiffer nanotube samples (including PR19PS). This provides further evidence that the MWNT9 nanotube sample could be used to reinforce and modify surfaces of biomaterials, as they seem to prompt lower inflammatory responses, especially in terms of frustrated phagocytosis, compared to the other types of carbon nanofilaments.

8. Conclusions

The CVD conditions used in this study successfully synthesised carbon nanofilaments with repeatable production of nanofilament structure and diameter range. Unsupported nickel catalyst encouraged synthesis of GNFs and the reaction temperature controlled the nature of the catalyst and hence the structure of nanofibres produced. Silica supported iron catalyst successfully produced nanotubes of uniform diameter and structure, which was attributed to silica pore size and prominence of tip growth during synthesis. CVD also provided high yields of nanofilaments ($\sim 19,000\%$ GNF and $\sim 1,550\%$ MWNT synthesis compared to mass of starting catalyst).

The substrates formed from nanofilaments pressed onto PEEK discs were dependent on the size and nature of the nanofilaments. Clustering of the PR19PS and MWNT9 samples was thought to contribute to the rougher micron-scale features of the substrates compared to GNF surfaces. Osteoblast attachment and spreading on the pressed nanofilament substrates was dependent on nanofilament diameter, but did not necessarily encourage proliferation. Cells attached and spread well on the commercial PR19PS sample (134 nm diameter and VGNF structure), but not on the MWNT9 sample (13 nm diameter and MWNT structure). Both samples showed osteoblast proliferation and differentiation over two weeks, signifying a delayed response of osteoblasts on the MWNT9 sample. Spread cells on the nanofibre samples were more rounded in morphology but, although exhibited many filopodia, did not encourage proliferation. Proliferation and differentiation was enhanced on PR19PS and MWNT9 surfaces with a higher surface roughness ($R_a > 2.5 \mu\text{m}$) compared to GNF substrates ($R_a < 2.0$), although the diameters of nanofilaments on MWNT9 (13 nm) and PR19PS

(134 nm) were also thought to have encouraged osteoblast growth by simulating the dimensions of extracellular matrix components of bone.

The size and nature of the nanofilaments also contributed to the bulk properties of PEMA/THFMA polymer composites. Dispersion was high in the GNF composite due to easy blending of short untangled GNFs, whereas clumped PR19PS and MWNT9 nanofilaments bundled together and affected the mechanical properties (storage modulus and damping) and electrical properties (resistivity) due to limited connectivity in the composites. In this study, the reduction in thermal and mechanical properties of PEMA/THFMA was attributed to inhibition of polymerisation due to presence of nanofilaments whilst curing. Despite this, 5 wt% MWNT9 –PEMA/THFMA samples promoted osteoblast attachment, proliferation and differentiation on their substrates. This was contrary to trends seen on the other composite samples, in which osteoblasts attached more to rougher surfaces. It is thought that results would be clearer by incorporating nanofilaments into a pre-polymerised matrix (i.e. melt-mixing), so to exclude the effects of hindered polymerisation of the PEMA/THFMA matrix.

There were also slight increases in proliferation and differentiation of electrically stimulated osteoblasts on 5 wt% MWNT9-PEMA/THFMA composites. It was not as much as the enhanced osteoblast growth reported in the literature,⁴ but this may have been due to the resultant electromagnetic field from Faradic stimulation method used in this study was not as high as the semi-capacitive stimulation method reported in the literature.^{134,224}

The MWNT9 nanotube sample showed the most potential for use in surface modification of total joint replacement components, bone cements or tissue engineering scaffolds. This was because human osteoblasts proliferated

and differentiated on both compacted and 5 wt% MWNT9-PEMA/THFMA composite surfaces, as well as slight enhancement of cell growth using electrical stimulation. The size and structure of the MWNT9 nanotubes also produced composites with the lowest electrical resistivity of the sample tested.

9. Suggested Future Work

There are many avenues of continued research brought out from this work. Carbon nanofilaments have many potentials and much work is required to understand and tailor their potential with respect to bone repair. Some of this work has begun but only touches the surface of their potential uses.

As nanofilaments can be functionalised,^{9,133} they could be functionalised with biological molecules to enhance cell and tissue growth^{150,156,158} or enhance dispersion and adhesion with polymer matrices.²²⁵ These factors are important in the improvement of both surface and bulk modification of bone repair implants. There are other ways of exploring different self-supporting nanofilament topographies especially with respect to osteoblast responses. This could be achieved by developing nanofilament bundles,¹²⁰ cross-linked networks,^{68,187,226} or aligned arrays.^{122,123,152,154}

There were problems with the *in situ* polymerisation procedure used in this investigation due to interactions of nanofilaments with the curing constituents. For this reason, it would be beneficial to research the reinforcing effects of the nanofilaments produced here in pre-polymerised polymer matrices, such as PMMA¹⁵⁰ and UHMWPE^{141,142} polymers. The effects of producing aligned nanofilaments composites could also be beneficial in these applications. Another route would be to produce composite scaffolds from the PEMA/THFMA composites produced in this study. PEMA/THFMA has been used to chemically and architecturally encourage chondrocyte and osteoblast migration and activity in porous supercritical carbon dioxide foamed PEMA/THFMA.¹²³ There are also other possibilities for nanofilament-polymer composites in orthopaedic application that have been briefly explored,

including reinforced composite rods^{122,227} that could be used for intramedullary rods, or composites used in low-wear applications, such as on the articulating surface of acetabular prostheses.

Maximised dispersion and connectivity of nanofilaments in composites is necessary as this would enhance electrical and mechanical properties. The potential of nanofilament polymer composites in use as devices to electrically stimulate bone cells or tissues can be further investigated by performing a full-scale test including all GNF and MWNT samples. This would highlight the electrical effects through different nanocomposites on osteoblasts. The assembly designed and tested in this study is versatile enough to test multiple triplicated composites, with a range of currents, pulsed frequencies, exposure durations and nanofilament loadings. It was clear from this study that the setup should be improved by modifying the amount of electrical current delivered to the surface of the composite. This could be done by changing the shape and position of the electrodes as detailed in section 6.4. Alternatively, the setup could be adjusted to deliver capacitive or inductive electrical pulses around osteoblasts more effectively. The setup could also be used to investigate the electrical stimulation of other cell types, especially neuronal cells.

10. References

1. Monthieux M, Kuznetsov VL. Who should be given the credit for the discovery of carbon nanotubes? *Carbon* 2006;44(9):1621-3.
2. Elias KL, Price RL, Webster TJ. Enhanced functions of osteoblasts on nanometer diameter carbon fibers. *Biomaterials* 2002;23(15):3279-87.
3. Webster TJ, Waid MC, McKenzie JL, Price RL, Ejirofor JU. Nanobiotechnology: carbon nanofibres as improved neural and orthopaedic implants. *Nanotechnology* 2004;15:48-54.
4. Supronowicz PR, Ajayan PM, Ullmann KR, Arulanandam BP, Metzger DW, Bizios R. Novel current-conducting composite substrates for exposing osteoblasts to alternating current stimulation. *J Biomed Mater Res* 2002;59(3):499-506.
5. Price RL, Haberstroh KM, Webster TJ. Improved osteoblast viability in the presence of smaller nanometre dimensioned carbon fibres. *Nanotechnology* 2004;15(8):892-900.
6. Price RL, Ellison K, Haberstroh KM, Webster TJ. Nanometer surface roughness increases select osteoblast adhesion on carbon nanofiber compacts. *Journal of Biomedical Materials Research Part A* 2004;70A(1):129-38.
7. Hu H, Ni YC, Montana V, Haddon RC, Parpura V. Chemically functionalized carbon nanotubes as substrates for neuronal growth. *Nano Letters* 2004;4(3):507-11.
8. Mattson MP, Haddon RC, Rao AM. Molecular functionalization of carbon nanotubes and use as substrates for neuronal growth. *J Mol Neurosci* 2000;14(3):175-82.
9. Zanello LP, Zhao B, Hu H, Haddon RC. Bone cell proliferation on carbon nanotubes. *Nano Letters* 2006;6(3):562-7.
10. McKenzie JL, Waid MC, Shi R, Webster TJ. Decreased functions of astrocytes on carbon nanofiber materials. *Biomaterials* 2004;25(7-8):1309-17.
11. Webster TJ, Ellison K, Price RL, Haberstroh KM. Increased osteoblast function on nanostructured materials due to novel surface roughness properties. *Thermec'2003, Pts 1-5 2003*;426-4:3127-32.
12. Ratner BD, Hoffman AS, Schoen FJ, Lemons JE. *Biomaterials Science: An introduction to Materials in Medicine*. Academic Press; 1996.
13. Kühn K-D. *Bone Cements: Up-to-Date Comparison of Physical and Chemical Properties of Commercial Materials*. Springer-Verlag; 2000.
14. <http://www.hesonline.nhs.uk>, accessed on 23-4-2007
15. Goldstein SA, Moalli MR. Current concepts in tissue engineering: cell, matrices, and genes. *Curr Opin Orthopaed* 2001;12:424-7.
16. Murugan R, Ramakrishna S. Development of nanocomposites for bone grafting. *Composites Science and Technology* 2005;65(15-16):2385-406.
17. Stevens MM, George JH. Exploring and engineering the cell surface interface. *Science* 2005;310(5751):1135-8.
18. Service RF. Self-assembling materials - Coated nanofibers copy what's bred in the bone. *Science* 2001;294(5547):1635.
19. <http://www.invibio.com/products/peekOptima/default.aspx>, accessed on 23-4-2007
20. Ajayan PM. Nanotubes from carbon. *Chem Rev* 1999;99(7):1787-99.
21. Bennell K, Brukner P. Preventing and managing stress fractures in athletes. *Physical Therapy in Sport* 2005;6(4):171-80.

22. Wiesmann HP, Hartig M, Stratmann U, Meyer U, Joos U. Electrical stimulation influences mineral formation of osteoblast-like cells in vitro. *Biochimica et Biophysica Acta (BBA) - Molecular Cell Research* 2001 Feb 5;1538(1):28-37.
23. Diniz P, Shomura K, Soejima K, Ito G. Effects of pulsed electromagnetic field (PEMF) stimulation on bone tissue like formation are dependent on the maturation stages of the osteoblasts. *Bioelectromagnetics* 2002;23(5):398-405.
24. El Hakim IE, Azim AMA, El Hassan MFA, Maree SM. Preliminary investigation into the effects of electrical stimulation on mandibular distraction osteogenesis in goats. *Int J Oral Maxillofac Surg* 2004 Feb;33(1):42-7.
25. Zhuang H, Wang W, Seldes RM, Tahernia AD, Fan H, Brighton CT. Electrical Stimulation Induces the Level of TGF- β 1 mRNA in Osteoblastic Cells by a Mechanism Involving Calcium/Calmodulin Pathway. *Biochem Biophys Res Commun* 1997 Aug 18;237(2):225-9.
26. Vaughan J. *The Physiology of Bone*. 2nd Ed. Clarendon Press, Oxford; 1975.
27. Lundon K. *Orthopedic Rehabilitation Science: Principles for Clinical Management of Bone*. Boston, USA: Butterworth-Heinemann; 2000.
28. Little K. *Bone behaviour*. London, New York: Academic Press; 1973.
29. Siebers MC, ter Brugge PJ, Walboomers XF, Jansen JA. Integrins as linker proteins between osteoblasts and bone replacing materials. A critical review. *Biomaterials* 2005 Jan;26(2):137-46.
30. Hancox NM. *Biology of Bone*. Cambridge University Press; 1972.
31. Elices M. *Structural Biological Materials: Design & Structure--Property Relationships*. Elsevier Science; 2000.
32. Simkiss K. *Bone and Biomineralization*. Studies in Biology no 53 Edward Arnold Ltd; 1975.
33. Bourne GH. *The Biochemistry and Physiology of Bone*. II Academic Press; 1971.
34. Parikka V, Lehenkari P, Sassi ML, Halleen J, Risteli J, Harkonen P, et al. Estrogen reduces the depth of resorption pits by disturbing the organic bone matrix degradation activity of mature osteoclasts. *Endocrinology* 2001;142(12):5371-8.
35. Blair HC, Kahn AJ, Crouch EC, Jeffrey JJ, Teitelbaum SL. Isolated Osteoclasts Resorb the Organic and Inorganic Components of Bone. *Journal of Cell Biology* 1986;102(4):1164-72.
36. Anselme K. Osteoblast adhesion on biomaterials. *Biomaterials* 2000;21(7):667-81.
37. Yamada KM. Adhesive Recognition Sequences. *J Biol Chem* 1991;266(20):12809-12.
38. Vogel V, Baneyx G. The Tissue Engineering Puzzle: A Molecular Perspective. *Annual Review of Biomedical Engineering* 2003;5(1):441-63.
39. Zigmond SH. Signal transduction and actin filament organization. *Curr Opin Cell Biol* 1996;8(1):66-73.
40. Stein GS, Lian JB, Stein JL, VanWijnen AJ, Montecino M. Transcriptional control of osteoblast growth and differentiation. *Physiol Rev* 1996;76(2):593-629.
41. Aaron RK, Boyan BD, Ciombor DM, Schwartz Z, Simon BJ. Stimulation of growth factor synthesis by electric and electromagnetic fields. *Clin Orthop* 2004;(419):30-7.
42. Brighton CT, Wang W, Seldes R, Zhang GH, Pollack SR. Signal transduction in electrically stimulated bone cells. *Journal of Bone and Joint Surgery-American Volume* 2001;83A(10):1514-23.

43. Kenley RA, Yim K, Abrams J, Ron E, Turek T, Marden LJ, et al. Biotechnology and Bone-Graft Substitutes. *Pharm Res* 1993;10(10):1393-401.
44. Park JB, Lakes RS. *Biomaterials: An Introduction*. Plenum Press; 1992.
45. Nomura N, Kohama T, Oh IH, Hanada S, Chiba A, Kanehira M, et al. Mechanical properties of porous Ti-15Mo-5Zr-3Al compacts prepared by powder sintering. *Materials Science & Engineering C-Biomimetic and Supramolecular Systems* 2005;25(3):330-5.
46. <http://www.matweb.com>, accessed on 14-2-2007
47. Huang ZM, Fujihara K. Stiffness and strength design of composite bone plates. *Composites Science and Technology* 2005;65(1):73-85.
48. Jacobs JJ, Gilbert JL, Urban RM. Corrosion of metal orthopaedic implants. *Journal of Bone and Joint Surgery-American Volume* 1998;80A(2):268-82.
49. Schaffler MB, Jepsen KJ. Fatigue and repair in bone. *International Journal of Fatigue* 2000;22(10):839-46.
50. Rodriguez NM. A Review of Catalytically Grown Carbon Nanofibers. *Journal of Materials Research* 1993;8(12):3233-50.
51. De Jong KP, Geus JW. Carbon nanofibers: Catalytic synthesis and applications. *Catalysis Reviews-Science and Engineering* 2000;42(4):481-510.
52. Iijima S. Helical Microtubules of Graphitic Carbon. *Nature* 1991;354(6348):56-8.
53. Askeland DR. *The Science and Engineering of Materials*. 3rd Ed. Cheltenham, UK: Stanley Thornes; 1996.
54. Mamalis AG, Vogtlander LOG, Markopoulos A. Nanotechnology and nanostructured materials: trends in carbon nanotubes. *Precision Engineering* 2004 Jan;28(1):16-30.
55. Ajayan PM, Charlier JC, Rinzler AG. Carbon nanotubes: From macromolecules to nanotechnology. *Proc Natl Acad Sci U S A* 1999;96(25):14199-200.
56. Saito R, Dresselhaus G, Dresselhaus MS. *Physical Properties of Carbon Nanotubes*. Imperial College Press; 1998.
57. Lair SL, Herndon WC, Murr LE, Quinones SA. End cap nucleation of carbon nanotubes. *Carbon* 2006 Mar;44(3):447-55.
58. Rodriguez NM, Chambers A, Baker RTK. Catalytic Engineering of Carbon Nanostructures. *Langmuir* 1995;11(10):3862-6.
59. McCaldin S, Bououdina M, Grant DM, Walker GS. The effect of processing conditions on carbon nanostructures formed on an iron-based catalyst. *Carbon* 2006;44(11):2273-80.
60. Ivanov V, Fonseca A, Nagy JB, Lucas A, Lambin P, Bernaerts D, et al. Catalytic production and purification of nanotubules having fullerene-scale diameters. *Carbon* 1995;33(12):1727-38.
61. Yu J, Zhang Q, Ahn J, Yoon SF, Li RYJ, Gan B, et al. Synthesis of carbon nanostructures by microwave plasma chemical vapor deposition and their characterization. *Materials Science and Engineering B-Solid State Materials for Advanced Technology* 2002;90(1-2):16-9.
62. Peng L-M, Shi ZJ, Zhang ZL, Ouyang L, Gu ZN, Xue ZQ, et al. Growth of compound single- and multi-walled carbon nanotubes. *Ultramicroscopy*. In press 2003.
63. Ledoux MJ, Vieira R, Pham-Huu C, Keller N. New catalytic phenomena on nanostructured (fibers and tubes) catalysts. *Journal of Catalysis* 2003;216(1-2):333-42.
64. Corrias M, Caussat B, Aryal A, Durand J, Kihn Y, Kalck P, et al. Carbon nanotubes produced by fluidized bed catalytic CVD: first approach of the process. *Chemical Engineering Science* 2003;58(19):4475-82.

65. Bai JB. Growth of nanotube/nanofibre coils by CVD on an alumina substrate. *Materials Letters* 2003;57(18):2629-33.
66. Oberlin A, Endo M, Koyama T. Filamentous growth of carbon through benzene decomposition. *Journal of Crystal Growth* 1976 Mar;32(3):335-49.
67. Fan YY, Cheng HM, Wei YL, Su G, Shen ZH. Tailoring the diameters of vapor-grown carbon nanofibers. *Carbon* 2000;38(6):921-7.
68. Li WZ, Xie SS, Qian LX, Chang BH, Zou BS, Zhou WY, et al. Large-scale synthesis of aligned carbon nanotubes. *Science* 1996;274(5293):1701-3.
69. Hernadi K, Fonseca A, Nagy JB, Bernaerts D, Fudala A, Lucas AA. Catalytic synthesis of carbon nanotubes using zeolite support. *Zeolites* 1996;17(5-6):416-23.
70. Hernadi K, Fonseca A, Piedigrosso P, Delvaux M, Nagy JB, Bernaerts D, et al. Carbon nanotubes production over Co/silica catalysts. *Catalysis Letters* 1997;48(3-4):229-38.
71. Seo JW, Couteau E, Umek P, Hernadi K, Marcoux P, Lukic B, et al. Synthesis and manipulation of carbon nanotubes. *New Journal of Physics* 2003;5:art-120.
72. Pradhan D, Sharon M. Carbon nanotubes, nanofilaments and nanobeads by thermal chemical vapor deposition process. *Materials Science and Engineering B-Solid State Materials for Advanced Technology* 2002;96(1):24-8.
73. Jourdain V, Kanzow H, Castignolles M, Loiseau A, Bernier P. Sequential catalytic growth of carbon nanotubes. *Chemical Physics Letters* 2002;364(1-2):27-33.
74. Baker RTK. Catalytic growth of carbon filaments. *Carbon* 1989;27(3):315-23.
75. Teo KBK, Singh C, Chhowalla M, Milne WI. Catalytic Synthesis of Carbon Nanotubes and Nanofibers. *Encyclopedia of Nanoscience and Nanotechnology* 2004;1:665-86.
76. Nagaraju N, Fonseca A, Konya Z, Nagy JB. Alumina and silica supported metal catalysts for the production of carbon nanotubes. *Journal of Molecular Catalysis A-Chemical* 2002;181(1-2):57-62.
77. Xie SS, Li WZ, Pan ZW, Chang BH, Sun LF. Carbon nanotube arrays. *Materials Science and Engineering A-Structural Materials Properties Microstructure and Processing* 2000;286(1):11-5.
78. Snoeck JW, Froment GF, Fowles M. Filamentous carbon formation and gasification: Thermodynamics, driving force, nucleation, and steady-state growth. *Journal of Catalysis* 1997;169(1):240-9.
79. Sinnott SB, Andrews R, Qian D, Rao AM, Mao Z, Dickey EC, et al. Model of carbon nanotube growth through chemical vapor deposition. *Chemical Physics Letters* 1999;315(1-2):25-30.
80. Bououdina M, Grant D, Walker G. Effect of processing conditions on unsupported Ni-based catalysts for graphitic-nanofibre formation. *Carbon* 2005;43(6):1286-92.
81. Harris PJF. *Carbon Nanotubes and related structures*. Cambridge University Press; 1999.
82. Sun XK, Zhao WM. Prediction of stiffness and strength of single-walled carbon nanotubes by molecular-mechanics based finite element approach. *Materials Science and Engineering A-Structural Materials Properties Microstructure and Processing* 2005;390(1-2):366-71.
83. Popov VN. Carbon nanotubes: properties and application. *Materials Science and Engineering: R: Reports* 2004 Jan 15;43(3):61-102.
84. Li CY, Chou TW. Elastic moduli of multi-walled carbon nanotubes and the effect of van der Waals forces. *Composites Science and Technology* 2003;63(11):1517-24.

85. Serp P, Corrias M, Kalck P. Carbon nanotubes and nanofibers in catalysis. *Applied Catalysis A: General* 2003 Oct 28;253(2):337-58.
86. Kim GT, Gu G, Waizmann U, Roth S. Simple method to prepare individual suspended nanofibers. *Applied Physics Letters* 2002;80(10):1815-7.
87. <http://www.apsci.com/ppi-pyro3.html>, accessed on 14-2-2007
88. Motojima S, Kawaguchi M, Nozaki K, Iwanaga H. Preparation of Coiled Carbon-Fibers by Catalytic Pyrolysis of Acetylene, and its Morphology and Extension Characteristics. *Carbon* 1991;29(3):379-85.
89. Dresselhaus MS, Dresselhaus G, Eklund PC. *Science of Fullerenes and Carbon Nanotubes*. Academic Press; 1996.
90. Yakobson BI. Mechanical relaxation and "intramolecular plasticity" in carbon nanotubes. *Applied Physics Letters* 1998;72(8):918-20.
91. Wong EW, Sheehan PE, Lieber CM. Nanobeam mechanics: Elasticity, strength, and toughness of nanorods and nanotubes. *Science* 1997;277(5334):1971-5.
92. Branca C, Magazu V, Mangione A. Determination of MWNTs length-to-diameter ratio by static and dynamic light scattering. *Diamond and Related Materials* 2005;14(3-7):846-9.
93. Berne BJ, Pecora R. *Dynamic Light Scattering. With Applications to Chemistry, Biology, and Physics*. Dover Publications; 2000.
94. Tirado MM, Martinez CL, Delatorre JG. Comparison of Theories for the Translational and Rotational Diffusion-Coefficients of Rod-Like Macromolecules - Application to Short Dna Fragments. *J Chem Phys* 1984;81(4):2047-52.
95. van Bruggen MPB, Lekkerkerker HNW, Dhont JKG. Long-time translational self-diffusion in isotropic dispersions of colloidal rods. *Physical Review e* 1997;56(4):4394-403.
96. van Bruggen MPB, Lekkerkerker HNW, Maret G, Dhont JKG. Long-time translational self-diffusion in isotropic and nematic dispersions of colloidal rods. *Physical Review e* 1998;58(6):7668-77.
97. Badaire S, Poulin P, Maugey M, Zakri C. In situ measurements of nanotube dimensions in suspensions by depolarized dynamic light scattering. *Langmuir* 2004;20(24):10367-70.
98. McKenzie JL, Cardona BE, Shi R, Webster TJ. Astrocyte Adhesion and Proliferation on Carbon Nanofibers. 2002 p. 597.
99. <http://dspace.library.drexel.edu/handle/1860/220>, accessed on 24-9-2003
100. Baughman RH, Cui CX, Zakhidov AA, Iqbal Z, Barisci JN, Spinks GM, et al. Carbon nanotube actuators. *Science* 1999;284(5418):1340-4.
101. Shearer MC, Fawcett JW. The astrocyte/meningeal cell interface - a barrier to successful nerve regeneration? *Cell Tissue Res* 2001;305(2):267-73.
102. Richards RG. The effect of surface roughness on fibroblast adhesion in vitro. *Injury-International Journal of the Care of the Injured* 1996;27:38-43.
103. Linez-Bataillon P, Monchau F, Bigerelle M, Hildebrand HF. In vitro MC3T3 osteoblast adhesion with respect to surface roughness of Ti6Al4V substrates. *Biomolecular Engineering* 2002;19(2-6):133-41.
104. Washburn NR, Yamada KM, Simon CG, Kennedy SB, Amis EJ. High-throughput investigation of osteoblast response to polymer crystallinity: influence of nanometer-scale roughness on proliferation. *Biomaterials* 2004;25(7-8):1215-24.
105. Curtis A, Wilkinson C. Nanotechniques and approaches in biotechnology. *Trends Biotechnol* 2001;19(3):97-101.
106. Curtis A, Wilkinson C. Topographical control of cells. *Biomaterials* 1997 Dec;18(24):1573-83.

107. Britland S, Perridge C, Denyer M, Morgan H, Curtis A, Wilkinson C. Morphogenetic guidance cues can interact synergistically and hierarchically in steering nerve cell growth. *Experimental Biology Online - EBO* 1996;1(2):1-15.
108. Price RL, Waid MC, Haberstroh KM, Webster TJ. Selective bone cell adhesion on formulations containing carbon nanofibers. *Biomaterials* 2003;24(11):1877-87.
109. Chlopek J, Czajkowska B, Szaraniec B, Frackowiak E, Szostak K, Beguin F. In vitro studies of carbon nanotubes biocompatibility. *Carbon* 2006 May;44(6):1106-11.
110. Webster TJ, Ergun C, Doremus RH, Siegel RW, Bizios R. Specific proteins mediate enhanced osteoblast adhesion on nanophase ceramics. *J Biomed Mater Res* 2000;51(3):475-83.
111. Schneider GB, Perinpanayagam H, Clegg M, Zaharias R, Seabold D, Keller J, et al. Implant surface roughness affects osteoblast gene expression. *J Dent Res* 2003;82(5):372-6.
112. Dalby MJ, McCloy D, Robertson M, Wilkinson CDW, Oreffo ROC. Osteoprogenitor response to defined topographies with nanoscale depths. *Biomaterials* 2006;27(8):1306-15.
113. Dalby MJ, Childs S, Riehle MO, Johnstone HJH, Affrossman S, Curtis ASG. Fibroblast reaction to island topography: changes in cytoskeleton and morphology with time. *Biomaterials* 2003;24(6):927-35.
114. Biggs MJP, Richards RG, Gadegaard N, Wilkinson CDW, Dalby MJ. The effects of nanoscale pits on primary human osteoblast adhesion formation and cellular spreading. *Journal of Materials Science-Materials in Medicine* 2007;18(2):399-404.
115. Dalby MJ, Riehle MO, Sutherland DS, Agheli H, Curtis ASG. Changes in fibroblast morphology in response to nano-columns produced by colloidal lithography. *Biomaterials* 2004 Oct;25(23):5415-22.
116. Wojciakstothard B, Curtis ASG, Monaghan W, Mcgrath M, Sommer I, Wilkinson CDW. Role of the Cytoskeleton in the Reaction of Fibroblasts to Multiple Grooved Substrata. *Cell Motil Cytoskeleton* 1995;31(2):147-58.
117. Walboomers XF, Croes HJE, Ginsel LA, Jansen JA. Contact guidance of rat fibroblasts on various implant materials. *J Biomed Mater Res* 1999;47(2):204-12.
118. Zreiqat H, Valenzuela SM, Nissan BB, Roest R, Knabe C, Radlanski RJ, et al. The effect of surface chemistry modification of titanium alloy on signalling pathways in human osteoblasts. *Biomaterials* 2005 Dec;26(36):7579-86.
119. Zhao G, Raines AL, Wieland M, Schwartz Z, Boyan BD. Requirement for both micron- and submicron scale structure for synergistic responses of osteoblasts to substrate surface energy and topography. *Biomaterials* 2007;28(18):2821-9.
120. Correa-Duarte MA, Wagner N, Rojas-Chapana J, Morsczech C, Thie M, Giersig M. Fabrication and biocompatibility of carbon nanotube-based 3D networks as scaffolds for cell seeding and growth. *Nano Letters* 2004;4(11):2233-6.
121. Carneiro OS, Covas JA, Bernardo CA, Caldeira G, van Hattum FWJ, Ting J-M, et al. Production and assessment of polycarbonate composites reinforced with vapour-grown carbon fibres. *Composites Science and Technology* 1998;58(3-4):401-7.
122. Yang Z, Dong B, Huang Y, Liu L, Yan FY, Li HL. A study on carbon nanotubes reinforced poly(methyl methacrylate) nanocomposites. *Materials Letters* 2005 Jul;59(17):2128-32.

123. Zeng J, Saltysiak B, Johnson WS, Schiraldi DA, Kumar S. Processing and properties of poly(methyl methacrylate)/carbon nano fiber composites. *Composites Part B: Engineering* 2004 Mar;35(2):173-8.
124. Hammel E, Tang X, Trampert M, Schmitt T, Mauthner K, Eder A, et al. Carbon nanofibers for composite applications. *Carbon* 2004;42(5-6):1153-8.
125. Price RL, Haberstroh KM, Webster TJ. Enhanced functions of osteoblasts on nanostructured surfaces of carbon and alumina. *Medical & Biological Engineering & Computing* 2003;41(3):372-5.
126. Price RL, Haberstroh KM, Webster TJ. Mechanism of Enhanced Osteoblast Adhesion on Carbon Nanofiber Substrates. 2003.
127. George JH, Shaffer MSP, Stevens MM. Investigating the Cellular Response to Multi-Walled Carbon Nanotubes. 2006 Jun 28; 2006.
128. <http://www.centropede.com/UKSB2006/ePoster/>, accessed on 14-2-2007
129. Shin H, Jo S, Mikos AG. Biomimetic materials for tissue engineering. *Biomaterials* 2003 Nov;24(24):4353-64.
130. Humphries MJ, Akiyama SK, Komoriya A, Olden K, Yamada KM. Identification of an alternatively spliced site in human plasma fibronectin that mediates cell type-specific adhesion. *J Cell Biol* 1986 Dec 1;103(6):2637-47.
131. Rho JY, Kuhn-Spearing L, Zioupos P. Mechanical properties and the hierarchical structure of bone. *Medical Engineering & Physics* 1998;20(2):92-102.
132. Fernando KAS, Lin Y, Sun YP. High aqueous solubility of functionalized single-walled carbon nanotubes. *Langmuir* 2004;20(11):4777-8.
133. Lin Y, Taylor S, Li HP, Fernando KAS, Qu LW, Wang W, et al. Advances toward bioapplications of carbon nanotubes. *Journal of Materials Chemistry* 2004;14(4):527-41.
134. Wang YB, Iqbal Z, Malhotra SV. Functionalization of carbon nanotubes with amines and enzymes. *Chemical Physics Letters* 2005;402(1-3):96-101.
135. Richards RG. Surfaces to control implant tissue adhesion for osteosynthesis: In vitro and in vivo evaluations. 19th European Conference on Biomaterials . 2005.
136. Hin TS. *Engineering Materials for Biomedical Applications*. World Scientific Publishing Company, Incorporated; 2004.
137. Morrison C, Macnair R, MacDonald C, Wykman A, Goldie I, Grant MH. In vitro biocompatibility testing of polymers for orthopaedic implants using cultured fibroblasts and osteoblasts. *Biomaterials* 1995 Sep;16(13):987-92.
138. Scotchford CA, Garle MJ, Batchelor J, Bradley J, Grant DM. Use of a novel carbon fibre composite material for the femoral stem component of a THR system: in vitro biological assessment. *Biomaterials* 2003;24(26):4871-9.
139. Wang A, Lin R, Polineni VK, Essner A, Stark C, Dumbleton JH. Carbon fiber reinforced polyether ether ketone composite as a bearing surface for total hip replacement. *Tribology International* 1998 Nov;31(11):661-7.
140. McFarland CD, Mayer S, Scotchford C, Dalton BA, Steele JG, Downes S. Attachment of cultured human bone cells to novel polymers. *J Biomed Mater Res* 1999;44(1):1-11.
141. Barry JJA, Gidda HS, Scotchford CA, Howdle SM. Porous methacrylate scaffolds: supercritical fluid fabrication and in vitro chondrocyte responses. *Biomaterials* 2004;25(17):3559-68.
142. Barry JJA, PhD Thesis. *A Supercritical Fluid Route to Cross-linked Polymeric Scaffolds* University of Nottingham; 2004.

143. Sawtell RM, PhD. An In Vitro Investigation of a Heterocyclic Methacrylate Polymer System for Cartilage Repair University of Nottingham; 1997.
144. Wyre RM, Downes S. The role of protein adsorption on chondrocyte adhesion to a heterocyclic methacrylate polymer system. *Biomaterials* 2002 Jan;23(2):357-64.
145. Wyre RM, Downes S. An in vitro investigation of the PEMA/THFMA polymer system as a biomaterial for cartilage repair. *Biomaterials* 2000 Feb;21(4):335-43.
146. Nussbaum DA, Gailloud P, Murphy K. The chemistry of acrylic bone cements and implications for clinical use in image-guided therapy. *J Vasc Interv Radiol* 2004;15(2):121-6.
147. Hutmacher DW. Scaffolds in tissue engineering bone and cartilage. *Biomaterials* 2000;21(24):2529-43.
148. Potschke P, bdel-Goad M, Alig I, Dudkin S, Lellinger D. Rheological and dielectrical characterization of melt mixed polycarbonate-multiwalled carbon nanotube composites. *Polymer* 2004;45(26):8863-70.
149. Zou YB, Feng YC, Wang L, Liu XB. Processing and properties of MWNT/HDPE composites. *Carbon* 2004;42(2):271-7.
150. Wang YP, Cheng RL, Liang LL, Wang YM. Study on the preparation and characterization of ultra-high molecular weight polyethylene-carbon nanotubes composite fiber. *Composites Science and Technology* 2005;65(5):793-7.
151. Martin CA, Sandlin JKW, Windle AH, Schwarz MK, Bauhofer W, Schulte K, et al. Electric field-induced aligned multi-wall carbon nanotube networks in epoxy composites. *Polymer* 2005;46(3):877-86.
152. Stephan C, Nguyen TP, de la Chapelle ML, Lefrant S, Journet C, Bernier P. Characterization of singlewalled carbon nanotubes-PMMA composites. *Synthetic Metals* 2000;108(2):139-49.
153. Park SJ, Lim ST, Cho MS, Kim HM, Joo J, Cho HJ. Electrical properties of multi-walled carbon nanotube/poly(methyl methacrylate) nanocomposite. *Current Applied Physics* 2005;5(4):302-4.
154. Cooper CA, Ravich D, Lips D, Mayer J, Wagner HD. Distribution and alignment of carbon nanotubes and nanofibrils in a polymer matrix. *Composites Science and Technology* 2002;62(7-8):1105-12.
155. Haggemueller R, Gommans HH, Rinzler AG, Fischer JE, Winey KI. Aligned single-wall carbon nanotubes in composites by melt processing methods. *Chemical Physics Letters* 2000;330(3-4):219-25.
156. Shi XF, Hudson JL, Spicer PP, Tour JM, Krishnamoorti R, Mikos AG. Rheological behaviour and mechanical characterization of injectable poly(propylene fumarate)/single-walled carbon nanotube composites for bone tissue engineering. *Nanotechnology* 2005;16(7):S531-S538.
157. Qian D, Dickey EC, Andrews R, Rantell T. Load transfer and deformation mechanisms in carbon nanotube-polystyrene composites. *Applied Physics Letters* 2000;76(20):2868-70.
158. Xie XL, Mai YW, Zhou XP. Dispersion and alignment of carbon nanotubes in polymer matrix: A review. *Materials Science & Engineering R-Reports* 2005;49(4):89-112.
159. Friedenberg ZB, Brighton CT. Bioelectric Potentials in Bone. *Journal of Bone and Joint Surgery-American Volume* 1966;A 48(5):915-&.
160. Zhou SA, Uesaka M. Bioelectrodynamics in living organisms. *International Journal of Engineering Science* 2006 Jan;44(1-2):67-92.
161. Krishnan V, Davidovitch Z. Cellular, molecular, and tissue-level reactions to orthodontic force. *Am J Orthod Dentofacial Orthop* 2006 Apr;129(4):469.
162. Perry CR. Bone repair techniques, bone graft, and bone graft substitutes. *Clin Orthop* 1999;(360):71-86.

163. Oishi M, Onesti ST. Electrical bone graft stimulation for spinal fusion: A review. *Neurosurgery* 2000;47(5):1041-55.
164. Miara B, Rohan E, Zidi M, Labat B. Piezomaterials for bone regeneration design--homogenization approach. *Journal of the Mechanics and Physics of Solids* 2005 Nov;53(11):2529-56.
165. Campbell CE, Higginbotham DV, Baranowski Jr TJ. A constant cathodic potential device for faradic stimulation of osteogenesis. *Medical Engineering & Physics* 1995 Jul;17(5):337-46.
166. Yonemori K, Matsunaga S, Ishidou Y, Maeda S, Yoshida H. Early effects of electrical stimulation on osteogenesis. *Bone* 1996;19(2):173-80.
167. Black J, Baranowski TJ, Brighton CT. Electrochemical aspects of d.c. stimulation of osteogenesis. *Bioelectrochem Bioenerg* 1984;12(3-4):323-7.
168. Tang Q, Chen G, Zhao N. Effects of ELF electric field on proliferation of mouse osteoblastic cells. *Bioelectrochem Bioenerg* 1998 Dec;47(2):349-53.
169. Chang WHS, Chen LT, Sun JS, Lin FH. Effect of pulse-burst electromagnetic field stimulation on osteoblast cell activities. *Bioelectromagnetics* 2004;25(6):457-65.
170. Eyres KS, Saleh M, Kanis JA. Effect of pulsed electromagnetic fields on bone formation and bone loss during limb lengthening. *Bone* 1996 Jun;18(6):505-9.
171. Inoue N, Ohnishi I, Chen D, Deitz LW, Schwarzt JD, Chao EYS. Effect of pulsed electromagnetic fields (PEMF) on late-phase osteotomy gap healing in a canine tibial model. *J Orthop Res* 2002 Sep;20(5):1106-14.
172. Pepper JR, Herbert MA, Anderson JR, Bobechko WP. Effect of capacitive coupled electrical stimulation on regenerate bone. *J Orthop Res* 1996;14(2):296-302.
173. Huang SH, Ajayan PM, Bizios R. Select Osteoblast Functions in Three-Dimensional Porous Poly L-Lactic Acid/Carbon Nanotube Composites. 2002 p. 181.
174. Service RF. American Chemical Society meeting: Nanomaterials show signs of toxicity. *Science* 2003;300(5617):243.
175. Bottini M, Bruckner S, Nika K, Bottini N, Bellucci S, Magrini A, et al. Multi-walled carbon nanotubes induce T lymphocyte apoptosis. *Toxicol Lett* 2006;160(2):121-6.
176. Muller J, Huaux F, Lison D. Respiratory toxicity of carbon nanotubes: How worried should we be? *Carbon* 2006 May;44(6):1048-56.
177. Nemmar A, Hoet PHM, Vanquickenborne B, Dinsdale D, Thomeer M, Hoylaerts MF, et al. Passage of inhaled particles into the blood circulation in humans. *Circulation* 2002;105(4):411-4.
178. Muller J, Huaux F, Moreau N, Misson P, Heilier JF, Delos M, et al. Respiratory toxicity of multi-wall carbon nanotubes. *Toxicol Appl Pharmacol* 2005;207(3):221-31.
179. Soutar CA, Miller BG, Gregg N, Jones AD, Cullen RT, Bolton RE. Assessment of human risks from exposure to low toxicity occupational dusts. *The Annals of Occupational Hygiene* 1997 Apr;41(2):123-33.
180. Donaldson K, Stone V, Clouter A, Renwick L, MacNee W. Ultrafine particles. *Occup Environ Med* 2001 Mar 1;58(3):211-6.
181. Hanein D, Geiger B, Addadi L. Differential Adhesion of Cells to Enantiomorphous Crystal-Surfaces. *Science* 1994;263(5152):1413-6.
182. Ando Y, Zhao X, Sugai T, Kumar M. Growing carbon nanotubes. *Materials Today* 2004 Oct;7(9):22-9.
183. Hernadi K, Konya Z, Siska A, Kiss J, Oszko A, Nagy JB, et al. On the role of catalyst, catalyst support and their interaction in synthesis of carbon nanotubes by CCVD. *Materials Chemistry and Physics* 2003;77(2):536-41.

184. Seuk Youn H, Ryu H, Cho TH, Choi WK. Purity enhancement and electrochemical hydrogen storage property of carbon nanofibers grown at low temperature. *International Journal of Hydrogen Energy* 2002 Sep;27(9):937-40.
185. Lakshminarayanan PV, Toghiani H, Pittman CU. Nitric acid oxidation of vapor grown carbon nanofibers. *Carbon* 2004;42(12-13):2433-42.
186. Gordeyev SA, Macedo FJ, Ferreira JA, van Hattum FWJ, Bernardo CA. Transport properties of polymer-vapour grown carbon fibre composites. *Physica B: Condensed Matter* 2000 Apr;279(1-3):33-6.
187. Fan S, Liang W, Dang H, Franklin N, Tomblor T, Chapline M, et al. Carbon nanotube arrays on silicon substrates and their possible application. *Physica E: Low-dimensional Systems and Nanostructures* 2000 Aug;8(2):179-83.
188. Pan ZW, Xie SS. Production of Very Long Aligned Carbon Nanotubes. In: Yang S, Sheng P, editors. *Physics and Chemistry of Nanostructured Materials*. Taylor and Francis; 2000. p. 140-3.
189. Barbucci R, Pasqui D, Wirsén A, Affrossman S, Curtis A, Tetta C. Micro and nano-structured surfaces. *Journal of Materials Science-Materials in Medicine* 2003;14(8):721-5.
190. Curtis ASG, Casey B, Gallagher JO, Pasqui D, Wood MA, Wilkinson CDW. Substratum nanotopography and the adhesion of biological cells. Are symmetry or regularity of nanotopography important? *Biophys Chem* 2001;94(3):275-83.
191. Webster TJ, Siegel RW, Bizios R. Osteoblast adhesion on nanophase ceramics. *Biomaterials* 1999;20(13):1221-7.
192. Hanein D, Geiger B, Addadi L. Cell-Adhesion to Crystal-Surfaces - A Model for Initial-Stages in the Attachment of Cells to Solid Substrates. *Cells and Materials* 1995;5(2):197-210.
193. O'Brien J, Wilson I, Orton T, Pognan F. Investigation of the Alamar Blue (resazurin) fluorescent dye for the assessment of mammalian cell cytotoxicity. *Eur J Biochem* 2000;267(17):5421-6.
194. Gonzalez RJ, Tarloff JB. Evaluation of hepatic subcellular fractions for Alamar blue and MTT reductase activity. *Toxicology in Vitro* 2001;15(3):257-9.
195. Marieb EN. *Human Anatomy and Physiology*. 3rd Ed. 1995.
196. Zhang H, Lewis C, Aronow MS, Gronowicz GA. The effects of patient age on human osteoblasts' response to Ti-6Al-4V implants in vitro. *J Orthop Res* 2004 Jan;22(1):30-8.
197. Folkman J, Moscona A. Role of Cell-Shape in Growth-Control. *Nature* 1978;273(5661):345-9.
198. Li LH, Kong YM, Kim HW, Kim YW, Kim HE, Heo SJ, et al. Improved biological performance of Ti implants due to surface modification by micro-arc oxidation. *Biomaterials* 2004;25(14):2867-75.
199. Arnold M, Cavalcanti-Adam EA, Glass R, Blummel J, Eck W, Kantslehner M, et al. Activation of integrin function by nanopatterned adhesive interfaces. *Chemphyschem* 2004;5(3):383-8.
200. Cavalcanti-Adam EA, Micoulet A, Blummel J, Auernheimer J, Kessler H, Spatz JP. Lateral spacing of integrin ligands influences cell spreading and focal adhesion assembly. *Eur J Cell Biol* 2006;85(3-4):219-24.
201. Muller K, Skepper JN, Posfai M, Trivedi R, Howarth S, Corot C, et al. Effect of ultrasmall superparamagnetic iron oxide nanoparticles (Ferumoxtran-10) on human monocyte-macrophages in vitro. *Biomaterials* 2007;28(9):1629-42.
202. Hussain SM, Hess KL, Gearhart JM, Geiss KT, Schlager JJ. In vitro toxicity of nanoparticles in BRL 3A rat liver cells. *Toxicology in Vitro* 2005;19(7):975-83.

203. Beyersmann D. Effects of carcinogenic metals on gene expression. *Toxicol Lett* 2002;127(1-3):63-8.
204. Messer RLW, Bishop S, Lucas LC. Effects of metallic ion toxicity on human gingival fibroblasts morphology. *Biomaterials* 1999;20(18):1647-57.
205. Scotchford CA, Garle MJ, Batchelor J, Bradley J, Grant DM. Use of a novel carbon fibre composite materials for the femoral stem component of a THR system: in vitro biological assessment. *Biomaterials* 2003;24(26):4871-9.
206. Desai AV, Haque MA. Mechanics of the interface for carbon nanotube-polymer composites. *Thin-Walled Structures* 2005;43(11):1787-803.
207. Reissis N, Kayser M, Bentley G, Downes S. A hydrophilic polymer system enhanced articular cartilage regeneration in vivo. *Journal of Materials Science-Materials in Medicine* 1995;6(12):768-72.
208. Woodruff MA. Proteomics techniques for Integration into the Biomaterials field: to study Cell/Surface Interactions 2006.
209. Lozano K, Yang SY, Zeng Q. Rheological analysis of vapor-grown carbon nanofiber-reinforced polyethylene composites. *Journal of Applied Polymer Science* 2004;93(1):155-62.
210. Guedes RM, Simoes JA, Morais JL. Viscoelastic behaviour and failure of bovine cancellous bone under constant strain rate. *J Biomech* 2006;39(1):49-60.
211. Saidpour SH. Assessment of carbon fibre composite fracture fixation plate using finite element analysis. *Ann Biomed Eng* 2006;34(7):1157-63.
212. Foreman J, Sauerbrunn R, Marcozzi CL. Exploring the Sensitivity of Thermal Analysis Techniques to the Glass Transition. Technical paper found at http://www.tainstruments.com/library_download.aspx?file=TA082.PDF.
213. Bleach NC, Nazhat SN, Tanner KE, Kellomaki M, Tormala P. Effect of filler content on mechanical and dynamic mechanical properties of particulate biphasic calcium phosphate-poly(lactide) composites. *Biomaterials* 2002;23(7):1579-85.
214. Patel MP, Braden M, Davy KWM. Polymerization Shrinkage of Methacrylate Esters. *Biomaterials* 1987;8(1):53-6.
215. Colbert DT. Single-wall nanotubes: a new option for conductive plastics and engineering polymers. *Plastics, Additives and Compounding* 2003;5(1):18-25.
216. Souza PPC, Aranha AMF, Hebling J, Giro EMA, Costa CA. In vitro cytotoxicity and in vivo biocompatibility of contemporary resin-modified glass-ionomer cements. *Dent Mater* 2006 Sep;22(9):838-44.
217. Geurtsen W, Spahl W, Leyhausen G. Residual monomer additive release and variability in cytotoxicity of light-curing glass-ionomer cements and compomers. *J Dent Res* 1998;77(12):2012-9.
218. Hutcheon GA, Messiou C, Wyre RM, Davies MC, Downes S. Water absorption and surface properties of novel poly(ethylmethacrylate) polymer systems for use in bone and cartilage repair. *Biomaterials* 2001;22(7):667-76.
219. Ajayan PM, Ebbesen TW. Nanometre-size tubes of carbon. *Reports on Progress in Physics* 1997;60(10):1025-62.
220. Xu J, Donohoe JP, Pittman CU. Preparation, electrical and mechanical properties of vapor grown carbon fiber (VGCF)/vinyl ester composites. *Composites Part A-Applied Science and Manufacturing* 2004;35(6):693-701.
221. Endo M, Takeuchi K, Hiraoka T, Furuta T, Kasai T, Sun X, et al. Stacking nature of graphene layers in carbon nanotubes and nanofibres. *Journal of Physics and Chemistry of Solids* 1997;58(11):1707-12.

222. Brighton CT, Okereke E, Pollack SR, Clark CC. In vitro Bone Cell Response to A Capacitively Coupled Electrical-Field - the Role of Field-Strength, Pulse Pattern, and Duty Cycle. Clin Orthop 1992;(285):255-62.
223. Hwang GL, Shieh YT, Hwang KC. Efficient load transfer to polymer-grafted multiwalled carbon nanotubes in polymer composites. Advanced Functional Materials 2004;14(5):487-91.
224. Shim M, Kam NWS, Chen RJ, Li YM, Dai HJ. Functionalization of carbon nanotubes for biocompatibility and biomolecular recognition. Nano Letters 2002;2(4):285-8.
225. Huang HJ, Kajiura H, Yamada A, Ata M. Purification and alignment of arc-synthesis single-walled carbon nanotube bundles. Chemical Physics Letters 2002;356(5-6):567-72.
226. Pan ZW, Xie SS, Chang BH, Sun LF, Zhou WY, Wang G. Direct growth of aligned open carbon nanotubes by chemical vapor deposition. Chemical Physics Letters 1999;299(1):97-102.
227. Chen MY, Bai Z, Tan SC, Unroe MR. Friction and wear scar analysis of carbon nanofiber-reinforced polymeric composite coatings on alumina/aluminum composite. Wear 2002;252(7-8):624-34.

11. Appendix: *An in vitro study of the potential of Carbon Nanotubes and Nanofibres to Induce Inflammatory Mediators and Frustrated Phagocytosis*

The samples used in this project were used by Brown *et al.* in the following investigation, which was accepted on 12th May 2007 to appear in the Journal of Carbon. The samples are the same as those used in this current study but have different sample names. The commercial PR19PS sample is denoted as NT2, the MWNT9 nanotube sample is denoted as NT3, and the nanofibre samples are denoted as NF2 (GNF1) and NF1 (GNF3).

An *in vitro* Study of the Potential of Carbon Nanotubes and Nanofibres to Induce Inflammatory Mediators and Frustrated Phagocytosis

D.M. Brown^{1*}, I.A. Kinloch^{2,3}, U. Bangert³, A.H. Windle², D.M. Walter⁴,
G.S.Walker⁴, C.A. Scotchford⁴, K. Donaldson⁵ and V. Stone¹

¹School of Life Sciences, Napier University Colinton Road, Edinburgh, EH10 5DT, ²Dept. of Materials Science and Metallurgy, University of Cambridge, Pembroke Street, Cambridge, CB2 3QZ, ³School of Materials, University of Manchester, Grosvenor Street, Manchester, M1 7HS, UK, ⁴Bioengineering Group, School of Mechanical, Materials and Manufacturing Engineering, University of Nottingham, Nottingham, NG7 2RD, UK, ⁵ELEGI UoE/MRC Centre for Inflammation Research, QMRI, Edinburgh EH16 4TJ

*Corresponding Author

Tel +44 (0)131 455 2393

FAX +44 (0)131 455 2291

Email da.brown@napier.ac.uk

Abstract

There has been little information to date based on the potential health effects and hazards associated with the inhalation of carbon nanofibrous materials by workers despite their growing use in industry. This study examines the *in vitro* effects of a range of nanofibres and nanotubes for their ability to stimulate the release of the pro-inflammatory cytokine TNF- α and reactive oxygen species (ROS) from monocytic cells. Also assessed were the

toxic effect of the nanomaterials on the cells and the phagocytic ability of the cells after exposure. Our studies showed that the cellular response varied with fibre morphology and state of aggregation; long, straight, well-dispersed nanofilaments produced significantly more TNF- α and ROS in monocytic cells compared with highly curved and entangled materials. We also demonstrated that monocytic cell phagocytic ability was reduced after exposure to all of the nanotubes used in this study. Microscopic examination of the cells after treatment with the nanotubes showed 'frustrated phagocytosis'. The frustrated phagocytosis suggests that clearance of nanotubes from the lungs by macrophages may be impaired. There was no evidence of a toxic effect at any of the doses or time points used. These considerations may have important consequences for workers exposed to these nanomaterials.

1. Introduction

Nanoparticles are defined as particles with at least one dimension less than 100 nm and include quantum dots, nanotubes and exfoliated clays (confinement in 3, 2 and 1 dimensions respectively). A number of reports [1] have suggested that risks associated with nanoparticles exposure require investigation due to evidence that these particles can be more inflammogenic and toxic than larger particles comprising of the same material. This study focuses on carbon nanofibres, which typically possess diameters below 100 nm and lengths of the order of tens of microns. There is broad range of different carbon nanofibre types, depending on the size and orientation of the graphene layers within their structure. It is generally accepted that the major types of nanofibre are nanotubes consisting of hollow tubes of graphene sheets with the graphene planes parallel to the long axis of the fibre, herringbone fibres which consist of stacked graphene cones with the planes typically ~ 30 to 60° to the long fibre axis and platelet fibres with the graphene planes perpendicular to the long axis of the fibre. Of these,

nanotubes have received the majority of the scientific interest due to their intriguing combination of electrical, thermal and mechanical properties. However all types of nanofibres are used in scientific studies and commercially, with applications including fillers in composites for anti-static applications, reducing surface wear, catalyst supports, and components within rechargeable battery electrodes [2,3]. The implications for the increasing use and production of nanotubes include the potential increases in health risks to workers exposed to these materials. Until now, there is little information on the potential health effects and in particular, the hazards associated with the inhalation of nanotubes and nanofibres. All types of carbon nanofibres can exist as individual entities, however typically they are aggregated into micron-sized agglomerates. If these aggregates are formed during nanotube growth, then the nanotubes are highly entangled and the aggregates can be very hard to separate [4]. However, particles which are respirable can be generated from these aggregates, and it is these fine particles which are the main risk if inhaled into the lungs [5].

In the case of nanoparticles in general, the various geometries and sizes which are produced in the manufacturing process provide a range of samples which suggest that potentially these materials may present a health risk. A relationship between increased exposure to nanoparticles and adverse health effects has been described [6] and in individuals with pre-existing lung disease, inhalation of nanoparticles may induce inflammation and exacerbate respiratory and cardiovascular effects through the induction of oxidative stress and inflammation [7,8,9]. Nanoparticles of various types have been used in inhalation studies and have demonstrated various conditions such as pulmonary fibrosis, lung tumours, epithelial cell hyperplasia, inflammation and increased cytokine expression [10,11,12,13]. It is widely recognized that the mechanisms of fibre-induced lung injury with mineral fibres such as asbestos

depend on several factors, for example, length [14,15], diameter, chemical nature [16,17] and biopersistence [18,19]. Particles which enter the lung become coated with lung lining material, which is likely to modify the surface reactivity and hence the oxidant generating ability and phagocytosis of the particles. Interaction between lung phagocytic cells such as macrophages, by their surface receptor leads to phagocytosis of foreign particles and possibly a secretory response which is enhanced in the presence of opsonins such as IgG [20,21,22,23,24]. Phagocytosis is a stimulus for superoxide anion release and it has been shown that when macrophages attempt to phagocytose long fibres such as crocidolite asbestos the process of phagocytosis is frustrated and, superoxide is released to the outside of the cell [25,24]. The release of reactive oxygen species may be the initiating factor in the pathogenesis of lung disease after exposure to respirable fibres [26,27].

Phagocytic cells play a key role in the removal of deposited material in the lung. However, cells may become overloaded, phagocytic ability impaired and consequently clearance from the lung is reduced. Impaired macrophage function has been described after instillation of nanoparticles into rat lungs [28]. Macrophages demonstrated increased sensitivity, with regard to their ability to migrate towards a chemoattractant, and impaired phagocytic ability after exposure. Impaired clearance can result in damage to macrophages and the lung epithelium and it has been suggested that translocation of spherical nanoparticles into the cardiovascular system from the lungs could take place [29,30]. Translocation for nanofibres and nanotubes has not as yet been investigated. Finally, exposure of macrophages to nanoparticles has previously been shown to stimulate release the pro-inflammatory cytokine TNF- α [31,32], and TNF- α can stimulate lung epithelial cells to produce IL-8, a potent chemotactic cytokine for neutrophils. Prolonged release of TNF- α may increase the inflammatory response with resulting pathological consequences.

The purpose of the present study has been to investigate the ability of various nanofibrous materials of different morphologies to stimulate the production of superoxide anions and release of the pro-inflammatory mediator TNF- α in human monocytes. Furthermore, the phagocytic ability of a human macrophage cell line after exposure to nanomaterials was assessed.

2. Methods

The methods are given in detail below but in summary, a variety of different nanotube and nanofibre samples were either synthesised by the authors or purchased and analysed by BET surface area, electron microscopy and elemental dispersive X-ray (EDX). These samples were then dispersed in a RPMI medium and introduced to cells at different concentrations. Two different cell types were used, human mononuclear cells derived from donor's blood and cells from an immortalised THP-1 cell line. The nanofibre treated cells were (1) examined by light microscopy to assess how well the nanofibres were phagocytosed (taken up) by the cells. Assays were also used to study (a) cell death by measuring the LDH enzyme which leaks out of dead cells (b) pro6 inflammatory effects as measured by the protein TNF- α (c) apoptosis (programmed cell death) (d) necrosis (cell death from acute damage, i.e., toxic reaction to the nanofibres) and (e) production of the superoxide anion which is produced by the macrophage oxidative burst. The ability of the nanomaterials to inhibit normal cellular function was assessed by exposing the cells first to the nanomaterials and then to *E-coli* bacteria and then measuring how effectively the *E-coli* were phagocytosed by the cells. Data from all of the experiments were analysed using a General Linear Model with analysis of variance with Tukey's multiple comparison test. Significance was set at $p < 0.05$.

2.1 Isolation of Human Peripheral Blood Mononuclear Cells

Human peripheral blood mononuclear cells were prepared according to the protocol of Dransfield et al, (1994) [35]. In brief, two separate volumes of 40 ml of blood were withdrawn from healthy consenting volunteers and transferred to 50 ml sterile Falcon tubes containing 4 ml of 3.8% sodium citrate solution. Tubes were gently inverted and centrifuged at 250g for 20 minutes, the plasma removed from each tube and pooled without disturbing the cell pellet. Dextran (Pharmacia), prepared as a 6% solution in saline was warmed to 37°C, before adding to the cell pellet (2.5 ml/10 ml cell pellet) and the volume made up to 50 ml with sterile saline solution. Tubes were gently mixed and the cells allowed to sediment at room temperature for 30 minutes. In order to prepare autologous serum, calcium chloride solution (220 µl 1M /10 ml), was gently mixed with the plasma and incubated in a glass tube at 37°C until the clot retracted. Percoll (Pharmacia) gradients were made from a stock solution of 90% (18 ml Percoll + 2 ml 10x PBS, (Life Technologies, Paisley) without calcium or magnesium) to give final concentrations of 81%, 70% and 55% using 1x PBS. The separating gradient was prepared by layering 2.5 ml of 70% percoll over 2.5 ml 81% percoll. The leukocyte-rich fraction from the dextran sedimentation was transferred to sterile falcon tubes, 0.9% saline added to give a final volume of 50 ml and the tubes centrifuged at 250g for 6 minutes. The pellet was resuspended in 55% percoll and 2.5 ml layered over the previously prepared separating gradients. Tubes were centrifuged at 290g for 20 minutes and the mononuclear cells collected from the 55/70 layer. Cells were washed twice with PBS, counted, and resuspended in RPMI medium at a concentration of 5×10^6 cells/ml and 1 ml added to each well of a 24 well plate. In some treatments, a sterile 10 mm glass coverslip was placed in wells of a 24 well plate prior to adding cells. The cells were incubated for 1 hour at 37°C, the medium removed and replaced with RPMI plus 10% autologous serum and incubated for 48 hours at 37°C.

After the second incubation, the medium was replaced and the cells incubated or a further 72 hours prior to treatment.

2.2 Human mononuclear cell treatments

The nanomaterials were stored at room temperature and weighed out using a microbalance contained within a glove-box. These were then suspended in RPMI medium and sonicated briefly for 2 minutes in a sonicating water bath to aid dispersion. In order to maintain sterility, a sonicating probe was not used for this process. The use of chemical dispersants for this procedure was avoided as these could potentially modify the material and therefore change the surface chemistry or they could have a toxic effect on the cells. A range of concentrations from 15.625 µg/ml to 62.5µg/ml were prepared and added to the cells. The differentiated cells (above) were washed using RPMI medium and 250 µl of appropriate sample suspension added to wells of a 24 well plate. Cells and treatments were incubated at 37°C for 4 hours, the supernatant removed, centrifuged for 5 minutes at 12000g and stored at -80°C until required. The nanomaterials appeared to be well dispersed as determined by light microscopy. Scanning electron microscopy (SEM) confirmed that the dispersion treatment used had not broken up these aggregates further into individually dispersed nanofibres, except for partially in the case of the aligned multi-walled nanotube sample (NT1). (See section 3.1.) Therefore the samples presented to the cells were aggregates of the same size and shape as in the as-produced samples and most relevant to the samples to which an industrial worker could potentially be exposed.

2.3 THP-1 Cell culture and differentiation

THP-1 cells were maintained in continuous culture in RPM-I medium containing 10% foetal calf serum, L-Glutamine and Penicillin/Streptomycin. When the flask was confluent (approximately after 3-4 days culture), IFN-γ

(Genzyme) was added to a flask to give a final concentration of 100 U/ml. The cells were incubated for 48 hours at 37°C, removed from the flask, washed with PBS and resuspended at the required concentration in RPM-I for use in phagocytosis and apoptosis experiments (see below).

2.3 Light microscopy of human mononuclear cells

Human monocytes were isolated and set up as previously described in 24 well plates, each well containing a sterile 10 mm diameter glass coverslip, and as described above. Cells were treated with suspensions of CNFs or CNTs at concentrations of ranging from 15.6 µg/ml to 125 µg/ml in a 250 µl volume of RPM-I medium without serum. Treatments were incubated for four hours at 37°C after which the supernatant was removed and stored at -80°C until required. Coverslips were washed using PBS and stained with DiffQuik (Raymond Lamb, London) before mounting on glass microscope slides.

2.4 LDH assay

Fifty microlitres of 0.75 mM aqueous sodium pyruvate (Sigma) solution containing NADH (Sigma) at a concentration of 1 mg/ml were pipetted into each well of a 96 well plate and incubated at 37°C for 5 minutes. A series of standards were prepared to give a range of dilutions representing 0-2000 Units/LDH/ml. Fifty microlitres of pyruvate/NADH solution gave a concentration of 2000 LDH Units/ml. Ten microlitres of previously prepared cell supernatants were added to the wells in triplicate groups and thoroughly mixed. The plate was incubated for exactly 30 minutes at 37°C. Fifty microlitres of 2,4-dinitrophenylhydrazine (Sigma) solution dissolved in 1M HCl (10 mg/dl) were added to each well and incubated at room temperature for 20 minutes. To develop the final colour, 50 µl of 4 M NaOH was added to each well, mixed and allowed to stand for 5 minutes. The absorbance was read at 540 nm on an automatic plate reader.

2.5 Apoptosis

Differentiated THP-1 cells were plated into wells of a 24-well plate at a concentration of 2.5×10^5 cells/ml in a 250 μ l volume. Nanotubes or CNF's were suspended in RPM-I, sonicated briefly, and added to appropriate wells in a 250 μ l volume to give final concentrations of 15.625 μ g/ml and 31.25 μ g/ml. The cell/treatment suspensions were incubated at 37°C for 4 and 24 hours. The supernatant from the 24 hour group were retained for TNF- α estimation. The cells were washed using PBS and stained with Annexin-V and propidium iodide according to the manufacturers instructions (Annexin-V Staining Kit, Roche Diagnostics). Cells were resuspended in 0.5 ml PBS and analysed by flow cytometry. Gates were set to measure the percentage of necrotic (Propidium Iodide stained cells) and apoptotic cells (Annexin-V stained).

2.6 TNF- α ELISA

The supernatants previously prepared were assayed for TNF- α protein content using a commercially available human TNF- α kit (Biosource) according to the manufacturer's instructions. Briefly, each well of a 96-well plate was coated overnight with capture antibody, before washing with PBS containing 0.05% tween, and then adding test supernatant to the appropriate wells in triplicate groups. After incubation for 2 hours at room temperature, the wells were washed, a detection antibody added and incubated for a further hour at room temperature. The wells were then washed with PBS/tween before addition of Horseradish peroxidase (HRP)-conjugated streptavidin and incubated for 45 minutes at room temperature. Finally, the colour was developed by adding peroxidase substrate to each well, before reading the absorbance at 450 nm using a Dynatec plate reader.

2.7 Superoxide anion assay

This assay was based on the reduction of Cytochrome C [36]. The reaction mixture consisted of 50 mg Cytochrome C; 100 mg Dextrose and 50 ml PBS. Nine-hundred microlitres of cytochrome C reaction mixture was pipetted into wells of a 24-well plate and 100 μ l of the appropriate CNT or CNF suspension to give the required concentration was added. Duplicate plates were set up to include a set of treatments for PMA stimulation. Differentiated human peripheral blood mononuclear cells (5×10^5 cells/well) were incubated with the nanomaterials at 37°C for 2 hours. Controls contained no CNTs. A control consisting of superoxide dismutase (SOD) was also included, consisting of cytochrome C mixture containing 0.1 μ g/ml PMA and 150 units SOD/ml. The wells were mixed and the plates incubated at 37°C for 1 hour. After 1 hour, one set of treatments received PMA to give a final concentration of 0.1 μ g/ml. After a further hour incubation, samples were transferred to triplicate groups of wells of a 96-well plate and read at 550 nm using a Dynatec plate reader. Results were expressed as nmoles O_2^- /500,000 cells/2 hours.

2.8 Effect of dose of nanomaterial on the phagocytic ability of THP-1 cells

Differentiated THP-1 cells were removed from culture, washed with PBS and resuspended at 0.5×10^6 cells /ml in RPM-I medium (serum free). The cell suspension (500 μ l) was added to wells of a 24-well plate and 0.5 ml of appropriate CNT or CNF suspension was added to give final concentrations of 15.625 μ g/ml and 31.25 μ g/ml. A control consisting of cytochalasin B at a concentration of 500 μ g/ml was included. The treatments were incubated for 4 hours at 37°C. After incubation, cells from each treatment were transferred to plastic FACS tubes (Falcon) and washed with PBS. Cells were incubated for 2 hours with a 50 μ l suspension of FITC labelled E. coli diluted according to the manufacturers instructions (Vibrant Phagocytosis Assay, Roche

Diagnostics). Cells uptake of the fluorescent *E-coli* was analysed by flow cytometry.

3 Results

3.1 Characterisation of nanofibre (CNF) and nanotube (CNT) materials

The nanofibres used in this study were obtained from the University of Cambridge [33], University of Nottingham and Applied Sciences Incorporated (ASI) and are summarised in Table 1. These samples can be split into carbon nanotubes (NTs) where the graphene planes are parallel to the fibre axis and nanofibres (NFs). The samples used were analysed by transmission electron microscopy (TEM, Jeol 200CX and FEI Tecnai), using bright field imaging, dark field imaging, electron diffraction and high resolution imaging to determine their structure. Figure 1 shows the results of these studies. NT1 consisted of very straight, long multi-walled carbon nanotubes, with the 002 perpendicular to the fibre axis. NT2 was found to consist of a mixture of multi-walled carbon nanotubes and bamboo fibres, both of which were relatively straight. The bamboo fibres had internal closure of the tube layers intermittently down their axis. NT3 comprised of highly curved, multi-walled nanotubes. The NF2 sample consisted of a mixture of short nanotubes and platelet nanofibres, with the 002 axis parallel to the fibre axis. Whereas, NF1 pre-dominantly contained a mixture of both these platelet nanofibres and herringbone nanofibres, with 002 plane $\sim 40^\circ$ to the fibre axis.

The size of the individual fibres was also assessed by electron microscopy. The diameters of each sample are given in Table 1, as measured by TEM. The lengths, though, were more difficult to obtain, particular in the highly entangled samples. The NT1 nanotubes were found to be up to 50 μm in length, which was determined by measuring the length of the high aligned mats in which they grew (Figure 2). NF2 and NF3 could be seen under TEM to

be typically on the order of a few microns long. However, the fibre lengths could not be obtained for all the other samples since they were too entangled to find two ends of the same nanotube. This problem is common for nanofibre aggregates.

All the nanofibres used were produced by the catalytic vapour deposition route which produces materials in relatively large quantities and high purity but with a large number of defects in the lattice. Typically, the catalyst remains in the final nanotubes but tends to be encapsulated and inaccessible to cells (SOM 1, see supplementary data). However, given the potential toxicological effects of certain metals (e.g. nickel), the residual catalyst content was measured by EDX in the SEM and listed in Table 1.

It was important to evaluate the aggregate structure of the as-produced carbon nanofibres since these aggregates were the particles that the workers would be exposed to and their cells potentially come in contact with. Therefore, scanning electron microscopy (SEM, Jeol 6340) was used to image the as-produced material. In general, the nanotubes and nanofibres in the samples were highly entangled into aggregates. These aggregates were ten's of microns in diameter, with only a few individually dispersed fibres (Figure 2). The material which appeared least entangled was NT1, which comprised of mats of highly aligned nanotubes which had been harvested from a silica growth substrate [33]. The unentangled nature of these flakes meant that the nanotubes could disperse into individual entities upon shear as highlighted in composite studies [34].

The materials were also examined after their dispersion in cell growth medium as these samples represented the aggregation state that the cell would actually observed in studies present herein. These SEM samples were

produced by taking samples from the treated dispersions, diluting them to prevent further aggregation and then drying them upon SEM stubs. As Figure SOM2 shows (see supplementary data), the ultra-sonic bath used to disperse the nanotubes was of suitably low power that the nanotubes and their aggregates were not chopped apart. (High power ultra-sonic waves can cut nanotubes into smaller segments.) In the case of NT1, the nanotubes were not shortened but the aggregates were partially separated into individual fibres due to the unentangled nature of the tubes. It can be therefore concluded, that with the exception of NT1, the samples introduced to the cells were comparable to those as-produced.

3.2 Treatment of cells with the nanomaterials

The appearance of human peripheral blood mononuclear cells after 4 hours treatment with nanotubes and nanofibres at a concentration of 15.6 µg/ml is shown in Figure 3. The carbon nanoparticles can clearly be seen in the images as the black regions. However, it should be noted that since their diameters are under the wavelength of light, it is impossible to see individual particles and to tell how many particles are lying next to each other. It appeared that the nanotube samples (NT1 and NT2) were not completely phagocytosed by the mononuclear cells, and some targets were too large to be fully phagocytosed, indicating frustrated phagocytosis in which no phagosome is formed by the cell. Frustrated phagocytosis appeared to be more extensive for NT1 than NT2. In general, NT3 appeared to be readily phagocytosed by the macrophages. Likewise, both the nanofibre samples (NF1 and NF2) were readily phagocytosed.

The LDH content of supernatants from CNT and CNF treated mononuclear cells is shown in Figure 4. Over the range of doses used, there

was no evidence of increased toxicity, as indicated by LDH release nor was there a clear dose effect of treatment.

In addition to measuring LDH as a marker of cell death, apoptosis and necrosis were assessed by flow cytometry. The apoptotic/necrotic status of THP-1 cells after treatment with 15.6 µg/ml and 31.25 µg/ml CNF's and CNT's was investigated using Annexin-V and Propidium iodide staining followed by flow cytometry analysis. After both 4 and 24 hours treatment, there was no increased apoptosis or necrosis in any of the particle treatments compared with the control (Figure 5). The surfactant used in this study, triton X-100 (0.01%) was used as a positive control and induced necrosis in approximately 25% of the cells at both particle concentrations. It was not possible to use primary human monocytes for this assay as they did not withstand the resuspension procedure prior to flow cytometry.

TNF- α release from human peripheral blood mononuclear cells treated at doses of 15.625 µg/ml to 62.5 µg/ml is shown in figure 6, with all data were normalised to the control. A clear dose effect of treatment was evident for the CNT's and CNF's, and there was a statistically significant difference between the control versus NT1 and NT2 samples ($p < 0.05$) at 4 hours. The straighter NTs showed the greatest TNF- α release at the highest dose compared with the other CNT samples (NT3) which did not produce significant TNF- α protein release at these particle concentrations. Neither CNF, nor the UfCB or LFA samples stimulated significant TNF- α release at the concentrations tested due to considerable variation in the data. TNF- α release from THP-1 cells after 24 hours treatment with NT1 and NT2 was increased compared with the control, but this difference was not statistically significant.

The number of nmols O_2^- /500,000 cells released from peripheral blood mononuclear cells in 2 hours is shown in Figure 7. Over the range of concentrations of treatment used, there was an apparent clear dose effect in the unstimulated series of experiments. The greatest increase in unstimulated O_2^- production was observed at a dose of 31.25 $\mu\text{g/ml}$ for NT2 and NF1 ($p < 0.05$) (Figure 7a). In PMA stimulated monocytes, the previously observed dose effect was no longer apparent, however, there was a statistically significant difference ($p < 0.05$) between the control and nanotube samples NT1 and NT2, the two rigid fibre-like samples. Conversely, UfCB decreased the phagocytic burst of the primed cells (Fig 7b) ($p < 0.05$), while LFA had no significant effect at these doses.

The ability of THP-1 cells to phagocytose fluorescently labelled *E-coli* bacteria was examined after treatment of the cells with NTs and NFs ranging from concentrations of 15.6 $\mu\text{g/ml}$ to 62.5 $\mu\text{g/ml}$ (Figure 8). After treatment with particles for four hours, there was clear impairment in the cells ability to phagocytose *E-coli* and this effect was dose dependent. There was a significant difference between the control and all particle samples ($p < 0.05$) with the exception of NF2. Typically, at a dose of 62.5 $\mu\text{g/ml}$ the phagocytic ability was reduced from 80% for the control to approximately 50 – 60% for the cells treated with CNT and CNF. The 'control' particle UfCB reduced the phagocytic ability of THP-1 cells to approximately 30% of the control at a dose of 62.5 $\mu\text{g/ml}$. Long fibre amosite asbestos decreased the phagocytic capacity at the two higher concentrations tested.

4. Discussion

Short-term in vitro studies have been a focus of testing, in the case of asbestos and man-made mineral fibres, in the hope that these tests may give a clear indication of the potential pathogenicity of different fibres and particles

[37]. The purpose of the present study was to investigate a range of nanomaterials in order to gain an understanding of the mechanisms by which nanoparticles of varying dimensions and composition interact with phagocytic cells of the lung. Apart from dimension, durability and physical structure, NPs may contain different amounts of impurities due to the manufacturing process, and these may be important in driving cellular reactions such as the production of reactive oxygen species (ROS). Nanoparticle surface chemistry and reactivity are important considerations when predicting pathogenicity and transition metal contamination may play a key role in driving ROS production.

Phagocytosis of particles and foreign material is an important first step in the production of ROS. Binding to the cell membrane triggers the NADPH oxidase system in macrophages which catalyses the reduction of molecular oxygen to O_2^- [38]. Therefore, the ability of macrophages to bind nanoparticles may be an important factor when considering the toxicity of these materials. All of the particles studied were taken up to some extent by macrophage phagocytosis. However, the straighter CNT samples with more individually dispersed fibres exhibited signs of incomplete uptake or frustrated phagocytosis. This correlated well with the superoxide anion study as these two samples also stimulate increased ROS production. The impairment of macrophage function, in particular the ability to phagocytose nanoparticles is a factor which could be used to determine the toxicity of nanoparticles. It is recognised that the phagocytic function of cells is modulated by cytokines and pro-inflammatory mediators [39] and the release of these from already stimulated cells may be a reason for the changes in phagocytic ability of cells demonstrated here. Nanotubes and nanofibres which undergo 'frustrated phagocytosis' may escape clearance by normal mechanisms and persist in the lung suggesting that the straight CNT may be more problematic than the tangled CNT or the CNF. Frustrated phagocytosis and decreased clearance

leads to increased inflammation, allowing inflammation to become chronic and pathological changes to proceed. In fact, the NT1 and NT2 were also more potent than the tangled CNT in terms of stimulating production of the proinflammatory cytokine TNF- α suggested an enhanced ability to promote inflammation. At a time point of 24 hours post treatment using THP-1 cells, increased TNF- α was observed again with the NT1 and NT2 samples compared with the control. This effect, however, was not statistically significant and suggests that the acute exposure time of 4 hours is a more realistic time point at which to study cytokine release. The importance of frustrated phagocytosis and the release of TNF- α has also been demonstrated by Ye *et al* [40]. Despite the apparent difference in terms of uptake by macrophages, all three CNT inhibited subsequent phagocytosis of *E-coli*, as observed for other nanoparticles such as UfCB. The nanomaterials were also shown to have no detrimental effects on cells as indicated by their lack of ability to produce apoptosis or necrosis at both 4 hours or 24 hours post treatment. These results do, however, suggest an impairment of macrophage function that would promote disease by decreasing particle and pathogen clearance.

The CNF's or the reference LFA asbestos sample tested in this study did not stimulate TNF- α release, or O₂⁻ in the PMA primed monocytes. However, NF1 did appear to increase O₂⁻ production in the unprimed monocytes and to inhibit phagocytosis of *E. coli*. This would suggest that the potency of CNF may depend on their graphene structure, with the platelet form being more potent than the platelet/herringbone, although further studies would be required to test this hypothesis further. LFA has been extensively studied for its ability to produce pathological change *in vivo*. The interaction between fibres and surfactant *in vivo* may be an important modifying factor of the fibres activity which is not observed in the *in vitro* experiments carried out here. Chemical dispersants were not in this study

added to promote disaggregation of the materials as we wished to obtain baseline information relating to the most simple exposure. These measurements may in the future be used to compare differences between chemically dispersed and non-chemically dispersed samples. These results also suggest that NF1 exhibits an effect on monocytes that is comparable to the straight CNT in some respects (O_2^- and inhibition of phagocytosis) but not in others (TNF- α production and O_2^- production in primed monocytes). These data show that different CNT and CNF vary considerably in their impact on macrophage function and activation, suggesting that their *in vivo* effects may also be variable. Superoxide production was in general modest and the impact on pathology and toxicity is debatable. This requires further analysis of oxidative stress in cells and ROS production by CNT to determine the potential for oxidative driven disease mechanisms using an appropriate exposure regime. A study of this type may provide information pertaining to the factors responsible for controlling or modulating nanofibre toxicity. Nanoparticles have been shown to generate ROS and cause oxidative stress [34] and various nanoparticles have been shown to generate more free radicals and ROS than fine particles [34,41]. Activation of the proinflammatory transcription factor NF- κ B is regulated by a number of second messengers, including Ca^{2+} [42] and ROS [43]. Hence, the production of ROS shown here by CNTs may be the trigger for transcription factor activation and may explain the release of the cytokine TNF- α . The role of Ca^{2+} in this series of events remains unknown and should be the focus of further investigation. It is not clear from this study whether the oxidative pathways which could drive TNF- α protein release could be due to ROS derived directly from the NP's or from cell generated ROS. Using an *in vitro* primary monocytic culture system, this study highlights potential differences between the toxic effects of different CNTs and CNFs. For example, at sub-lethal doses, although all nanoparticles tested were taken up by macrophages, the longer and straighter CNTs (NT1

and NT2) exhibited signs of inducing frustrated phagocytosis as exemplified by microscopy images and O_2^- production by PMA stimulated cells. In contrast the tangled CNT (NT3) was easily engulfed by the cells and did not enhance O_2^- production.

A further important consideration is whether or not any 'leachable' products from the NPs themselves may be important in driving the mechanisms we have reported. Transition metals are a definite source of free radicals which are important in ultrafine particle stimulated lung inflammation [44]. Other authors have reported that metal impurities contained in CNT products induced dosedependent lung granulomas when instilled into the lungs of mice [45]. This appeared to be a feature of the CNTs themselves rather than contamination, since acid treated CNTs also produced granuloma formation in mice. In the *in vitro* experiments we have carried out, the role of a leachable product in producing the effects we have demonstrated cannot be ruled out and further investigations are required. It is worth noting that there is considerable variability in the data which we initially assumed was due to donor variation and hence differences in the amplitude of cellular responses. In future we suggest that the toxicity of CNT should be considered when freshly generated and at specific times subsequent to manufacture in order to investigate this further. However, in this study, the cellular and CNT sources of variation have prevented fairly substantial changes in endpoints, for example a 4-fold increase in TNF- α release, to be regarded as not significant.

Conclusions

We have demonstrated here that the ability of nanomaterials to stimulate the release of the pro-inflammatory mediator TNF- α and the release of ROS in monocytic cells *in vitro* may depend to a large extent of the geometry and surface characteristics of the nanomaterial. We have also

shown that all the materials used here had a negative impact on the phagocytic ability of cells, which may in turn be the reason for 'frustrated phagocytosis'. These important considerations may have important consequences for workers exposed to these materials, and demonstrate that at this time new nanofibres may need to be tested on a case by case basis.

One should consider that the risk of exposure from nanofibrous materials comprises two factors, the hazard of the material should it enter the body and the exposure (chance of the material entering the body in the first place.) While this paper addresses the former in some detail, the latter still requires further investigation. The large body of literature on the issues of processing nanotubes highlights how difficult it is to disperse or break up the nanotubes in order to get them airborne. The location where these airborne aggregates will deposit in the lung will depend on their air-dynamic radius. Furthermore, various air monitoring systems have been run in Cambridge under profession occupational hygiene guidance and no nanotubes have ever been observed within the air of the laboratory.

Acknowledgements

This study was generously funded by the COLT Foundation, the Royal Academy of Engineering and the EPSRC.

References

- [1] Nanoscience and nanotechnologies: opportunities and uncertainties The Royal Society and The Royal Academy of Engineers.. 2004.
- [2] Arepalli S, Nikolaev P, Holmes W, Files BS. Production and measurements of individual single-wall nanotubes and small ropes of carbon. *Appl. Phys. Lett.* 2001; 78: 1610-1612
- [3] Ball P. Roll-up for the revolution. *Nature* 2001; 414: 142-144
- [4] Ajayan PM, Ebbesen TW Nanometre-size tubes of carbon. *Rep. Prog. Phys.* 1997; 60: 1025-1062
- [5] Maynard A.D, Baron P.A, Foley M, Shvedova AA, Kisin ER, Castranova V. Exposure to carbon nanomaterial I: Aerosol release during the handling of unrefined single walled carbon nanotube material. *J. Toxicol. Environ. Health.* 2004; 9: 67(1) 87-107
- [6] Meiring JJ, Borm PJA, Bagate K, Semmler M, Seitz J, Takenaka S, et al. The influence of hydrogen peroxide and histamine on lung permeability and translocation of iridium nanoparticles in the isolated perfused rat lung. *Particle and Fibre Toxicology* 2005; 2:3

- [7] Ferin J, Oberdoster G, Penney DP. Pulmonary retention of ultrafine and fine particles in rats. *Am. J. Respir. Cell Mol. Biol.* 1992; 6: 535-542
- [8] Seaton A, MacNee W, Donaldson K, Godden D. Particulate air pollution and acute health effects. *Lancet* 1995; 345: 176-178
- [9] Utell MJ, Frampton MW. Acute health effects of ambient air pollution: The ultrafine particle hypothesis. *J. Aerosol Med.* 2000; 13: 355-359
- [10] Dasenbrock C, Peters L, Creutzenberg O, Heinrich U. The carcinogenic potency of carbon particles with and without PAH after repeated intratracheal administration in the rat. *Toxicol. Lett.* 1996; 88: 15-21; 1996
- [11] Driscoll KE, Carter JM, Howard BW, Hassenbein DG, Pepelko W, Baggs RB, et al. Pulmonary inflammation, chemokine, and mutagenic responses in rats after subchronic inhalation of carbon black. *Toxicol. Appl. Pharmacol.* 1996; 136: 372-380 21
- [12] Oberdoster G, Ferin J, Lehnert BE. Correlation between particle-size, *in vivo* particle persistence, and lung injury. *Environ. Health Perspect.* 1994; 102: 173-179
- [13] Nikula KJ, Snipes MB, Barr EB, Griffith WC, Henderson RF, Mauderly JL. Comparative pulmonary toxicities and carcinogenicities of chronically inhaled diesel exhaust and carbon black in F344 rats. *Fund. Appl. Toxicol.* 1995; 25: 80-94
- [14] Donaldson K, Brown GM, Brown DM, Bolton RE, Davis JMG. The inflammatory generating potential of long and short fibre amosite asbestos samples. *Br. J. Ind. Med.* 1989; 46: 271-276
- [15] Donaldson K, Miller BG, Sara E, Slight J, Brown RC. Asbestos fibre lengthdependent detachment injury to alveolar epithelial cells *in vitro*: role of a fibronectin-binding receptor. *Int. J. Exp. Pathol.* 1993; 74: 243-250
- [16] Hesterberg TW, Barrett JC. Dependence of asbestos and mineral dustinduced transformation of mammalian cells in culture on fibre dimension. *Cancer Res.* 1984; 44: 2170-2180
- [17] Hart GA, Kathman LM, Hesterberg TW. In vitro cytotoxicity of asbestos and man-made vitreous fibres: roles of fibre length, diameter and composition. *Carcinogenesis.* 1994; 15: 971-977
- [18] Morgan A, Holmes A. Solubility of asbestos and man-made mineral fibres *in vitro* and *in vivo*: its significance in lung disease. *Environ. Res.* 1986; 39: 475-484
- [19] Donaldson K. Biological activity of respirable industrial fibres treated to mimic residence in the lung. *Toxicol Lett.* 1994; 72:(1-3):299-305
- [20] Scheule RK, Holian A. IgG specifically enhances chrysotile asbestosstimulated superoxide anion production by the alveolar macrophage. *Am. J. Respir. Cell Mol. Biol.* 1989; 1: 313-318
- [21] Nyberg P, Klockars M. Effect of immunoglobulins on mineral dustinduced production of reactive oxygen metabolites by human macrophages. *Inflammation* 1990; 14: 671-679 22
- [22] Perkins RC, Scheule RK, Holian A. *In vitro* bioactivity of asbestos for the human alveolar macrophage and its modification by IgG. *Am. J. Respir. Cell Mol. Biol.* 1991; 4: 532-537
- [23] Donaldson K, Li XY, Dogra S, Miller B, Brown G. Asbestos-stimulated tumour necrosis factor release from alveolar macrophages depends on fibre length and opsonisation. *J. Pathol* 1992; 168: 243-248
- [24] Hill IM, Beswick PH, Donaldson K. Differential release of superoxide anions by macrophages treated with long and short fibre amosite asbestos is a consequence of differential affinity for opsonin. *Occup. Environ. Med.* 1995; 52: 92-96
- [25] Goodlick LA, Kane AB. Role of reactive oxygen metabolites in crocidolite asbestos toxicity to mouse macrophages. *Cancer Res* 1986; 46: 5558-5566
- [26] Vallyathan V, Mega JF, Xianglin S, Dalal NS. Enhanced generation of free radicals from phagocytes induced by mineral dusts. *Am. J. Respir. Cell Mol. Biol.* 1992; 6: 404-413
- [27] Kamp DW, Graceffa P, Pryor WA, Weitzman SA. The role of free radicals in asbestos-induced diseases. *Free Rad. Biol. Med.* 1992; 12: 293-315
- [28] Renwick L, Brown D, Clouter A, Donaldson K. Increased inflammation and altered macrophage chemotactic responses caused by two ultrafine particle types. *Occup. Environ. Med.* 2004; 61(5): 442-447
- [29] Nemmar A, Vanbilloen H, Hoylaerts MF, Hoet PH, Verbruggen A, Nemery B. Passage of intratracheally instilled ultrafine particles from the lung into the systemic circulation in hamsters. *Am. J. Respir. Crit. Care Med.* 2001; 164(9): 1665-1668
- [30] Nemmar A, Hoet PH, Vanquickenborne B, Dinsdale D, Thomeer M, Hoylaerts MF, et al. Passage of inhaled particles into the blood circulation in humans. *Circulation* 2002; 105(4): 411-414
- [31] Jimenez LA, Drost EM, Gilmour PS, Rahman I, Antonicelli F, Ritchie H, et al. PM₁₀-exposed macrophages stimulate a proinflammatory response in lung epithelial cells via TNF- α . *Am. J. Physiol. Lung Cell Mol. Physiol.* 2002; 282(2): L237-L248 23
- [32] Brown DM, Donaldson K, Borm PJ, Schins RP, Denhardt M, Gilmour P, et al. Calcium and ROS-mediated activation of transcription factors and TNF- α cytokine gene expression in macrophages exposed to ultrafine particles. *Am. J. Physiol. Lung Cell Mol. Physiol.* 2004; 286: L344-L353
- [33] Singh CS, Shaffer MSP, Windle AH. Controlled Production of Controlled Architectures of Aligned Carbon Nanotubes by an Injection Chemical Vapour Deposition Method. *Carbon* 2003; 41: 359-368.

- [34] Stone V, Shaw J, Brown DM, MacNee W, Faux SP, Donaldson K. The role of oxidative stress in the prolonged inhibitory effect of ultrafine carbon black on epithelial cell function. *Toxicol. In Vitro*. 1998; 12: 649-659
- [35] Dransfield I, Buckle AM, Savill JS, McDowall A, Haslett C, Hogg N. Neutrophil apoptosis is associated with a reduction in CD 16 (FcγRIII) expression. *J. Immunol*. 1994; 153: 1254-1263
- [36] Johnston RB, Keele BB, Misra HP, Lehmeyer JE, Webb LS, Baehner RL, et al. The role of superoxide anion generation in phagocytic bacterial activity. Studies with normal and chronic granulomatous disease leukocytes. *J. Clin. Invest*. 1975; 55: 1357-1372
- [37] McClellan RO, Miller FJ, Hesterberg TW, Warheit DB, Bunn WB, Kane AB, et al. Approaches to evaluating the toxicity and carcinogenicity of man-made fibers: summary of a workshop held November 11-13, 1991, Durham, North Carolina. *Regul. Toxicol. Pharmacol*. 1992; 16(3): 321-364
- [38] Channock S.J., El Benna J., Smith R.M., Babior B.M. The respiratory burst oxidase. *J. Biol. Chem*. 1994; 269: 24519-24522
- [39] Brown EJ. Phagocytosis. *Bioessays*. 1995; 17: 109-117
- [40] Ye J, Shi X, Jones W, Rojanasakul Y, Cheng N, Schwegler-Berry D, et al. Critical role of glass fiber length in TNF- production and transcription factor activation in macrophages. *Am J Physiol Lung Cell Mol Physiol*, 1999; 276: 426-434
- [41] Wilson MR, Stone V, Cullen RT, Searl A, Maynard RL, Donaldson K. In vitro toxicology of respirable Montserrat volcanic ash. *Occup. Environ. Med*. 2000;57(11): 727-733 24
- [42] Staal FJT, Roederer M, Herzenberg LA, Herzenberg LA. Intracellular thiols regulate activation of nuclear factor kappa-B and transcription of human immunodeficiency virus. *Proc. Natl. Acad. Sci*. 1990; 87(24): 9943-9947
- [43] Rahman I, MacNee W. Role of transcription factors in inflammatory lung diseases. *Thorax* 1998; 53: 601-612
- [44] MacNee W, Donaldson K. Particulate air pollution: Injurious and protective mechanisms in the lungs. In *Air Pollution and Health* (S.T. Holgate, J.M. Samet, H.S. Koren and R.L. Maynard Eds.) 1999; pp653-672. Academic Press, London.
- [45] Lam CW, James JT, McCluskey R, Hunter RL. Pulmonary toxicity of singlewalled carbon nanotubes in mice 7 and 90 days after intratracheal instillation. *Toxicol. Sci*. 2004; 77: 126-134

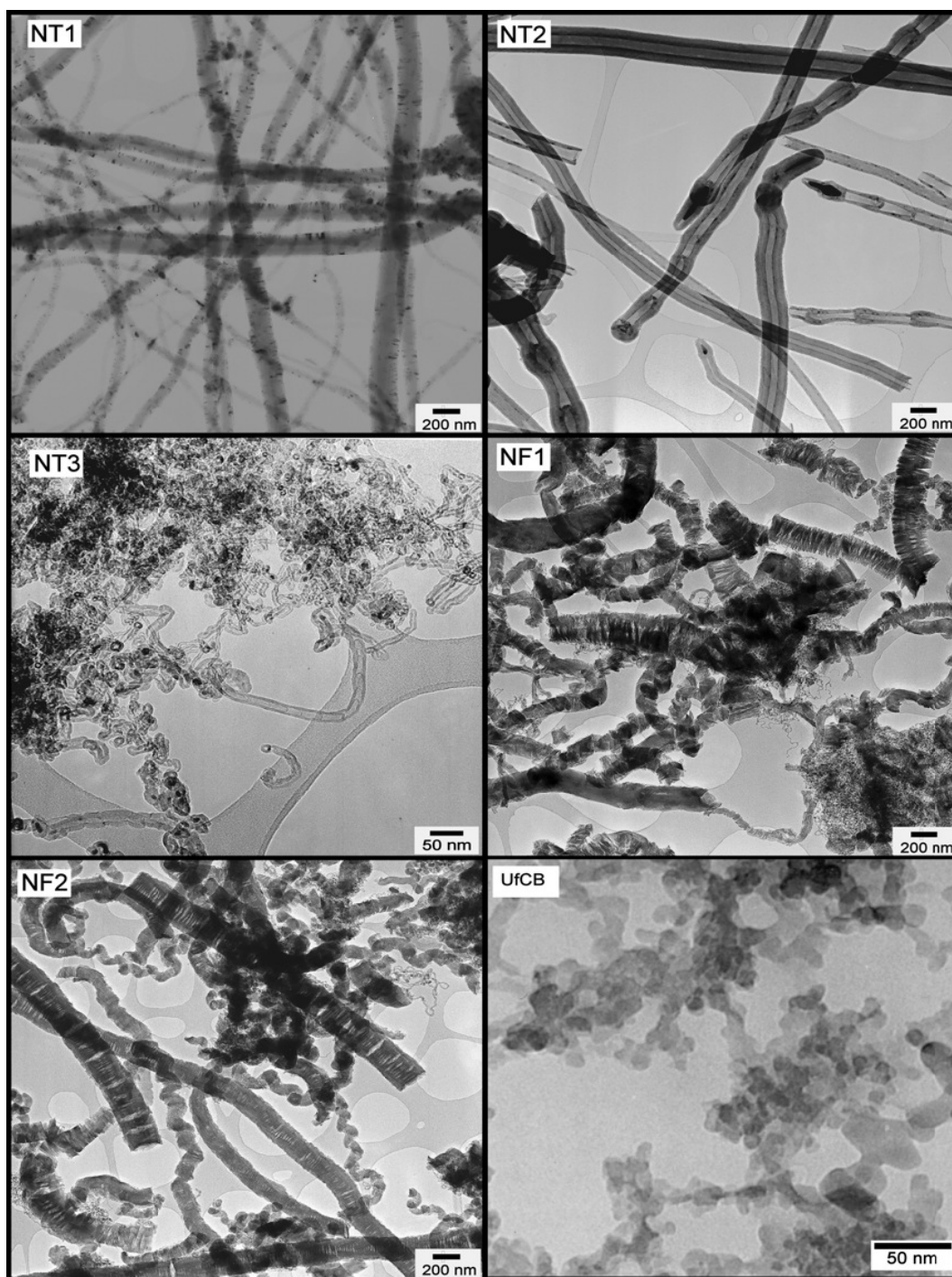


Figure 1: Bright field TEM micrograph of the carbon nanoparticles used in this study.

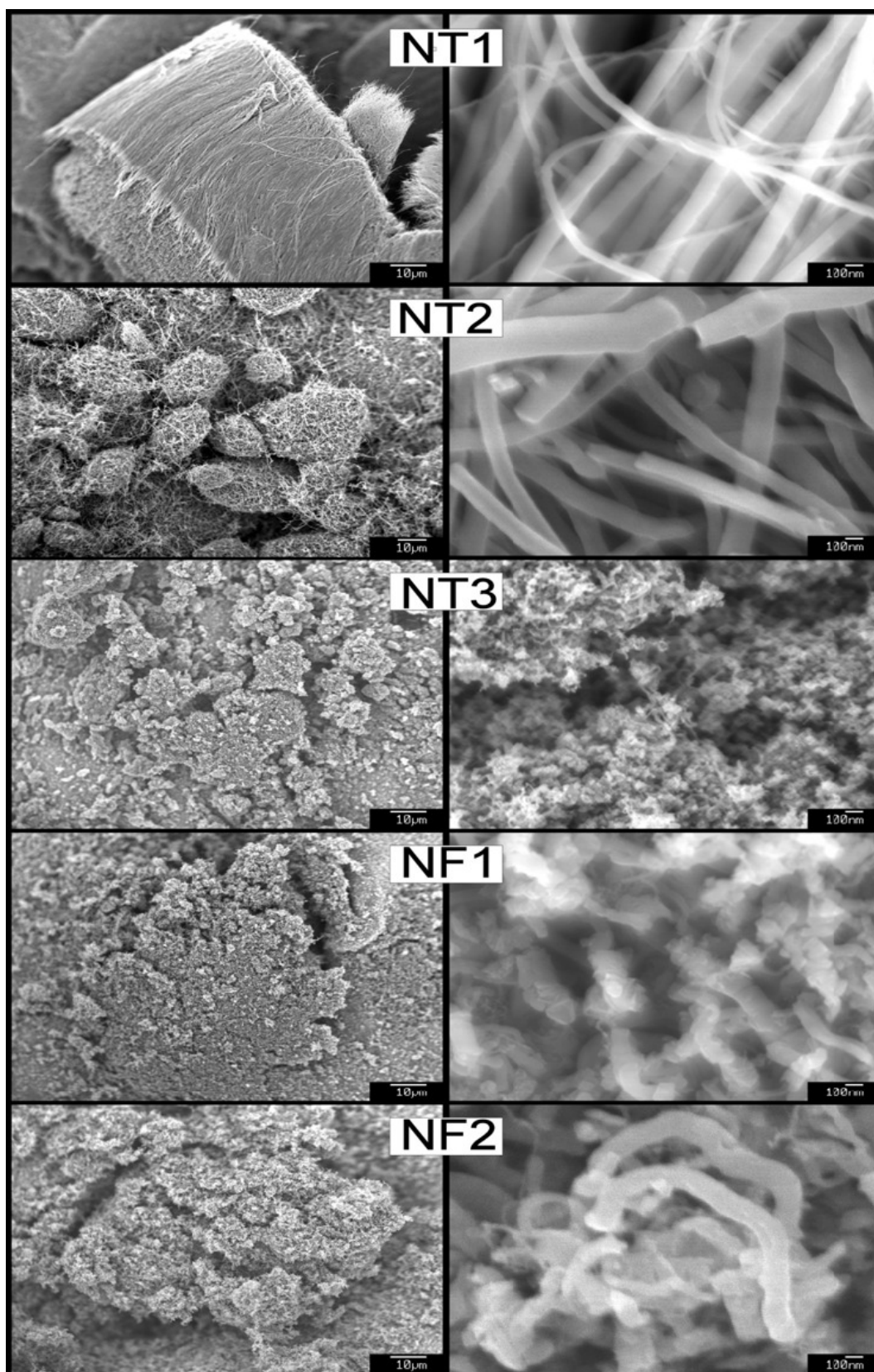


Figure 2: Micrographs of the as-produced nanoparticle samples used in this study.

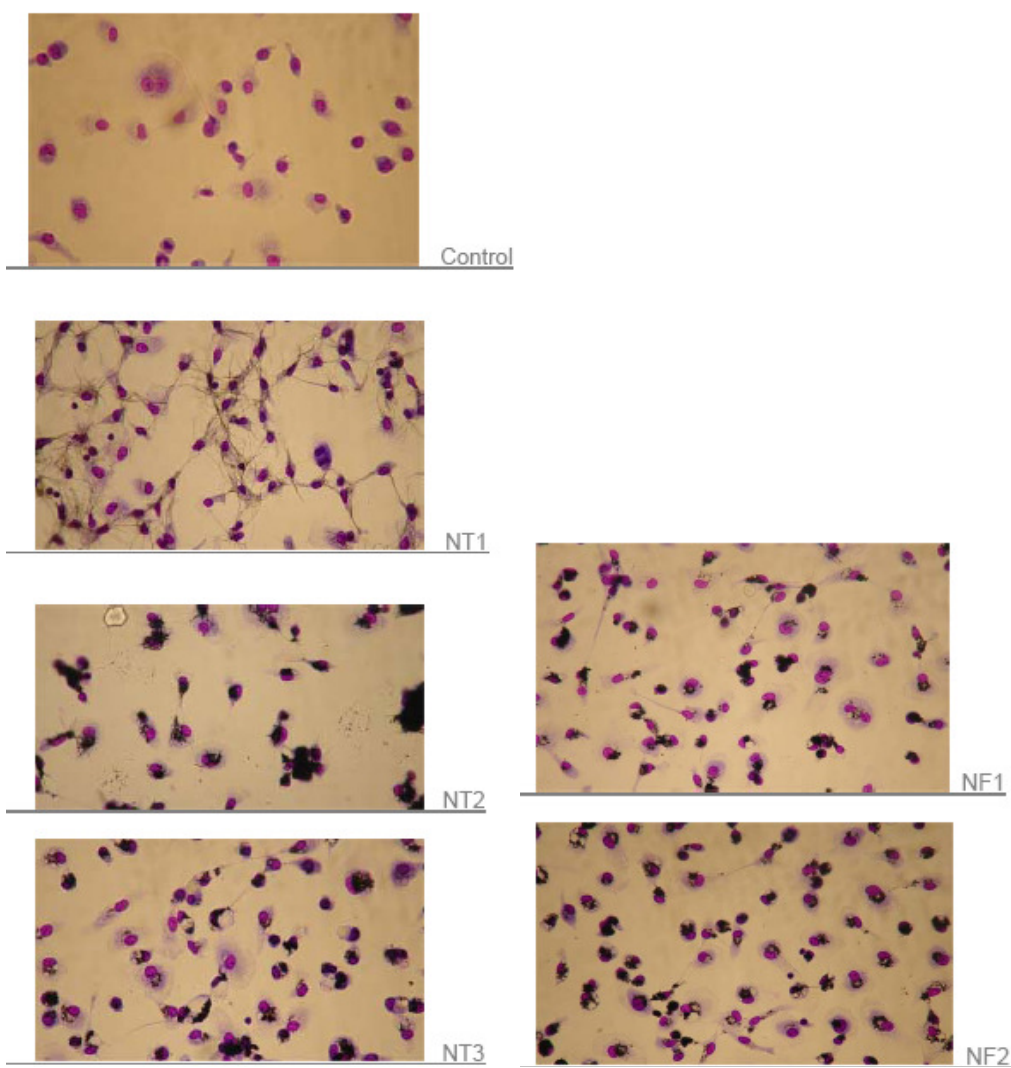


Figure 3 Light microscope images of human peripheral blood mononuclear cells after 4 hours treatment with carbon NTs and NFs (magnification x400). In general, the CNF appeared to be readily phagocytosed by the macrophages

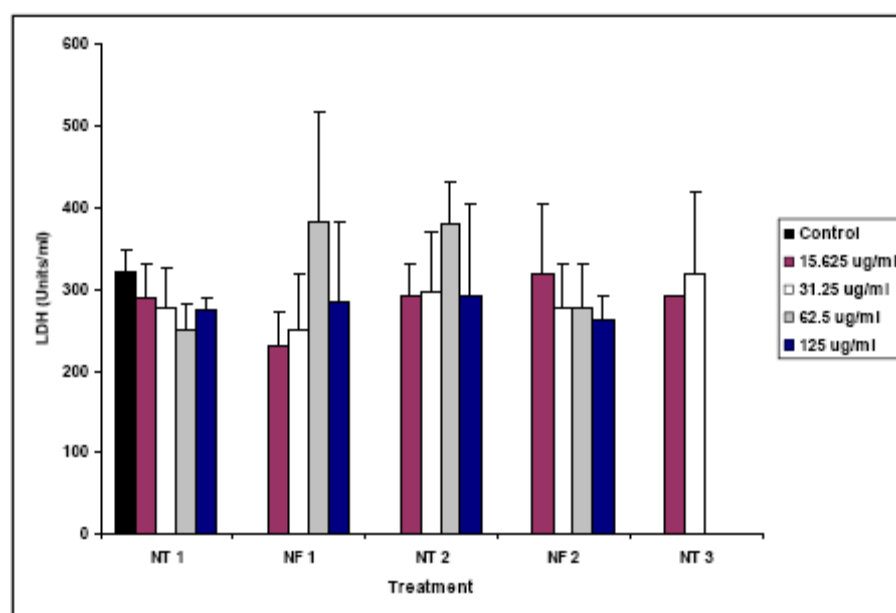
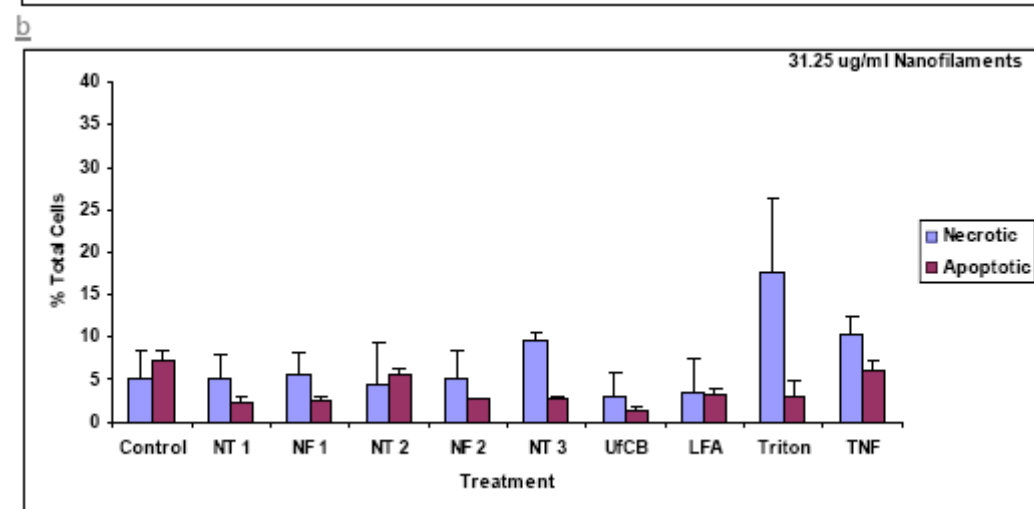
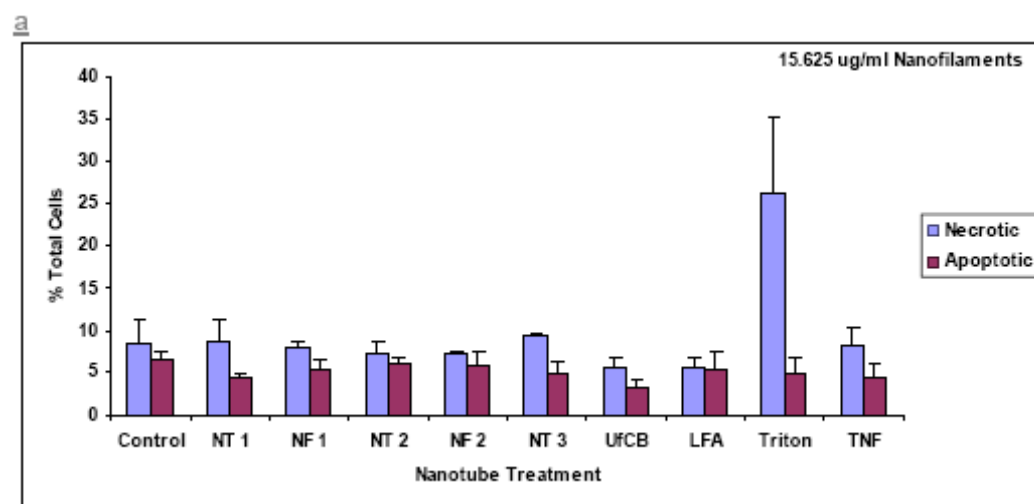
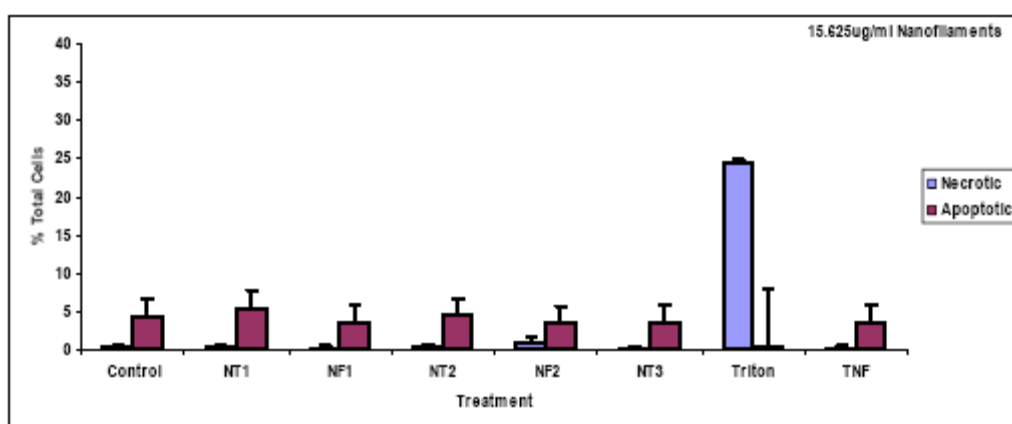


Figure 4 LDH release by human mononuclear cells after 4 hour treatment with carbon CNT's and CNFs. Data represents the mean \pm SEM of the number of LDH units/ml supernatant. There was no significant difference between the control and any of the treatments at any concentration (n=3).



c



d

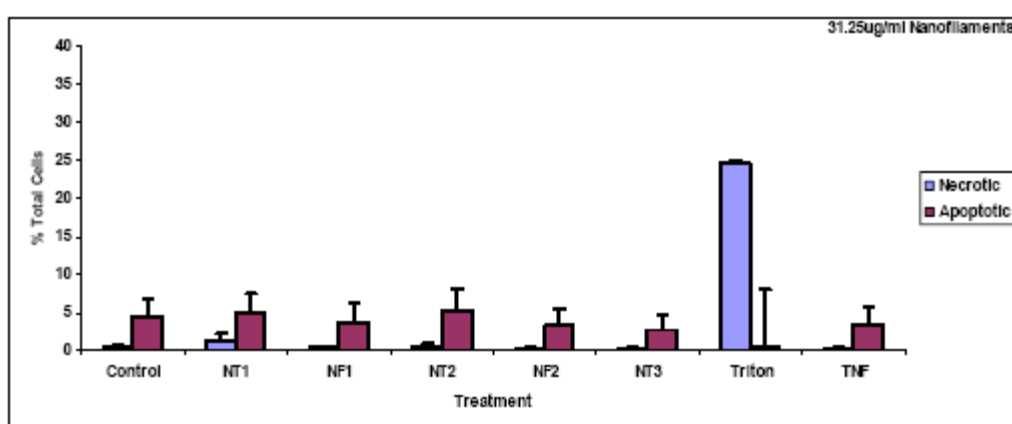


Figure 5 The percentage of apoptotic and necrotic THP-1 cells after treatment with CNFs or CNT's for 4 hours (a and b) and for 24 hours (c and d) Cells were treated with particles at 15.625 µg/ml and 31.25 µg/ml. The data represents the mean±SEM of two separate experiments.

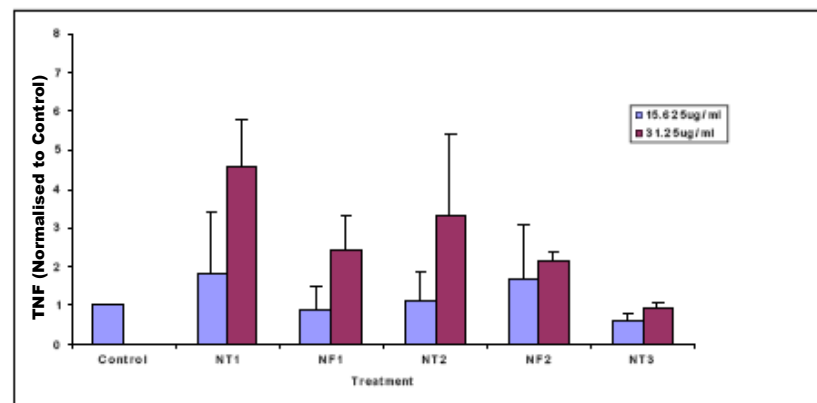
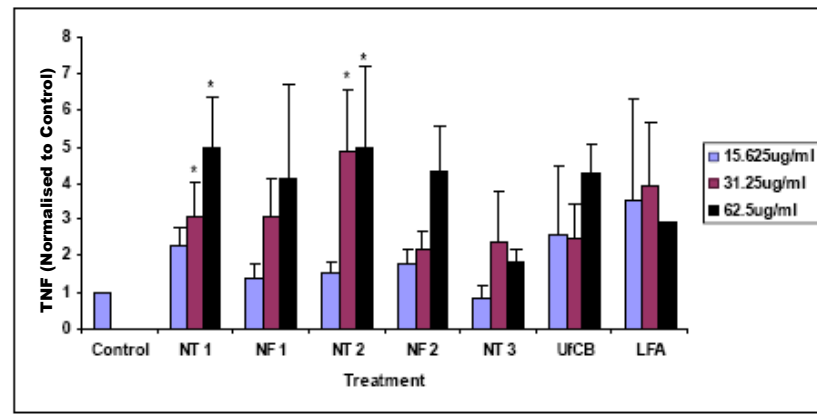


Figure 6 (a) TNF- α release by human mononuclear cells after 4 hours treatment with carbon NTs. Data represents the mean \pm SEM of the number of units of TNF- α released into the culture medium (Data was normalised to the control). There was a significant difference ($p < 0.05$) between the control and NT1 and NT2 treatments at 31.25ug/ml and 62.5ug/ml. (b) TNF- α release by THP-1 cells after 24 hours treatment with carbon NTs. Data represents the mean \pm SEM of the number of units of TNF- α released into the culture medium (Data was normalised to the control). There was no significant difference ($p > 0.05$) between the control and any of the treatments at both concentrations.

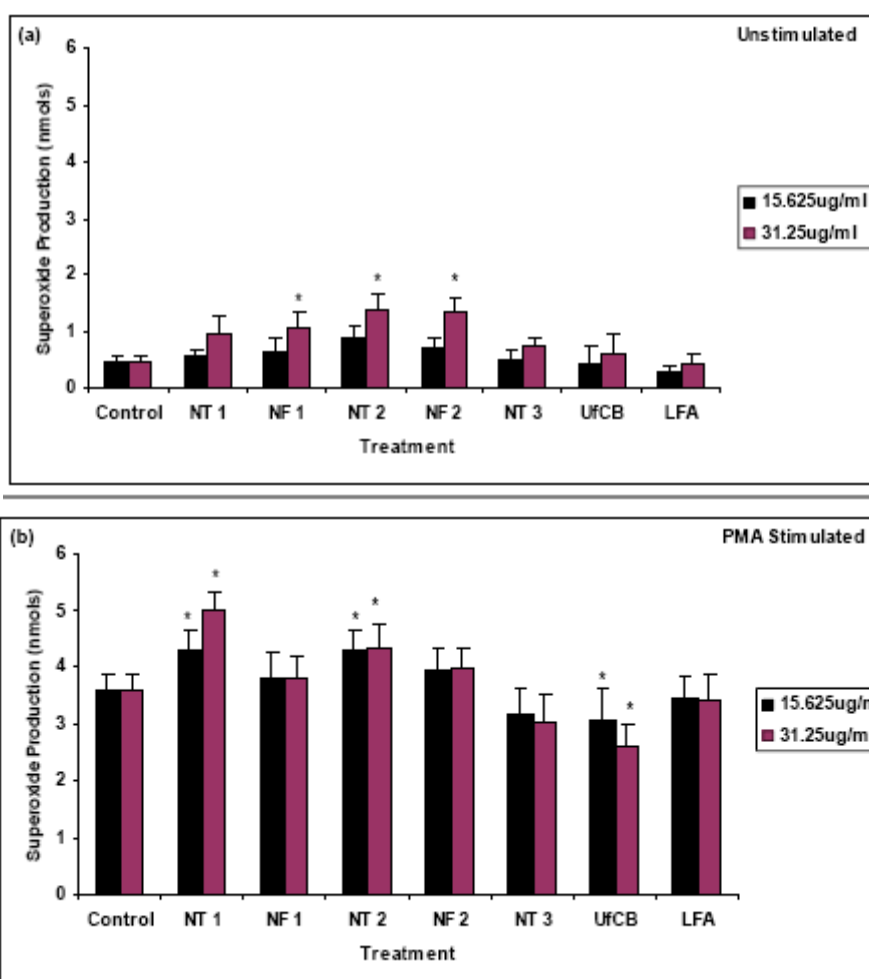


Figure 7 Superoxide production by human peripheral blood mononuclear cells after 2 hours treatment with carbon NTs and NF's in the presence or absence of PMA. Data represents the mean \pm SEM number of nmols of O_2^- per 500,000 cells/2 hours. There was no significant difference between any of the treatments in the unstimulated experiments. There was a significant difference ($p<0.05$) between the control and treatments NT1, NT2 and UfCB at both concentrations in PMA treated cells ($n=3$).

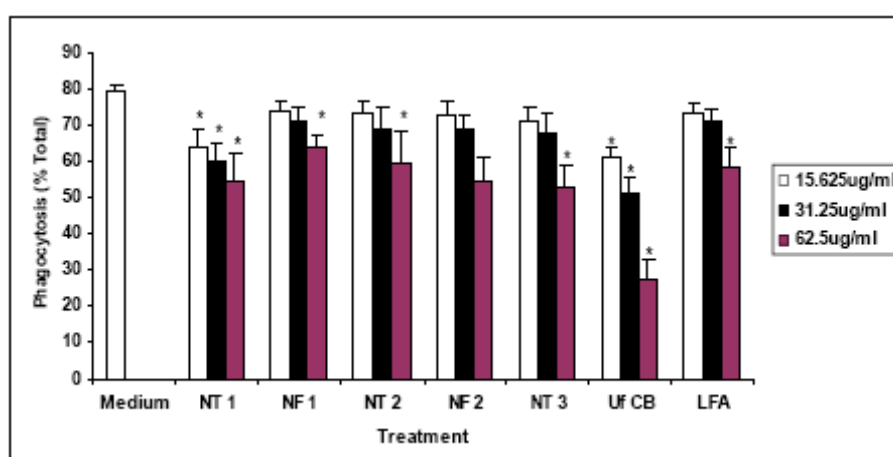


Figure 8 The ability of THP-1 cells to phagocytose fluorescently labelled *E-coli* bacteria after 4 hours treatment with carbon NTs. Data represents the mean \pm SEM of the number of *E-coli* bacteria in cells. There was a significant difference ($p<0.05$) between the control and all treatments except NF2 at a concentration of 62.5 μ g/ml ($n=3$).

<u>Sample No.</u>	<u>Structure</u>	<u>Source</u>	<u>Metal content (wt%)</u>	<u>Fibre Diameter (nm)</u>	<u>Surface area (m²/g)</u>	<u>Aggregation state</u>
<u>NT1</u>	<u>Nanotubes</u>	<u>Uni. of Cambridge</u>	<u>Fe: 5.1 ± 0.6</u>	<u>20-100</u>	<u>180</u>	<u>Individual fibres & in mats</u>
<u>NT2</u>	<u>Nanotubes & nanofibres</u>	<u>ASI (PR19)</u>	<u>Fe: 1.3 ± 0.1 (Trace S present)</u>	<u>~ 150</u>	<u>25</u>	<u>Predominantly micron-sized aggregates</u>
<u>NT3</u>	<u>Nanotubes</u>	<u>Uni. of Nottingham</u>	<u>Fe: 2.7 ± 0.2</u>	<u>~ 20</u>	<u>183</u>	<u>Predominantly micron-sized aggregates</u>
<u>NF1</u>	<u>Platelets and herringbone</u>	<u>Uni. of Nottingham</u>	<u>Ni: 0.3 ± 0.1</u>	<u>50-150</u>	<u>144</u>	<u>Predominantly micron-sized aggregates</u>
<u>NF2</u>	<u>Platelets</u>	<u>Uni. of Nottingham</u>	<u>Ni: 0.4 ± 0.1</u>	<u>50-150</u>	<u>88</u>	<u>Predominantly micron-sized aggregates</u>
<u>UfCB</u>	<u>Carbon black</u>	<u>Degussa Printex 90</u>	<u>None</u>	<u>Primary particle size is 14 nm</u>	<u>300</u>	<u>Predominantly micron-sized aggregates</u>
<u>LFA</u>	<u>Long fibre asbestos</u>	<u>Canadian Asbestos Institute</u>	<u>Fe 0.49±0.13</u>	<u><200nm</u>	<u>8.3</u>	<u>Predominantly micron-sized aggregates</u>

Table 1 Characteristics of the samples used in this study